Quarkonium azimuthal anisotropy in ultrarelativistic heavy-ion collisions with ALICE at the LHC

Robin Caron

To cite this version:

Robin Caron. Quarkonium azimuthal anisotropy in ultrarelativistic heavy-ion collisions with ALICE at the LHC. High Energy Physics - Experiment [hep-ex]. Université Paris-Saclay, 2021. English. NNT : 2021UPASP084 . tel-03387833v2

HAL Id: tel-03387833
https://theses.hal.science/tel-03387833v2
Submitted on 25 Oct 2021

Anisotropie azimutale de quarkonium dans les collisions d’ions lourds ultrarelativistes avec ALICE au LHC

Quarkonium azimuthal anisotropy in ultrarelativistic heavy-ion collisions with ALICE at the LHC

Thèse de doctorat de l’université Paris-Saclay

École doctorale n° 576, Particles, Hadrons, Energy, Nuclei, Intrumentation, Imaging, Cosmos et Simulation (PHENIICS)

Spécialité de doctorat: Physique Hadronique

Unité de recherche: Université Paris-Saclay, CEA, Département de Physique Nucléaire, 91191, Gif-sur-Yvette, France

Référent: : faculté des sciences d’Orsay

Thèse présentée et soutenue à Paris-Saclay, le 28/09/2021, par

Robin CARON

Composition du Jury

Patrick Robbe Directeur de recherche, Université Paris-Saclay, IJCLab	Président
Roberta Arnaldi Directrice de recherche, INFN di Torino	Rapporteur
Frédéric Fleuret Directeur de recherche, Institut Polytechnique de Paris	Rapporteur & Examinateur
Pol-Bernard Gossiaux Professeur des Universités, IMT Atlantique, Subatech	Examinateur
Jean-Yves Ollitrault Directeur de recherche, Universté Paris-Saclay, IPhT	Examinateur
Alexandre Zabi Directeur de recherche, Institut Polytechnique de Paris	Examinateur

Direction de la thèse

Javier Castillo Castellanos Directeur de recherche, Université Paris-Saclay, Irfu	Directeur de thèse
Stefano Panebianco Directeur de recherche, Université Paris-Saclay, Irfu	Co-directeur de thèse

Thèse de doctorat

NNT: 2021UPASP084

Abstract

The inclusive J/ψ elliptic (v_2) and triangular (v_3) flow coefficients measured at forward rapidity ($2.5 < y < 4$) in Pb–Pb collisions at $\sqrt{s_{\mathrm{NN}}} = 5.02$ TeV using the ALICE detector at the LHC are reported. The entire Pb–Pb data sample collected during Run 2 is employed, amounting to an integrated luminosity of 750 μb^{-1} at forward rapidity. The results are obtained using the scalar product method and are reported as a function of transverse momentum p_{T} and collision centrality. The centrality averaged results indicate a positive J/ψ v_3 with a significance of more than 5σ at forward rapidity in the p_{T} range $2 < p_{\mathrm{T}} < 5$ GeV/c. The forward rapidity v_2, v_3, and v_3/v_2 results at low and intermediate p_{T} ($p_{\mathrm{T}} \lesssim 8$ GeV/c) exhibit a mass hierarchy when compared to pions and D mesons, while converging into a species-independent behavior at higher p_{T}. At low and intermediate p_{T}, the results could be interpreted in terms of a later thermalization of charm quarks compared to light quarks, while at high p_{T}, path-length dependent effects seem to dominate. The J/ψ v_2 measurements are further compared to a microscopic transport model calculation. Using a simplified extension of the quark scaling approach involving both light and charm quark flow components, it is shown that the D-meson v_{n} measurements can be described based on those for charged pions and J/ψ flow.

The first measurement of the Υ(1S) elliptic flow coefficient is also reported at forward rapidity ($2.5 < y < 4$) in Pb–Pb collisions at $\sqrt{s_{\mathrm{NN}}} = 5.02$ TeV. The results are also obtained with the scalar product method and are reported as a function of transverse momentum up to 15 GeV/c in the 5–60% centrality interval. The measured Υ(1S) v_2 is consistent with both zero and with the small positive values predicted by transport models within uncertainties. The v_2 coefficient in $2 < p_{\mathrm{T}} < 15$ GeV/c is lower than that of inclusive J/ψ mesons in the same p_{T} interval by 2.6 standard deviations. These results, combined with earlier suppression measurements, are in agreement with a scenario in which the Υ(1S) production in Pb–Pb collisions at LHC energies is dominated by dissociation limited to the early stage of the collision whereas in the J/ψ case there is substantial experimental evidence of an additional regeneration component.

Remerciements

Un certain nombre de personnes ont contribué à ma formation, à la réalisation et à l'aboutissement de ce travail de thèse, cette partie à pour but de remercier toutes ces personnes.

Tout d'abord, mes plus chaleureux remerciements vont à mon directeur de thèse Javier. De par son experience scientifique, sa disponibilité, et sa bienveillance, j'ai pu bénéficier de ses précieux conseils avisés et apprendre ce qu'est la rigueur d'une mesure expérimentale. Bien sûr durant ces trois années de thèse il y a de multiples épisodes de hauts et de bas, mais il a toujours su m'aiguiller dans les bonnes directions lors de nombreuses discussions, pour finalement mener à bien ces travaux, et à terme ce manuscript. Sa patience et ses jugements toujours très justes ont permis de débloquer de nombreuses situations. Je tiens aussi à remercier très particulièrement mon co-directeur de thèse Stefano. Ce fut la première personne avec qui j'ai fait connaisance au cours d'un stage de master, sans lui je n'aurais certainement pas effectué ces quelques années de thèse ici. Ses grandes qualités scientifiques, son sens critique, sa pédagogie, et ses encouragements ont permis de garantir un encadrement très appréciable durant cette thèse, tant sur le plan proffessionnel que humain. Je me souviendrais toujours de la première fois où je suis venu au CERN en mission (comme un petit rêve de gosse), j'en retiens un très bon souvenir. J'exprime ici toute ma gratitude. Merci pour tout !

Je remercie l'ensemble des membres du jury pour avoir pris le temps de lire et juger mes travaux de recherche : en particulier Patrick Robbe pour avoir accepté de présider le jury, mes rapporteurs Roberta Arnaldi et Frédéric Fleuret pour leurs commentaires et leur relecture critique du manuscrit, et enfin Pol-Bernard Gossiaux, Jean-Yves Ollitrault et Alexandre Zabi pour leurs nombreux commentaires instructifs.

Bien évidemment je souhaite dire un grand merci à tous les membres du groupe ALICE du DPhN. En premier lieu, je remercie grandement notre directeur Alberto, pour m'avoir accueilli au sein du laboratoire LQGP. Mes remerciements vont aussi tout particulièrement à Michael, pour ses nombreux conseils, sa disponibilité, et pour sa manière inspirante d'aborder certains aspects de la physique. Je remercie également tous les autres physiciens dont j'ai pu faire la connaissance et discuter de nombreuses fois : Hugo, Andry, Satoshi, Hervé, et Andrea. Enfin, j'ajoute un grand merci aux autres thèsards que j'ai pu connaître, tous participent à un dynamisme intellectuel et à la bonne entente dans le groupe : Florian avec qui j'ai partagé deux années très complètes, des bières et de bonnes discussions, et puis bien sûr Aude, Sébastien, Maurice qui apportent constamment de la nouveauté et de la bonne humeur, je vous souhaite plein de réussite pour le futur de vos projets communs et personnels.

Je souhaite aussi remercier le directeur du département Franck, pour m'avoir accueilli et donné l'opportunité de réaliser cette thèse dans de très bonnes conditions matérielles. Je remercie l'ensemble du personnel du DPhN, qu'il soit scientifique, technique ou administratif. Je tiens à remercier Christophe, Danielle (la maman des doctorants), Isabelle (toujours sympatique et très efficace comme interlocutrice pour les démarches administratives), Francesco (mon tuteur), Loïc (pour les sorties running)... J'aimerais dire aussi un grand merci aux autres doctorants du DPhN pour les nombreuses discussions autour d'un café, d'un repas, ou d'une bière : Charles, Vladimir, Zoé, Brian, Mickael, Benjamin, Christopher, Antoine... Je prie ceux que j'aurais pu oublier de ne pas m'en vouloir.

Je tiens à remercier l'ensemble de la collaboration ALICE, sans qui cette thèse et ces résultats n'auraient pas vu le jour. Plus particulièrement les membres du groupe de Lyon avec qui j'ai pu collaborer de nombreuses fois : Cvetan Cheshkov et Antonio Uras. Je remercie aussi mes collaborateurs du groupe de Oslo : Ionut Arsene et Alexandra Neagu. Ce fut un réel plaisir de travailler avec vous.

Enfin, je souhaite remercier personnellement mes amis, et ma famille, pour ces trois années passées. Leur présence et leur soutien tout au long de cette thèse a clairement rendu cette petite partie de ma vie nettement plus agréable.

> *"Un soir consacré à la lecture des grands livres est pour l'esprit ce qu'un séjour en montagne est pour l'âme."*
>
> — André Maurois, Romancier (1885 - 1967)

Figure 1: Brumes matinales dans les Alpes Françaises.

Contents

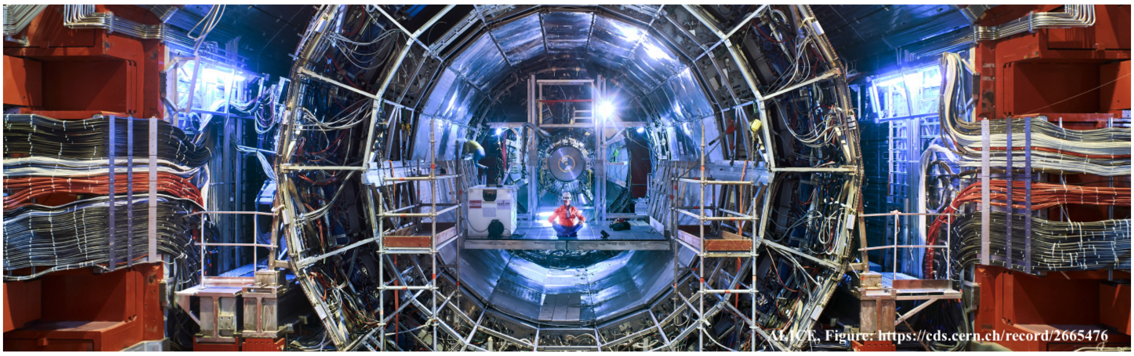

ALICE, Figure: https://cds.cern.ch/record/2665476

General introduction

What is matter made of? What are the laws that govern our world? What is the origin of the Universe? These fundamental questions are certainly those which have animated physicists for many years, and which remain. Quarks and gluons as elementary particles, went on to become the constitutive “bricks” of neutrons and protons (nucleons), what the matter is mainly made of. Due to a strong interaction, these particles are confined inside atomic nuclei. However at high energy or temperature, this interaction becomes weaker and weaker, and then it becomes impossible to see any kind of bricks assembly.

One of the most ambitious program from the high energy nuclear physics community is certainly trying recreate on earth the unique conditions that have been existed in the first microseconds of our universe. This program would not have emerged without the great prowess of particle accelerators and electronic developments during the last decades, which were able to produce many collisions of nuclei at unprecedented high energies. Based on our current knowledge and observations, the early universe had to be an extremely dense and super-hot liquid, where all the existing elementary constituents were deconfined, which means evolving like quasi-free particles. Recreating such a state in the lab, requires a great collaborative, scientific and technical effort. In particular there is one place on earth where these conditions are met together, and it is located at the Large Hadron Collider near Geneva, at the Franco-Swiss border. Four experiments using the LHC beams study the results of collisions of ultra-relativistic systems with a very high center-of-mass energy.

The idea behind one of these experiments, ALICE, is to recreate the exotic primordial “soup of elementary particles” known as quark-gluon plasma that appeared microseconds after what the so-called Big-Bang. In order to achieve its goals, the experiment started in 2010, colliding the nuclei of lead atoms inside the LHC’s circular tunnel to produce incredibly dense and hot fireballs of subatomic particles at over 10 trillion °C. The lifetime of this state is extremely short, roughly $\sim 10^{-23}$s, hence it is clear that we can not study it directly. Instead, we have to wait until the moment when its temperature becomes low enough ($\sim$ 2 trillion of °C) so that many particles (called mesons and baryons) are produced from the quarks and gluons, and then these resulting particles can be tracked and measured in our detectors. The study of different particle species and their production in such ultra-relativistic heavy-ion collisions allows us to go back to the quark-gluon plasma properties. In addition, the production of rare heavy quarks in the very early stages makes also possible to probe the microscopic transport properties and the fluid dynamics, so particular to this state.

In this manuscript, the first chapter defines succinctly the main concepts related to the study of matter at very high energies. In particular, the important points associated to the strong interaction, the evolution of an ultrarelativistic heavy-ion collision, the plasma of quarks and gluons, its hydrodynamics behavior are described. Then, the theoretical basis and the previous experimental results are outlined emphasizing the interest of anisotropic flow measurements, heavy quarks and quarkonia. The second chapter presents the ALICE experimental setup which among other subdetectors, disposes of a forward muon spectrometer, this thesis work is devoted to exploit its performances to detect dimuons in order to measure quarkonia. The third chapter addresses the general analysis techniques and the event calibration used to produce the results. The fourth chapter presents the main part of the flow-specific data analysis, which contains the different steps leading to the final measurements, from the event and track selection criteria, to the quarkonium raw yield extraction and azimuthal anisotropy measurements, to Monte Carlo studies and systematic uncertainties determination. In the fifth chapter, the final results obtained in this thesis are presented. The measured experimental data are compared to theoretical calculations from various models, the interpretations that emerge are discussed. Finally, the results of this thesis will be briefly condensed into a general conclusion.

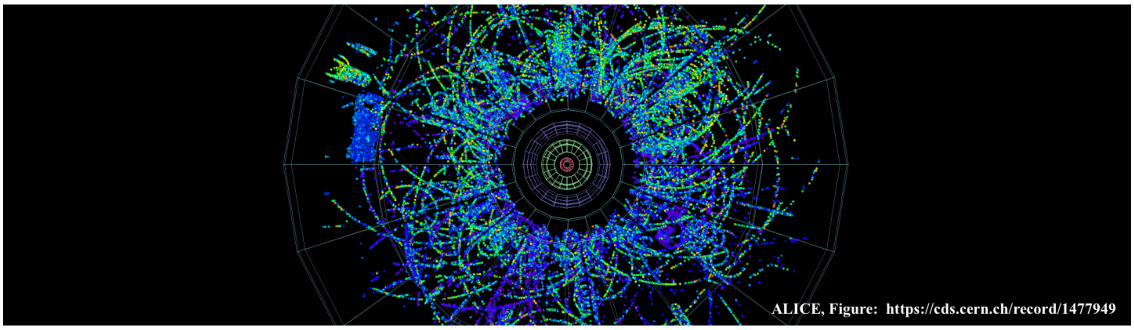
ALICE, Figure: https://cds.cern.ch/record/1477949

Chapter 1

Introduction to high energy nuclear physics

In this introduction chapter, the basic framework within which the phenomenom of anisotropic flow associated to the quarkonium states can be studied and understood is presented. The starting point is about the basics of the Standard Model of particles physics and the theory describing the cohesion of matter, the interactions between quarks and gluons via the strong force, the quantum chromodynamics (QCD). The second section describes how the ultrarelativistic heavy-ion collisions at LHC can be used to study the strong interaction and the matter under extreme conditions. In the third section, the quark-gluon plasma (QGP) is introduced, a state of matter existing only at extremely high temperature and energy density. The fourth section explains how the anisotropic flow phenomena emerge in the relativistic hydrodynamics framework. Then, the basic methodology to extract anisotropic flow coefficients is described. Finally, the heavy-quark properties, from their initial production to their bound states are introduced. The natural units $c = \hbar = k_B = 1$ and the Minkowski metric $g^{\mu\nu} = \mathrm{diag}(1, -1, -1, -1)$ are used throughout this chapter.

Contents

1.1 Exploring matter under extreme conditions

The matter inside and around us, from the biggest star in the space to the smallest visible grain, is composed of a large amount of atoms. These objects have been known for nearly a century, the atom size is roughly 10^{-10} m, it is made of electrons "orbiting" via electromagnetic force around the nucleus, which is composed of protons and neutrons, with a size of the order of 10^{-15} m. However, in the 60s, experimental physicists [1] discover that the nucleons (protons and neutrons) are composite systems made of elementary particles called *quarks*, interacting together via the strong force, which holds also the nucleons inside the nucleus.

The Standard Model is one of the successful tools that began to be developed [2, 3] to describe the three main interactions observed in our Universe. This model attempts to explain matter in the simplest way in terms of elementary particles and their interactions. From this point of view, matter is composed of particles divided in two types: the *fermions* which are particles that follow Fermi–Dirac statistics and have fractional spin (these particles obey to the Pauli exclusion principle), and the *bosons* which are particles that follow Bose–Einstein statistics and have an integer spin.

- Fermions are classified in three families of quarks: $(u,\ d)$, $(c,\ s)$, $(t,\ b)$ corresponding to six "flavours" ($N_f = 6$) denoted as *up, down, strange, charm, beauty,* and *top*, ordered from the lighter to the heavier. Three other families of leptons exist: $(e,\ \nu_e)$, $(\mu,\ \nu_\mu)$, $(\tau,\ \nu_\tau)$. For each quark and lepton, the corresponding anti-quark and anti-lepton also exist.

- Bosons are the mediators of the fundamental interactions, the photon (γ) carries the electromagnetic force, the $W^{\pm}$ and Z^0 the weak force (affecting all fermions and governing the nuclear reactions), and the gluons (g) associated to the strong force (leading to the cohesion of nucleons inside the nucleus). A last boson (H) was recently discovered in 2012 and theorised by Brout, Englert and Higgs in 1964 [4, 5] in order to explain why fermions, as well as the $W^{\pm}$ and Z^0, remain massless in the Standard Model. In order to perfectly complete the story, the gravity as one of the fundamental interactions should also be described by a boson, for which we do not have yet any sign of its discovery.

The relativistic quantum field theory is the way that the Standard Model describes the interactions between elementary particles (which have no known substructure) by the exchange of force carriers called gauge bosons [6]. In this picture, the interactions are classified into two fundamental sectors: the strong and electroweak. At low energies (< 100 GeV/c) the symmetry of the electroweak interaction (represented by the special unitary `SU(2)`×`U(1)` group) is spontaneously broken by the Higgs mechanism, which means that all particles interact more or less with the H field, in order to be massive or not (the photon and the gluon do not interact with this field, their masses remain zero). Also at this low energy regime, the electromagnetic and weak force manifest themselves as two distinct forces. Both the weak and electromagnetic interaction are well understood and can be described by quantum electrodynamics (QED) and the electroweak theory (EWT).

The strong interaction is described by quantum chromodynamics (QCD) [7], a non-abelian quantum field gauge theory (based on local symmetry of the `SU(3)` group) that focuses on the dynamics of the color charged particles. The contributions of the propagators, the interactions between gluons and between quarks and gluons can be recognizable in the gauge invariant QCD Lagrangian (see first symbolic Feynman diagrams on Fig. 1.1), one of these formulation is given by [8]

$$\mathcal{L} = \sum_{q=1}^{N_f} \bar{\psi}_{q,a}(i\gamma^\mu \partial_\mu \delta_{ab} - g\gamma^\mu t^C_{ab} A^C_\mu - m_q \delta_{ab})\psi_{q,b} - \frac{1}{4} G^A_{\mu\nu} G^{A,\mu\nu}, \tag{1.1}$$

where repeated indices are summed over, $\psi_{q,a}$ denote the quark fields spinors associated to a flavor q, a color-index $a = \{r, g, b\}$, and for a quark mass m_q. A^C_μ represent the vector gluon fields (with C running from 1 to $N_c^2 - 1 = 8$ corresponding to the possible quantum color combinations for a gluon), γ^μ represent the Dirac γ-matrices, $t^C_{ab} = \lambda^C_{ab}/2$ correspond to the eight 3×3 Gell-Mann matrices and are the generators of the `SU(3)` group. The quantity g is the QCD coupling constant and δ_{ab} is the Kronecker delta symbol. In order to satisfy the gauge invariance (where $G^A_{\mu\nu}$ could be modified, in some ways, with unaffected particle behavior), the gluon field strength tensor is constructed as

$$G^A_{\mu\nu} = \partial_\mu A^A_\nu - \partial_\nu A^A_\mu - g f_{ABC} A^B_\mu A^C_\nu, \qquad [t^A, t^B] = i f_{ABC} t^C, \tag{1.2}$$

where the canonical commutation relation introduces the structure constant f_{ABC}. Each term in the lagrangian could be associated to a corresponding Feynman diagram. In this simplistic representation, the quark and gluon propagator can be associated to the two first terms (assimilate to $\sim \psi\bar{\psi}$ and $\sim A^2$). The quark-gluon interaction can also be distinguished as the third term ($\sim g\psi\bar{\psi}A$). The remaining two terms correspond to the three ($\sim gA^3$) and four ($\sim g^2A^4$) gluon self interactions.

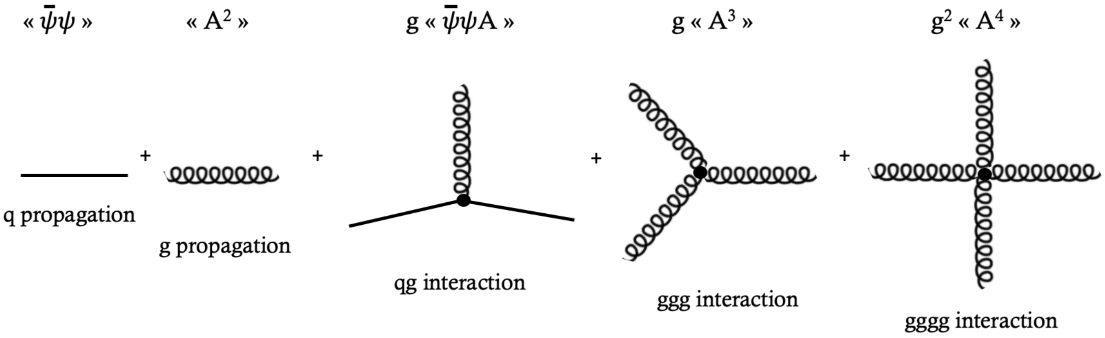

Figure 1.1: Symbolic representation of the first terms in the QCD Langrangian.

The gluon self interactions are unique to QCD and cause anti-screening effects. In both QCD and QED, loop diagrams are allowed, which effectively decrease the coupling strength at increasing distances, as the pair of virtual particles in the loop briefly polarizes the vacuum (an effect called screening). However, in QCD, loop diagrams with self-interaction of gluon are also allowed because gluons, in contrast to electroweak bosons, can self interact. Since gluons are charged, these loops anti-screen increase the color fields. The QCD coupling strength, governed by the coupling constant α_s, increases for interactions with low momentum transfer (Q^2) as a result of this strong anti-screening (e.g. quarks are strongly bound into proton or neutron). Whereas at high energies (or equivalently at short distances) α_s asymptotically decreases to zero meaning that quarks interact weakly, as it is shown in Fig. 1.2. The coupling constant formula taken from [9] is defined as

$$\alpha_s(Q^2) = \frac{4\pi}{(11 - \frac{2}{3}N_f)\ln(\frac{Q^2}{\Lambda^2_{\text{QCD}}})}, \tag{1.3}$$

where Q^2 is the transferred momentum, N_f the number of quark flavor, and Λ_{QCD} is the typical energy scale of the strong interaction.

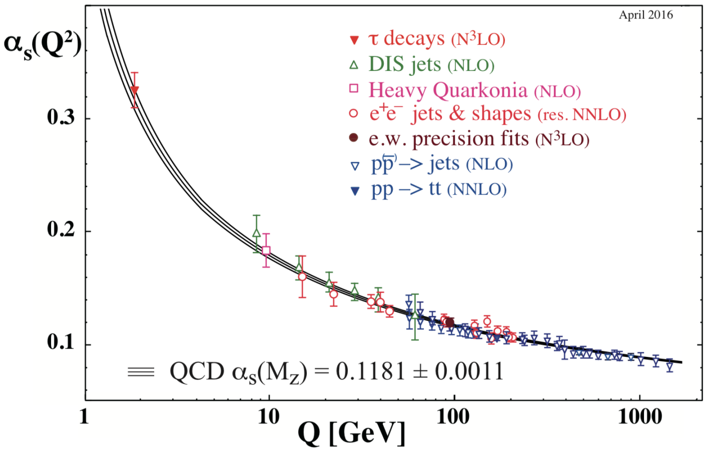

Figure 1.2: Evolution of α_s as a function of Q^2. Figure taken from [8].

The lagrangian complexity which mainly arises from the non-linearity of the interactions of the gluons, the strong coupling, the dynamical many body system and confinement, lead to the fact that it is very difficult to make any predictions directly from QCD. Neththeless, at high energy or short distance interactions, the coupling is small enough that this infinite number of terms can be approximated accurately by a finite number of terms, thus, perturbation theory techniques can be applied (pQCD). A well-established non-perturbative approach to solve the lagrangian, is the lattice QCD (lQCD), which is a lattice gauge theory formulated on a grid or lattice of points in space and time. The continuum QCD is recovered when the size of the lattice is taken infinitely large, and its sites infinitesimally close to each other.

One of the major phenomenons associated to QCD is the *confinement*, which results of the experimental observation that neither quarks nor gluons are observed as free particles in the nature. Indeed, they are confined via the strong force into hadrons as color-singlet (or color-neutral) combinations of quarks, anti-quarks and gluons. The hadrons are classified in two types, the quark-antiquark pairs ($q\bar{q}$) called mesons, and the three quark states (qqq) called baryons (see examples of different hadrons and their quark content in Fig. 1.3). The strong interaction is mediated by the exchange of color (the QCD analogue of electrical charge) with "charges" red, green, and blue (opposed to anti-red, anti-green, and anti-blue), which are strictly conserved. Instead of quark that carries a single color charge, gluon carry two charges, color and anti-color. The key difference between the electroweak and strong interaction is that as a result of this, gluons can self-interact, giving rise to QCD phenomena of color confinement and asymptotic freedom [10].

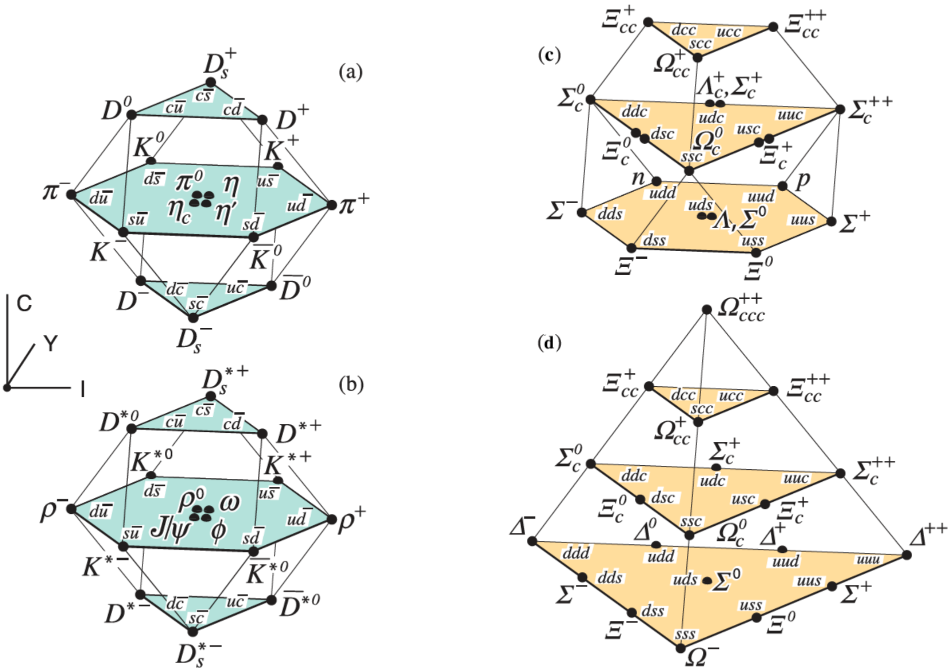

Figure 1.3: Quark model for different hadrons (with isospin I, charm $\mathcal{C}$, and hypercharge Y $= \mathcal{S} + \mathcal{B} - \mathcal{C}/3$, where $\mathcal{S}$ and $\mathcal{B}$ are the strangeness and baryon number). Strong interactions conserve hypercharge, but weak interactions do not. Figures [8]

A second major phenomenon related to QCD is the *chiral symmetry restoration*, which refers to the invariance under parity transformation by a fermion, corresponding to the symmetry of the left- and right-handed parts of the quarks (it is right-handed when the direction of its spin is the same as the direction of its motion, while it is left-handed when the directions of spin and motion are opposite). In the limit of vanishing quark masses ($m_q \approx 0$) the QCD Lagrangian shows no interactions between left- and right-handed quarks. This symmetry is approximately restored when quark masses are reduced from their large effective values in hadronic matter to their small bare ones at sufficiently high temperatures and energy densities. It can be usually represented with the chiral condensate as $\langle\bar{\psi}\psi\rangle = \langle\bar{\psi}_L\psi_R + \psi_L\bar{\psi}_R\rangle$. In the vacuum, the right-handed quarks interact with the left-handed quarks due to the non-zero quark masses, the chiral symmetry is then spontaneously broken $\langle\bar{\psi}\psi\rangle \neq 0$. However, at high energies one expects a restoration of the chiral symmetry, $\langle\bar{\psi}\psi\rangle = 0$, which is a sufficient condition to predict a phase transition related to it. Chiral symmetry restoration is predicted for light quarks (u, d and s), but not for heavier quarks (c, b or t), their mass term in the Lagrangian being more important.

Based on the asymptotic phenomenon, it was expected by a large majority of theorists, that a new state of matter containing deconfined quarks and gluons could exists at very high temperature and energy densities. It was also suggested that if such a state could be produced in laboratory, for example by colliding heavy ions at high energy, it should exhibit the same properties or similarly to a weakly interacting gas.

1.2 Ultrarelativistic heavy-ion collision evolution

The space-time evolution of the hadronic matter produced in the mid rapidity region of ultrarelativistic nucleus-nucleus collisions was clearly formulated by Bjorken in 1982 [11]. In this scenario, due to the Lorentz contraction, the accelerated heavy ion can be assimilated to a surface like a pancake along the z axis (i.e. the beam axis), because at $v \simeq c$, all moving objects observed from a system at rest shrink into plane structures. These objects have a typical nuclear radius R, which is around ten times larger than the nucleon size. The collision of highly relativistic nuclei offers the possibility of producing quasi-macroscopic systems of dense nucleonic and/or quark and gluon matter at relatively high temperature. A critical temperature T_c is needed for the phase transition from hadronic gas (where quarks are confined into hadrons) to a deconfined phase, where quarks and gluons are moving like quasi-free particles. Figure 1.4 shows the evolution of a heavy-ion collision. Let summarize below the time intervals expected in a central collision of high-energy heavy nuclei.

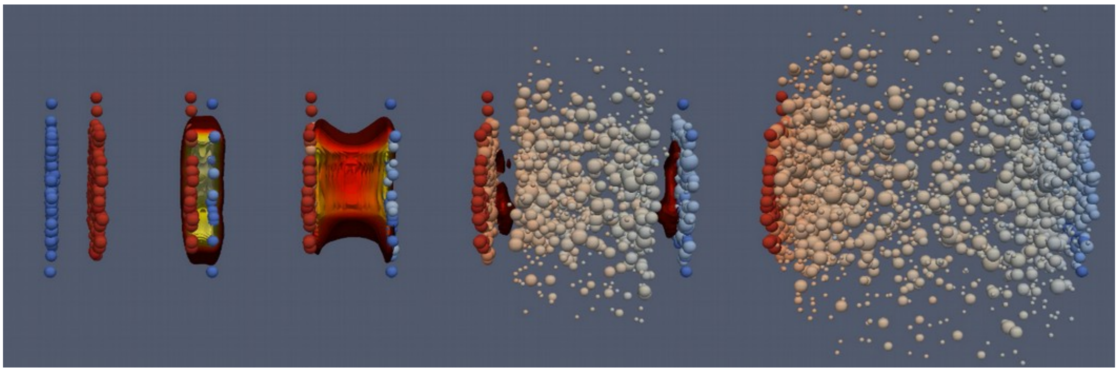

Figure 1.4: From the left to the right, screenshot of the evolution of an ultrarelativistic heavy-ion collision. Figure taken from [12].

- **Collision** ($t = 0$): The two colliding systems moving close to the speed of light c which are strongly Lorentz-contracted along the collision axis, collide at $t = 0$ in the collision evolution. If the time taken by the nuclei to cross each other is infinitesimal compared to $\tau_0 \approx 1/\Lambda_{\mathrm{QCD}} \approx 1$ fm/c (the typical time scale of QCD), then the collision is ultrarelativistic, which means that the phase transition occurs.

- **Pre-equilibrium** ($0^+ \lesssim t \lesssim 0.1$ fm/c): Very closely after the collision, a strong quasi-classical transverse gluon field (glasma) emerges (where its evolution is dictated by classical Yang-Mills equations [13]). Hard scattering processes take place (e.g. jet or heavy quark pairs production) where particles are produced from the energy deposited in the interaction region formed by the colliding ions.

- **Out-of equilibrium** ($0.1 \lesssim t \lesssim \tau_0$ fm/c): The system is now described by a set of particles and evolves according to a Boltzmann equation. The expansion is unstable and asymmetric between the transverse and longitudinal plane, the equilibration process builds up longitudinal pressure. The thermal equilibrium will be reached when the phase space density becomes isotropic.

- **Thermal equilibrium and hydrodynamics** ($\tau_0 \lesssim t \lesssim 10$ fm/c): The matter undergoes into a state where the color charges (quarks and gluons) are deconfined, and in a thermal equilibrium. This leads to the creation of the quark-gluon plasma at around $\tau_0 \sim 1$ fm/c. At this stage, the matter behaves as almost perfect fluid, which can be described by hydrodynamics. This system then expands to the surrounding vacuum and cools down.

- **Phase transition and chemical freeze-out** ($10 \lesssim t \lesssim 15$ fm/c): The end of hydrodynamics is approximately around $t \sim 10$ fm/c, which is precipitated by the fast cooling and a quick expansion of the created matter. The phase transition is characterized when the temperature of the medium becomes lower than the critical one T_c. The color charges initially present in the system and during its expansion will hadronize to form the hadrons (pions $\pi^{\pm}$, kaons $K^{\pm}$, protons $p + \bar{p}$, ...). Therefore, there is no well-defined separation of phases, but it can instead be estimated from the point where the thermodynamic properties change rapidly. The system continues to expand and cool down, and the hadrons continue to interact with each other. The so-called chemical freeze-out is the point where the inelastic processes cease and the chemical composition of the system (i.e., composition of hadrons) does not change anymore. This occurs almost at the same time as the hadronization, which represents the phase transition to the hadron gas.

- **Kinetic freeze-out and free stream** ($15 \lesssim t < \infty$ fm/c): Hadrons might still interact via elastic scatterings until their density is too low that no more elastic collisions take place, the end of this phase is called kinetic freeze-out. The formed hadrons fly into the vacuum (some of them can possibly decay into other particles) and are finally detected in the detectors, where the spectrum of emitted particles is measured.

In practice, the main focus of experimentation with nuclear beams at the LHC is to study the quark-gluon plasma properties, before that, many heavy-ion experiments exploited the result of these collisions but at lower energies (over a very wide energy range). Hence, our final goal is to learn how collective phenomena and macroscopic properties involving many degrees of freedom, emerge under extreme conditions (generated by the ultrarelativistic heavy-ion collisions) from the microscopic laws of strong-interaction physics.

1.3 Accessing the quark-gluon plasma properties

Edward Shuryak in 1978, realized that the thermal fluctuations of gauge fields might actually produce a dominant effect over vacuum fluctuations, which would translate into dominant screening over anti-screening of color fields [14]. For this reason he coined the term quark-gluon plasma (QGP), for a state of matter consisting of deconfined quarks and gluons.

Experiments with heavy-ion collisions at RHIC and LHC create and diagnose the strongly-interacting matter under the most extreme conditions, in terms of density and temperature, which are the highest accessible in the laboratory. Under these conditions, the lattice QCD calculations predict that matter undergoes a phase transition to a QGP, in which color charges are deconfined and chiral symmetry is restored. Figure 1.5 shows the phase diagram of the hadronic matter and illustrates such a transition. Aside of its intrinsic interest, this line of research is central to our understanding of the Early Universe and the evolution of ultra-dense stars.

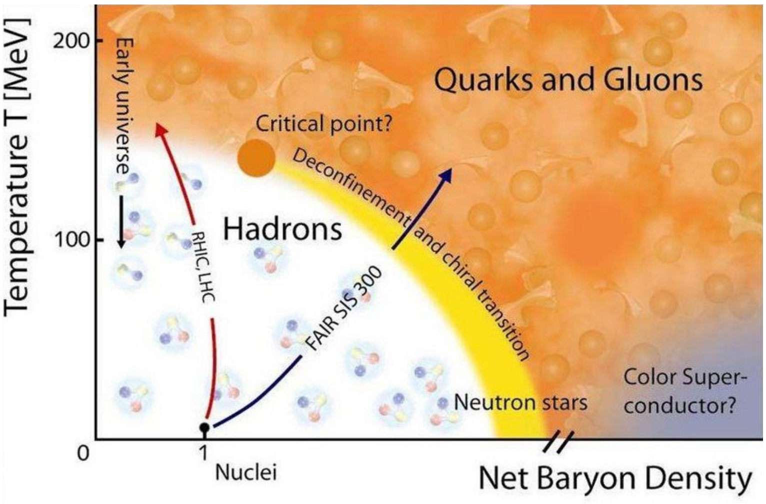

Figure 1.5: Sketch of the phase diagram (T, μ_{B}) representing the transition from a hardon gas (confined) to a deconfined phase (quark-gluon plasma). Figure taken from GSI heavy-ion group theory.

During an ultrarelativistic heavy-ion collision, the created hot and dense matter undergoes into a hadron gas through a phase transition, which can be characterized by a QCD phase diagram (T, μ_{B}). This transition occurs when sufficient energy density and temperature are reached, which is estimated from lattice QCD calculations to be

$$\begin{aligned} \varepsilon_{\mathrm{c}} &\approx 0.18 - 0.5 \quad \mathrm{GeV/fm^3} \qquad &\text{(critical energy density)},\\ T_{\mathrm{c}} &\approx 145 - 165 \quad \mathrm{MeV} \qquad &\text{(critical temperature)}. \end{aligned} \tag{1.4}$$

The scan of the boundary of the phase transition can be performed by varying the energy of collisions of heavy nuclei. Heavy-ion collisions at the highest possible energy at RHIC and the LHC probe the region of almost zero μ_{B} and very high T, while the ordinary nuclear matter is located at approximately $T \approx 0$ and $\mu_B \approx 1$ GeV. In the mid-rapidity region (defined in Eq. 1.6), where the net baryon density is zero, according to the Bjorken regime[1]. Assuming that the medium evolution does not change the final entropy per unit of rapidity $\mathrm{d}S/\mathrm{d}y$, one can estimate the initial temperature (or energy density) using lattice QCD equation of state and the initial entropy density defined as

$$s(\tau_0) = \frac{1}{A\tau_0} \frac{\mathrm{d}S}{\mathrm{d}y}\bigg|_{y=0}, \tag{1.5}$$

where τ_0 is the formation time and A is the transverse surface. Values of the total entropy per final state charged hadron S/N_{ch} are listed by [15] (table IV), which also reminds that the Bjorken formula underestimates the initial temperature.

Experiments commonly define the two quantities:

$$\begin{aligned} y =& \frac{1}{2} \ln \frac{(E + p_z)}{(E - p_z)} && \text{(rapidity)}, \\ \eta =& -\ln(\tan(\theta/2)) = \frac{1}{2} \ln \frac{(p + p_z)}{(p - p_z)} && \text{(pseudo-rapidity)}, \end{aligned} \tag{1.6}$$

where θ is the polar angle (between the beam axis and the direction of the emitted particle). In the limit of transverse momentum $p_{\mathrm{T}} = \sqrt{p_x^2 + p_y^2} \gg E$, we have the approximation $\eta \approx y$, which justifies the use of η as a measure of the longitudinal particle coordinate. η is also a measure of how boosted a particle is along the z direction with respect to the laboratory frame. Therefore, $\mathrm{d}N_{\mathrm{ch}}/\mathrm{d}\eta$ measured at mid-rapidity can be used to have an estimate of the energy density of the medium created in heavy-ion collisions using the Eq. 1.5 defined above. Using the typical time scale of QCD as $\tau_0 \approx 1$ fm/c and the multiplicity measured at LHC, it gives $\varepsilon \approx 15$ GeV/fm^3, which is an energy density value well above the critical value obtained previously.

As it was mentioned previously, due to the extremely short lifetime of the QGP, this state of matter can only be observed indirectly. Hence, the goal is to find the best observables that can be modified or affected by the the presence of this deconfined state. Its properties are then accessible via experimental measurements in ultrarelativistic heavy-ion collisions, through the following probes:

- **Global probes:** this first kind of probes is related to the main characteristics of the collisions such as the initial geometry or energy density. The multiplicity of the charged particles produced in the collisions or the spectator ion energy are among them. The centrality of the reaction (defined later) can be obtained from measurements of charged particle multiplicity N_{ch} and of the energy carried by participant and spectator nucleons of the collision.

---

[1] Nuclei are considered to be infinitely thin pancakes moving at c, the beam remnants continue moving forward, but mid-rapidity is dominated by produced particles. The created matter expands homogeneously in the longitudinal direction, until a specific time where particles materialize and will be in free streaming up to our detectors.

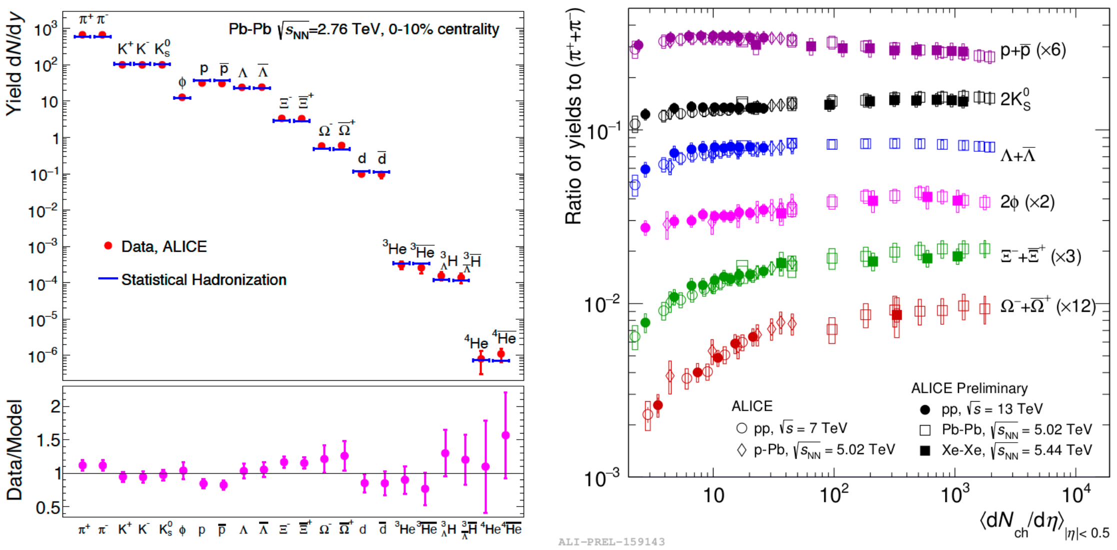

Figure 1.6: Left : for the most-central Pb–Pb collisions at 2.76 TeV, the best description of yields of particles per unit of rapidity at midrapidity, is obtained with $T_{\rm cf} = 156.5 \pm 1.5$ MeV, $\mu_{\rm B} = 0.7 \pm 3.8$ MeV, and a volume $V = 5280 \pm 410$ fm^3. Right: hadron yield ratio to pions as a function of the particle multiplicity in different collision systems. Figures taken from [16, 17].

- **Soft probes:** this second type of probes is used to study the hadronic phase and the freeze out. It is also a great tool to understand and measure the medium properties such as temperature T or baryo-chemical potential μ_B. The baryon chemical potential is the energy needed to increase the system's baryon number by one unit (by adding more quarks), and scales with the system's net quark density. Basically, the relative production of hadrons with light quarks (u, d, and s) depends on the state of the system at the chemical freeze-out. Thus, measuring the relative yields of different hadrons (pions π, kaons K, lambda Λ, protons p, ...) can be used in order to calculate the temperature of the system at the chemical freeze-out and the baryo-chemical potential [16]. This is usually done by fitting the measured relative yields with statistical models (see Fig. 1.6, left panel). In these models, the system can be considered as a *grand-canonical ensemble*, where the abundance of a particle species i can be written as

$$n_i(T, \mu_i, V) = \frac{g_i V}{2\pi^2} \int_0^\infty \frac{p^2 \mathrm{d}p}{e^{(E-\mu_i)/T} \pm 1}, \tag{1.7}$$

where g_i is the degeneracy, μ_i the chemical potential, and V the volume of the system at the chemical freeze-out. Another interesting phenomenon can be accessed with soft probes in particular when the quark mass is restored in the deconfined matter (known as the chiral symmetry restoration) [18, 19]. As a consequence, the energy threshold of $s\bar{s}$ pair production becomes smaller in the presence of the QGP. Experimentally, measuring an enhancement of the production of strange hadrons in heavy-ion collisions with respect to what is expected from collisions where no QGP is formed (e.g. low multiplicity proton-proton collisions) can be understood as a signature of the QGP formation [17] (see Fig. 1.6, right panel).

- **Initial state probes:** among these probes, there are the electroweak bosons Z^0, $W^\pm$ and directs photons. Since, they are created by initial hard collisions and do not have color charges, these particles are not affected by the presence of the hot color charges in the medium. The measurements of their decay products allow us to estimating the momentum/energy of the particle. The Z^0 and $W^\pm$ bosons can be used to study the parton distribution fonction (PDF) inside a hadron. Moreover, the study of their production in heavy-ion collisions makes it possible to probe the nuclear effects that are present in the absence of the QGP. In the early years of the heavy ion collider era, small colliding systems such as p–p, or p–A were regarded as control measurements, for example, in constraining nuclear modified parton distribution functions (nPDFs) that determine the initial gluon distributions (the cold nuclear matter effects) [2].

- **Hard probes:** these probes are created by initial hard scatterings and they can possibly interact with the surrounding color charges. Hence, they are used to study the first stages of the collision evolution (as the pre-equilibrium, thermalization of the medium, phase transition,...). The related observables are the measurement of jets (which is a narrow cone of hadrons and other particles produced by the hadronization of a quark or gluon), thermal photons and dileptons, the production of open-heavy flavor mesons (D and B mesons, particles made of at least one heavy quark (c or b) and an other light quark), and high momentum hadrons. Finally, the production of bound states of heavy quarks pairs, the so-called quarkonia, such as the charmonium or bottomonium families ($c\bar{c}$ and $b\bar{b}$ quark pairs, respectively) are also particularly sensitive to the presence of the QGP, and thus represent excellent probes. The higher is the initial temperatures compared to T_c, the longer the duration of the QGP phase will be. The much more abundant production of hard probes expected at the LHC are likely to result in really relevant probes of the deconfined medium, that depend much less (compared to colliders at lower energies) on details of the later hadronic phase.

The detailed study of the medium transport properties and the potential observation of the weakly or strongly interacting quark–gluon plasma will require key measurements in high energy heavy-ion collisions. In order to connect the in-medium QCD properties to relevant observables, one promising strategy is to introduce hydrodynamics as a phenomenological theory.

---

[2] However, in 2010 and 2012, ultrahigh multiplicity p–p collisions and p–Pb were examined at the LHC (also d–Au data at RHIC), and revealed that most of the signatures for hydrodynamic flow in A–A collisions also existed in these smaller systems.

1.4 Ideal and viscous relativistic fluid dynamics

The viscous relativistic hydrodynamics was introduced by Israel and Stewart in 1979 [20], and more recently brought to light by Romatschke *et al.* [21, 22]. The resulting fluid dynamic equations can be applied to both weakly and strongly coupled systems, which turns out to be very useful for the problem of ultrarelativistic heavy-ion collisions. The emerging picture in ultrarelativistic heavy-ion collisions is that of the formation of a strongly interacting medium with negligibly small viscosity and energy densities reaching several times the critical one, leading to the perfect fluid picture (as illustrated in the Fig. 1.7).

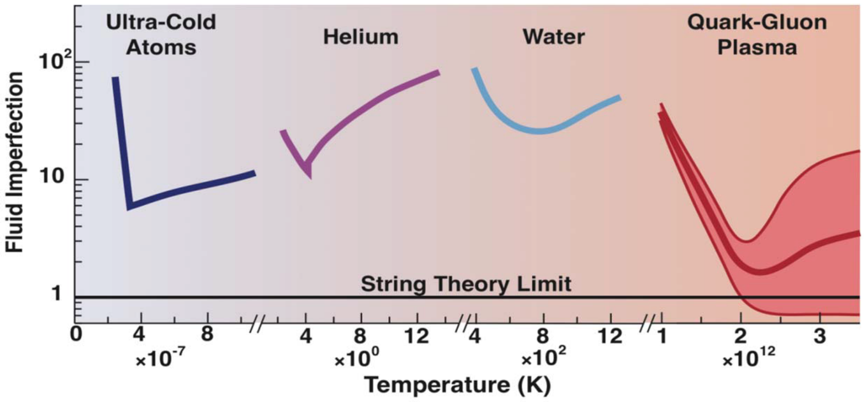

Figure 1.7: Temperature dependence of the viscosity for different state of matter up to the nearly perfect fluid, the quark-gluon plasma. Figure taken from [23].

The four-vectors, like the momentum $p^\mu = (p^0; \mathbf{p})$ (where $\mathbf{p} = (p_x, p_y, p_z)$, and p^0 equal to $E = \gamma m$, with m the rest mass of the particle and $c = 1$), are used to be able to transform appropriately under Lorentz transformations (where Greek indices denote the Minkowski four-space). The kinetic theory treats the evolution of the one-particle distribution function $f(\mathbf{p}, \mathbf{x}, t)$, which can be associated with the number of on-shell particles per unit phase space (as a phase space density). The moments of f help us to find the transition from kinetic theory to fluid dynamics, by introducing the energy-momentum tensor as

$$\int \frac{\mathrm{d}^3 p}{(2\pi)^3 p^0} p^\mu p^\nu f(\mathbf{p}, \mathbf{x}, t) \equiv T^{\mu\nu}, \tag{1.8}$$

where the left-hand side can be understood as a sum over momenta. This relation is true in the ultrarelativistic regime, where particles can be considered massless. The system thus follows a Boltzmann equation within the boost-invariant picture of Bjorken. Then, if there are no external sources, the basics and starting point of fluid dynamics need to solve the conservation equation as

$$\partial_\mu T^{\mu\nu} = 0, \tag{1.9}$$

where the energy-momentum tensor is applied on a four-position $x = (it, x, y, z)$, with the proper time $\tau = \sqrt{t^2 - z^2}$. This conservation equation is also applicable to the conserved charges N such as baryon number, strangeness, electric charges and so on. In a general form the energy momentum tensor can be defined as the following formula

$$T^{\mu\nu} = \varepsilon \cdot u^\mu u^\nu - \mathcal{P}\Delta^{\mu\nu} + \pi^{\mu\nu}, \tag{1.10}$$

where $\Delta^{\mu\nu} = (g^{\mu\nu} - u^\mu u^\nu)$ is the local 3-metric, u^μ denotes here the local flow velocity with the normalization $u^\nu u_\nu = 1$. Hence, contracting each term gives us the following definitions

$$\begin{aligned} \varepsilon &= u_\mu T^{\mu\nu} u_\nu && \text{(energy density)}, \\ \mathcal{P} = (P + \Pi) &= -\frac{1}{3}\Delta_{\mu\nu} T^{\mu\nu} && \text{(hydrostatic + bulk pressure)}, \end{aligned} \tag{1.11}$$

where $\pi^{\mu\nu}$ and Π are referred to the shear and bulk stress tensors, respectively. $T^{\mu\nu}$ can be decomposed into an ideal part and the second one related to the dissipative terms (Π and $\pi^{\mu\nu}$), as

$$T^{\mu\nu} = T^{\mu\nu}_{\text{ideal}} + \delta T^{\mu\nu} \quad = (\varepsilon \cdot u^\mu u^\nu - P\Delta^{\mu\nu}) + \delta T^{\mu\nu}. \tag{1.12}$$

In this context, the flow velocity is defined as the time-like eigenvector of $T^{\mu\nu}_{\text{ideal}}$. The basics of thermodynamics show that $\varepsilon = Ts + \mu n$, where T is the temperature, s the entropy, μ the chemical potential and n the number of particles. The entropy current can be defined as $S^\mu = s \cdot u^\mu$. Now, by calculating the product of the temperature T and the divergence of entropy current S^μ as

$$T\partial_\mu S^\mu = u_\nu \partial_\mu T^{\mu\nu}_{\text{ideal}} = -u_\nu \partial_\mu \delta T^{\mu\nu} = \pi_{\mu\nu} \cdot \nabla^{\langle\mu} u^{\nu\rangle} - \Pi \cdot \partial_\mu u^\nu, \tag{1.13}$$

where the vector $\nabla^\mu = (g^{\mu\nu} - u^\mu u^\nu)\partial_\nu$ (the energy-momentum conservation Eq. 1.9 has been used here), we obtain a term associated to the thermodynamic force $\nabla^{\langle\mu} u^{\nu\rangle}$ which is the shear viscosity, and another term associated to the second thermodynamic force $\partial_\mu u^\nu$ which is the bulk viscosity. The brackets indicate a symmetrized and traceless tensor $\nabla^{\langle\mu} u^{\nu\rangle} \equiv \nabla^\mu u^\nu + \nabla^\nu u^\mu - \frac{2}{3}\Delta^{\mu\nu}\nabla_\alpha u^\alpha$. Moreover, we suppose here the case of viscous hydrodynamics including these two types of viscosity, but neglecting the heat conduction (because $\mu_B \approx 0$). One can notice that in case of massless partons the bulk viscosity can be neglected. Then, the two following phenomenological definitions can be introduced as

$$\begin{aligned} \pi^{\mu\nu} &= 2\eta \cdot \nabla^{\langle\mu} u^{\nu\rangle} && \text{(shear stress tensor)}, \\ \Pi &= -\zeta \cdot \partial_\mu u^\nu && \text{(bulk pressure)}, \end{aligned} \tag{1.14}$$

where η and ζ are the so-called shear and bulk viscosities, respectively. The quantity η/s corresponding to the shear viscosity over entropy, is often used to characterize the viscosity of the QGP. Experimental heavy-ion data suggest that $\eta/s \approx 0.08 - 0.20$, which is close to the lowest possible value of $1/4\pi$ conjectured by string theory models [22, 24, 25].

Hydrodynamics involves the pressure gradients which drive the medium expansion in the transverse plane, but what about longitudinal pressure? About this point, it can be demonstrated that in the early stage of the collision, the longitudinal pressure $\mathcal{P}_L$ seems to be weaker than the transverse one $\mathcal{P}_T$ [26] and both tend to equilibrate when hydrodynamics start. This extremely short time window during which QGP expansion is dominated in the transverse plane instead of the longitudinal one, constitutes the non equilibrium phase. Thus, the system thermalization is a process that builds up the longitudinal pressure, corresponding to a transformation from $\mathcal{P}_T = \varepsilon/2$, $\mathcal{P}_L = 0$, to $\mathcal{P} = \mathcal{P}_T = \mathcal{P}_L$, within a time span around 1 fm/c (as illustrated in the Fig. 1.8).

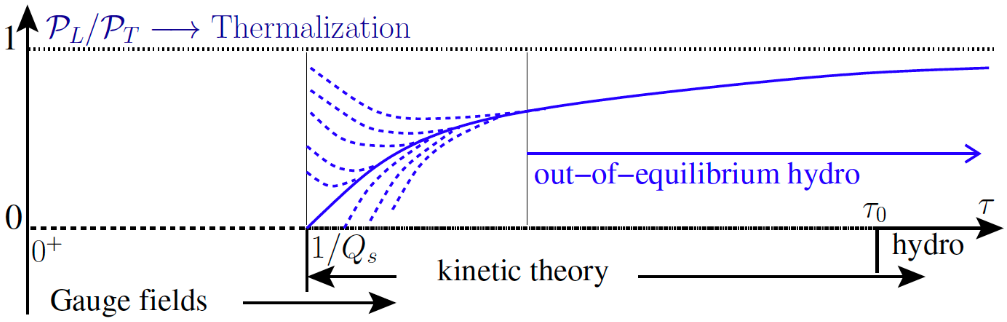

Figure 1.8: Time dependence of the ratio of longitudinal over transverse pressure, during the pre-equilibrium phase, before hydrodynamics. Figure taken from [26].

At equilibrium, if the system is locally isotropic, the equation of state of QCD at high temperature can be related to the hydro-static pressure $P(\varepsilon) = \frac{1}{3}\varepsilon$, associated to the definition of the speed of sound $c_s^2 = \partial P/\partial\varepsilon$, when no dissipative currents are present in the system. Starting from the Navier-Stokes equation for an ideal fluid and considering now a relativistic fluid (where the mass density can be replaced by the enthalpy density $\varepsilon + P$), the time derivative to the four velocity of the flow can be computed. Then, inserting the decomposition of the energy-momentum tensor into the conservation laws (and keeping only non-dissipative terms) it produces

$$\frac{\partial u^\mu}{\partial t} = \frac{\nabla^\mu P}{\varepsilon + P}. \tag{1.15}$$

It is clearly visible from this equation that pressure gradients, quantified via the term $\sim \nabla^\mu P$, cause a fluid element to accelerate. As an example, the equilibrated matter produced in an anisotropic volume when two heavy-ions collide in non-central collisions will give rise, as a consequence of this anisotropy in coordinate space, to anisotropic pressure gradients. These pressure gradients will cause, via the above Eq. 1.15, the created fluid elements to move, or to flow, anisotropically.

1.5 Anisotropic flow and initial collision geometry

The connection between collective effects and fundamental nuclear-matter properties was initially suggested 60 years ago [27], when fluid dynamical models were used to describe the collisions of nucleons and nuclei. It was possible to predict experimental observables assuming local equilibrium and introducing an equation of state that relates the pressure of a fluid cell to its density and pressure. Shock waves were predicted by early hydrodynamics calculations [28] that resulted in structures in the angular distributions of particles indicating that they were emitted with a common velocity into the same direction. Collectivity in this context means that an emitted particle or fluid cell exhibits a common property, and in this sense several phenomena could be related to a collective behavior in a heavy-ion collision:

- **Longitudinal flow**: describes the collective motion of the particles in their original direction defined by the beam.
- **Radial flow**: characterizes particles that are emitted from a source with a common velocity field independent of the direction, i.e. for a velocity field with spherical symmetry. At thermal equilibrium, the transverse-momentum spectrum at low-p_{T} can be described approximately by the Maxwell-Boltzmann distribution
$$\frac{1}{p_{\mathrm{T}}}\frac{\mathrm{d}N}{\mathrm{d}p_{\mathrm{T}}} \propto e^{-\sqrt{m^2+p_{\mathrm{T}}^2}/T_{\mathrm{s}}}, \tag{1.16}$$
where the slope parameter $T_{\mathrm{s}} = (T_{\mathrm{fo}} + \frac{m}{2}\langle\beta_{\mathrm{T}}\rangle^2)$ was observed to be different for particles with different masses m in nucleus-nucleus collisions, T_{fo} being the thermal freeze-out temperature and $\langle\beta_{\mathrm{T}}\rangle$ the average collective transverse velocity of the medium.
- **Elliptic flow**: describes an emission pattern in which particles are found to be preferentially emitted (from an elliptic freeze out surface) with respect to a certain azimuthal angle and with back-to-back symmetry. This section will describes in detail this phenomenon.

In a pioneering publication, J-Y.Ollitrault demonstrated in 1992 [29] that at very high collision energies the longitudinal dynamics decouples from the midrapidity flow generation, thus reducing the relevant degrees of freedom to the transverse plane: a cylindrical geometry reflecting the onset of boost invariance.

1.5.1 Basics of azimuthal anisotropy measurements

In non-central heavy-ion collision, the overlapping volume between the two colliding nuclei at $t = 0$ imprints an initial spatial anisotropy in coordinate space (as illustrated in Fig. 1.9). Due to the multiple microscopic interactions between the constituents (macroscopically described by the presence of strong pressure gradients), this spatial anisotropy is transferred into the momentum space. Figure 1.10 illustrates this transformation from τ_0 to the end of the equilibrium phase at ~ 10 fm/c. The periodicity of the azimuthal distribution of a physical quantity allow us to decompose it into a Fourier series [30, 31]. This interesting property can be applied to the azimuthal distribution of produced particles in heavy-ion collisions as the following formula

$$r(\varphi) = x_0 + 2\sum_{n=1}^{\infty} x_n \cos(n\varphi) + y_n \sin(n\varphi), \tag{1.17}$$

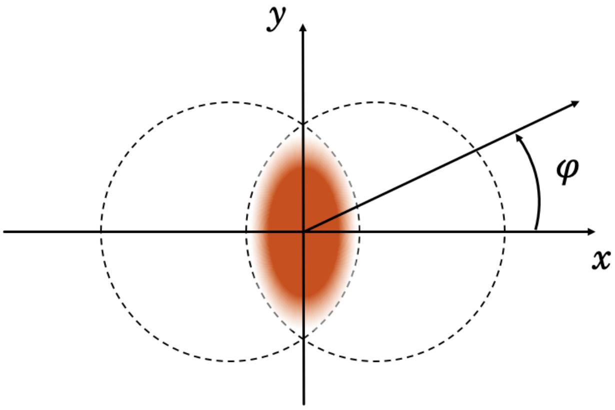

Figure 1.9: Sketch illustrating a non-central collision with the coordinate space anisotropy (in the transverse plane). The azimuthal angle φ is defined for a moving element or emitted particle, from the initial overlapping volume.

where the Fourier coefficients of the series are defined as

$$\begin{aligned} x_n &= \frac{1}{2\pi}\int_0^{2\pi} r(\varphi)\cos(n\varphi)\mathrm{d}\varphi, \\ y_n &= \frac{1}{2\pi}\int_0^{2\pi} r(\varphi)\sin(n\varphi)\mathrm{d}\varphi, \end{aligned} \tag{1.18}$$

and φ denotes the azimuthal angle (see Fig. 1.9). Using this definition, the flow harmonics (v_n coefficients) can be formulated as the module

$$v_n = \sqrt{x_n^2 + y_n^2}. \tag{1.19}$$

In the case of a heavy-ion collision with two identical colliding nuclei, due to symmetry the y_n coefficients are zero, for all n. It also implies that x_n coefficients vanish, for odd n. This property can be understood by the fact that in this symmetry, it is equally probable for an emitted particle to have an azimuthal angle φ or $\varphi + \pi$, simply because $\cos(n\varphi) + \cos(n\varphi + \pi) = \cos(n\varphi)(1 + (-1)^n)$ is zero, for odd n. Moreover, due to these symmetries the harmonics v_n are equal to x_n for symmetric colliding systems (e.g. lead-lead beams), and are non zero only for even n. Hence, the definition of the v_n can be explicitly constructed using the azimuthal distribution $r(\varphi)$ in the following way

$$\langle\cos(n\varphi)\rangle = \frac{\frac{1}{2\pi}\int_0^{2\pi} r(\varphi)\cos(n\varphi)\mathrm{d}\varphi}{\frac{1}{2\pi}\int_0^{2\pi} r(\varphi)\mathrm{d}\varphi} = \frac{\frac{1}{2\pi}v_n\int_0^{2\pi}\cos^2(n\varphi)\mathrm{d}\varphi}{v_0} = \frac{v_n}{v_0} \tag{1.20}$$

where in the integration the orthogonality relationship of the sine and cosine functions are used. Finally, for a normalized distribution $r(\varphi)$, the property $v_0 = \frac{1}{2\pi}\int_0^{2\pi} r(\varphi)\mathrm{d}\varphi = 1$ brings directly the standard formulation of the flow harmonics as $v_n = \langle\cos(n\varphi)\rangle$.

The first term $n = 0$ is understood to be caused by the uniform radial flow expansion of the fireball source. The coefficient v_1 is called directed flow, the second coefficient v_2 is the elliptic flow (illustrated in Fig. 1.10), the third coefficient v_3 corresponds to the triangular flow, etc... Figure. 1.11 shows the corresponding spatial anisotropy, related to the eccentricity ε_n, of these coefficients.

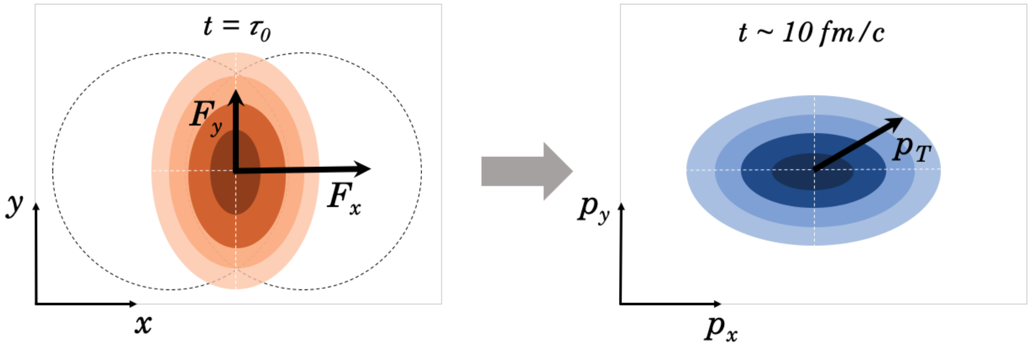

Figure 1.10: Sketch of the spatial anisotropy, where pressure gradient forces $\vec{F} = -\vec{\nabla} P$ at time τ_0 are present inside the collision overlap volume, and will be transferred later into a momentum anisotropy.

An alternative formulation of v_n can be constructed by using the well known identities $\cos(n\varphi) = \frac{1}{2}(e^{in\varphi} + e^{-in\varphi})$ and $\sin(n\varphi) = \frac{1}{2i}(e^{in\varphi} - e^{-in\varphi})$. Hence, the v_n can be rewritten in a different way by using the complex notation. In this case, we define

$$v_n = \begin{cases} x_n + iy_n & \text{for } n < 0, \\ x_n - iy_n & \text{for } n > 0, \\ x_0 & \text{if } n = 0. \end{cases} \tag{1.21}$$

Inserting these separated cases into the previous definition Eq. 1.17, this implicates that the azimuthal distribution can be formulated in a general complex form as

$$r(\varphi) = \sum_{n=-\infty}^{+\infty} v_n e^{in\varphi}. \tag{1.22}$$

Moreover, the azimuthal distribution is a real quantity, hence we have $r(\varphi) = r(\varphi)^*$, then it also gives $v_n = v_n^*$. Now, since v_n is complex, it can be written as $v_n = |v_n| e^{-in\Psi_n}$. Inserting these results in the definition of a real probability density function $r(\varphi)$ and treating the separated cases, the general form can be thus formulated as

$$r(\varphi) = v_0 + 2 \sum_{n=1}^{+\infty} |v_n| \; \Re\Big[e^{in(\varphi - \Psi_n)}\Big]. \tag{1.23}$$

In this alternative definition of $r(\varphi)$, it is clear that the azimuthal measurement φ is with respect to the introduced variable, the so-called symmetry plane Ψ_n, which corresponds to an estimation of the hypothetical reaction plane Ψ_R. Finally, as previously, it is straightforward to show for a normalized distribution than the v_n can be now written as

$$v_n = \langle \cos n(\varphi - \Psi_n) \rangle, \tag{1.24}$$

where $\langle ... \rangle$ denotes the average over all particles in the event.

The eccentricity that defines the initial geometry can be formulated as

$$\varepsilon_n = \frac{\sqrt{\langle r^n \cos n\varphi \rangle^2 + \langle r^n \sin n\varphi \rangle^2}}{\langle r^n \rangle}, \tag{1.25}$$

where $r = \sqrt{x^2 + y^2}$ is the distance from the center. The average $\langle ... \rangle$ is weighted by the local energy density. The initial ellipticity ε_2 (which is geometry derived) increases faster from central to peripheral collisions than the initial triangularity ε_3. Here, these non-central collisions are characterized by a non-zero impact parameter ($\mathbf{b}$), defined as the vector connecting the centers of two colliding nuclei. This impact parameter changes event-by-event, and produces a random reaction plane angle Ψ_R, which is defined as the plane spanned by $\mathbf{b}$ and the beam axis z.

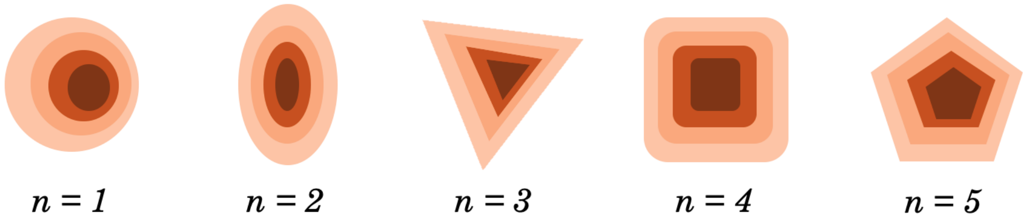

Figure 1.11: Illustration of pressure gradient forces corresponding to different eccentricity ε_n for different harmonic n (ε_1 is the dipole asymmetry, ε_2 ellipticity, ε_3 the triangularity,...). The directions of the symmetry plane Ψ_n can also be imagined from the initial collision geometry.

The azimuthal distribution of hadrons measured in heavy-ion collisions is characterized by different degrees of anisotropy, and a full spectrum of non-zero Fourier harmonics. In hydrodynamics, the final anisotropy in momentum space originates from the spatial anisotropy in the density profile at the initial condition. Elliptic flow is the largest anisotropy because the corresponding spatial anisotropy, the eccentricity ε_2, is mostly induced by the non-zero impact parameter. At a given collision centrality, the v_n and ε_n are in a linear relation, only for harmonic $n = 2, 3$ [32] (higher harmonics contain non-linear terms) as the formula

$$v_n = \kappa_n \varepsilon_n, \tag{1.26}$$

where the parameter κ_n is associated to the response of the system. This relation makes the elliptic flow v_2 a privileged observable to study the response of the system (and then, the viscosity [33]). The linear expression is also true for v_3, but in this case the triangular flow is driven by fluctuations in the energy density profile.

Because the flow planes are not experimentally known, the anisotropic flow coefficients are calculated using azimuthal angular correlations between the observed particles. In the case of two particle correlations $\langle\langle e^{in(\varphi_1 - \varphi_2)} \rangle\rangle$ the measurement is proportional to $\langle v_n^2 \rangle$. Under the assumption that only the azimuthal correlation between particles is due to the common correlation with the flow plane, this correlator can be factorized into $\langle\langle e^{in(\varphi_1-\Psi_n)}\rangle\langle e^{in(\varphi_1-\Psi_n)}\rangle\rangle \equiv \langle v_n^2\rangle$. Using this method, the experimentally reported anisotropic flow coefficients can therefore be obtained as the root-mean-square value $\sqrt{\langle v_n^2\rangle}$. One can notice that, due to event-by-event fluctuations in the anisotropic flow, the event averaged $\langle v_n^k\rangle$ is not equal to $\langle v_n\rangle^k$ for $k > 2$. The notation $v_n\{2\} \equiv \sqrt{\langle v_n^2\rangle}$ represents the anisotropic flow extracted from two-particle correlations. In practice, not all azimuthal correlations in the data are from collective origin. Additional non-flow correlations arise from resonance decays, jet fragmentation, and Bose–Einstein correlations.

The properties of the most abundant hadrons produced in ultrarelativistic heavy-ion collisions (such as $\pi^\pm$, $K^\pm$, $p+\bar{p}$, ϕ, K^0_S, and $\Lambda+\bar{\Lambda}$) can be well studied with the current experiments. Their anisotropic flow coefficients, in particular their v_2 exhibit a particle mass dependence for p_T below 3 GeV/c. At intermediate p_T and beyond, the particles show an approximate grouping according to their type, as illustrated in Fig. 1.12 (left panel).

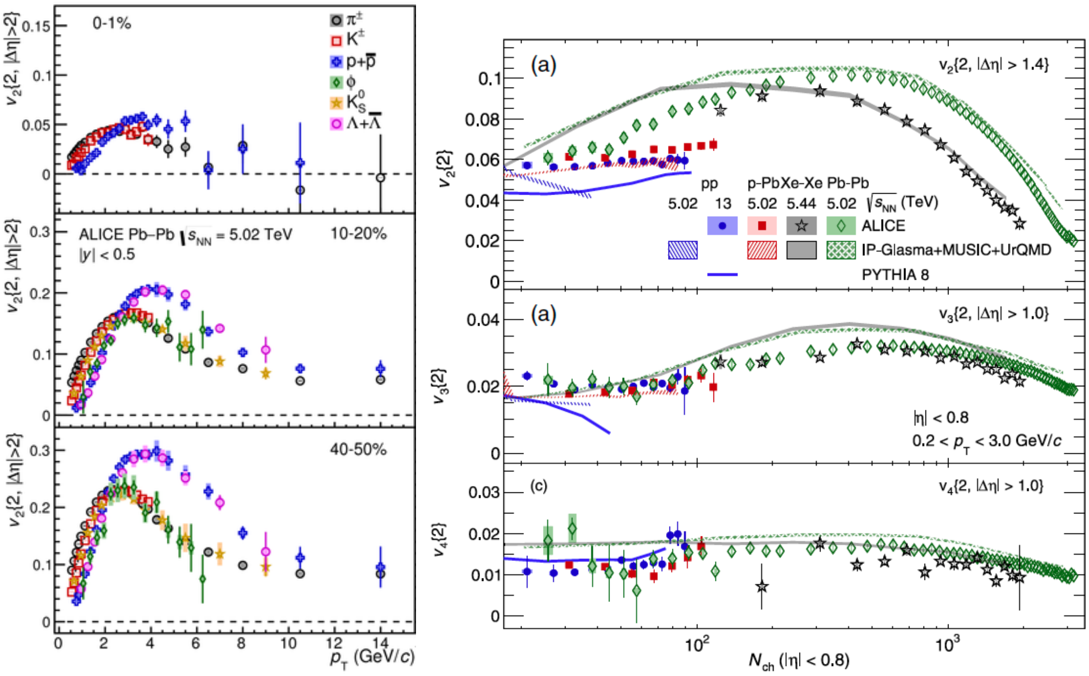

Figure 1.12: Left: p_T-differential v_2 of identified particles in Pb–Pb collisions for various centrality classes. Right: Anisotropic flow measurements (v_2, v_3 and v_4) of charged particles in different collision systems (p–p, p–Pb, Pb–Pb, and Xe–Xe) as a function of the multiplicity N_ch (number of charged particles produced per event). Figures taken from [34] and [35], respectively.

The viscosity of quark-gluon plasma created in heavy-ion collisions can be quantified by measuring elliptic flow, which is mainly driven by the initial geometry. It is clear that the viscous terms go against the pressure-gradient force, and then against the development of anisotropic flow. This phenomenon can be illustrated by defining the non-relativistic Navier-Stokes equation containing both shear and bulk viscosity (η and ζ) as

$$\rho\frac{d\mathbf{v}}{dt} = -\vec{\nabla}\mathcal{P} + \eta\vec{\nabla}^2\cdot\mathbf{v} + \vec{\nabla}\Big[\vec{\nabla}\cdot\mathbf{v}\Big(\zeta+\frac{2}{3}\eta\Big)\Big], \tag{1.27}$$

where $\mathbf{v} = (v_x, v_y, v_z)$ is the flow velocity vector and $\frac{\mathrm{d}}{\mathrm{d}t} = (\partial_t + \mathbf{v}\cdot\vec{\nabla})$ is the so-called material derivative. The first term corresponds to the pressure gradient and forces a fluid element to flow anisotropicaly. Due to the system size dependence, the second and last terms related to viscous corrections are important for central collisions where the overlap volume is large, otherwise these terms are minor for peripheral collisions, or smaller colliding systems. Then, the viscosity of the QGP can be studied in details through v_2 measurements, by varying the size of the system, which help us to understand the role of η and ζ. The effect of the viscous corrections is simply that of damping the value of the response κ_2.

The flow-like phenomena emerge essentially from all measured soft particle spectra and particle correlations, this observation supports the idea of understanding bulk properties of heavy-ion collisions in terms of viscous fluid dynamics. The fluid-dynamic evolution is solely based on combining conservation laws with thermodynamic transport theories that are calculable from first principles in quantum field theory. This fact provides an experimentally accessible inroad to constraining QCD matter properties via soft flow, correlation and fluctuation measurements [36].

As it is shown in the Fig. 1.12 (right panel), the multiplicity dependence of $v_n\{2\}$ is studied in a very wide range from 20 to 3000 charged particles produced in the midrapidity region $|\eta| < 0.8$, for the transverse momentum range $0.2 < p_{\mathrm{T}} < 3.0$ GeV/c. An ordering of the coefficients $v_2 > v_3 > v_4$ is found in p–p and p–Pb collisions, similar to that seen in large collision systems, while a weak v_2 multiplicity dependence is observed relative to nucleus-nucleus collisions in the same multiplicity range. In contrast to the case of nucleus-nucleus collisions, anisotropic flow measurements in small collision systems turn out to be strongly impacted by the initial conditions, as suggested by the `IP-GLASMA` framework [37] which describes the system only up 0.1 fm/c. Recent developments allowed to couple it with the `KøMPøSt` framework (describing up to 1 fm/c [38]), and to the `MUSIC` hydrodynamic code [39], in order to have a full description (from initial to final states effects).

1.5.2 Initial conditions and system size dependence

As introduced here, anisotropic flow is a physical observable and can be related to the geometry of colliding heavy ions. This geometry is determined event-by-event by the positions of the participating nucleons in the initial overlap area. In order to characterize a collision of two heavy ions, the Glauber Model [40] can be used to infer different quantities that are not accessible directly, such as the impact parameter **b** (defined previously), the number of participating nucleons N_{part}, and the number of binary collisions N_{coll}.

Figure 1.13 illustrates the Glauber Model, which modelises the collision of two nuclei as the superposition of consecutive individual interactions of the constituent

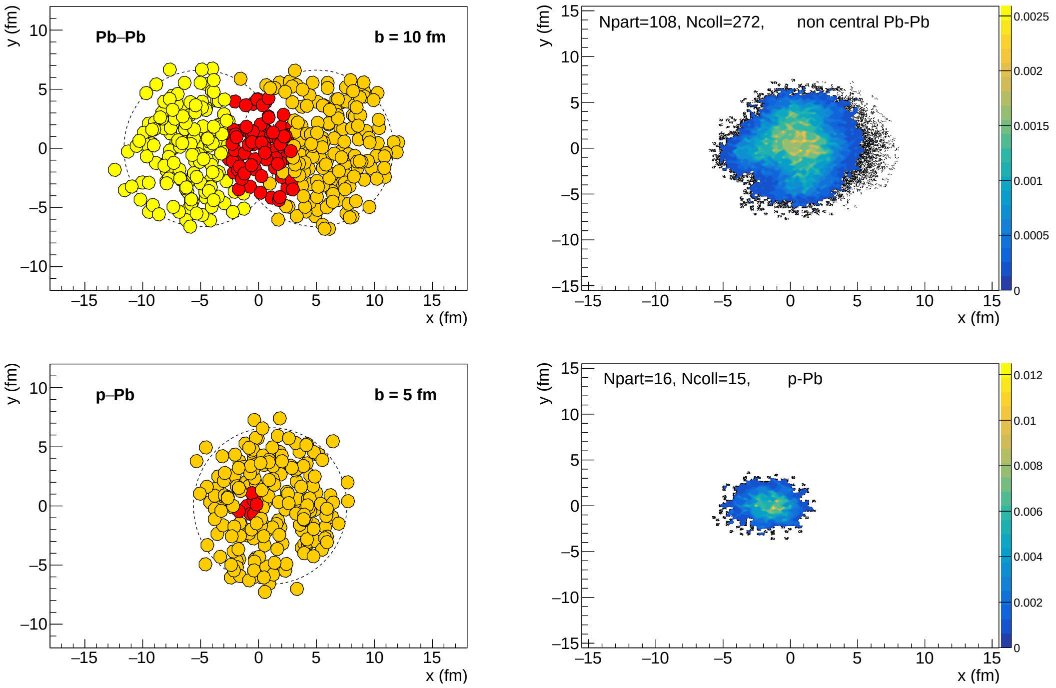

Figure 1.13: Nucleons positions and the associated normalized energy density profile in the transverse plane for different p–Pb and Pb–Pb collisions, with non zero impact parameter **b**. These graphs illustrate the participant nucleons (red markers), and spectators (yellow and orange markers) for the collision. Figures obtained using the open-source MC Glauber code taken from [41], with standard input parameters.

nucleons. Starting from such a picture, it is natural to expect that the geometry of a heavy-ion collision will be strongly related to the different geometric quantities **b**, $N_{\rm part}$ and $N_{\rm coll}$. The number of participating nucleons, $N_{\rm part}$, represents the total number of nucleons which undergo at least one inelastic nucleon-nucleon collision (such nucleons are also called wounded nucleons, while on the other hand the nucleons which do not participate in collisions are usually referred to as spectators). $N_{\rm coll}$ is the total number of binary nucleon-nucleon collisions (the quantity also takes into account the fact that each nucleon can interact multiple times, with different nucleons it encounters on its trajectory though the volume of the opposing nucleus). For head-on collisions, one can show approximately that $N_{\rm coll} \propto N_{\rm part}^{4/3}$, irrespectively of the nucleus size.

In order to use the Glauber formalism, two important inputs from experimental data are needed, which can both be measured and determined independently in a separate experimental setup. The first one is the nuclear density, which is usually parameterized with a Woods-Saxon distribution:

$$\rho(r) = \rho_0 \cdot \frac{1 + w(\frac{r}{R})^2}{1 - e^{(r-R)/a}}, \tag{1.28}$$

where ρ_0 is the nucleon density in the center of the nucleus, R is the radius of the

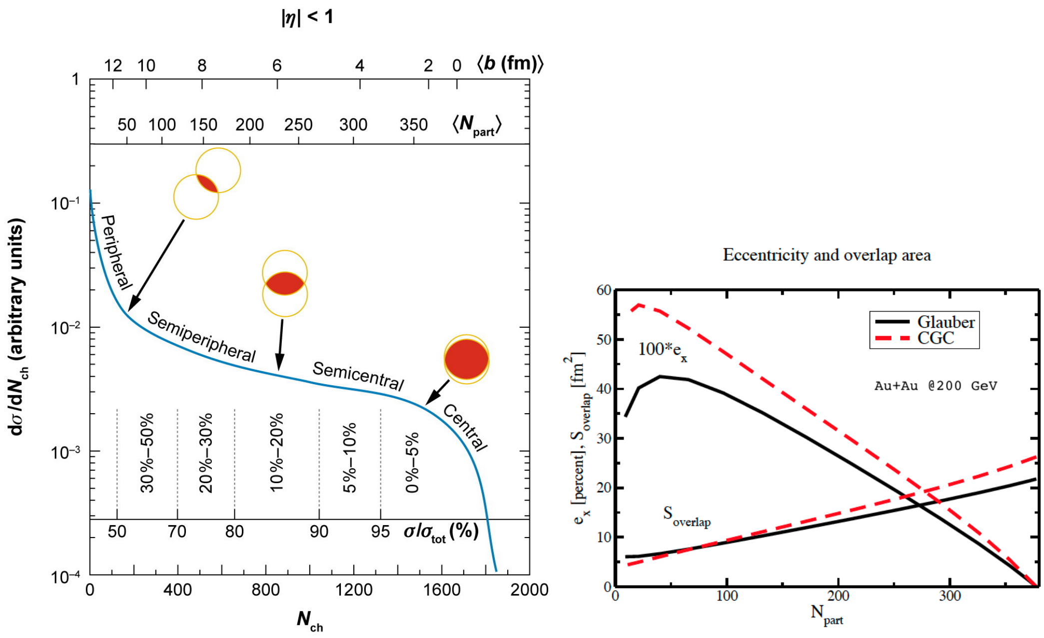

Figure 1.14: Left: centrality determination in heavy-ion collisions using the MC Glauber. Right: comparison of the eccentricity ε_x obtained from MC Glauber or CGC, as a function of the number of participating nucleon. Figures from [22, 40].

nucleus, a represents the thickness of the nucleus surface (the so-called skin depth), and w describes deviations from a smooth spherical shape (for Au, Cu and Pb, w is zero, but the value differs from zero for Xe). All these parameters can be determined independently in low-energy electron scattering experiments. The second input to Glauber Model is the inelastic nucleon-nucleon cross section $\sigma_{\mathrm{NN}}^{\mathrm{inel}}$, which serves as an input due to the main assumption that in this model nucleus-nucleus collisions are treated as a superposition of many nucleon-nucleon collisions. Two nucleons can collide only if the distance d from each other in the transverse plane follows the relation $d < \sqrt{\sigma_{\mathrm{NN}}^{\mathrm{inel}}/\pi}$. The quantities N_{part} and N_{coll} can be then deduced from this description. Figure 1.14 (left panel) illustrates the relation between N_{part}, **b** and the multiplicity N_{ch} of a Pb–Pb collision.

The Color Glass Condensate (CGC) model is an alternative way to describe initial conditions. This model is based on the fact that a nucleus consists of quarks and gluons, which will interact according to the laws of QCD. The total number of gluons can be taken to be roughly proportional to the number of partons in a nucleus, and hence also to its atomic weight A. Therefore, the density of gluons in the transverse plane is approximately $A/(\pi R_0^2)$, where R_0 is the nuclear radius. Gluons will start to interact with each other if the scattering probability becomes of the order of unity,

$$1 \sim \frac{A}{\pi R_0^2}\sigma = \frac{A}{Q^2 R_0^2}\alpha_s(Q^2), \tag{1.29}$$

where σ is the typical parton cross-section. Therefore, one finds that there is a typical momentum scale $Q_s^2 = \alpha_s \frac{A}{R_0^2}$, which separates perturbative phenomena ($Q^2 \gg Q_s^2$)

from non-perturbative physics ($Q^2 \ll Q_s^2$), sometimes called "saturation". The CGC formalism was proposed by [42, 43] to include the saturation physics at low momenta Q^2 in high-energy nuclear collisions.

- **CGC vs. Glauber**: CGC model typically calculates larger eccentricity for a collision than the Glauber model, which will appear to have consequences for the subsequent hydrodynamic evolution. To see this, note that if the eccentricity along the x-direction is positive ($\varepsilon_x > 0$, see definition in Eq 1.25 by replacing $r = x$ for $n = 2$), the energy density drops more quickly in this direction than in the y-direction because the overlap region is shaped elliptically. The equation of state $P = P(\varepsilon)$ implies that the mean pressure gradients are unequal, $\partial_x P > \partial_y P$, and according to the hydrodynamic equations, one expects a larger fluid velocity to build up in the x direction than in the y direction. Since the CGC model calculates larger ε_x than the Glauber model, this anisotropy in the fluid velocities should be larger for the CGC model, as it is shown in Fig. 1.14 (right panel).

The perfect liquid picture introduced previously emerges from the ideal hydrodynamics description of collective elliptic flow, and the large energy loss suffered by energetic quarks and gluons traversing the system. For the soft and light sectors the typical observables are related to collective phenomena on the hydrodynamical hypersurface, for which the memory of microscopic interactions is lost [44, 45]. For heavy quarks, however, some of this memory is kept because they are sensitive to the early stage dynamics of the collision evolution, thus on can study their dynamics in order to learn about the underlying QCD force.

1.6 Heavy-quark dynamics and hadronization

Heavy quarks, especially charm and bottom, have since long been considered valuable probes of the properties of the QGP. While the standard description of the space-time evolution of the bulk medium produced in heavy-ion collisions typically relies on a plasma phase that can be described by hydrodynamics, the heavy-quarks are produced in initial hard scatterings and should in principle not be equilibrated with the QGP at τ_0, the initial time of hydrodynamics. This section will discuss the various mechanisms that might affect the open-heavy flavor and quarkonium production in proton-proton, proton-nucleus and nucleus-nucleus collisions.

1.6.1 Initial heavy-flavor production

Heavy-quark production

It is commonly accepted that at LHC energies the main production mechanism of heavy quarks originates from a gluon initiated processes (like fusion $gg \to Q\bar{Q}$, where negligible contributions might come from quark-antiquark anihilation and exclusive photoproduction). The two gluons from the nucleus wave function will produce a pre-resonance in an approximated hard production time τ_p as

$$\tau_p \approx \begin{cases} \frac{E}{p_{\mathrm{T}}^2} = p_{\mathrm{T}}^{-1} & \text{for } p_{\mathrm{T}} \ll m_Q, \\ m_Q^{-1} & \text{for } p_{\mathrm{T}} \gg m_Q, \end{cases} \tag{1.30}$$

where E is the relativistic pair energy, p_{T} the transverse momentum of the heavy-quark pair and m_Q the heavy quark mass. Then, when $p_{\mathrm{T}} \sim m_Q$ the production time of charm and beauty pre-resonance pairs would be about 0.15 fm/c for charmonium and 0.05 fm/c for bottomonium. The production time is then much smaller than 1 fm/c (the thermal equilibrium time scale), and they are formed at a relative distance around $1/m_Q \ll 1$ fm. In order to have an idea of the number of heavy quarks involved, a central Pb–Pb collision at LHC is expected to produce around ~ 150 $c\bar{c}$ pairs and 5 $b\bar{b}$ pairs [42, 46].

Quarkonium production in the vacuum

After the initial production, the $Q\bar{Q}$ pairs travel extremely close, and to form a $Q\bar{Q}$ resonance they need to expand untill the characteristic size of the resonance. It can be interpreted as the time that the pair takes to "decide" which of the possible $Q\bar{Q}$ bound-states it will couple to (one with mass m_A or one with m_B). This formation time can be approximated using the formula

$$\tau_f \approx \frac{2E}{m_A^2 - m_B^2}. \tag{1.31}$$

Hence, for example, the formation time for the $c\bar{c}$ pair to decide to form a J/ψ (ground state) rather than a ψ(2S) is around 1 fm/c, at $E = 10$ GeV (see Fig. 1.17 and Fig. 1.18 for quarkonium level schemes). At the same energy, a $b\bar{b}$ pair takes 0.36 fm/c to decide to form a Υ(1S) (ground state) rather than a Υ(2S) state. This τ_f increase significantly with E which is proportional to the particle momentum, in particular at 30 GeV, this formation time goes up to 3 fm/c for a pair to decide to be a J/ψ rather than a ψ(2S).

1.6.2 Open-heavy flavor hadrons

Since a significant number of charm and then also bottom quarks can be produce at RHIC and the LHC, the theoretical description of their hadronization and interactions with the medium has produced a variety of models.

In-medium heavy-quark interactions

After the equilibration time of the QGP medium (τ_0), the heavy quarks start interacting with the medium. Heavy quarks traversing the QGP are good probes for the transport properties of the medium, in particular because they interact with the medium constituents via elastic (collisional) and inelastic (gluon radiation) processes. The typical momentum exchange with the heat bath is of the order of the medium temperature T, and thus typically small compared to their thermal momentum, $p_Q = \sqrt{2m_QT}$. A good approximation would be to consider the interaction of heavy quarks with the medium as uncorrelated momentum kicks. Hence, the Boltzmann equation describing their momentum evolution will be approximated with the Fokker-Planck equation, or even more reduced, the macroscopic Langevin equation [47].

Given an estimate of the light quark relaxation time $\sim \eta/(e+P)$ [47] (called the hydrodynamic diffusion coefficient D_{s}, or shear viscosity over enthalpy, where its evolution is plotted in Fig. 1.16), the heavy quark relaxation time is

$$\tau_{\mathrm{r}} \sim \frac{m_Q}{T} \cdot \frac{\eta}{e+P} = \frac{m_Q}{T} D_s. \tag{1.32}$$

As a consequence, for a charm quark in a medium at $T \approx 250$ MeV, we expect a equilibration time approximately 6 times larger than the light quark equilibration time. This means that the expected charm quarks elliptic flow will be smaller than the flow of light hadrons [47]. In this picture, the heavy-quark flow is acquired from the medium collective flow mainly due to scatterings between medium constituents and heavy quarks. The space-time evolution of heavy quarks undergoing multiple elastic scatterings in the QGP can be described using the Boltzmann equation

$$\left(\frac{\partial}{\partial t} + \frac{1}{E_Q}\frac{\partial}{\partial \mathbf{x}} + \mathbf{F} \cdot \frac{\partial}{\partial \mathbf{p}}\right) f_Q(t, \mathbf{x}, \mathbf{p}) = C[f_Q], \tag{1.33}$$

where f_Q is the phase-space distribution function, $\mathbf{F}$ is the force induced from external (color or electromagnetic) field, and $C[f_Q]$ is the collisional integral containing the parton-parton scattering amplitude. If heavy quarks are thermalized in the medium, this equation can be approximated by the Fokker-Planck equation [48]

$$\frac{\partial}{\partial t} f_Q(t, \mathbf{p}) = \frac{\partial}{\partial \mathbf{p}}\left(\mathbf{p}A(\mathbf{p}) + \frac{\partial}{\partial \mathbf{p}} B(\mathbf{p})\right) f_Q(t, \mathbf{p}), \tag{1.34}$$

where the medium properties are encoded in temperature and momentum-dependant transport coefficients A and B, representing the relaxation rate (or drag) and the momentum diffusion of the heavy quark, respectively. Thus, depending on the dynamical evolution equation, the interaction can be described via Fokker-Planck transport coefficients, or from scattering cross sections with the medium constituents.

In this description, low-p_{T} heavy quarks execute a Brownian motion in the medium, undergoing several momentum kicks. However, at high-p_{T}, their mass becomes negligible $m_Q \ll p_{\mathrm{T}}$, and thus behave as light particles, losing their energy mainly via gluon radiation. The characteristic energy of the emitted gluons for a finite path length L traversed by the parton is expressed as $\omega_c = \frac{1}{2}\hat{q}L^2$, where $\hat{q}$ is the transport coefficient, defined as the average squared transverse momentum transferred to the projectile per unit of path length. The usual energy loss mechanisms can be defined as

$$\begin{aligned}
\langle \Delta E_{\mathrm{col}} \rangle &\approx \frac{1}{\sigma T} \int t \frac{\mathrm{d}\sigma}{\mathrm{d}t} \mathrm{d}t, \qquad \frac{\mathrm{d}\sigma}{\mathrm{d}t} \approx \frac{4\pi C_i \alpha_s^2}{t^2} \qquad \text{(collisional) } m_Q \gg p_{\mathrm{T}}, \\
\langle \Delta E_{\mathrm{rad}} \rangle &\approx \int_0^{\omega_c} \omega \frac{\mathrm{d}I_{\mathrm{rad}}}{\mathrm{d}\omega} \mathrm{d}\omega \propto \alpha_s C_R \omega_c \propto \alpha_s C_R \hat{q} L^2 \qquad \text{(radiative) } m_Q \ll p_{\mathrm{T}},
\end{aligned} \tag{1.35}$$

where t is the transferred momentum, σ the integrated cross section of the particle medium interaction, T the temperature of the medium, and $\mathrm{d}\sigma/\mathrm{d}t$ the parton–parton differential elastic cross section. The parameter C_i is the color factor for gg, gq and $q\bar{q}$ scatterings, while C_R is the Casimir factor for the QCD vertices, which is equal to 4/3 for quark-gluon coupling and to 3 for gluon-gluon coupling. In the limit $E_Q \gg m_Q^2/T$, the collisional energy loss $\langle \Delta E_{\text{coll}} \rangle$ is found to be linearly dependent on the medium thickness L, and logarithmically dependent on the initial parton energy. Concerning the radiative one, $\langle \Delta E_{\text{rad}} \rangle$ is found to be an L^2 dependency, but independent of the hard parton energy that traverse the QGP, and proportional to the transport coefficient $\hat{q}$ and $\alpha_s C_R$. Hence, $\langle \Delta E_{\text{rad}} \rangle$ is larger by a factor 9/4 for gluons than for quarks. Figure 1.15 shows the energy loss suffered by the heavy quarks in the medium.

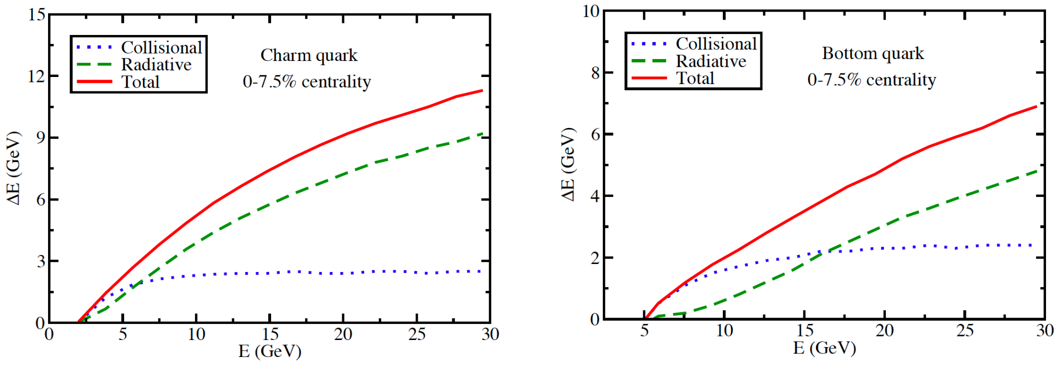

Figure 1.15: Energy dependence of different energy loss mechanisms applied on charm and beauty quark. Figure taken from [49].

In-medium hadronization

Since the initial production gives way to plenty of heavy quarks which many of them can not be a quarkonium bound state, all remaining single charm and bottom quarks will interact with the medium and finally will be hadronized into D or B mesons, this is the open-heavy flavor hadronization.

This hadronization occurs around the transition temperature of the deconfinement and confinement phase transition. There are basically two different mechanisms (to describe how the heavy quark becomes a hadron): *coalescence* of a heavy quark with a light quark of the medium, which is most likely to happen at small p_{T}, and *fragmentation* of a energetic heavy quark, predominantly happening at larger momenta [53, 54]. Purely collisional and radiative processes lead to a significant suppression of final D-meson spectra at high p_{T} and a finite flow of heavy quarks inside the fluid dynamical evolution of the light partons [52] (as illustrated in Fig. 1.16, right panel).

For a long time, the eventual hadronic final interactions seemed not so relevant for final D and B meson spectra as the hadronic cross sections were expected to be small. There is, however, growing awareness that around the pseudo-critical

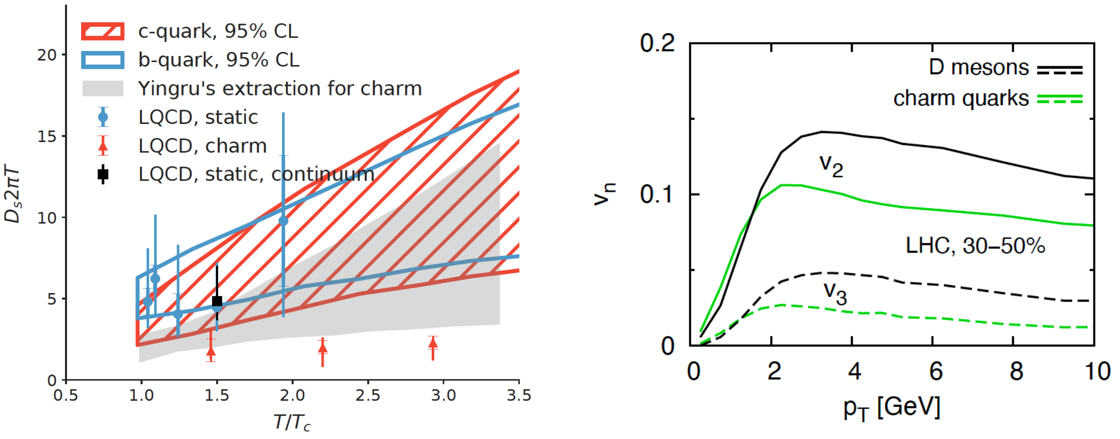

Figure 1.16: Left: heavy quark spatial diffusion coefficient as a function of temperature ratio T/T_c. Figure taken from [50]. Right: elliptic and triangular flow of charm quarks and D mesons. The model (MC@,HQ+EPOS2) couples a Monte Carlo propagation of heavy quarks to the 3+1 dimensional fluid dynamical evolution of the QGP from EPOS initial conditions [51]. Figure taken from [52].

temperature T_{pc} (where chemical freeze-out takes place), interaction can also be strong on the hadronic side [55, 56]. One can notice that looking to the repartition of charm cross-section into hadrons (in p–p collisions), the fraction of produced charmonia is expected to be really small (only few percentages) compared to the varieties of charm hadrons created (D^0, D^+, D_s^+, D^{*0}, D^{*+}, Λ_c^+, Ξ_c^0, Ω_c^0).

1.6.3 Quarkonium spectroscopy: from vacuum to in-medium

Spectral properties

Quarkonium states are typically categorised according to: the total spin S of the $Q\bar{Q}$ system, the orbital angular momentum L between the $Q\bar{Q}$ pair, and the total angular momentum $\vec{J} = \vec{L} + \vec{S}$. The common spectroscopic notation $n^{2S+1}L_J$, where n is the principal quantum number, is used to label the quarkonium states. The parity ($P = (-1)^{L+1}$) and charge conjugate parity ($C = (-1)^{L+S}$) of quarkonium states, are both conserved quantities in the strong and electromagnetic decays. Figures 1.17 and 1.18 show the level scheme of the charmonium and bottomonium family, respectively.

A golden age for quarkonium physics dawned two decades ago, initiated by the confluence of recent progress in QCD and an explosion of related experiments [57]. The heavy quark bound states are stable under strong decay. The charm quark mass is around 1.3 GeV/c^2, while the beauty quark mass is 4.7 GeV/c^2. As opposed to light particles, the quarkonium velocity $v_\perp^2$ is roughly $0.3\,c^2$ for charmonia and around $0.1c$ for bottomonia. Then, the quarkonium spectroscopy might be studied via the non-relativistic potential theory. This approach consists of defining a confining potential for the $Q\bar{Q}$ pair separated by a distance r.

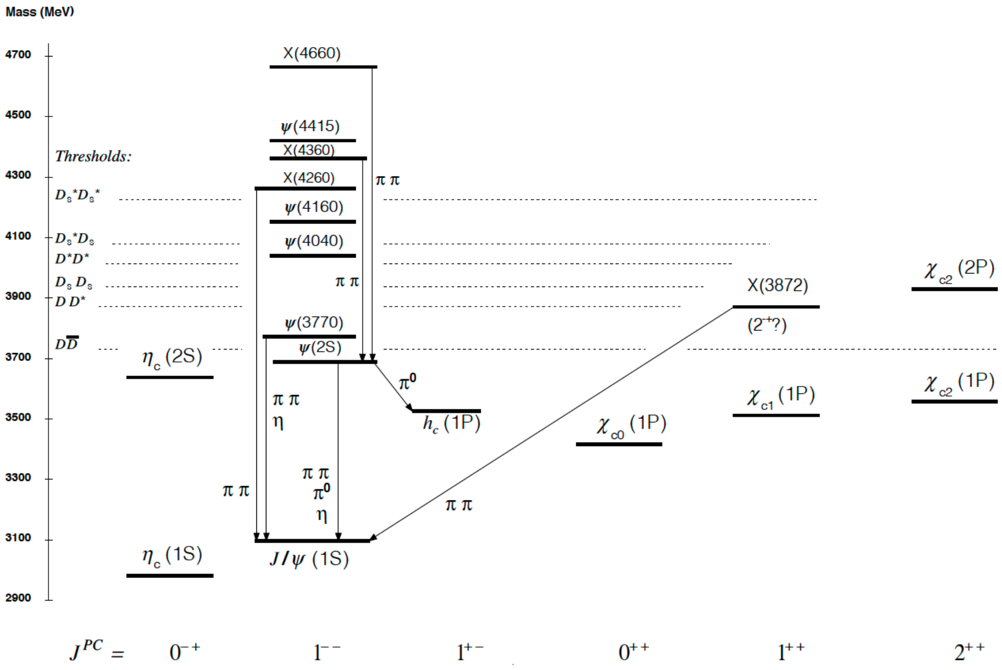

Figure 1.17: Level scheme of the charmonium family. Figure taken from [8].

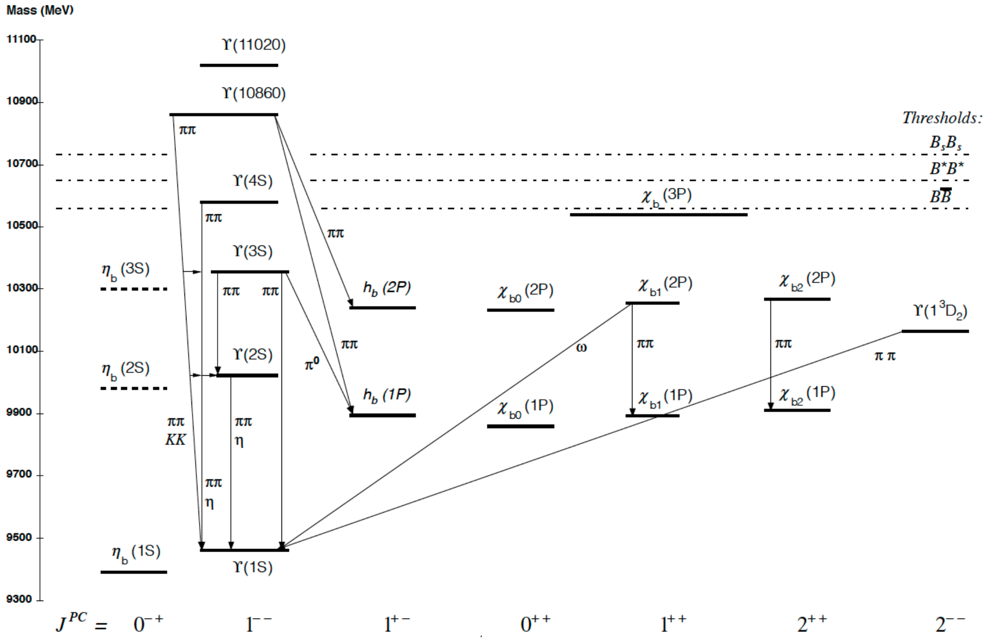

Figure 1.18: Level scheme of the bottomonium family. Figure taken from [8].

To obtain the quarkonium spectral properties, the basic method is to solve the Schrödinger equation where the problem can be reduced to the radial coordinate

(since we use a spherically symmetric central potential in polar coordinates)

$$\Big(-\frac{1}{m_Q}\nabla^2 + V_{Q\bar{Q}}(r)\Big)\Phi_i(r) = E_i\Phi_i(r), \tag{1.36}$$

which determines the bound state masses $M_i = (2m_Q + E_i)$, where i labels different quantum number channels, E_i is the binding energy associated to the wave functions $\Phi_i(r)$. The average radii of these wave functions can be then defined as

$$\langle r_i^2 \rangle = \int \mathrm{d}r^3 r^2 |\Phi_i(r)|^2. \tag{1.37}$$

A rough estimate of this binding radius for the most common charmonia and bottomonia is shown in Table 1.1, as well as their other main spectral properties.

	J/ψ(1S)	χ_{c0}(1P)	ψ(2S)	Υ(1S)	χ_b(1P)	Υ(2S)	χ_b(2P)	Υ(3S)
M_i [GeV]	3.10	3.41	3.69	9.46	9.86	10.02	10.23	10.36
E_i [GeV]	0.64	0.20	0.05	1.10	0.67	0.54	0.31	0.20
r_i [fm]	0.25	0.36	0.45	0.14	0.22	0.28	0.34	0.39
T_d/T_c	2.1	1.16	1.12	> 4.0	1.76	1.60	1.19	1.17

Table 1.1: Dissociation/recombination temperature for charmonium and bottomonium families from lQCD. $E_i = 2M_{\mathrm{D(B)}} - M_i$ is the binding energy of the pair with respect to the open-charm(beauty) threshold, and r_i is the typical radius. The value T_d is the dissociation temperature which is compared to the critical temperature T_c. Values taken from [58, 59].

Suppression by color screening

The "Cornell" potential produces satisfying results in the determination of quarkonium spectral properties in the vacuum. While the in-medium potential for the $Q\bar{Q}$ pair differs from the vacuum one, and does not contain anymore a confining term. These two potentials can be formulated as

$$\begin{aligned} V_{Q\bar{Q}}(r) &= \sigma r - \frac{\alpha_\mathrm{eff}}{r} && \text{(vaccum) } T \approx 0, \\ V_{Q\bar{Q}}(r,T) &= -\frac{\alpha_\mathrm{eff}}{r} e^{-r/r_\mathrm{D}(T)} && \text{(in-medium) } T > T_\mathrm{c}, \end{aligned} \tag{1.38}$$

where the string tension σ reflects the gluon field between the two heavy quarks (with $\sigma \approx 0.216$ GeV), and α_eff is the effective gauge coupling of the strong force ($\alpha_\mathrm{eff} \approx \pi/12$). The first term $\sim r$ is known as the confinement part, and the second term $\sim 1/r$ is identical to the well-known Coulomb potential, analog induced from the electromagnetic force [60].

Above T_c quarks and gluons are no longer confined, then the large number of color charges present in the medium screens the effective heavy-quark potential, the so-called *color screening* (illustrated in Fig. 1.19). It can be understood by introducing the Debye screening length $r_\mathrm{D}(T)$ (or the screening mass $m_\mathrm{D} \sim 1/r_\mathrm{D}$), which

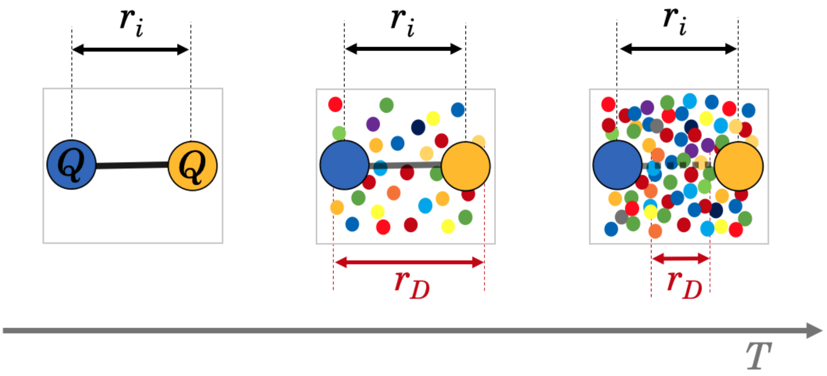

Figure 1.19: Sketch of in-medium color screening of an heavy quark pair as a function of the temperature of the bath (left = vaccum, center = $T \sim T_{\rm c}$, right = $T > T_{\rm c}$).

represents an average distance between color charges, it becomes smaller when T increases. As a consequence of this, when T is high enough and $r_{\rm D}(T) < r_i$, the quarks cannot hold together and they dissociate (two distinct dissociation mechanisms may be identified at leading order: the gluo-dissociation which is dominant for $Mv^2 \gg m_{\rm D}$, e.g. J/ψ $+g \rightarrow c+\bar{c}$, and dissociation by inelastic parton scattering if $Mv^2 \ll m_{\rm D}$).

Extension to other suppression mechanisms

Recently, many improvements have been done in the determination of the solutions of the Schrödinger equation, in particular by using a $Q\bar{Q}$ potential containing both real and imaginary parts. The effect of color screening is mainly encoded in the real part of the potential, while the dissipative effects are encoded in the imaginary part of the potential [61].

The effect of the dissipation plays an important role in the explanation of the broadening of the quarkonium spectral functions when the temperature of the medium increases beyond $T_{\rm c}$. Figure 1.20 shows that for $T \sim 450$ MeV (red curve) only the Υ(1S) ground state survives, while the others are dissociated. At $T \sim 330$ MeV (green dotted curves), the J/ψ, Υ(1S), and Υ(2S) spectral functions are still visible.

In-medium regeneration

An alternative hadronization scenario for quarkonia is the in-medium recombination of heavy quarks. By recombination, we mean here that the heavy-quark pairs are separated by large distance $> 1/m_Q$ at the beginning of the medium expansion when temperature is extremely high, and can recombine later with other heavy quarks during the evolution of the medium when temperature becomes lower. This production mechanism is only possible (or measurable) when heavy quarks are produced in a sufficiently large numbers, which is the case for charm quarks at LHC in central Pb–Pb collisions.

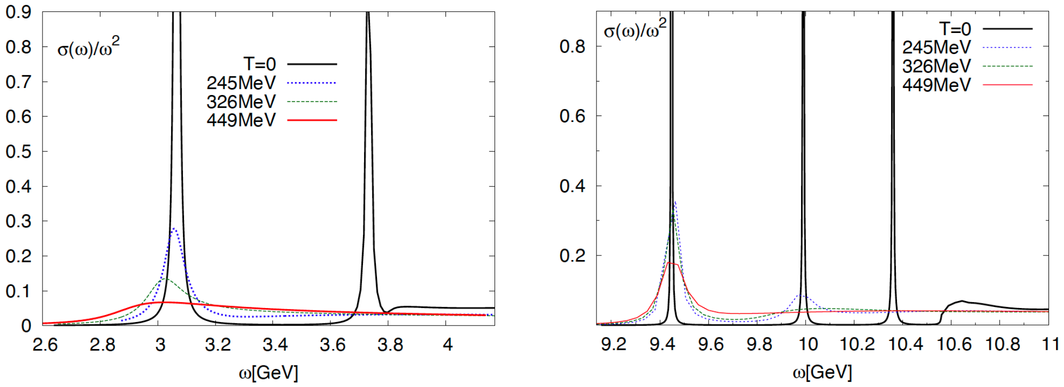

Figure 1.20: Broadenning of the quarkonium spectral functions due to the increasing medium temperature. A complex $Q\bar{Q}$ potential was used in the resolution of the problem. Left: charmonium spectral functions. Right: bottomonium spectral functions. Figure taken from [62].

The recombination of individual charm quarks $c+\bar{c} \rightarrow$ J/ψ $+g$ inside the medium is expected to occur mainly at low p_{T} $(0.1 < p_{\mathrm{T}} < 3$ GeV/$c)$ since it is a thermal process during the QGP evolution [63, 64]. On the one hand, the number of charm quarks $N_{c\bar{c}}$ increase with the number of binary nucleon-nucleon collisions N_{coll}. On the other hand, the produced light hadrons N_{h} increase with the number of participant N_{part}. As a consequence of this fact, the number of regenerated J/ψ increases faster with the energy density compared to the number of primordial J/ψ, thus $N^{\mathrm{reg}}_{\mathrm{J}/\psi} \propto N^2_{c\bar{c}}/N_{\mathrm{h}}$.

Quarkonium decays

Later in the evolution of the heavy-ion collision, the initially created $Q\bar{Q}$ resonance being not a stable particle will decay with a characteristic proper time inversely proportional to its width, as $\tau_d \approx 1/\Gamma$. Then, we can estimate the decay time for the J/ψ or Υ(1S) (using their PDG widths values), which is around 2.1×10^3 fm/c and 3.7×10^3 fm/c, respectively. These lifetimes confirm that quarkonium states can be qualified as probes of the QGP, since the end of the equilibrium phase is of the order of 10 fm/c.

In principle one could expect that the easier to measure should be the lowest mass charmonium state η_c(1S) (2.98 GeV/c and $J^{PC} = 0^{-+}$). However, the difference between the scalar and the vector states ($L = 0$ and $S = 1$) is that the latter have a significant branching ratio (BR) for the double-lepton decay (BR = 5.9% for J/ψ with $J^{PC} = 1^{--}$, decaying into e^+e^-, and the same for J/ψ decaying into $\mu^+\mu^-$), while the former can only be detected through hadronic decay.

1.6.4 Heavy flavor final state observables

Open-heavy flavor production

From the study of charm dynamics in nucleus–nucleus collisions in the last decade there is a general consensus that the details of hadronization have a large effect on both the heavy-flavour observables R_{AA} and v_2 [44]. The elliptic flow v_2 has been already defined in the previous section, being the second coefficient of the Fourier series which decompose the azimuthal distributions of emitted particles. On the other side the nuclear modification factor (R_{AA}) in A-A collisions is defined as

$$R_{\mathrm{AA}} = \frac{1}{\langle N_{\mathrm{coll}}\rangle} \frac{\mathrm{d}^2 N_{\mathrm{AA}}/\mathrm{d}p_{\mathrm{T}}\mathrm{d}y}{\mathrm{d}^2 N_{\mathrm{pp}}/\mathrm{d}p_{\mathrm{T}}\mathrm{d}y}, \tag{1.39}$$

where $\mathrm{d}^2 N_{\mathrm{pp(AA)}}/\mathrm{d}p_{\mathrm{T}}\mathrm{d}y$ are the p_{T} and y-differential yields of hadrons measured in pp (AA) collisions. $\langle N_{\mathrm{coll}}\rangle$ is the number of binary nucleon-nucleon collision, already defined in the previous section. The R_{AA} is expected to be equal to unity in absence of medium effects, while a difference from unity implies modifications of the p_{T} distributions of the produced hadrons due to the medium.

Other effects not related to the presence of the QGP, the cold nuclear matter (CNM) effects, can cause a deviation from unity. These effects can be assessed by studying the nuclear modification factor in p–A collisions. The main phenomena related to these CNM effects are: the modifications of nuclear parton distribution function (nPDF) denoted as shadowing or anti-shadowing (nPDFs become only ingredient different from the case of p–p collisions), the coherent energy loss, and the final state mechanisms (like comovers interactions or nuclear absorption).

One can notice that the temperature dependence of the heavy quark spatial diffusion $D_s 2\pi T$ (see Fig. 1.16, left panel) is essential in order to explain simultaneously the v_2 and R_{AA} [65, 66]. Figure 1.21 shows the p_{T}-differential R_{AA} (left) and v_2 (right) of the D mesons (only the average D^0, D^+, and D^{*+} is plotted for the v_2). Different models are available to describe the open-heavy flavor data, both nuclear modification factor and elliptic flow, some of them are described bellow.

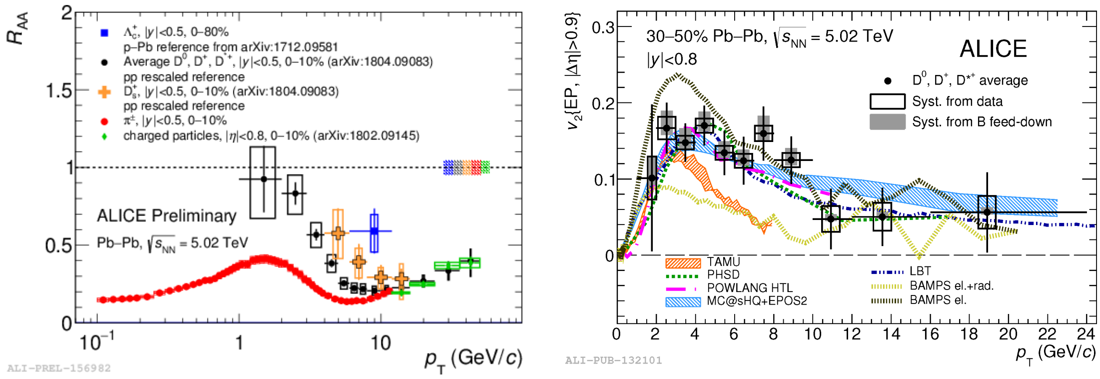

Figure 1.21: Left: $R_{\mathrm{AA}}(p_{\mathrm{T}})$ for $\pi^{\pm}$, D mesons, Λ_c^+, and high-p_{T} charged particles. Right: $v_2(p_{\mathrm{T}})$ of D mesons measured in Pb–Pb collision. Figures taken from [67]

- **MC@,HQ+EPOS2** [68, 69]: Heavy quarks are initialized randomly at the original nucleon-nucleon scattering points in these initial fluid dynamical fields according to the p_{T}-distribution from FONLL (fixed-order next-to-leading logarithm) calculations [70–72], and implementing PDF shadowing. The medium modelling is a 3+1d expansion using the EPOS model [73]. The quark-medium interactions are described by transport (Boltzman equation) and implementing radiative and collisionnal energy loss. The heavy-quark hadronization mechanism is fragmentation and coalescence. The QGP transport coefficient is fixed at LHC.

- **BAMPS** [74]: Heavy-quark production is following MC@NLO [75] and no PDF shadowing is implemented. The medium modelling is a full 3+1d expansion using parton cascade. Elastic and radiative heavy quark interactions with light partons are described with the partonic transport model (Boltzmann approach) to multiparton scatterings (BAMPSs). The heavy-quark hadronization mechanism is only fragmentation. The model initially created for describing RHIC data, is typically scaled with $\mathrm{d}N_{\mathrm{ch}}/\mathrm{d}\eta$ for the LHC.

- **TAMU** [76]: This is a heavy-flavour transport model based on the Langevin equation with collisionnal energy loss and diffusion in the hadronic phase.. Heavy quarks are generated with FONLL, EPS09 (NLO) calculations, and implementing the nPDF shadowing. The medium modelling is a 2+1d expansion using ideal fluid dynamics. The heavy-quark hadronization mechanisms are fragmentation and coalescence. The model assumes the lQCD data to use real and imaginary potential.

Charmonium production

The quarkonium production in nuclear collisions have been studied through many experiments at different center-of-mass energies per nucleon pair ($\sqrt{s_{\mathrm{NN}}}$) starting from AGS (∼5 GeV), to the SPS (∼17 GeV), then to RHIC (∼200 GeV) and finally, with an unprecedented energy, at the LHC (∼5 TeV). The suppression of charmonium bound states, in particular the J/ψ, was proposed 30 years ago as a smoking-gun signature for quark–gluon plasma formation [77]. The increase in temperature from the SPS to RHIC is not enough to dissolve the J/ψ, which is then only indirectly suppressed due to the lack of feed-down contributions from the dissociated χ_{c} and ψ(2S) states. Alternative explanations point out that the recombination of charm and anticharm quarks in the thermal bath could compensate almost exactly the additional suppression [58], and then the similarity of the suppression between the SPS and RHIC energies.

At the LHC, the created medium is measured to be much denser and hotter than that at RHIC or even more than that at the SPS, this means that the number of $c\bar{c}$ pairs initially created will be larger, which lead to important level of recombination as an alternative production mechanism of J/ψ. Figure 1.22 (left panel) demonstrates that the data at $p_{\mathrm{T}} < 5$ GeV/c cannot be explained through current transport models without a scenario including recombination of charm quarks. Indeed, this effect has a surprising impact on the data, because a large J/ψ R_{AA} is observed in

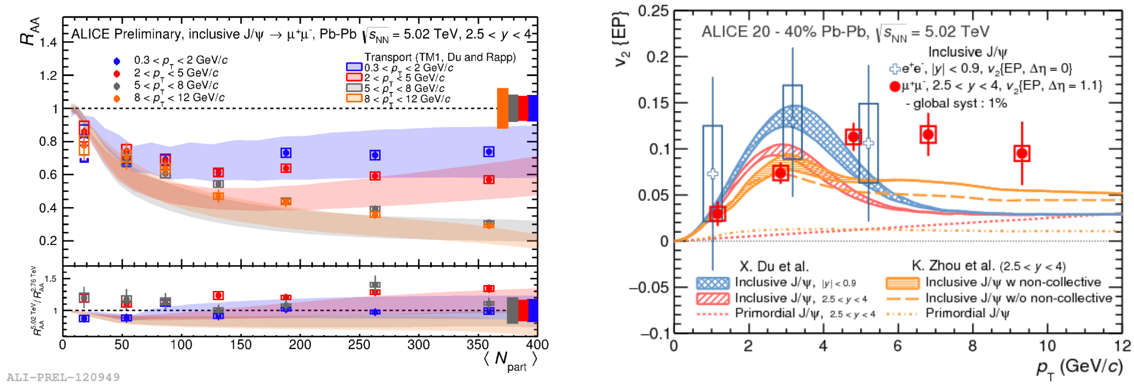

Figure 1.22: Left: R_{AA} of J/ψ as a function of the number of participating nucleons (related to the centrality of the collision) for different p_{T} range, compared to the transport model TAMU. Figure taken from [78]. Right: transverse momentum dependence of J/ψ v_2 measured in Pb–Pb collision, and comparison with TAMU model (red and blue curve). Figure taken from [79].

central collisions (with $\langle N_{\mathrm{part}} \rangle > 200$), at 2.76 TeV [80] and also at 5.02 TeV [78], with respect to the level of suppression observed at high-p_{T}, or at RHIC [81].

Complementary conclusions can also be drawn looking at the non-zero J/ψ v_2 in Fig. 1.22 (right panel), firstly measured in Run 1 [82] and then confirmed in the Run 2 [79]. The elliptic flow measured is positive at low-p_{T}, where regeneration plays a crucial role to understand how J/ψ inherits its anisotropic flow from the charm quarks interacting with the medium during the expansion. The charm quarks flow can only be understood if c quarks are thermalized (or at least partially) in the thermal medium, which depends of the charm quark relaxation time. At high-p_{T} (beyond 5 GeV/c), most of the J/ψ mesons are considered to be originated from the primordial production, and their v_2 is explained by the path length suppression (distance to travel is larger in the out-of-plane than the in-plane direction). Even if a scenario of a suppression dominated by energy loss effects could be favored, no clear statement is yet drawn on the production mechanisms involved at high-p_{T}. Two contributions could be distinguished in the inclusive J/ψ production in hadronic collisions:

- Prompt J/ψ: which comes from the direct production (from hadronization of the initial $c\bar{c}$ pair, either from recombination or from primordial) and the production via decay of higher charmonium states (feed-down).

- Non-prompt J/ψ: which originates from a secondary displaced vertex corresponding to the decay of b-hadrons (mostly B mesons, with a typical lifetime of $c\tau_B \sim 500$ μm).

The models trying to describe the relevant observables implement rather different mechanisms than those of open-heavy flavor, and in this case, the spectral properties of quarkonium families appear to be an important ingredient to be able to describe well the data. Below the description of a microscopic transport model for charmonia or bottomonia is given:

- **TAMU** [64, 83]: Heavy quarks are generated using FONLL calculations [70–72], and including PDF shadowing. The medium modelling is a 2+1d expansion using ideal fluid dynamics. The quark-medium interaction is described by transport-Boltzman equation, accounting for both suppression and regeneration. The hadronization is then described by a primordial and a regenerated component. The quarkonium transport in the medium is described by the kinetic rate equation [84] as

  $$\frac{\mathrm{d}N_{Q\bar{Q}}}{\mathrm{d}t} = -\,\Gamma_{Q\bar{Q}}(T)\Big(N_{Q\bar{Q}} - N^{\mathrm{eq}}_{Q\bar{Q}}(T)\Big), \tag{1.40}$$

  where the two transport coefficients are the inelastic reaction rate, $\Gamma_{Q\bar{Q}}$, and the equilibrium limit, $N^{\mathrm{eq}}(T)$. Here, $N_{Q\bar{Q}}$, T and $\Gamma_{Q\bar{Q}}$ are time dependent quantities. The model assumes lattice-QCD based equation of state for the bulk medium. The spectral properties are also from lattice, using real and imaginary heavy quark potentials, leading to temperature-dependent binding energies. This model takes the initial temperature values in the range $T = 550 - 800$ MeV, and describes R_{AA} and v_2 for both charmonium and bottomonium families.

Bottomonium production

Bottom observables are considered as the cleanest probe of a strongly-coupled QGP, in terms of the implementation of both microscopic interactions and transport, and as a measure of coupling strength without saturation due to thermalization [65]. The initial $b\bar{b}$ production is expected to be much lower than the $c\bar{c}$. As a consequence of this, in particular for the ground state Υ(1S), the recombination will play minor role compared to the one played for the J/ψ production in nucleus-nucleus collisions at the LHC. Figure. 1.23 (right panel) shows that Υ(2S) state is more suppressed than the Υ(1S), as it is expected comparing their different spectral properties. Also, the observed Υ(1S) suppression increases with the centrality of the collision and no significant variation is observed as a function of transverse momentum and rapidity.

Figure. 1.23 (left panel) shows that the R_{AA} of quarkonium states reveals a similar level of suppression in central Pb–Pb collisions between high-p_{T} J/ψ and Υ(1S) (and also between ψ(2S) and Υ(2S)), observed by ALICE [88] and CMS [85, 86]. This observation can be understood from the feed-down fractions involved [59], indeed, a large fraction of expected quarkonium is coming from decay of excited states (e.g. mainly ψ(2S) and χ_c for J/ψ, and Υ(2S), Υ(3S) and χ_b for Υ(1S)), the hot medium dissociates these higher states at lower temperatures than the more tightly bound ground states, leading to a sequential suppression pattern. The feed-down fraction of J/ψ is around 20% at low-p_{T} (< 8 GeV/c) and 35% at high-p_{T}, while for the Υ(1S), these fractions are around 30% at low-p_{T} and 55% at high-p_{T} (values taken from [89]). The level of suppression of Υ(1S) R_{AA} could be therefore explained mostly by the suppression of excited states.

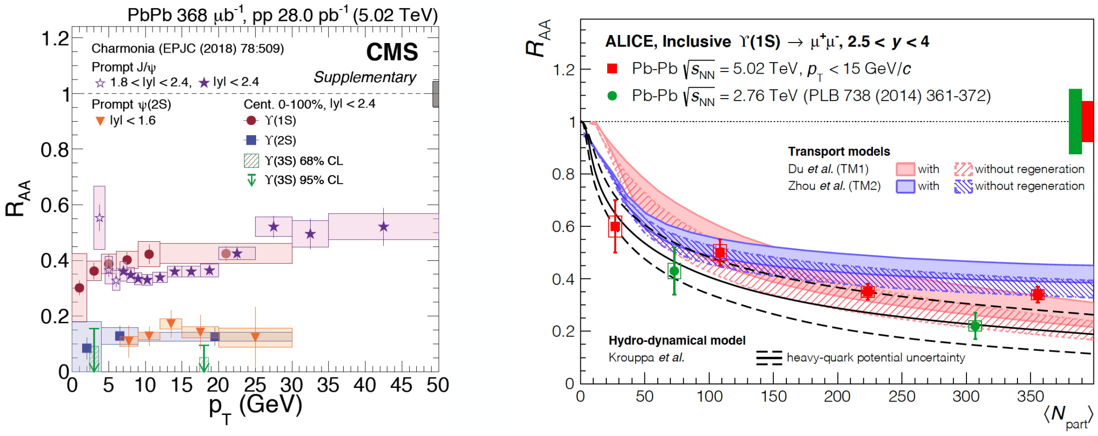

Figure 1.23: Left: Compilation of R_{AA} measurements for different quarkonia as a function of p_{T}. Figure taken from [85, 86]. Right: $\Upsilon(1\mathrm{S})$ R_{AA} as a function of N_{part} in Pb–Pb collisions at 5.02 TeV, and comparison with different theoretical models [87] and [83]. Figure taken from [88].

Moreover, the negligible recombination of individual b quarks at LHC suggests that the v_2 of $\Upsilon(1\mathrm{S})$ is expected to be very small [83], indeed the time window for beauty quarks to interact with the medium is very short ($T > 600$ MeV is needed), which is also expected to be in the early stage of the QGP evolution, where temperature is extremely high but the medium anisotropic flow is not fully developed. An alternative explanation formulated by [90], which introduces an anisotropic escape mechanism, predicts also a very small v_2 for $\Upsilon(1\mathrm{S})$.

- **Hydro-BBJS** [87, 90]: Bottomonium states are generated using PYTHIA, scaled by the mass number of the colliding nuclei [91]. Initial conditions are generated using the Glauber model to construct the energy density profile in the transverse plane. The initial central temperature is assumed to be $T_0 = 600$ MeV corresponding to $\eta/s = 0.2$ (or tries different values of η/s associated to different T_0). The model implements temperature-dependent decay widths for the various bottomonium states. No regeneration or cold nuclear matter effects are considered. The space-time medium evolution is modelled with a 3+1d quasiparticle anisotropic hydrodynamic simulation. One can notice that in this model the bottomonia do not “flow” with the medium, it is purely due to an anisotropic escape mechanism. This model describes the bottomonium R_{AA} and v_2.

Brief summary

The J/ψ production in Pb–Pb collisions at LHC characterized by the R_{AA} and v_2 measurements, has gathered a great interest in the heavy-ion community, in particular due to the spectacular effect of regeneration at low-p_{T}, fairly well included in the microscopic transport models describing both J/ψ R_{AA} and v_2. However, the v_2 at intermediate and high p_{T} seems to deviates from the transport calculations, suggesting missing ingredients in the model. Moreover, no firm conclusions are drawn about the mechanisms governing the J/ψ production at high-p_{T}. In order to add further constraints in the current transport description and the different scenario in the J/ψ production, precise measurements of R_{AA} and specifically the v_2 are needed, in a large p_{T} range. In addition, the latest J/ψ triangular flow v_3 measurement performed [92] was only able to conclude a positive v_3 by 3.7σ, then a larger data set is needed to claim of an observation, which could be a new interesting feature in the story of hidden-charm flow.

The Υ(1S) production in Pb–Pb collisions is currently characterized only by R_{AA} measurements [88], since more Υ(1S) candidates are needed to perform azimuthal anisotropy measurements such as the v_2. For this reason a large data sample is required in order to obtain results with a sufficiently reasonable statistical uncertainty, to be able to further constrain the microscopic transport model for Υ(1S). On the flow aspect, such measurement for Υ(1S) will be considered as a closing picture of the compilation of v_2 from different particle species, from the lightest to the heaviest one, the bottomonium states.

Finally, this thesis manuscript will address the measurement of azimuthal anisotropies (defined using the v_n) of charmonium and bottomonium in Pb–Pb collisions at the LHC, through the J/ψ and Υ(1S) ground states.


LHC, Image credit: CERN

Chapter 2

Experimental setup

ALICE (A Large Ion Collider Experiment) is one of the four major experiments installed at CERN using the LHC beams. It is a detector focused on strong-interaction related physics, and designed to address the properties of the strongly interacting matter and the quark-gluon plasma, at extreme values of energy density and temperature through heavy-ion collisions. In this chapter, the LHC will be briefly introduced, and a quick revue of the ALICE apparatus will be given. Then, the details concerning the trigger systems, the event centrality determination, the vertex and track reconstruction, the unique Particle Identification (PID), and finally the Muon Spectrometer will be presented. A last part will describe the Muon Forward Tracker (MFT), one of the main upgrade projects of ALICE, as well as a brief overview of its alignment.

Contents

2.1 The LHC, a brief overview

The Large Hadron Collider (LHC) is a hadron accelerator and collider, built at CERN, between 1998 and 2008. With its 26.7 km of circumference, it is the world largest and most powerful particle accelerator. The aim of the LHC detectors is to allow physicists to test the predictions of different theories of particle physics (e.g. study the Higgs boson properties, searching for supersymmetric theories through new particles, as well as other unsolved questions in fundamental physics).

It consists of two concentric rings (kept in an ultrahigh vacuum) where the beams are moving in opposite direction, and a large number of superconducting magnets and accelerating cavities. The charged particles in the beams are guided around the accelerator tubes by a strong magnetic field maintained by superconducting electromagnets (which are cooled down to -271.3 °C, a temperature colder than outer space). It is located between 50 and 175 meters underground, forming a tunnel 3.8 meters wide. The two hadrons beams travel in the beam pipe close to c, before they collide at height crossing points. The results of these collisions are studied in four interaction points (IP), by four experiments located at each IP, corresponding to ATLAS, ALICE, CMS, and LHCb positions.

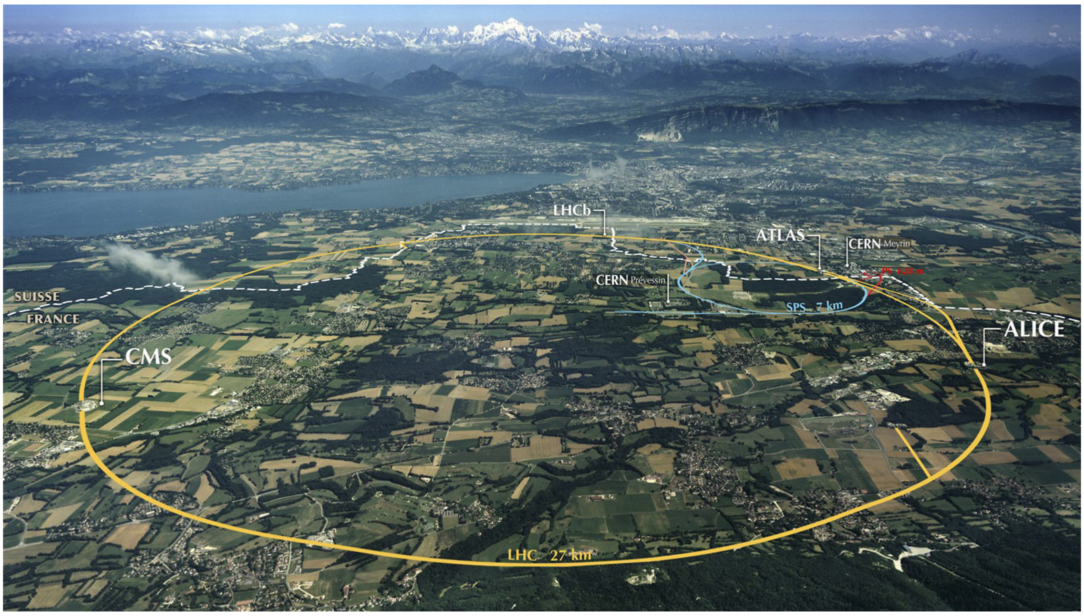

Figure 2.1: Artist view of the LHC, with its four experiments (Image: Maximilien Brice, CERN).

Before being injected into the main accelerator, the particles (protons or ions) are pre-accelerated by a series of systems that successively increase their energy. For example in p–p collisions, the first system is a linear particle accelerator generating 160 MeV negative hydrogen ions (H^- ions), which feeds the Proton Synchrotron Booster (PSB) (electrons are stripped from the hydrogen atom leaving only the nucleus containing one proton). Protons are then accelerated to 2 GeV and injected into the Proton Synchrotron (PS), where they are accelerated to 26 GeV. The Super Proton Synchrotron (SPS) is finally used to increase their energy further to 450 GeV before they are injected into the main ring (LHC), where the proton bunches are accumulated, accelerated to their peak energy in order to collide at the interaction points. After an upgrade of the ion injector chain, a sizeable part of the LHC physics program implying lead-lead collisions was allowed. The LHC accelerates lead ion that contains 126 neutrons and 82 protons ($^{208}_{82}$Pb). Since protons and neutrons have approximately the same mass, an LHC lead ion weighs roughly 208 times more than a proton. The LHC acceleration process gradually strips away all of the lead atoms' electrons, leaving a beam composed only of lead nuclei.

A quantity commonly used in accelerator physics is instantaneous luminosity (L), which is defined as the ratio of the number of events detected (N) in a certain time (t), corresponding to the interaction cross-section (σ). Instead of L, we prefer to use the integrated luminosity, which is the integral of the luminosity in a given time interval

$$\mathcal{L}_{\text{int}} = \int L\text{d}t = \int \frac{1}{\sigma}\frac{\text{d}N}{\text{d}t}\text{d}t. \tag{2.1}$$

The LHC is designed to collides proton beams at a maximum centre-of-mass energy of $\sqrt{s} = 14$ TeV at a luminosity of 10^{34} cm^{-2}s^{-1}. On the heavy-ion side, it can collide lead ions at an centre-of-mass energy per nucleon of $\sqrt{s_{\text{NN}}} = 5.02$ TeV, with a luminosity of $\mathcal{L}_{\text{int}} \sim 10^{27}$ cm^{-2}s^{-1}.

2.2 ALICE apparatus

The physics program of high-energy heavy-ion collisions and the study of QGP properties, started in 1986 at the CERN-SPS accelerator and, simultaneously, at the Brookhaven AGS in the US. ALICE started to be designed in 1994, many observables included in its initial menu became clearly important only after results appeared from RHIC [93]. Then, various additional detection systems were added to the original design over time, from the muon spectrometer in 1995, the transition radiation detector in 1999, to a large jet calorimeter added as recently as 2007.

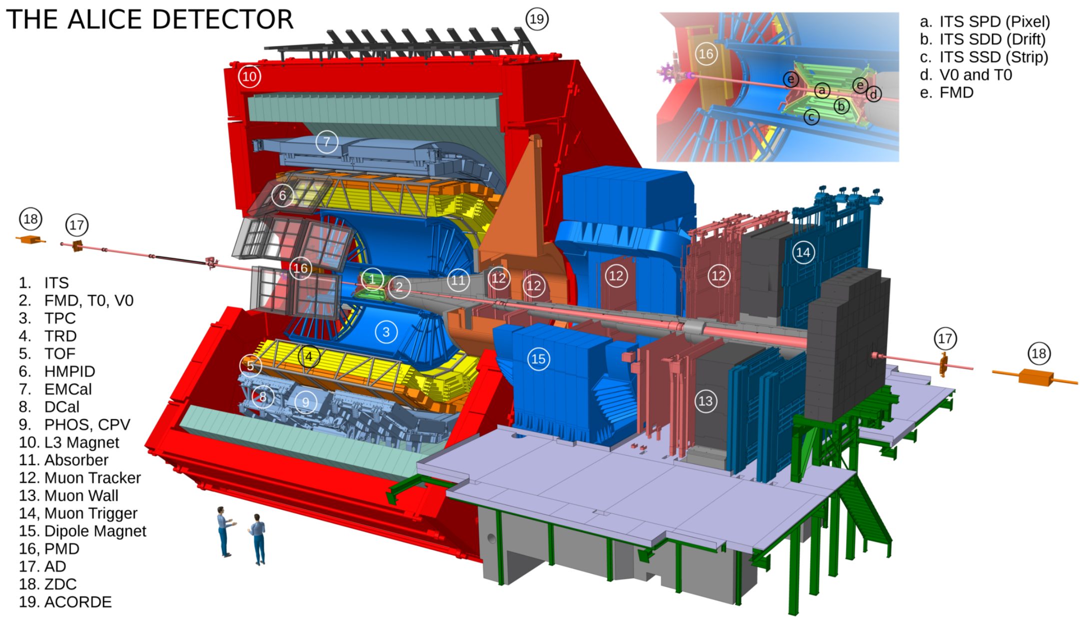

Figure 2.2: ALICE detector schematics (Figures from ALICE repository).

The ALICE Collaboration has built a dedicated detector to exploit the unique physics potential of nucleus-nucleus collisions at LHC energies. Hence, its aim is to study the physics of strongly interacting matter at the highest energy densities reached so far in the laboratory. For this purpose, a comprehensive study of the hadrons, electrons, muons and photons produced in the collisions of heavy nuclei are carried out. Since ALICE is a general purpose detector, it is also studying proton-proton and proton-nucleus collisions on their own, and as a comparison with nucleus-nucleus collisions. A key feature of the ALICE detector is to be able to track charged particles with transverse momentum down to about 80 MeV/c [94], which is a strong requirement to extract QGP physics. However, the ultrarelativistic heavy-ion collisions create an environment with large charged-particle multiplicity (between 2000 to 8000 charged tracks in central Pb–Pb), and for this reason, detectors with high granularity and low material budget are used.

The experimental setup can be separated in two sections, the "central barrel" embedded in a large solenoid magnet ($B = 0.5$ T) which defines the detectors with a pseudorapidity range $|\eta| < 0.9$, and a muon spectrometer which covers the forward region in the interval $-4 < \eta < -2.5$. Several detectors located at forward and backward rapidity are not in these two parts, and are used for the global event characterisation and triggering (ZDC, PMD, FMD, T0, V0A and V0C). The particle detection principles are based on the fact that a charged particle (hadron, electron, muon, ...) traversing the detector material loses its energy, and this phenomenon is described by the well-known Bethe–Bloch formula. A brief description of the major detectors in ALICE is presented below.

Inner Tracking System (ITS)

It is the closest detector to the interaction point, made of two silicon pixel layers (SPD), two silicon drift layers (SDD) and two silicon strip layers (SSD) [95]. The total material traversed by a particle crossing the ITS, at $\eta = 0$, is around 7.2% of the interaction length X_0 (which is related to the energy loss of high energy particles interacting electromagnetically with the material), including the thermal shields and support structures.

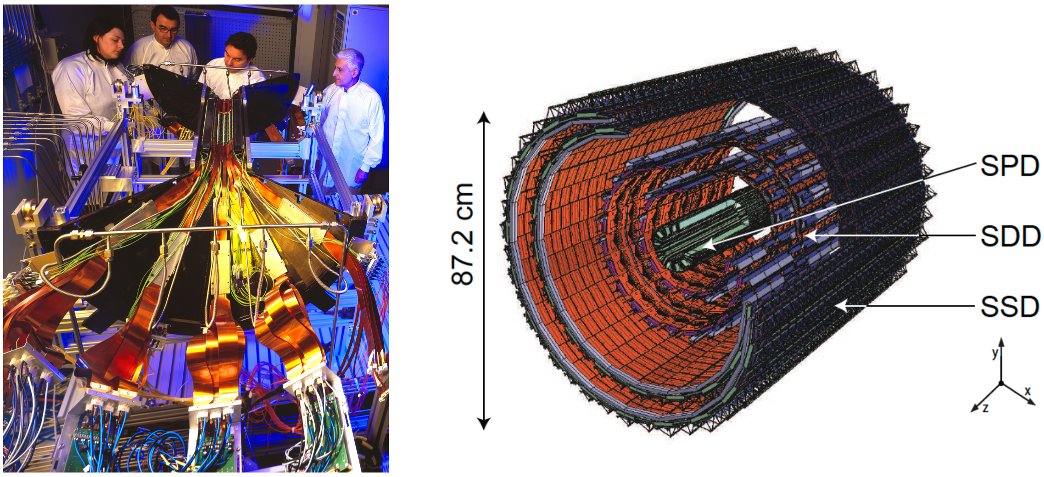

Figure 2.3: First half barrel of the SPD (left) and schematic of the ITS with its different layers (right). Figures taken from [96, 97].

The basic building block of the SPD layers is a module consisting of a two-dimensional sensor matrix of reverse-biased silicon detector diodes bump-bonded to 5 front-end chips. The sensor matrix consists of 256×160 cells, each measuring 50 μm ($r\varphi$) by 425 μm (z). The position resolution of the SPD sensor is determined by the pixel cell size, the track incidence angle on the detector, and by the threshold applied in the readout electronics. The values of spatial precision along $r\varphi$ and z extracted from beam tests are 12 and 100 μm, respectively.

The SDD layers are composed of modules divided into two drift regions where electrons move in opposite directions under a drift field of ~ 500 V/cm, with hybrids housing the front-end electronics on either side. The SDD modules are mounted on linear structures called ladders. There are 14 ladders with six modules each on the inner SDD layer, and 22 ladders with eight modules each on the outer SDD layer. The values of resolution along $r\varphi$ and z are expected to be around 38 and 28 μm, respectively.

The SSD is built using double-sided strip sensors connected to two hybrids hosting the front-end electronics. Each sensor has 768 strips on each side with a pitch of 95 μm. The values of resolution along $r\varphi$ and z are expected to be around 20 and 830 μm, respectively.

Time Projection Chamber (TPC)

The TPC is the main tracking detector of the central barrel and it is optimised to provide charged particle momentum measurement with good two-track separation and PID via the energy loss of the charged particle (dE/dx). The TPC, is a cylindrical detector that covers the full azimuthal angle, having an active radial range from about 85 cm to 250 cm and an overall length along the beam direction of 500 cm [98]. Each end plate is divided in 18 trapezoidal sectors, where multi-wire proportional chambers (MWPC) are mounted.

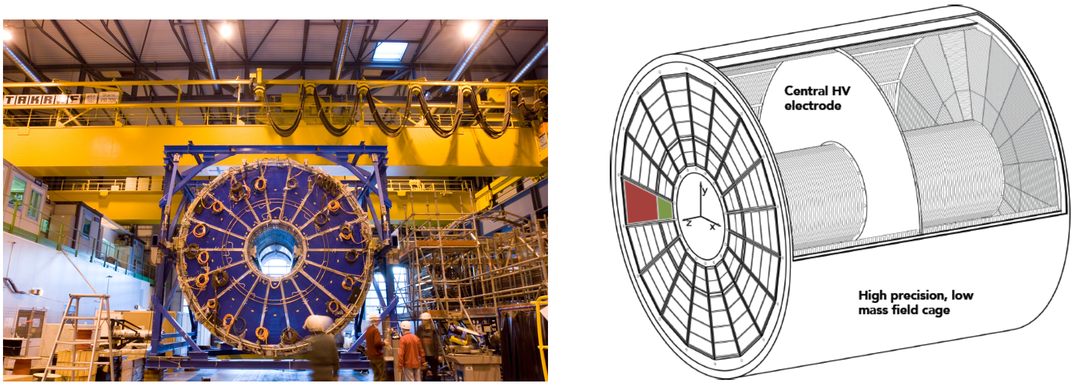

Figure 2.4: TPC installations and its schematics (Figures from [99, 100]).

The field cage is based on a design with a central high-voltage electrode and two opposite axial resistive potential dividers, which create a highly uniform electrostatic field in the common gas volume. The detector covers the pseudorapidity range $|\eta| < 0.9$ for tracks with full radial track length (matches in ITS, TRD and TOF), and up to $|\eta| = 1.5$ for reduced track length. The TPC allows the charged particle reconstruction in a wide range of transverse momentum, from low-p_{T} around 100 MeV/c, up to 100 GeV/c.

Transition Radiation Detector (TRD)

The TRD is able to detect the transition radiation (TR) photons by using either straw tubes or by MWPC [101]. The TRD covers the full azimuth and the pseudorapidity range $-0.84 < \eta < 0.84$. It consists of 522 chambers arranged in 6 layers at a radial distance from 2.90 m to 3.68 m from the beam axis, which are built with low material budget. The extracted temporal information represents the depth in the drift volume at which the ionisation signal was produced, and thus allows the contributions of the TR photon and the specific ionisation energy loss of the charged particle $\mathrm{d}E/\mathrm{d}x$ to be separated. Electrons can be distinguished from other charged particles by producing TR, and having a higher $\mathrm{d}E/\mathrm{d}x$ due to the relativistic rise of the ionisation energy loss.

Time of Flight (TOF)

The TOF detector is a large area detector arranged around the TRD that covers the same pseudorapidity range of ITS, TPC and TRD ($|\eta| < 0.9$). Its main purpose is the particle identification in the intermediate momentum range, up to 2.5 GeV/c (4 GeV/c) for the separation of pions (protons), from kaons by more than 3 times the time-of-flight resolution. The time of flight (t_{flight}) for each particle is given by the information of the time in which the particle hits the detector (t_{hit}) and the initial time of the event t_0, which is computed as the average of time signals from both T0A and T0C ($t_{\mathrm{flight}} = t_{\mathrm{hit}} - t_0$). The start time t_0 is determined with the T0 detector, or using the particle arrival times at the TOF. The overall TOF resolution is around 60–80 ps (for tracks with $p \approx 1$ GeV/c) in Pb–Pb collisions and 100 ps in proton-proton collisions, where there is a larger uncertainty on the determination of the t_0.

V0

The V0 detector is composed of two arrays of 32 scintillator counters each, covering $2.8 < \eta < 5.1$ (V0A) and $-3.7 < \eta < -1.7$ (V0C). The V0A and V0C are used for triggering, for the beam induced background rejection, and for the determination of the collision centrality [100]. The V0 amplitude obtained is then used to evaluate the centrality of the events via a Glauber fit (described in details in the next section). The 32 channels are arranged in four concentric rings with full azimuthal coverage allowing for the calculation of the event flow vector (Q_n).

T0

The T0 detector has a similar geometry than the V0, it is composed of two arrays of detectors (T0A and T0C) corresponding to 24 Cherenkov counters, located on both sides of the IP next to the V0 (at z = 350 cm, and z = -70cm). The detector has a excellent time resolution (better than 50 ps), and provides the collision signal for the

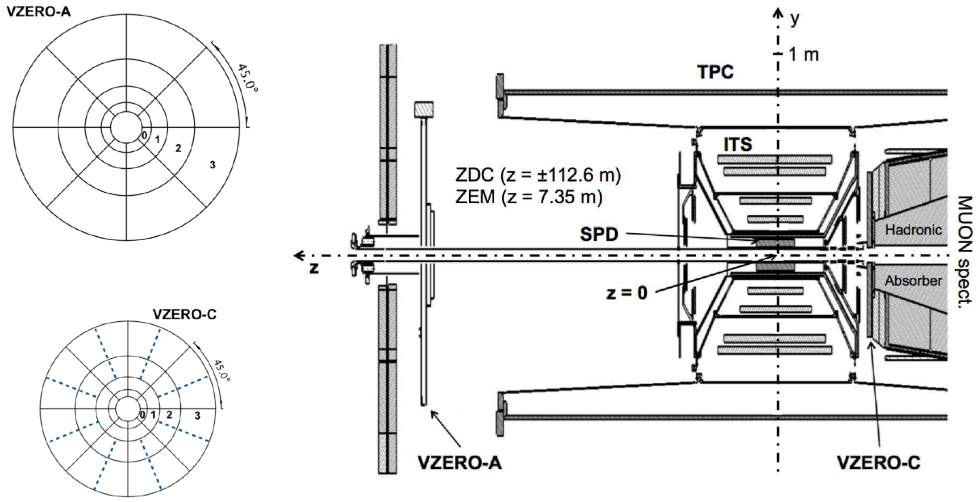

Figure 2.5: Positions of the V0A and V0C detector. Figures taken from [100, 102].

TOF detector, can determine the vertex position, estimate the particle multiplicity, and serve as a minimum-bias trigger.

Zero Degree Calorimeters (ZDC)

The ZDC is installed at ±112.5 m from the nominal IP along the beam axis. [103]. This detector includes two electromagnetic calorimeters (ZEM), two hadronic calorimeters for the detection of protons (ZP) and two for the detection of neutrons (ZN). The ZN and ZP calorimeters, detect spectator nucleons that emerge at 0° from the collisions. The ZDC is mainly used to remove the parasitic beam-gas background events, and to determine the centrality in p–Pb and Pb–Pb collisions by measuring the energy deposited by spectator nucleons, which decreases with increasing centrality.

Electromagnetic Calorimeter (EMCal)

The EMCal, a lead-scintillator electromagnetic calorimeter covering 107 degrees in azimuth and $|\eta| < 0.7$, is used to trigger on jets and to detect the photons (also available with the Photon Spectrometer (PHOS)). Jets are the measured using charged particle tracks in ITS, charged hadronic energy in the TPC, and neutral hadronic energy carried by photons measured with the electromagnetic calorimetry.

Muon spectrometer

The muon spectrometer is designed to reconstruct muons tracks. The properties of quarkonia and electroweak bosons can be investigated in their di-muon decay channel in the forward rapidity region, down to zero transverse momentum [104]. The muon spectrometer covers the pseudorapidity region $-4 < \eta < -2.5$ and consists of the following components:

- a passive front absorber in order to suppress the charged hadrons and muons from π or K decays. The absorber length is about 4.13 m, a nuclear interaction length (the mean distance travelled by a hadronic particle before undergoing an inelastic nuclear interaction) of ~10 λ_{int}, and corresponding to ~60 X_0.

- a high-granularity tracking system of ten detection planes (multiwire proportional chambers (MWPC) with cathode pad read-out, grouped into five stations). One can notice that the stations 1 and 2 have a quadrant geometry, while stations 3, 4 and 5 have a rectangular (slat) geometry, see the Fig. 2.6.

- a large dipole magnet (where $\int B\mathrm{d}z = 3$ Tm), which bends the tracks vertically

- a passive muon-filter wall with a thickness of about 1.2 m, and ~7.2 λ_{int}

- four planes of Resistive Plate Chambers (RPC) grouped into two stations for the muon triggering system (MTR)

- an inner beam shielding to protect the detection chambers from the primary and secondary particles produced at large rapidities

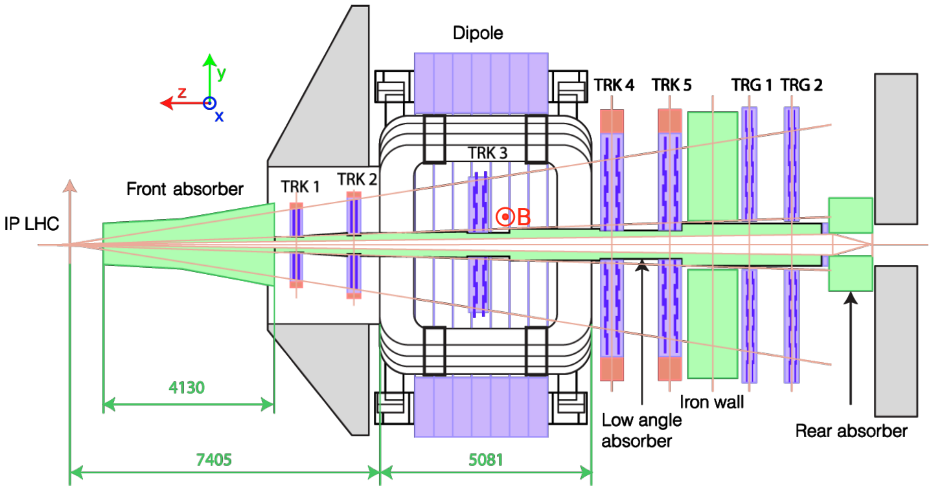

Figure 2.6: Geometry of the muon spectrometer (Figure taken from [105]).

Each MWPC constitutes of a central plane of anode wires sandwiched between two cathode planes, where the space between the anode and cathodes is filled with the gas mixture Ar + CO_2. The high voltage needed is around 1600 V, which is applied to the anode plane creating an internal electric field. As a consequence of a charged particle crossing the detector volume and ionises the gas, electrons are produced and travel towards the anode, and will produce an avalanche in the immediate proximity of the wire. The electrons are then captured by the anode, while the ions travel towards the cathode. The segmentation of the detection planes (separated between: bending and non-bending planes) allows a 2D-localisation of the hit, corresponding to the distribution of the charges.

Coordinates system

The ALICE global reference system is a right-handed Cartesian system which has the z axis on the beam line, pointing towards the ATLAS experiment. The transverse plane is defined using the x axis in the LHC (horizontal) plane pointing to the center of the accelerator, and the y axis pointing upward. The polar angle θ is defined with respect to the z direction, and the azimuthal angle φ, increases counter-clockwise starting from the x axis towards the CMS side.

Triggers systems

The collision events can be studied using the triggers data acquisition system, which is working through a three-level trigger architecture, named the Central Trigger Processor (CTP), selecting the potentially interesting events and dealing with detector latencies. Depending on the physics program, trigger classes are defined as the logical combination of several detector inputs.

The first trigger inputs (L0) are sent by fast trigger detectors 1.2 μs after the collision (V0, T0, SPD, EMCal, PHOS, and Muon Trigger (MTR)). If the conditions of the trigger class are fulfilled, the CTP sends a signal to the corresponding readout detectors. The second (L1) and third (L2) level trigger systems are slower and correspond to a latency of around 6.5 μs and 100 μs after the collision, respectively. For the L1, this is due to a computation time in the TRD and EMCal, and the propagation times to the ZDC. For the L2 trigger, the latency is mainly due to the electron drift time in the TPC. Detector data are sent subsequently to the ALICE data acquisition system and to the High Level Trigger (HLT). If all selection requirements are met, the event is registered to permanent data storage, where it will be processed and reconstructed in order to be ready for data analysis.

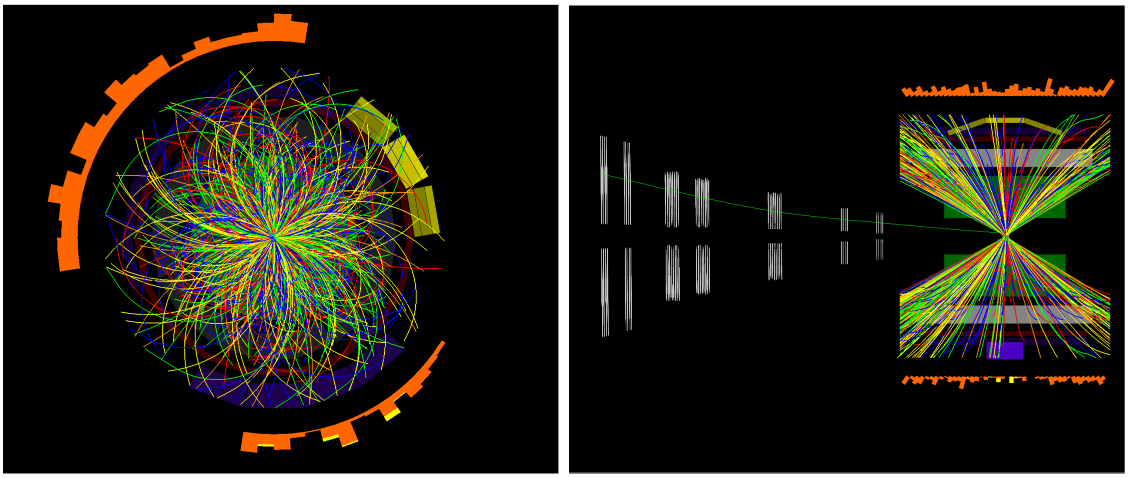

Figure 2.7: Event display of a Pb–Pb collision reconstructed using the ALICE detectors, in the beam-line view (left) and side-view (right). Figures taken from [106].

2.3 ALICE Offline framework

The offline software of ALICE, called `AliRoot`, is based on `ROOT`, a scientific software designed for high-energy physics experiments. It is mainly written in `C++` and usually used for processing data, storage, and visualisation. The simulation of proton–nucleus and nucleus–nucleus collisions is performed using the `HIJING` [107] and `DPMJET` [108] Monte Carlo generators, while the proton-proton collisions are simulated using `PYTHIA` [109] and `HERWIG` [110]. The passage of the particles through materials and their responses in the detector is simulated in `AliRoot` by using different transport packages (`GEANT3` and `GEANT4`). Since simulation, data reconstruction, and analyse use significant computing resource, they are performed using the Worldwide LHC Computing Grid (WLCG), which is a geographically distributed infrastructure that connects several computing centres from more than 40 countries.

2.3.1 Centrality determination

The centrality is defined as the percentile of the hadronic cross section corresponding to a particle multiplicity, or an energy deposited, measured in ALICE, above a given threshold ($N_{\mathrm{ch}}^{\mathrm{T}}$) [111]

$$c \approx \frac{1}{\sigma_{\mathrm{AA}}} \int_{N_{\mathrm{ch}}^{\mathrm{T}}}^{\infty} \frac{\mathrm{d}N_{\sigma}}{\mathrm{d}N_{\mathrm{ch}'}} \mathrm{d}N_{\mathrm{ch}'} \approx \frac{1}{\sigma_{\mathrm{AA}}} \int_{0}^{E_{\mathrm{ZDC}}^{\mathrm{T}}} \frac{\mathrm{d}N_{\sigma}}{\mathrm{d}E'_{\mathrm{ZDC}}} \mathrm{d}E'_{\mathrm{ZDC}}, \tag{2.2}$$

where the cross section may be replaced with the number of observed events n (corrected for the trigger efficiency and for the non-hadronic interaction background).

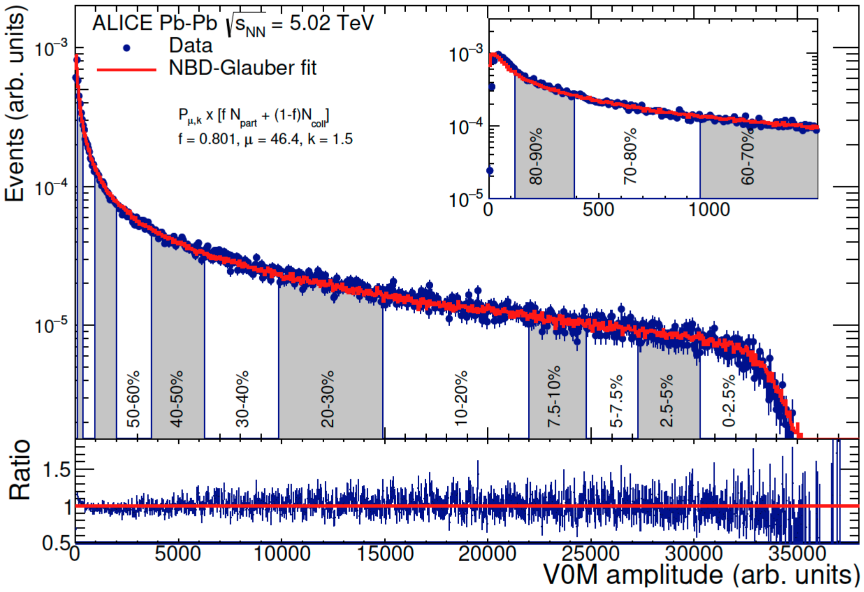

Figure 2.8: Centrality determination using energy deposited in the V0 (V0A+V0C) detector (Figure taken from [111]).

The centrality determination via particle multiplicity in Pb–Pb collisions is typically performed with the V0 detectors [100], as it is shown in Fig. 2.8. The percentile of the hadronic cross section is obtained for each measured value of amplitude of the V0 (sum of V0A+V0C) signals by integrating the distribution of the V0 signal normalised at an anchor point, corresponding to 90% of the total hadronic cross section. The events with multiplicity lower than that of the anchor point are contaminated by background electromagnetic events, and are therefore not considered for the centrality determination. The V0-signal distribution is finally fitted with a parameterisation based on a Glauber Monte Carlo simulation, after this step, the mean values of geometrical quantities (N_{part}, N_{coll}, or b) can be extracted from the fit for different centrality classes, which are defined by classifying the events according to their multiplicity.

2.3.2 Muon measurements

The light (ω and ϕ), heavy (J/ψ and Υ families) vector mesons production, and Z^0 boson can be studied using the muon spectrometer through their $\mu^+\mu^-$ decay channel [104]. The spectrometer is also used to measure the production of single muons from decays of heavy-flavor hadrons and electroweak bosons ($W^{\pm}$). The acceptance going down to $p_{\text{T}} = 0$ and the high readout granularity (resulting in an occupancy of 2% in central Pb–Pb collisions) constitutes the key features of the muon spectrometer. The combined effect of the front absorber (which stops primary hadrons) and of the muon-filter wall (which suppresses the low momentum muons from pion and kaon decays) leads to a detection threshold of $p > 4$ GeV/c for tracks matching the trigger.

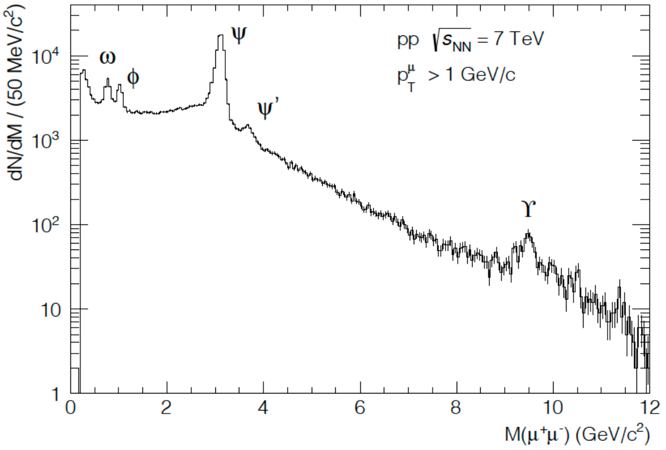

Figure 2.9: Di-muons invariant mass spectrum, in p–p collisions (Figure [94]).

The final reconstructed tracks (matched with a trigger track) are extrapolated to the vertex (measured with the SPD). The track parameters are corrected for energy loss and multiple scattering in the front absorber. In order to trigger and identify muons (or reduce the combinatorial background in the J/ψ or Υ(1S) analyses), the system has two programmable cuts corresponding to, low p_{T} (typically 0.5 GeV/c, but it was set at 1 GeV/c for Pb–Pb data taking) and high p_{T} (4.2 GeV/c). Different triggers are usually defined for muon data taking, corresponding to at least one reconstructed:

- muon satisfying the low-p_{T} cut (`MSL`),
- muon satisfying the high-p_{T} cut (`MSH`)
- unlike sign dimuon pair, satisfying the low-p_{T} cut (`MUL`),
- like sign dimuon pair, satisfying the low-p_{T} cut (`MLL`).

Tracks reconstructed in the tracking chambers (MCH) are required to match a trigger track, they must coincide within the pseudorapidity range $-4 < \eta < -2.5$, and their transverse radius coordinate at the end of the front absorber must be in the range 17.6 cm $< R_{\mathrm{abs}} <$ 89 cm. One can notice that, the deviation suffered by the muon tracks (mainly through multiple Coulomb scattering in the absorber) is taken into account by correcting the initial track orientation. Similarly, the muon particle momenta is also corrected following the Bethe-Bloch formula for the stopping power encountered.

An additional cut on p×DCA, the product of the track momentum and the distance between the vertex and the track extrapolated to the vertex transverse plane, may also be applied to further reduce residual contamination. Using these cuts, a large fraction of the remaining fake tracks are removed. Finally, instead of the e^+e^- decay channel (accessible in the central barrel), which had a large remaining background, the $\mu^+\mu^-$ appears as a privileged decay channel to study the properties of quarkonia in ALICE.

2.4 The Muon Forward Tracker upgrade

A factor 10 to 100 increase in the Pb–Pb integrated luminosity is planned by the LHC for Run 3 and Run 4, depending on the observables, with respect to the previous runs. In order to be prepared for this future interaction rate corresponding to 50 kHz in Pb–Pb collisions (200 kHz is expected for p–p and p–Pb), ALICE is now finalizing a major upgrade of its detectors, to take advantage of this luminosity increase, and also preparing a full upgrade of the detector readout architecture and computing.

Besides the fact to be able to increase the luminosity, the ALICE upgrade is also improving the vertexing capabilities and the tracking at low-p_{T}, essential for studying the fundamental QGP properties. All the significant improvements of the ALICE detector can be listed as follow:

- a **new integrated online-offline computing system** (O2) to be able to manipulate large amount of data (3.4 TB/s of data flow and 100 GB/s of data-to-storage rate as detector read-out, and will mainly operate in a continuous mode) [112]
- **new readout electronics architecture** for the TPC, Muon Spectrometer, TRD, TOF, PHOS, EMCAL/DCAL, and ZDC

- a **new smaller beam pipe**, reducing the radius from 29.8 mm down to 19.2 mm

- **new readout chambers in the TPC replacing MWPC** with Gas ElectronMultiplier (GEM) detectors [113]

- a **new fast interaction trigger**, to handle with the large interaction rate [114]

- two **new high resolution silicon trackers** built of Monolithic Active Sensors (MAPS), based on Complementary Metal Oxide Semiconductor (CMOS) (using TowerJazz 0.18 μm technology, a spatial resolution of 5 μm, 130 000 pixels/cm^2, a detection efficiency $> 99\%$, and an event-time resolution < 4 μs, see the Fig. 2.15 for the ALPIDE chip design) [115, 116]:

    - the Inner Tracking System (ITS) will be replaced by seven new layers of sensors for an improved tracking efficiency and resolution (particularly at low-p_{T}), and an increased read-out rate. The new large area will be around 10 m^2 of silicon pixel sensors ($|\eta| < 1.22$), the thickness sensor is 50 μm and 100 μm for inner and outer ITS, respectively. The total material traversed by a particle will be around 0.3% X_0 per layer, in the 3 inner most layers.

    - a new forward rapidity tracker named the Muon Forward Tracker (MFT), to add vertexing capabilities to the current Muon Spectrometer. The surface of the MFT is around 0.4 m^2 corresponding to 936 silicon pixel sensors (thickness of 50 μm) assembled on 10 detection planes each, grouped on 5 disks. All the silicon pixel sensors of the MFT are assembled, using the same technology as for the new ITS, on 280 ladders (of 2 to 5 sensors each), the ITS read-out electronics will be also used for the MFT. The CMOS technology is commonly used in many tracking devices involving silicon micro-strip or pixel sensors, it point out great features in terms of granularity, material thickness, power consumption, read-out speed, and radiation hardness. The unique particularity of the CMOS-MAPS technology is to integrate both sensor and read-out electronics into a single detection device, which allow an interface optimisation between the sensor and the read-out electronics. The main advantage with respect to hybrid pixels is a low material budget and a power consumption reduced, but the radiation tolerance is limited.

The addition of the MFT extends the central barrel pseudo-rapidity coverage ($|\eta| < 0.9$) to large pseudo-rapidities ($-3.6 < |\eta| < -2.45$).

2.4.1 Brief physics motivations

A significant part of the ALICE physics program after the second LHC Long Shutdown (LS2) is dedicated to high precision measurements of hard probes (heavy-flavour hadrons, quarkonia, photons and jets). The MFT will improve the present

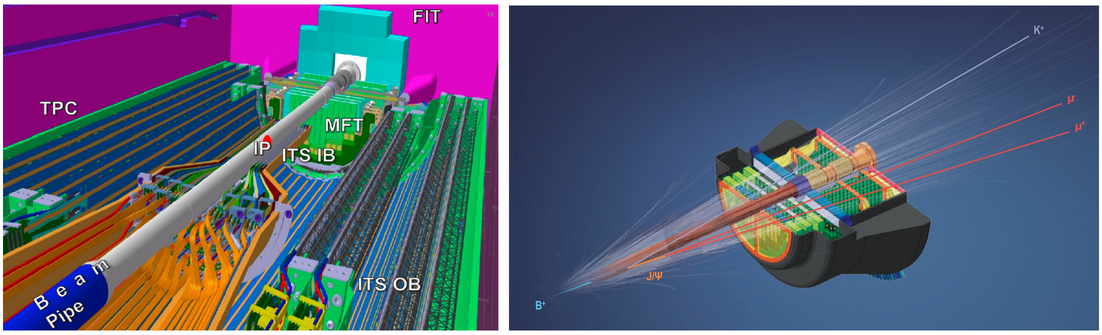

Figure 2.10: (left) Geometry of the installed new detectors [117]. (right) Non-prompt J/ψ reconstruction from B-meson decay with secondary vertex. (Figures from [116]).

performance of the Muon spectrometer and open a way for new precision measurements not accessible with the present apparatus (open charm/beauty separation, ψ(2S) in central Pb–Pb collisions, and J/ψ from b-hadron decays measurements). The addition of the MFT to the current Muon spectrometer will help to better understand:

- the in-medium charmonium dynamics (with the competition between dissociation and regeneration mechanisms), probe the medium temperature and the $Q\bar{Q}$ interaction in a deconfined system, and will be accessible via the measurements of prompt J/ψ and ψ(2S) production and nuclear modification factors (R_{AA}) down to zero p_{T}.

- the thermalization of heavy quarks in the medium, accessible via the elliptic flow (v_2) measurements of charm down to $p_{\mathrm{T}} = 1$ GeV/c (in semi-muonic decays), beauty (in semi-muonic and J/ψ decays) and prompt charmonium down to zero p_{T}.

- the medium density and the mass dependence of the in-medium parton energy loss, which can be studied through measurements of charm and beauty p_{T}-differential production yields.

- the QCD phase transition with its chiral nature, which can be studied via the measurement of the QGP thermal radiation and the spectral shape of low mass vector mesons.

The excellent detection efficiency ($> 99\%$), the low integration-time (< 20 μs) and event-time resolution (< 4 μs) allow the MFT to collect a large amount of data to perform these measurements over a broad transverse momentum interval and with high statistical precision. Additionally to these measurements, the MFT will be also an important forward detector in order to reconstruct the event flow properties with high precision.

2.4.2 Details concerning the alignment strategy

The aim of the MFT is to measure charged tracks produced in each event with a high spatial resolution in front of the Muon spectrometer and inside its acceptance ($-4 < \eta < -2.5$). The position of the MFT surrounds the vacuum beam-pipe, inside the ITS outer barrel, along the beam axis between the ITS inner barrel and the front absorber of the Muon spectrometer (see Fig. 2.10). The basic detection element is a silicon pixel sensor, developed by the ALICE pixel groups for both ITS and MFT [115, 116].

This section focuses on the study of misalignment effects on reconstructed tracks and the alignment of the detector, both performed as a part of this thesis.

Study of misalignment effects

The silicon pixel sensors (or chip) are the most fundamental detection element, they are mounted on ladder, themselves glued on disks, which are assembled into two half-cones. The chip dimension has a width of 1.5 cm, and a length of 3 cm. The whole MFT assembly is based on an ideal geometry, however despite very precise positionning procedure, the true positions of the different elements do not coincide with the ideal one. As a consequence of this, residual misalignments exist from few micrometers to few millimeter for the positions of the disks. Before correcting these residual misalignments (originated from shifts, deformations, glue width,...) in the final geometry, their effects in the track reconstruction need to be evaluated. The simulations are performed using the `PYTHIA` event generator (e.g. here we simulate 1000 events with 10 muons per event) and the `TGEANT3` transport package are used, to reproduce the transport of the particles through the detector.

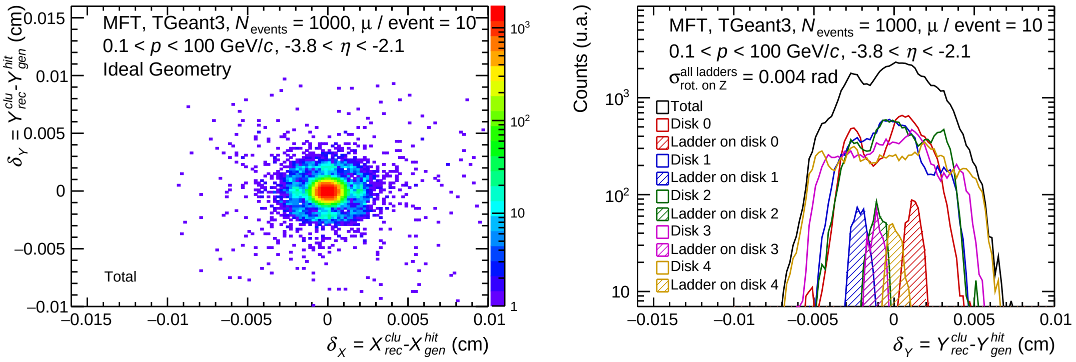

Figure 2.11: 2D cluster-track residual distribution ideal (left) and after applying rotation on X and Y axis to the ladders.

The principles of positioning a volume are governed by the common translation and rotation matrices, where both can be multiplied or additioned. The translation could be represented by the parameters T_x, T_y, and T_z, which are referring to the displacements on X, Y, and Z from a reference point, respectively. The rotation is usually describes by 3 angles, the ψ, θ, and ϕ, which denotes the rotation on X, Y, and Z axis, respectively. The rotation matrix can be decomposed using the common roll, yaw, and pitch matrices ($R_z(\phi)R_y(\theta)R_x(\psi)$) as

$$R = \begin{bmatrix} \cos\phi & -\sin\phi & 0 & 0 \\ \sin\phi & \cos\phi & 0 & 0 \\ 0 & 0 & 1 & 0 \\ 0 & 0 & 0 & 1 \end{bmatrix} \begin{bmatrix} \cos\theta & 0 & \sin\theta & 0 \\ 0 & 1 & 0 & 0 \\ -\sin\theta & 0 & \cos\theta & 0 \\ 0 & 0 & 0 & 1 \end{bmatrix} \begin{bmatrix} 1 & 0 & 0 & 0 \\ 0 & \cos\psi & -\sin\psi & 0 \\ 0 & \sin\psi & \cos\psi & 0 \\ 0 & 0 & 0 & 1 \end{bmatrix}, \tag{2.3}$$

while the translation matrix is represented by a simple column vector as

$$T = \begin{bmatrix} 1 & 0 & 0 & T_x \\ 0 & 1 & 0 & T_y \\ 0 & 0 & 1 & T_z \\ 0 & 0 & 0 & 1 \end{bmatrix}. \tag{2.4}$$

Track residual are computed as the distance between the reconstructed cluster and the hit generated. The effect of a displacement of any detection element will increase the distance between the generated MC hit and the reconstructed cluster, it results of an increase of the track residuals, denoted here as $\delta_\mathrm{X} = \delta^\mathrm{clu}_\mathrm{rec} - \delta^\mathrm{hit}_\mathrm{gen}$, for the X axis.

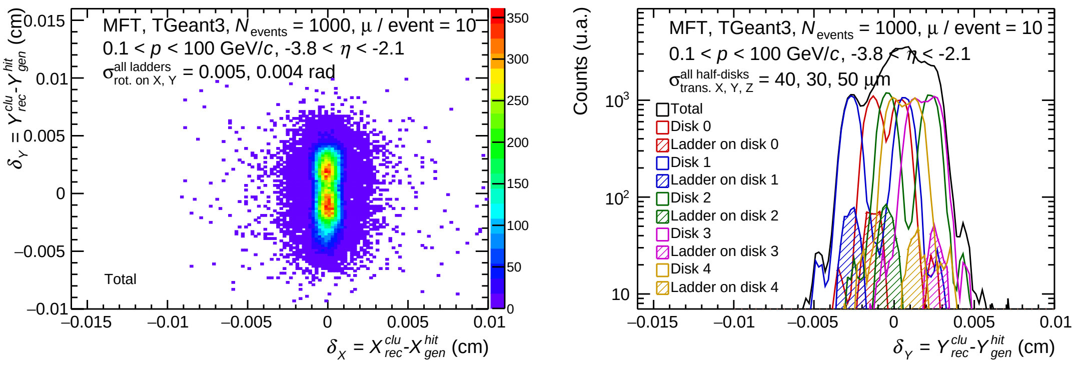

Figure 2.12: 2D cluster-track residual distribution ideal (left) and after applying rotation on X and Y axis to the ladders.

The ideal geometry produces track residuals corresponding to a Gaussian profile centerred on zero on X and Y axis (the width is around ∼8.5 μm, which correspond to the intrinsic spatial resolution), the 2D-profile of these track residuals on X and Y axis is shown in Fig. 2.11 (left panel). The translation or rotation of either chip, ladders, disks, half-cone is simulated using a random selection in a gaussian distribution centerred in a average value. The effect of a simulated rotation of all ladders by 0.004 radians on Z axis, on the track residuals is shown on Fig. 2.11 (right panel). Other examples of 2D-profile of track residuals corresponding to rotation on X and Y axis, and alternatively the effect of translations of the disks on X, Y, and Z axis, are shown on the Fig. 2.12.

Alignment procedure and results

The misalignment effects on track residuals have been described in the previous section, however the goal is to correct these observed displacements by implementing specific transformations on different detector elements. The transformation matrices needed to apply on either chip, ladder, disk, or half, are obtained bu using a least square minimization. This procedure takes as inputs the displaced and the ideal 3D positions of different points (or markers) of the detector element, computes the residual (F_j) and then, run step-by-step over a set of 6 parameters `x,y,z,rx,ry,rz` (3 for translation and 3 for rotation) in order to found the best transformation to apply, which is characterised by the minimum of the χ^2 values. The minimization function is implemented with `TMinuit`, through `MIGRAD` with a sufficient number of iterations.

$$\chi^2_{\rm chip} = \sum_{j=1}^{N_{\rm pads}} \chi^2_{\rm j} = \sum_{j=1}^{N_{\rm pads}} \frac{F_j(|\mathbf{r}_{\rm misaligned} - \mathbf{r}_{\rm ideal}|; {\rm par}_{\rm align})^2}{\sigma^2}, \tag{2.5}$$

where $\chi^2_{\rm chip}$ is denote the minimization values obtained for a chip, ${\rm par}_{\rm align}$ is the set of 6 alignment parameters `x,y,z,rx,ry,rz`, and σ is the intrinsic resolution parameter (around 8.5 μm).

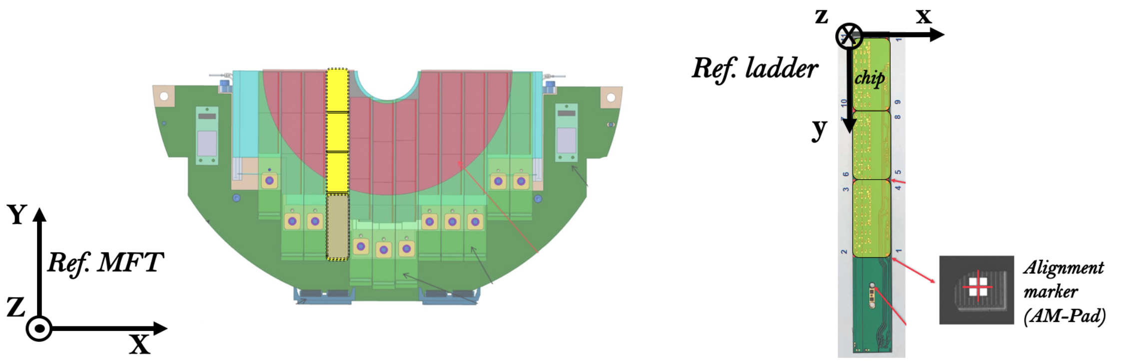

Figure 2.13: Left panel: Description of the geometry of the disk with the ladders mounted on it. Right panel: Alignment markers visible on each corner of the chip.

As it can be visible on Fig. 2.13, the $\chi^2_{\rm chip}$ is computed with 4 points (alignment markers, with x, y, z position) per chip, corresponding to 3744 positions, with an ideal and a survey position. Here, the ideal positions are defined within the framework of an ideal MFT geometry, while the survey positions represent the measurements performed at different steps by the surveyors engineers during the installation. Chip alignment marker positions are measured using a precise machine before gluing ladders on disks, while disk alignment markers are measured before and after MFT insertion, and after ITS insertion. Figure 2.15 shows the ALPIDE chip design (left panel), mounted on a flat printed circuit (FPC) which constitute the ladder (center panel), and the final MFT-ITS insertion around the beam pipe, close to the interaction point (right panel). For the disks, the $\chi^2_{\rm disk}$ is computed with only 2 points or markers per half-disk corresponding to 20 positions (with an ideal and a survey one). One can mention that the fact only 2 markers per disk are available could be problematic, because one degree of freedom of rotation is lost. The transformation matrix $\mathcal{M}$ (composed of previously defined T and R matrices) is apply on the position $\mathbf{r}_{\text{ideal}}$, during the minimization procedure

$$\mathcal{M} \cdot \mathbf{r}_{\text{ideal}} = \begin{bmatrix} r_{11} & r_{12} & r_{13} & T_x \\ r_{21} & r_{22} & r_{23} & T_y \\ r_{31} & r_{32} & r_{33} & T_z \\ 0 & 0 & 0 & 1 \end{bmatrix} \cdot \mathbf{r}_{\text{ideal}}. \tag{2.6}$$

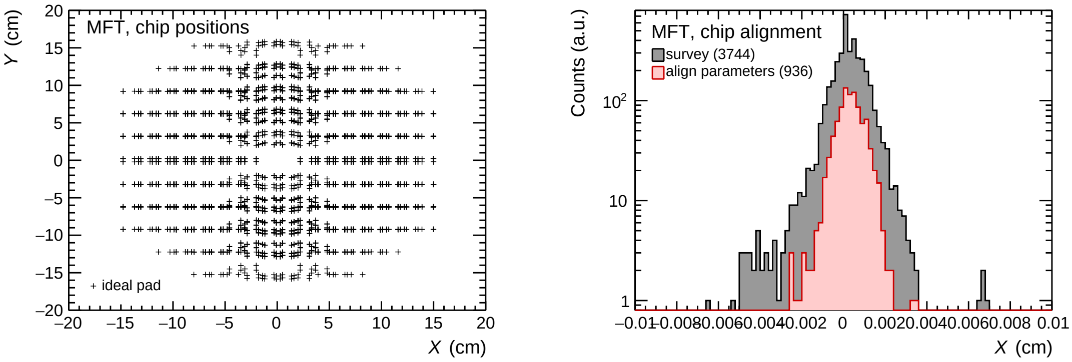

Figure 2.14: Left panel: Ideal geometry of the alignment markers positioned on each chip corner. Right panel: Chip alignment parameters obtained after the minimization, for the X-axis.

The ideal geometry corresponding to the alignment markers (4 per chip) for all the chip in all the disk is visible in the transverse profile in Fig. 2.14 (left panel). The final result of the minimization corresponds to a set of 6 alignment parameters associated to each detector element, which could be stored, in order to modify the ideal geometry and obtain the true one needed in the final track reconstruction.

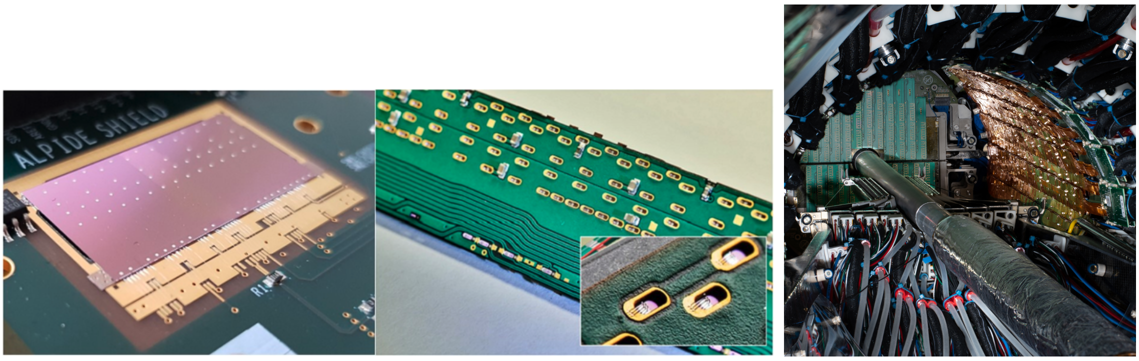

Figure 2.15: Left panel: ALPIDE chip design [118]. Center panel: FPC and wire bonding technology used for ITS and MFT. Right panel: Insertion of the MFT and the ITS in their final positions. Figures from [119, 120]

Figure 2.14 (right panel) shows the result of the minimization using all markers at the sensor corners (3744), for all the chips (936), corresponds to the translation

X. The alignment parameters obtained for X translation (red curve) is centered on zero, with maximal values around 20 μm. Each corner of a chip has a particular shift on X, the minimization finds the best transformations (or alignment parameters) to apply to the chip volume. Similar distributions are obtained for the other alignment parameters. Similar χ^2 minimization procedures is applied on other degree of freedom, and for all the half-disks.

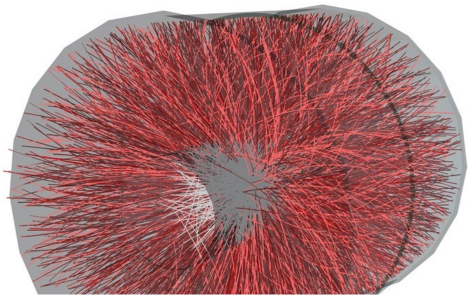

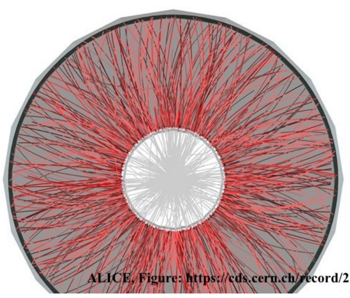

ALICE, Figure: https://cds.cern.ch/record/2202730

Chapter 3

Event properties and calibration

This chapter will be dedicated to the introduction of the analysis techniques and data calibration. After defining the methods for the determination of anisotropic flow coefficients, the reconstruction strategy and how to process the data will be explained. Then, a brief overview of the event flow vector calibration will be presented. Finally, the event flow properties and in particular its resolution will be described.

Contents

3.1 Azimuthal anisotropy measurement methods

The anisotropic flow coefficient v_n for a set of particles, with an azimuthal angle φ, can be estimated with the following relation:

$$v_n = \langle \cos[n(\varphi - \Psi_n)] \rangle \,, \tag{3.1}$$

which is derived from the standard decomposition of $\mathrm{d}N/\mathrm{d}\varphi$ in Fourier series, solely by using the orthogonality properties of trigonometric functions. In the absence of fluctuations all symmetry planes Ψ_n are identical and equal to the hypothetical reaction plane Ψ_{RP}, which is spanned by the beam axis z and the impact parameter b. Ψ_n is estimated by computing the azimuthal angle of the event flow vector $\mathbf{Q}_n$, which is constructed summing over all unitary vectors $\mathbf{u}_n$ of charged particles in an event, for the harmonic n :

$$\mathbf{Q}_n = \sum \mathbf{u}_n = \sum_{j=1}^{N} \cos(n\varphi_j) + i\sin(n\varphi_j) = |Q_n| e^{in\Psi_n}, \tag{3.2}$$

where the summation over unitary vectors is performed on a set of particles in a single event, φ_j is the azimuthal angle of the particle j, N is the number of charged particles in an event. The $\mathbf{Q}_n$ multiplicity dependence is removed by dividing it with the square root of N. $Q_{n,x}$ and $Q_{n,y}$ are the real and imaginary part of the $\mathbf{Q}_n$ vector. Then, the n-th harmonic of the event-plane angle Ψ_n is obtained by taking the ratio between each $\mathbf{Q}_n$ component Eq. (3.3). This event-plane angle gives an estimate of the true symmetry plane:

$$\Psi_n = \frac{1}{n}\arctan(\frac{Q_{n,y}}{Q_{n,x}}). \tag{3.3}$$

Each component of the $\mathbf{Q}_n$ vector can be estimated using the particle multiplicities, which are decomposed using the azimuthal angle of charged particles with the following formulas:

$$Q_{n,x} = |Q_{n,x}|\cos(n\Psi_n) = \sum_j w_j \cos(n\varphi_j), \tag{3.4}$$

$$Q_{n,y} = |Q_{n,y}|\sin(n\Psi_n) = \sum_j w_j \sin(n\varphi_j), \tag{3.5}$$

where the w_j represent the weight associated. These weights can depend on azimuthal angle, transverse momentum, or to be the multiplicity of the channel j (in case of a tracklet $w_j = 1$). For a segmented detector, such as the V0A or V0C, the weights are taken as the corresponding channel amplitudes.

The aim of this thesis is to access to the anisotropic flow coefficients of rares and heavy particles, the quarkonia (which decay into other particles e.g. dimuon, dielectron). Several methods using the general event flow properties are able to perform such measurements, two well-known of them are described below.

3.1.1 Event-plane based method

This method typically correlates each particle with the event plane of other particles. The event-plane based method is an historically standard approach used in heavy-ion collision to extract the v_n, introduced by Poskanzer and Voloshin [121]. The correlation formula between a di-lepton azimuthal angle ($\varphi = \varphi_{ll}$) and the symmetry or event-plane angle Ψ_n is given by

$$v_n = \frac{v_n^{obs}}{R_n} = \frac{\langle\langle \cos n(\varphi - \Psi_n)\rangle\rangle}{\sqrt{\langle \cos n(\Psi_n^A - \Psi_n^B)\rangle}}, \tag{3.6}$$

where the v_n^{obs} is the v_n coefficient not corrected by the event-plane resolution R_n. The bracket $\langle ... \rangle$ represents the average over all particles. The double brackets $\langle\langle ... \rangle\rangle$ correspond to the average over all particles in all events. The factor R_n can be determined from the correlation between event-plane angles of two independent "sub-event" A and B. However, a method based on 3 sub-events (A, B, and C) gives better results, in particular because these classes of events can also be related to 3 different η gap (or 3 different detectors), then it is like giving 3 different point of view. The event-plane resolution for a detector A, R_n^A is $\sqrt{\langle \cos n(\Psi_n^A - \Psi_{\mathrm{RP}})\rangle}$ (where Ψ_{RP} is the hypothetical symmetry or reaction plane) and can be obtained as

$$R_n^A = \sqrt{\frac{\langle \cos n(\Psi_n^A - \Psi_n^B)\rangle \langle \cos n(\Psi_n^A - \Psi_n^C)\rangle}{\langle \cos n(\Psi_n^B - \Psi_n^C)\rangle}}. \tag{3.7}$$

Figure 3.1 illustrates the fact that the Ψ_{RP} angle differs from a participant plane angle Ψ_{PP}, in the sense where the principal axes of the participant zone (which define the participant plane coordinate system), deviate from those of the overlap surface. For a given orientation of the participant plane, the anisotropic flow will be developed along this plane. The orientation of the participant plane can be also characterized by the components of the eccentricity vector [25] as

$$\Psi_{\mathrm{PP}} = \arctan(\frac{\varepsilon_y}{\varepsilon_x}). \tag{3.8}$$

The v_n coefficients (for $n = 2, 3$) is driven by the initial eccentricity of the overlap region, which fluctuates event-by-event. These fluctuations have several sources, in particular from the impact parameter and the position of participant nucleons. These fluctuations make a $\langle v_n \rangle$ in the participant plane Ψ_{PP} larger than in the reaction plane Ψ_{RP}. The magnitude of flow fluctuations is characterized by the parameter σ_v. Hence, the event-plane method yields ambiguous v_n measurements which are somewhere between $\langle v_n \rangle$ and $\sqrt{\langle v_n^2 \rangle}$, due to fluctuation term σ_v^2 in $\langle v_n^2 \rangle$ measurement [25, 122].

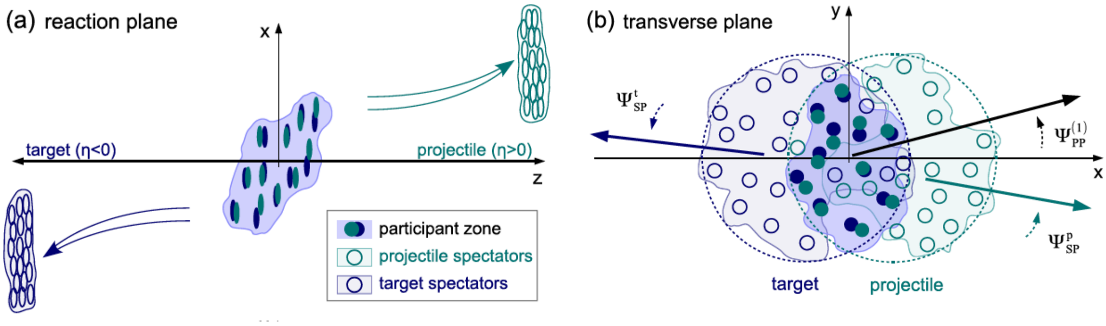

Figure 3.1: Sketch of a non-central heavy-ion collision. Ψ_{RP} is corresponding to the x axis in (b). Figure taken from [123].

3.1.2 Scalar product based method

An alternative way to extract the dilepton v_n is the scalar product method, which correlates the azimuthal properties of the dilepton pair with the event flow vector components. This method provides a direct measure using the product of the unitary vector $\mathbf{u}_n$ and the $\mathbf{Q}_n$ flow vector, and it is independent of the experimental setup. Hence, it leads to the exact values $\sqrt{\langle v_n^2 \rangle}$, defined as

$$v_n = \left\langle \langle \mathbf{u}_n \mathbf{Q}_n^* \rangle \big/ R_n \right\rangle = \sqrt{\langle v_n^2 \rangle}. \tag{3.9}$$

In this case, the R_n factor is called *reference flow* and is conceptually different than the resolution factor defined with the EP method. R_n is evaluated using the 3 sub-event method, by constructing the products between Q_n^{A}, Q_n^{B}, Q_n^{C} (with A, B, C corresponding to SPD, V0A, V0C in our case) averaging over all particles, as the following formula :

$$R_n^{\mathrm{A}} = \sqrt{\frac{\langle \mathbf{Q}_n^{\mathrm{A}} \mathbf{Q}_n^{*\mathrm{B}} \rangle \langle \mathbf{Q}_n^{\mathrm{A}} \mathbf{Q}_n^{*\mathrm{C}} \rangle}{\langle \mathbf{Q}_n^{\mathrm{B}} \mathbf{Q}_n^{*\mathrm{C}} \rangle}}. \tag{3.10}$$

Instead of the event-plane method, the measurements are slightly more precise, indeed the absolute statistical uncertainty is reduced by a factor around 10 %. Therefore, the final results will be preferably computed using the scalar product method.

3.2 General event and track selection

Regardless of the flow analysis, the v_n measurement needs access to the event flow properties. The selected trigger event appears to be crucial as a first step of the analysis. This analysis is performed using a data sample corresponding to Pb–Pb collision at $\sqrt{s_{\mathrm{NN}}} = 5.02$ TeV recorded during the Run 2, with a data taking corresponding to 137 runs in 2015 (15o) and 130 + 99 runs in 2018 (18q + 18r), where each run dataset has been processed, reconstructed, and passed the quality assurance (QA) in order to be ready for data analysis.

One need to separate in two parts the sample of triggered events when the heavy-ion beams collide. On the one hand, the beam-beam interactions (equivalent to Pb–Pb events) are kept as “physics events”, and are selected through timing cuts on signals in V0A and V0C, but also using the T0A and T0C. On the other hand, the beam-gas and beam-collider interactions, which usually take place outside of the nominal interaction points, are delayed with respect to the beam-beam events. The discriminating process between these two types of events is called “physics selection” (PS).

During this analysis, all the data sample were collected using the minimum bias (`MB`) trigger, which corresponds to the coincidence of signals in both V0A and V0C detectors. This minimum bias data sample will be used for the calibration of the event flow properties, and also allows us to select different sub-events (useful for cross-check the calibration or determining the event plane resolution). Figure 3.2 shows the different triggered events as a function of the run number. This minimum bias strategy corresponds to a triggered event `MB`, `kINT` (similar to the first one) or alternatively `kINTinMUON` (meaning `MB` trigger that trigger muon cluster, and `kMUU7` represents a subset of `MB`). The selection of different sub-events is referring to the following list:

- signal or energy deposited in the V0A detector ($2.8 < \eta < 5.1$)
- signal or energy deposited in the V0C detector ($-3.7 < \eta < -1.7$)
- coincidence of signals in V0A and V0C detectors (V0M)

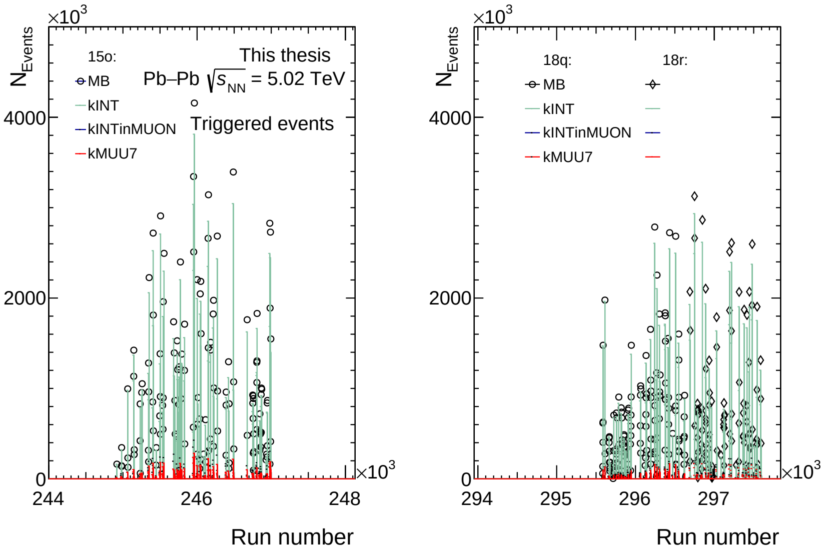

Figure 3.2: Number of triggered events for the different data taking period 2015 (left) and 2018 (right).

- charged tracklets reconstructed in the SPD detector ($-1.4 < \eta < 1.4$)

Figure 3.3 (left panel) shows the selection on the position of the primary vertex along the beam axis $|z| < 10$ cm, in order to ensure an uniform SPD acceptance (the two first layers of the ITS, the closest tracker detector). A selection on the centrality for each Pb–Pb event is also applied, which must be in the interval 0–90 % (see Fig. 3.3, right panel), this selection criteria does not affect the flat distribution of the multiplicity obtained in the V0, with `MB` events.

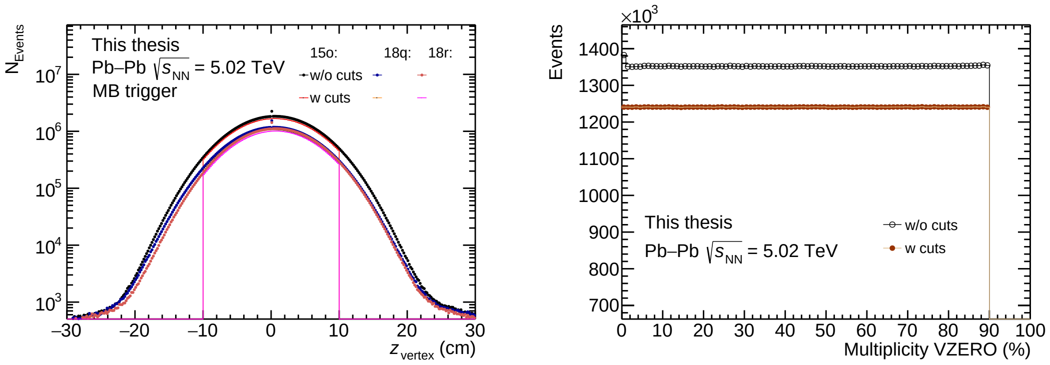

Figure 3.3: Left: Interaction vertex z position before and after cut (in red). Right: Multiplicity in percentage obtained in the V0M (V0A+V0C) detector before and after the selection cuts (centrality in 0–90 % and $|z| < 10$ cm), based on minimum bias events.

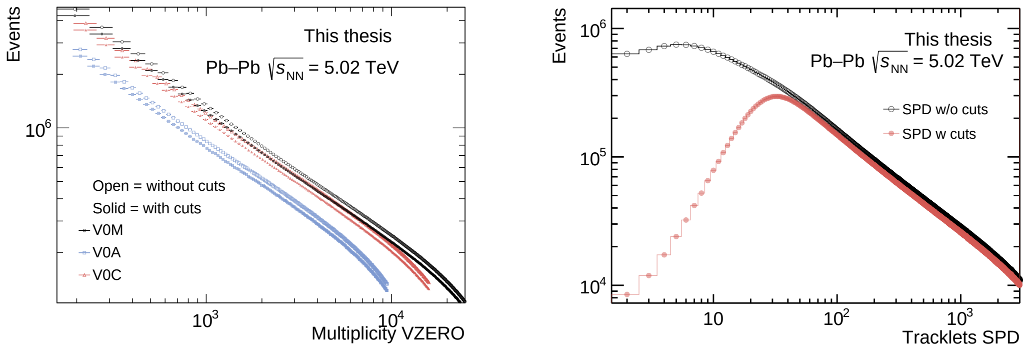

Figure 3.4: Multiplicity in the V0 detector and number of tracklets in the SPD before and after applied selection cuts, based on minimum bias events.

The selection criteria (Physics selection, z vertex, centrality, ...) on minimum bias events is able to remove many events which can cause trouble later in the event flow vector calibration. This essential procedure keeps only Pb–Pb physics events, with accessible properties as the multiplicity (obtained from either V0 or SPD), and a position z of the vertex reconstructed from the SPD. In particular these selections remove the parasitic events with very low multiplicity measured in the SPD (see Fig. 3.4, right panel). The multiplicity selection process in the V0A, V0C, or the combination of both, the V0M, is shown in Fig. 3.4 (left panel).

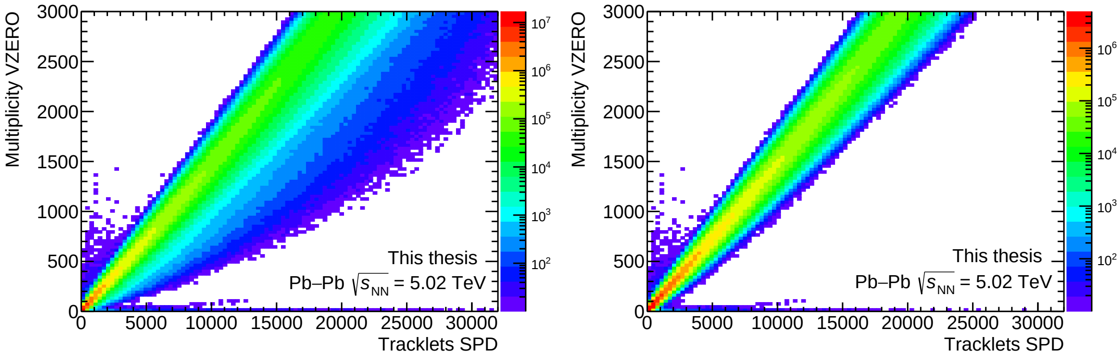

Figure 3.5: Multiplicity in the V0 versus number of tracklets in the SPD, before (left) and after selection cuts (right).

Figure 3.5 shows the multiplicity measured the V0 versus the number of tracklets obtained in the SPD, before and after the selection of the events (on the position of the primary vertex and the centrality). The remaining events for which the multiplicity values measured in the two detectors do not follow the expected correlation are most probably affected by pile-up (events containing more than one collision). The selected minimum bias events (obtained from tracklets in the SPD, or charged particle multiplicity from the V0M) are used to characterise the event flow vector as a function of the centrality of the collision. However, some corrections and calibrations are necessary, which will be discussed next.

3.3 Calibration procedure for flow analyses

Regardless of the detector used, the symmetry planes Ψ_n are randomly distributed, with no preferred orientation. A consequence of this is that the event-plane distribution and consequently the event-averaged φ-distribution of the emitted particle are expected to be uniform. However, the measured event-plane distribution typically shows a modulation in the azimuthal direction due to the detector inefficiencies (see Fig. 3.6, right panel), this could lead to fake correlations, and finally produce a bias in the results. Figure 3.6 (left panel) shows the corresponding pseudo-rapidity distribution of minimum bias events obtained for the different data-taking periods. Therefore, the event flow vectors $\mathbf{Q}_n$ need to be corrected for the non-uniform acceptance of the detectors, that are used to compute them.

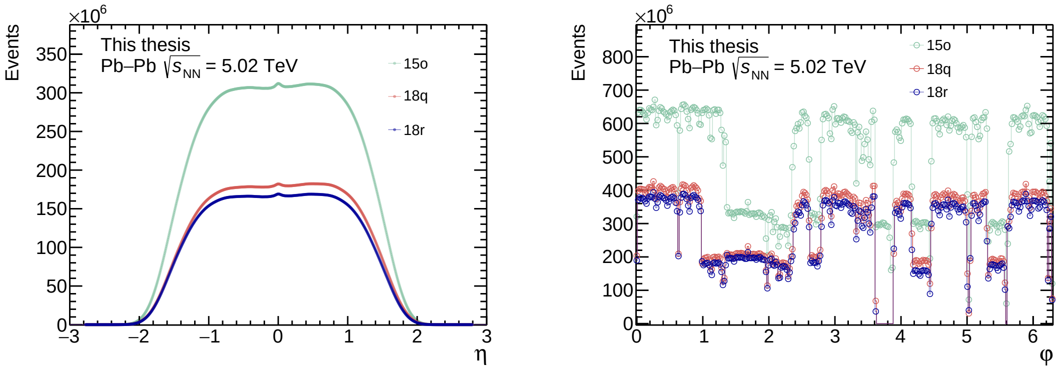

Figure 3.6: Distribution of the pseudo-rapidity η (left) and azimuthal angle φ (right) for minimum bias trigger, corresponding to different data taking period.

The $\mathbf{Q}_n$ vector calibration is performed within the *FlowVectorCorrection* framework, and the calibration steps are based on the article [124], which studied the effects of non-uniform acceptance in anisotropic flow measurements. The *QnFramework* interface is a framework which extracts and applies azimuthal non-uniformity corrections for the defined $\mathbf{Q}$-vectors which can be further used for any event-plane dependent analysis.

All the corrections applied on $\mathbf{Q}_n$ are calculated in an iterative procedure. Up to four passes on the same data are needed to complete the process. The corrections are applied on a run-by-run basis as a function of the z vertex position and the centrality. The centrality estimator used for this calibration is the V0M (the multiplicity is associated to the energy deposited in the V0A and V0C). The framework uses 10 bins in z (in $[-10;+10]$ cm), and 100 bins in centrality (in $[0;100]$ %).

The corrections are applied on $Q_{n,x}$ and $Q_{n,y}$. The acceptance corrected $\mathbf{Q}_n$ vector has the same average $\langle Q_n \rangle$ with respect to the symmetry plane, as in the case of a detector with perfect acceptance. The SPD, V0A, V0C detectors will be

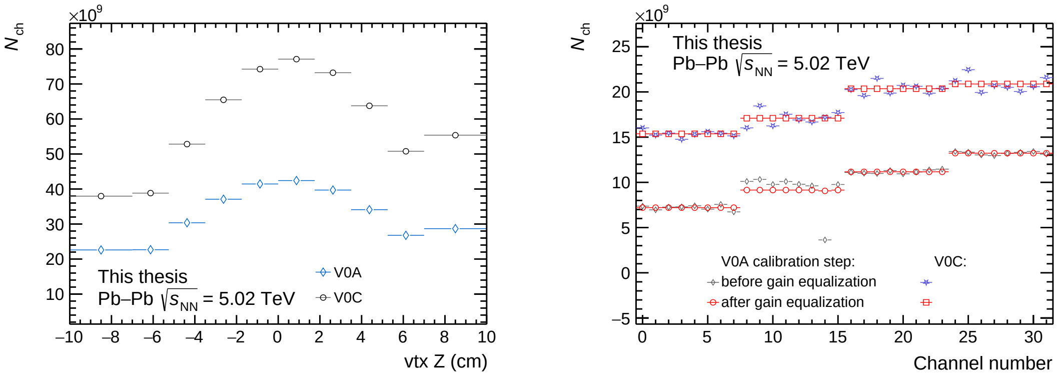

Figure 3.7: Left: Multiplicity of the V0 detector as function of z vertex reconstructed from the SPD. Right: The V0A and V0C multiplicity distribution as a function of channel number before and after gain equalization procedure.

used to determine the **Q**-vector. Here, the idea is to use three different detectors with different pseudo-rapidity η gaps (e.g. $\Delta\eta_{\mathrm{V0A-SPD}} = 1.6$ and $\Delta\eta_{\mathrm{SPD-V0C}} = 0.5$), which provides independent measurement of the same quantity to check the self-consistency. These corrections can be listed with the following ordered steps :

1. **Gain equalization**: is a first correction applied on the individual detector channels, usually done separately for each ring of the V0A and V0C detector. The goal is to equalize the multiplicity (denoted N_{ch} here) measurement as function of the V0 channels. Figure 3.7 (left panel) shows the uncorrected N_{ch} as a function of the vertex position z. Since the V0 detector is divided in two arrays of 32 channels (corresponding to the V0A and V0C), the multiplicity correction for a channel k can be defined as

$$N'_{\mathrm{ch,k}} = \frac{N_{\mathrm{ch,k}}}{\langle N_{\mathrm{ch,k}} \rangle}, \tag{3.11}$$

where $N'_{\mathrm{ch,k}}$ is the multiplicity (or gain) corrected for the channel k, $N_{\mathrm{ch,k}}$ is the measured raw multiplicity, and $\langle N_{\mathrm{ch,k}} \rangle$ is the average multiplicity. Figure 3.7 (right panel) shows the result of this step, before (gray and blue marker) and after (open red markers), then all channels return the same corrected multiplicity average, the RMS values become flat for each ring of V0 detector.

2. **Re-centering (and width equalization)**: is a procedure applied on $Q_{n,x}$ and $Q_{n,y}$, for SPD, V0A, V0C. This correction is typically needed due to non-zero values in the components of the unitary vector u_n, and in principle the event flow vectors should not have no preferred value or direction. This procedure is applied as function of z and centrality. The re-centering and width equalization can be briefly resumed in the two following formula:

$$Q'_{n,x} = Q_{n,x} - \langle Q_{n,x} \rangle, \tag{3.12}$$

$$Q''_{n,x} = \frac{Q'_{n,x}}{\sigma}, \tag{3.13}$$

where $Q'_{n,x}$, $Q''_{n,x}$ are the corrected $Q_{n,x}$ components, σ is the width of the $Q_{n,x}$ distribution, and $\langle Q_{n,x}\rangle$ its mean value. Figure 3.8 shows the important effect on $Q_{2,i}$ (where $i = x, y$) provided by this correction, as function of z (left panel) and as function of centrality (right panel) for the SPD. The effects of this correction are also shown in Fig. 3.9 for the $Q_{2,x}$ component for the V0A and V0C.

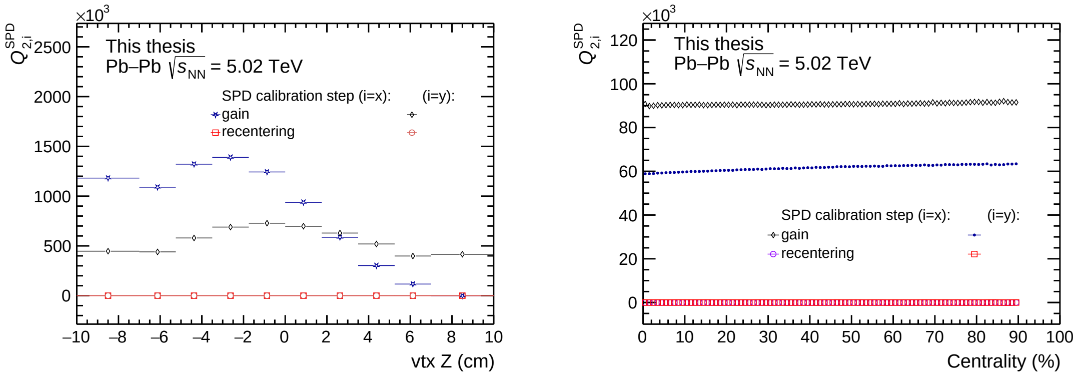

Figure 3.8: Distribution of $Q_{2,x}$ and $Q_{2,y}$ computed with the SPD as function of z vertex (left) and as function of centrality (right) before and after the recentering calibration step.

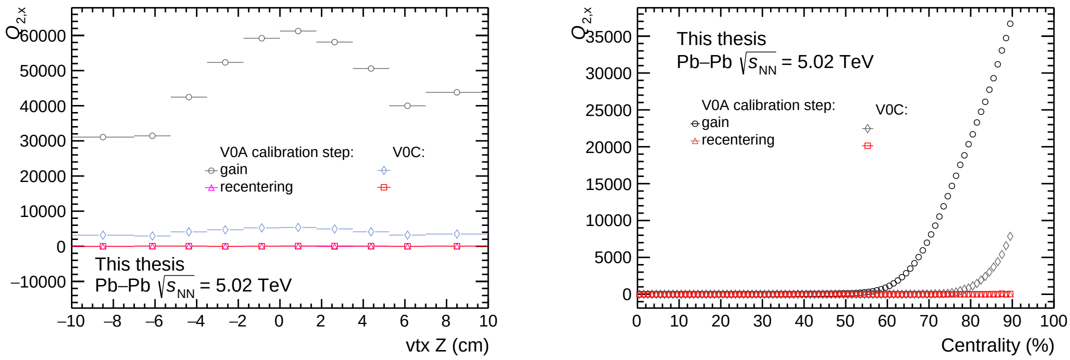

Figure 3.9: Distribution of $Q_{2,x}$ computed with the V0 as function of z vertex (left) and as function of centrality (right) before and after the recentering calibration step.

3. **Alignment**: is a procedure only applied for V0A and V0C. The event flow vectors are corrected from rotation $\mathcal{R}$ by choosing a detector configuration as an alignment reference

$$Q'''_{n,x} = Q''_{n,x} \cdot \mathcal{R}(\Delta\varphi_n), \tag{3.14}$$

where the rotation angle $\Delta\varphi_n$ is determined from a given detector configuration A and an other harmonic m

$$\Delta\varphi_n = \frac{1}{m}\arctan\left(\frac{\langle Q_{n,x}Q^A_{n,y}\rangle - \langle Q_{n,y}Q^A_{n,x}\rangle}{\langle Q_{n,x}Q^A_{n,x}\rangle + \langle Q_{n,y}Q^A_{n,y}\rangle}\right), \tag{3.15}$$

where $\langle ... \rangle$ is an average over all events in a given centrality class or z bin. After this step, the event flow vector components are already very close to their final values.

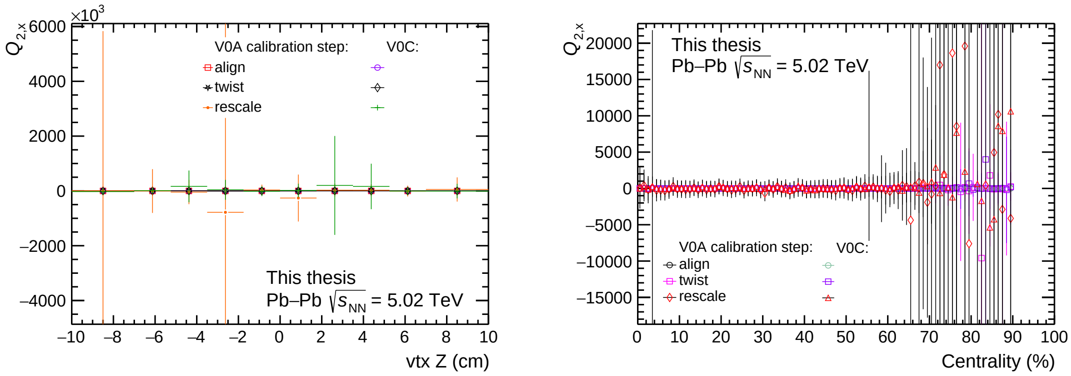

Figure 3.10: Distribution of the event flow vector computed with the V0 as function of z vertex (left) and as function of centrality (right) before and after the alignment, twist and rescale calibration step.

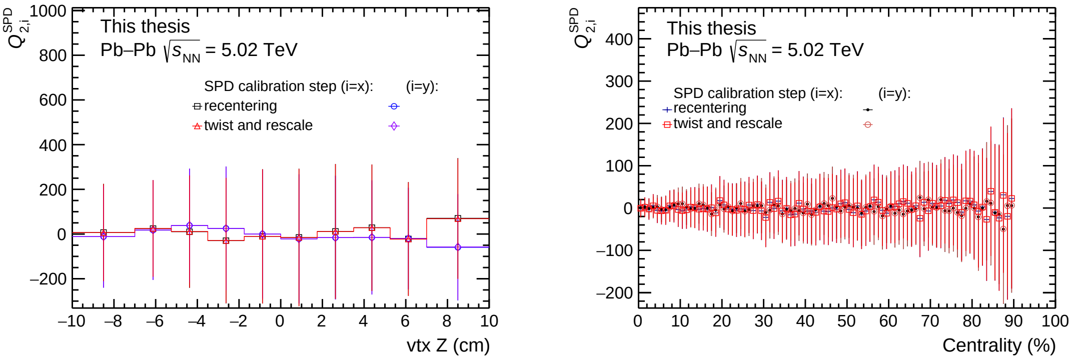

Figure 3.11: Distribution of the event flow vector computed with the SPD as function of z vertex (left) and as function of centrality (right) before and after the alignment, twist and rescale calibration step.

4. **Twist and re-scaling**: is a final correction which takes its origin from the fact that, for a given reaction plane, some residual terms appear in x_n and y_n components (where $\langle Q_n \rangle_{\Psi_{\rm RP}} = \langle x_n \rangle_{\Psi_{\rm RP}} + i \langle y_n \rangle_{\Psi_{\rm RP}}$), due to a non-uniform detector acceptance. Vector twist results in sinus terms in the equation of $\langle x_n \rangle_{\Psi_{\rm RP}}$ and cosine terms for $\langle y_n \rangle_{\Psi_{\rm RP}}$ as

$$\begin{aligned} \langle x_n \rangle_{\Psi_{\rm RP}} &= a^+[\cos(n\Psi_{\rm RP}) + \Lambda^+ \sin(n\Psi_{\rm RP})], \\ \langle y_n \rangle_{\Psi_{\rm RP}} &= a^-[\cos(n\Psi_{\rm RP}) + \Lambda^- \sin(n\Psi_{\rm RP})], \end{aligned} \tag{3.16}$$

The non-zero coefficients $\Lambda^{\pm}$ defined by detector acceptance and ratio between different harmonic flow coefficients, are used for correction through a diagonalisation procedure (twist) as

$$Q''''_{n,(x,y)} = \frac{Q'''_{n,(x,y)} - \Lambda^{(+,-)} Q'''_{n,(y,x)}}{1 - \Lambda^{-}\Lambda^{+}}. \tag{3.17}$$

Then, the re-scaling can be expressed using the acceptance coefficients ($a^{(+,-)}$)

$$Q'''''_{n,(x,y)} = \frac{Q''''_{n,(x,y)}}{a^{(+,-)}}, \tag{3.18}$$

where $Q''''_{n,x}$, $Q'''''_{n,x}$ is the fourth and fifth time corrected $Q_{n,x}$ component. These corrections are applied on the $\mathbf{Q}_n$ components due to the non-uniformity of the detector acceptance. Figure 3.10 and Fig. 3.11 show the results of the twist and rescale procedure for the SPD and for the V0, respectively. One can notice that the two last steps do not seem to bring any major improvements, in particular the rescaling which induces counterproductive effects, therefore the final corrected $\mathbf{Q}_n$-vector is taken after the twist procedure.

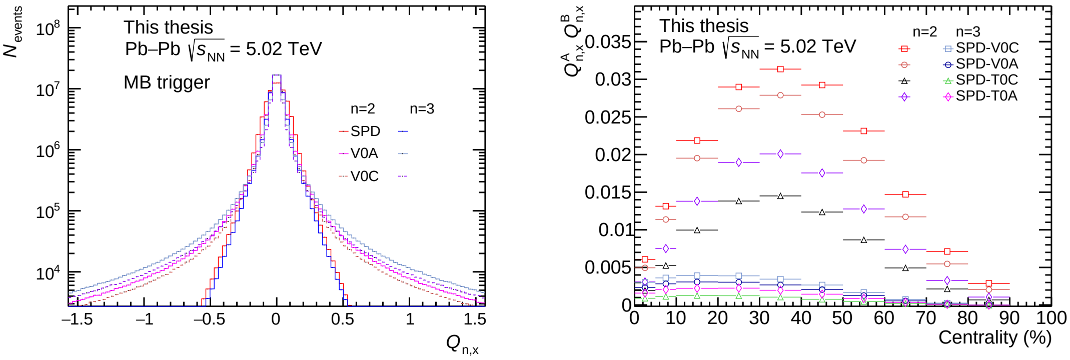

Figure 3.12: (left) Distributions of $Q^{\mathrm{A}}_{n,x}$. (right) Comparison of the product $Q^{\mathrm{A}}_{n,x}Q^{\mathrm{B}}_{n,x}$, computed with different detectors (A = SPD, and B = V0A, T0A, T0C) as function of centrality.

The $\mathbf{Q}_n$ vector corrections are calculated and applied iteratively for each harmonic ($n = 1, 2, 3, 4$), this procedure is performed independently for each flow vector detector. However, in our case the harmonic $n = 1$ and $n = 4$ do not make sense because these detectors used are not sensitive to them (SPD is sensitive to the fourth harmonic, but not the V0). After all the corrections, the final corrected $Q_{n,x}$ and $Q_{n,y}$ values are centered to zero, for each detector and each harmonic (see Fig. 3.12, left panel). Due to detector performance and specific $\Delta\eta$ gap, the linear product of $\mathbf{Q}_n$ vectors from detector A and B in Fig. 3.12 (right panel), show that the SPD-V0C couple produces the highest values for each harmonic, while the SPD-T0A produces the lowest values.

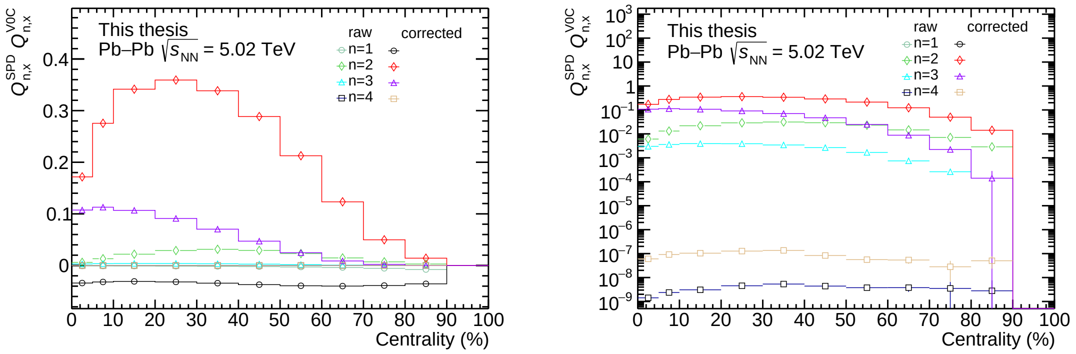

Figure 3.13: $Q^{\mathrm{SPD}}_{n,x} Q^{\mathrm{V0C}}_{n,x}$ distribution as function of centrality before (raw) and after corrections, for different harmonics ($n = 1, 2, 3, 4$).

As introduced in section 1.5, the second harmonic $n = 2$ corresponds to highest flow values due to geometric consideration of the collision. This fact is clearly visible in the product $Q^{\mathrm{SPD}}_{n,x} Q^{\mathrm{V0C}}_{n,x}$ in Fig. 3.13, which is related to the v_n^2 values of charged particles. Here, the raw and corrected labels are simply referring to the non-divided and divided $\mathbf{Q}_n$-vector components by the event multiplicity, taken after the calibration steps. The maximum value of these products for $n = 2$ is around 20–40% centrality class (which is understood by linking the centrality and eccentricity quantities, which are convoluted with the multiplicity of the event). Moreover, this maximum value is displaced toward central collisions for $n = 3$, which is mainly drived by fluctuations.

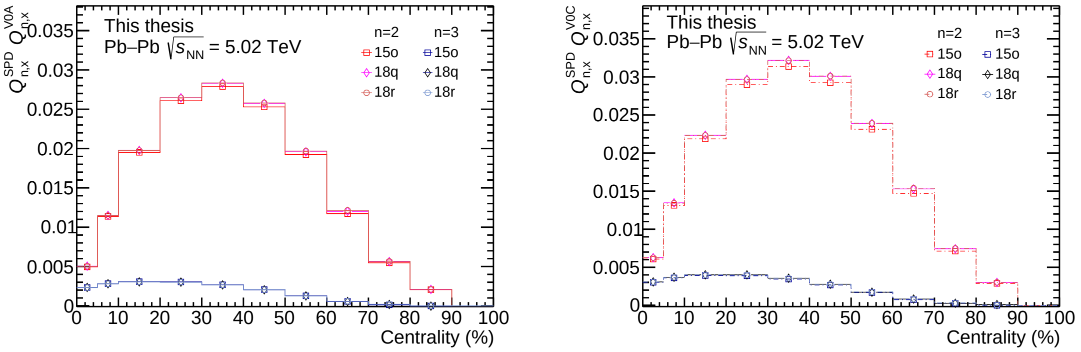

Figure 3.14: Raw $Q^{\mathrm{SPD}}_{n,x} Q^{\mathrm{V0A}}_{n,x}$ and $Q^{\mathrm{SPD}}_{n,x} Q^{\mathrm{V0C}}_{n,x}$ distributions as function of centrality, for the second and third harmonics ($n = 2, 3$).

The linear products $Q^{\mathrm{SPD}}_{n,x} Q^{\mathrm{V0A}}_{n,x}$ and $Q^{\mathrm{SPD}}_{n,x} Q^{\mathrm{V0C}}_{n,x}$ (see Fig. 3.14) show similar magnitude and centrality dependence, between the different data taking periods, for both $n = 2$ and 3. However, the cross-products $Q^{\mathrm{SPD}}_{n,x} Q^{\mathrm{V0A}}_{n,y}$ and $Q^{\mathrm{SPD}}_{n,x} Q^{\mathrm{V0C}}_{n,y}$ (see Fig. 3.15) reveal non-zero values, more pronounced in 2015 than 2018, which point out at a remaining non-uniform detector acceptance, and then a residual miscalibration of

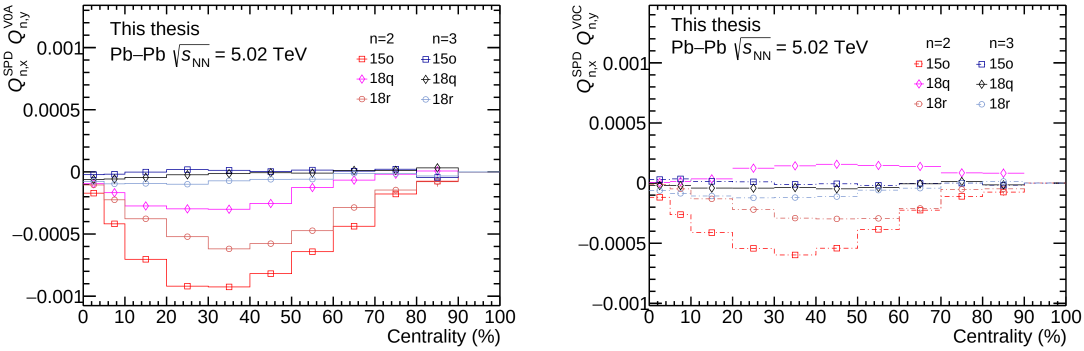

Figure 3.15: Raw $Q^{\rm SPD}_{n,x}Q^{\rm V0A}_{n,y}$ and $Q^{\rm SPD}_{n,x}Q^{\rm V0C}_{n,y}$ distributions as function of centrality, for the second and third harmonics ($n = 2, 3$).

the event flow vector. These non-zero values in the cross-products (`X-Y`, `Y-X`) do not exceed an average of 1-2% relatively to the standard linear-products (`X-X`, `Y-Y`). The detector acceptance could be deteriorated by multiple dead zones depending of the data taking period. Similar observations can be drawn looking to the $Q^A_{n,y}Q^B_{n,y}$ components and the cross-products $Q^A_{n,y}Q^B_{n,x}$ (see Fig. 3.16 and Fig. 3.17). One can also mention that the number of recorded `MB` events is different for these three data taking periods, which can induce different precision in these curves of event flow vector products.

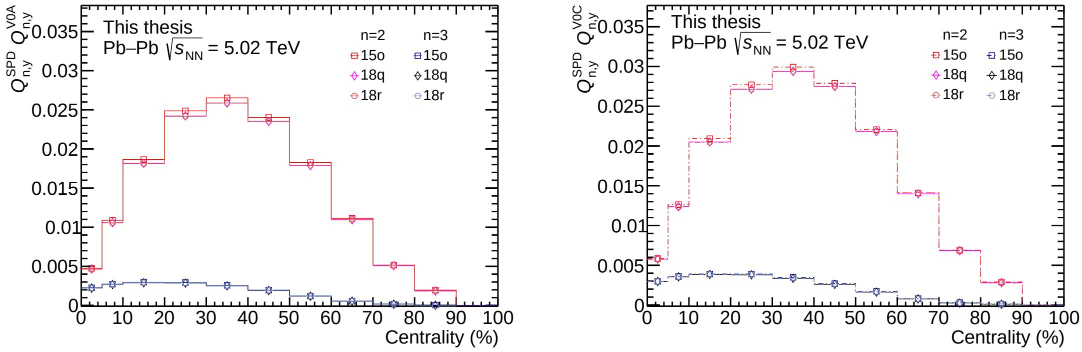

Figure 3.16: Raw $Q^{\rm SPD}_{n,y}Q^{\rm V0A}_{n,y}$ and $Q^{\rm SPD}_{n,y}Q^{\rm V0C}_{n,y}$ distributions as function of centrality, for the second and third harmonics ($n = 2, 3$).

The complex $\mathbf{Q}_n$ vector contains the event flow properties (preferred direction of the charged tracks, amplitudes in the transverse plane). In order to determine the anisotropic flow coefficients for rare heavy particles, it is needed to access to the corrected event-by-event flow properties and in particular to the so-called factor R_n, before starting to correlate dilepton azimuthal properties with the general event flow properties represented by the large number of charged particles.

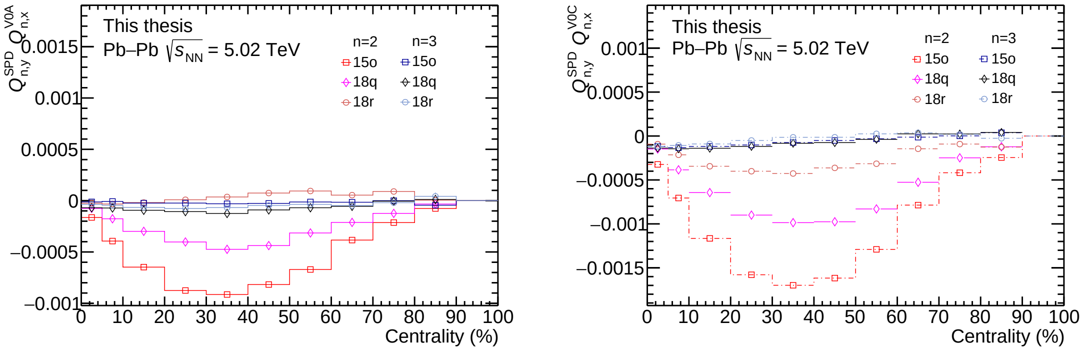

Figure 3.17: Raw $Q^{\rm SPD}_{n,y} Q^{\rm V0A}_{n,x}$ and $Q^{\rm SPD}_{n,y} Q^{\rm V0C}_{n,x}$ distributions as function of centrality, for the second and third harmonics ($n = 2, 3$).

3.4 Event flow properties and resolution

Due to the event-by-event random fluctuations of the impact-parameter vector, the event-plane shall also randomly fluctuate event-by-event. The distribution of the symmetry plane Ψ_2 computed with Eq. 3.3 corresponding to a random single run is shown in Fig. 3.18. The event flow vector equalisation procedure does not reproduce a perfectly flat distribution for the Ψ_2^{SPD} in most of the centrality classes. The Ψ_2^{V0A} and Ψ_2^{V0C} distribution seems globally flat for centrality up to 70 %. These remaining modulations are visible, which is most likely due to non-uniformity, large vertex bins during the calibration, and the correlation with harmonic $n = 4$. Nevertheless, this residual miscalibration will produce negligible impact on final v_n measurement, as checked with the cross-terms products between the components of the $\mathbf{Q}_n$ vector (computed from the SPD, V0A, V0C).

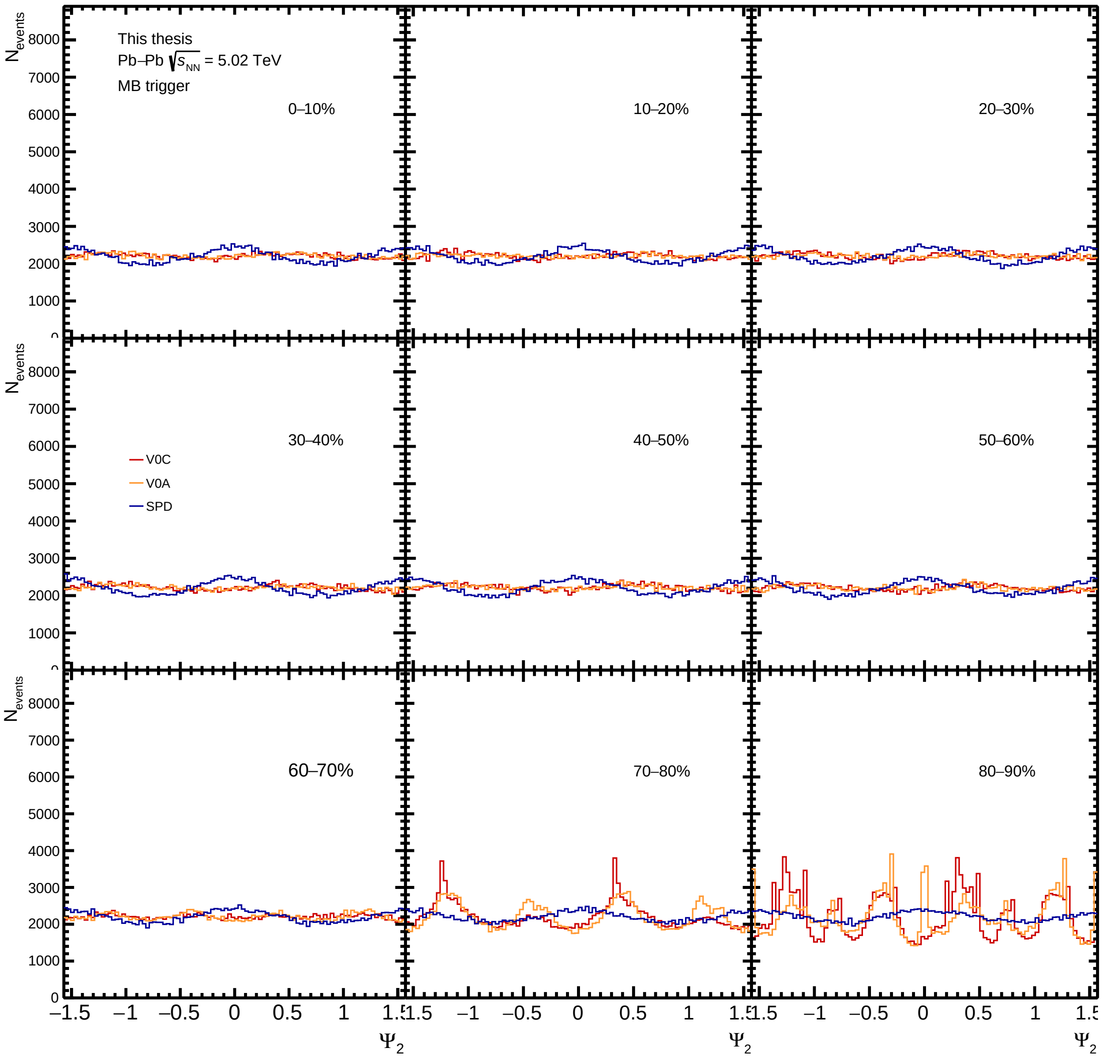

Figure 3.18: Distribution of the symmetry plane angle Ψ_2 for various centrality intervals, the events recorded correspond to a single run (296510).

One can notice that, in very central collisions, all harmonics originate solely from fluctuations and are comparable in magnitude, then remaining harmonics can appear in the Ψ_n distribution for this centrality interval. The Ψ_3^{SPD} has a globally flat distribution for all centrality classes, contrary to the Ψ_3^{V0A} and Ψ_3^{V0C} which present strong modulations between 50 and 90%.

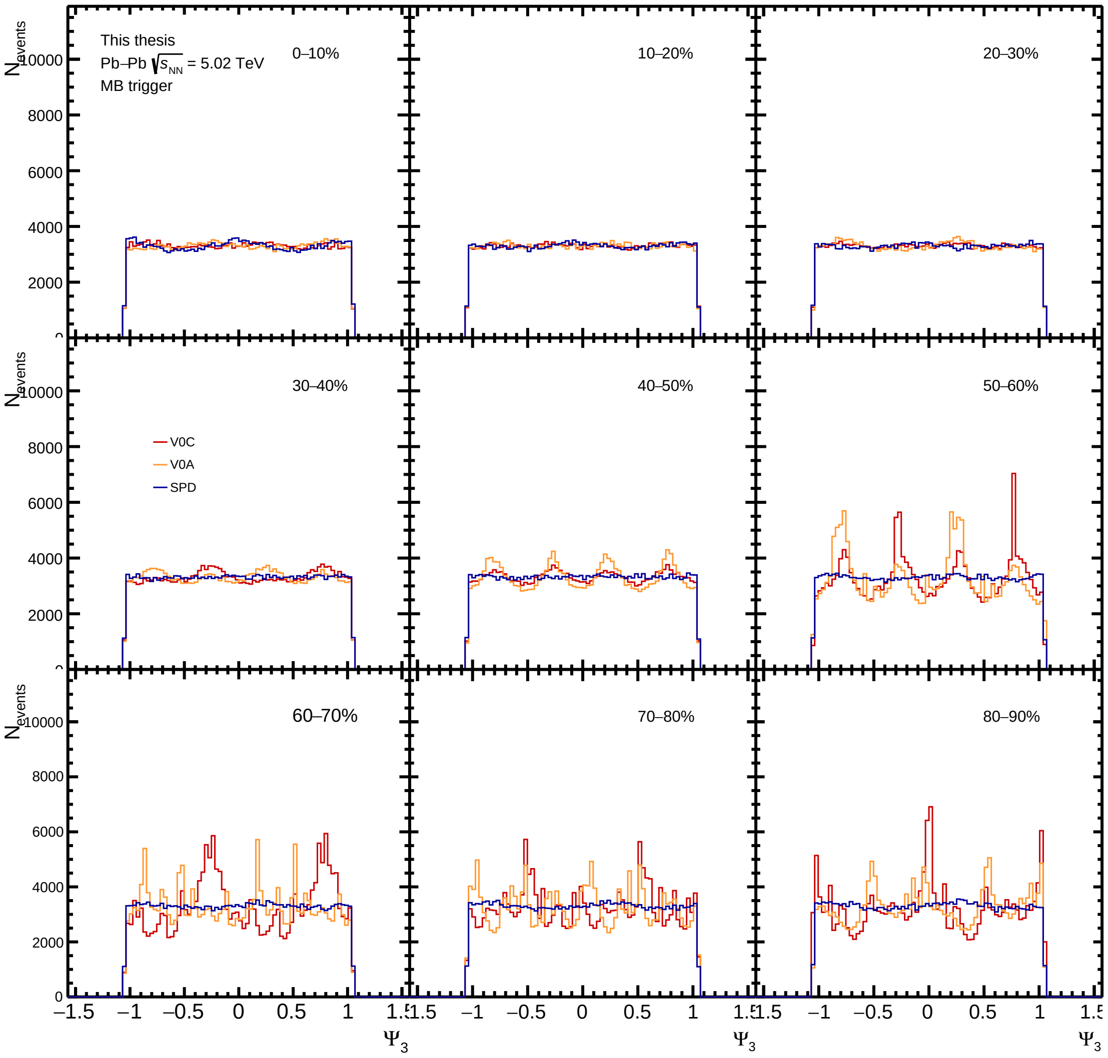

Figure 3.19: Distribution of the symmetry plane angle Ψ_3 for various centrality intervals, the event recorded correspond to a single run (296510).

The event-plane resolution factor R_2 and R_3 are computed using the 3-subevent method formula (Eq. 3.7), using the SPD, V0A, and V0C as reference detectors. This method suppress directly the non-flow component due to the large η gap between V0A and SPD. Since the V0C has a common pseudo-rapidity acceptance with the muon spectrometer and thus an auto-correlation, it will not be used later in the quarkonium v_n extraction. Using the V0A as reference detector would have the advantage of further reducing possible non-flow correlations, since the rapidity gap with the muon spectrometer is larger than for the SPD. Figure 3.20 shows the event-plane resolution factor R_n. The magnitude of R_2 (left panel) and R_3 (right panel) is higher using the SPD as reference detector, instead of using the V0A or V0C. Then for for A = SPD, the R_2 factor is around 90% in 10-40% centrality, and goes up to 60% for R_3 in central collisions.

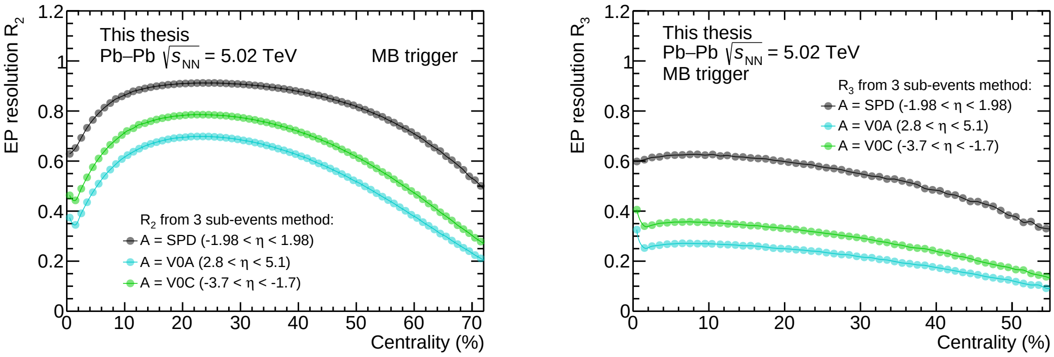

Figure 3.20: R_2 and R_3 event-plane resolution distribution as function of centrality, computed using the 3 sub-event method for different detectors.

The R_n factor decreases toward more central or more peripheral collisions. In most peripheral collisions, R_n decreases simply because the multiplicity is smallest there, and the resolution strongly depends on it. For most central collision, the sum of charged particle unitary vector are not able to give some unique direction, this lead to a regime where fluctuations are dominant (due to the random nature of the interaction between constituents of the two nuclei). In a simplified picture (for $n = 2, 3$), events with low space eccentricity (ϵ_n) produce low v_n values, while those with large ϵ_n produce large v_n (and the resolution factor will be also scaled to the v_n).

The calculations of the reference-flow R_n with the 3-sub-event method using SPD as reference detector (using Eq. 3.10) are shown in Fig. 3.21. This factor, used in the scalar product method, is intrinsically different than the resolution obtained for the event-plane method, and have lower values, where the maximum are displaced around the 40-50% centrality interval. The R_n factors are calculated from the minimum bias triggered events, but it can alternatively be calculated with events recorded using others triggers (e.g. events containing at least one selected muon or dimuon, the differences between both methods do not exceed 1% for R_2 and 2-3% for R_3).

For all centrality intervals, the SPD has the higher R_n in comparison with the V0C and even more with the V0A, favored by a larger acceptance and better azimuthal segmentation. One can finally note that, when final v_n values are computed in large centrality ranges and then divided by R_n, due to the fact that R_n are computed using minimum bias events (where N_{MB} is constant as function of centrality), the R_n should be weighted by a quantity related to the number of dimuon events (N_{CMUL} events or by quarkonium raw yield). However, this weighting procedure will not be needed in our case, simply because the v_n will be corrected by R_n di-

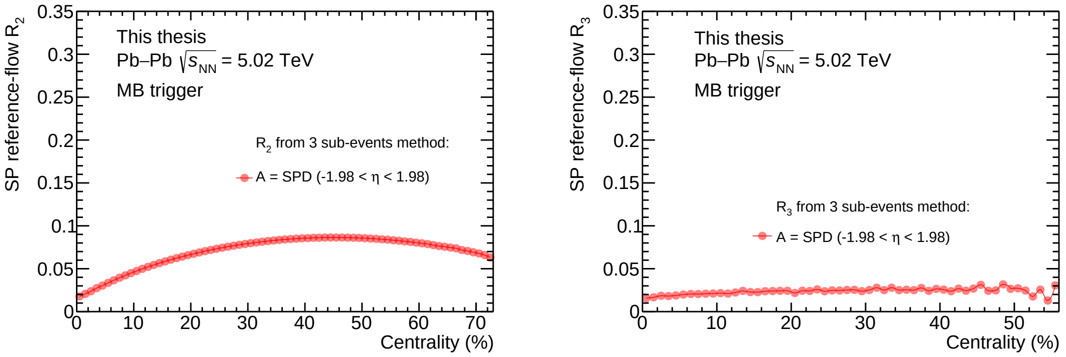

Figure 3.21: Centrality dependence of the scalar product reference-flow R_2 and R_3 distribution, computed using the 3 sub-event method using the SPD.

rectly candidate by candidate, using a parametrization of the curves obtained in this section. The final corrected dimuon v_n will be used to extract the azimuthal anisotropies of the quarkonium signal in the Pb–Pb collisions.

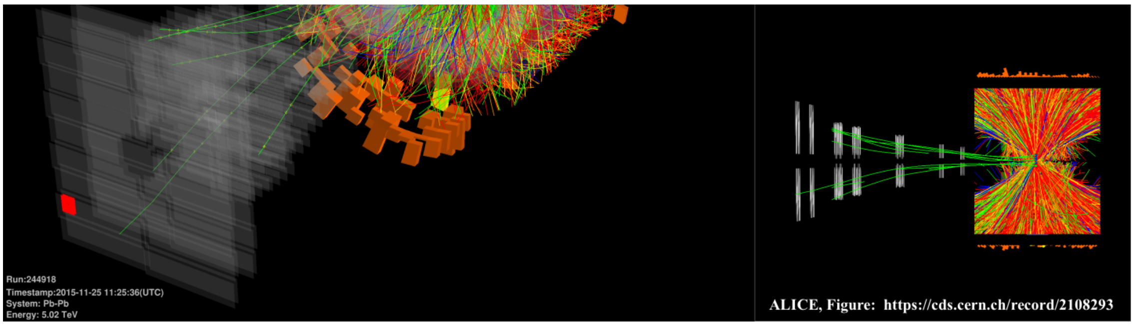

ALICE, Figure: https://cds.cern.ch/record/2108293

Chapter 4

Data analysis

This chapter describes the second part of the analysis using the Pb–Pb data sample recorded in 2015 and 2018, leading to the final quarkonium v_n results. First, the general event properties, the triggers used and the selection criteria will be described. Secondly, the extraction of J/ψ and Υ(1S) raw yield and their signal-over-background ratio will be presented. Thirdly, a brief overview of the quarkonium v_n extraction will be given. Finally, the different sources of systematic uncertainties will be discussed and quantified.

Contents

This thesis will study the dimuon decay channel in order to reconstruct the charmonium (J/ψ, ψ(2S)) and bottomonium (Υ(1S), Υ(2S), Υ(3S)) states. Muon tracks are measured using the Muon Spectrometer, and the unlike sign dimuon pairs are formed by associating two muons of opposite sign.

4.1 Event, muon and dimuon selection criteria

Data were collected requiring the coincidence of the minimum bias (`MB`) and unlike-sign dimuon triggers (`CMUL` in this analysis, or `kMUU7` in Fig. 4.1). The former is defined by the coincidence of signals in the V0A and V0C arrays (and it is used for the event flow vector calibration), while the latter requires, in addition to the `MB` condition, at least a pair of opposite-sign track segments in the muon trigger stations. In the previous section, Fig. 3.2 has shown the corresponding number of `MB` events (black open circles) and unlike sign dimuon events (red curves), as a function of the run number for the 2015 and 2018 data sample.

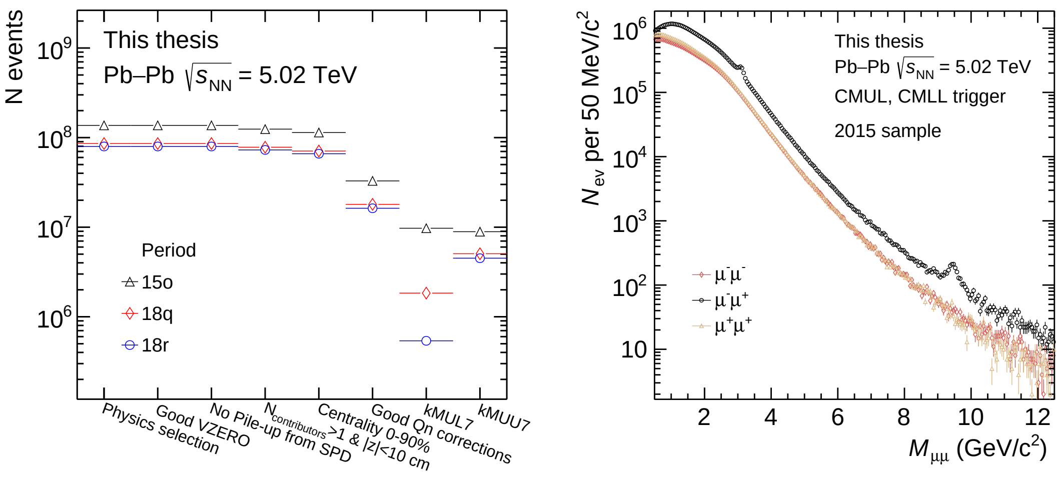

Figure 4.1: Left: Number of events for different cuts or triggers selection. Right: Integrated dimuon invariant mass spectra, where J/ψ and Υ(1S, 2S, 3S) peaks are visible.

The centrality of a Pb–Pb collision event can be estimated with several detectors, in this analysis the V0M estimator will be used. Dimuon events satisfy the `MB` trigger conditions which was already defined in the previous Chapter 3. Events containing more than one collision (pile-up) are removed by exploiting the correlations between the number of clusters in the SPD, the number of reconstructed SPD tracklets, and the amplitude signals measured in the V0A and V0C detectors. In addition, it is also necessary to find a SPD vertex in the muon trigger operations, in particular in the reconstruction of muon tracks with the Muon Spectrometer. In order to study the background, additional samples of single muon (`CMSL7`) and like-sign dimuon (`CMLL`) events were also collected by requiring, in addition to the `MB` condition and the low-p_T threshold, a pair of same-sign track segments in the trigger system, respectively.

To make sure that all accepted tracks are muons reconstructed within the detector acceptance, the following criteria to be full-filled by each individual track are required:

- the track must be within the pseudorapidity range ($-4 < \eta < -2.5$).
- the transverse radius coordinate of the track at the end of the front absorber must be in the range 17.6 cm $< R_{\mathrm{abs}} <$ 89 cm. This selection corresponds to an angle within $2^{\circ} < \theta < 10\ ^{\circ}$.
- the reconstructed track in the tracking chambers must match a trigger track reconstructed in the trigger chambers (with $p_T >$ 1.0 GeV/c in Pb–Pb).
- a standard cut on the $p \times$ DCA (at 6σ) is used (defined as the product of the track momentum and distance of the closest approach to the primary vertex).

It is able to remove tracks from beam-gas events (i.e. muons from non-prompt J/ψ (not from the IP are not removed).

The selected muons are then combined into dimuon pairs, the candidates that do not meet the following criteria are rejected:

- the two reconstructed muons must have opposite charges (`CMUL` trigger), since the J/ψ or Υ(1S) are neutral mesons.
- the dimuon must be reconstructed within the rapidity window $2.5 < y < 4.0$, which correspond to $-4.0 < y < -2.5$ in the detector frame.

The programmable threshold of the muon trigger algorithm was set so that the trigger efficiency for muon tracks with $p_{\mathrm{T}} = 1$ GeV/c is 50%, and reaches a plateau value of about 98% at $p_{\mathrm{T}} \approx 2.5$ GeV/c. Figure 4.1 (right panel) shows the results of the dimuon invariant mass spectra for `CMUL` and `CMLL` triggered events, which are divided into three samples of dimuons ($\mu^+\mu^-$, $\mu^+\mu^+$, and $\mu^-\mu^-$).

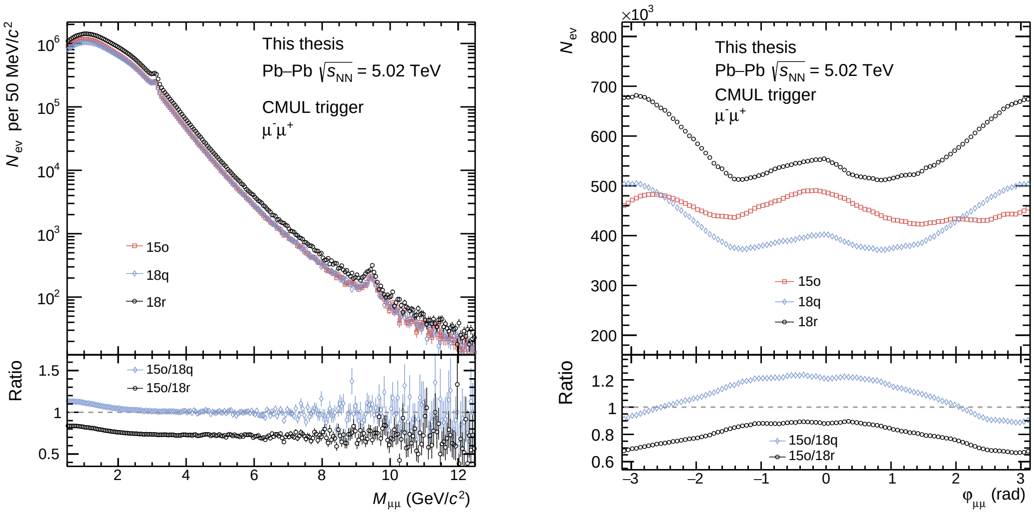

Figure 4.2: Left: Dimuon invariant mass spectra for unlike sign dimuon events for the different data taking periods. Right: Distribution of the reconstructed dimuon azimuthal angle.

The reconstructed number of J/ψ and Υ can be studied through the dimuon invariant mass spectra. For a two-particle collision (or a two-particle decay), the square of the invariant mass is defined as

$$M_{12}^2 = (E_1 + E_2)^2 - ||\mathbf{p}_1 + \mathbf{p}_2||^2 = m_1^2 + m_2^2 + 2(E_1E_2 - p_1p_2\cos\theta_{12}), \tag{4.1}$$

where θ_{12} is the pair relative angle, in our case it will be associated to the initial angle formed between the two muon tracks. Figure 4.2 shows the obtained dimuon invariant mass $M_{\mu\mu}$ and rapidity $y_{\mu\mu}$ distributions for different data taking periods and their ratio, after the final dimuon selection procedure. Similarly in Fig. 4.3, the dimuon p_{T} and rapidity $y_{\mu\mu}$ distributions are presented.

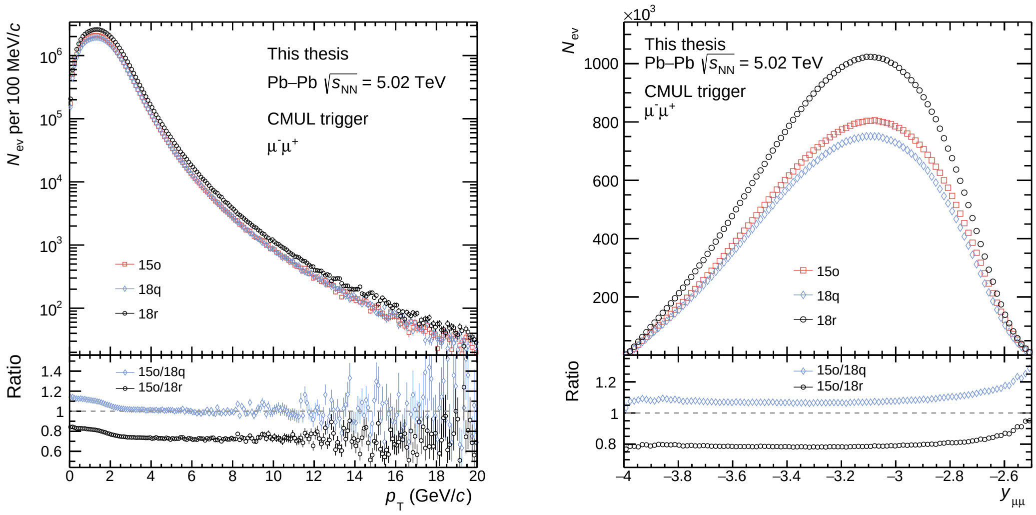

Figure 4.3: Left: Dimuon p_T spectra for unlike sign dimuon events for the different data taking periods. Right: Distribution of the reconstructed dimuon rapidity y.

One can also notice that the dimuon like-sign trigger (`CMLL` or `kMUL7`) was downscaled for the 2018 data taking period, as visible in Fig. 4.1 (left panel). This trigger is not used in the main analysis, which is performed on unlike-sign muon pairs. Typically, this like-sign trigger can be used for reproducing the background under the J/ψ or Υ peaks (e.g. producing dimuons using two muons from different events, the so-called *event mixing* technique). This problem can be solved simply by selecting other triggers, or alternatively, downscaling factors can be applied on the selected runs in order to correct these numbers of events.

After combining the three Pb-Pb data taking periods at 5.02 TeV, the integrated luminosity for the main dimuon analysis is found to be approximately 750 μb^{-1} (corresponding to 225 μb^{-1} for 2015, and 210 plus 312 μb^{-1} for 2018).

4.2 Quarkonium raw yield extraction

The two muons are reconstructed in the forward muon spectrometer, then the number of quarkonia is extracted using the invariant mass distribution of opposite sign muon pairs. The total recorded data sample in 2015 and 2018, corresponds to approximately 3.3 times more than those of 2015. Hence, one can expect a reduction of the statistical uncertainties by approximately 1.8 with respect to the previously published results [79, 92], which are based only on the 2015 sample.

In order to describe the J/ψ, ψ(2S) and Υ(1S, 2S, 3S) peak shapes in the dimuon invariant mass spectra, the extended Crystal Ball (CB2) function is used as a signal fit function (details can be found in the Appendix A). This function is described by a Gaussian core (3 parameters), and two tails (4 parameters) [125]. In the fit, the J/ψ mass peak position is left free, while for the ψ(2S) it is fixed to its PDG value [8]. For the Υ states, the 1S and 2S mass peak position are left free, while it is fixed for the 3S. In the fit, the J/ψ and Υ(1S) widths are left free, their CB2 tail parameters are fixed to the values reported in Ref. [126] (or in the Appendix A). These tail parameters can be, either fixed from results obtained in p–p collisions (better signal to background ratio) or fixed from simulation, corresponding to a pure Monte Carlo (MC) event generation (J/ψ, $\Upsilon \rightarrow \mu\mu$) embedded into real `MB` triggered events (explained in detail later). Finally, each width of excited state is fixed from the width fit result from the 1S state scaled by the mass ratio (as $\frac{m_{2S}}{m_{1S}}$ or $\frac{m_{3S}}{m_{1S}}$).

Correlated muon pairs, which are originated from the same resonance decay in the same-event, have an invariant mass distribution confined in a narrow mass region due to their correlation. Whereas the invariant mass of the uncorrelated pairs (which point to two different resonance decays in the same-event) would follows a much broader distribution than resonance peak. This part of invariant mass distribution was named as combinatorial background. Thus, to extract the resonance signal from all these correlated and uncorrelated muon pairs, one must first manage to reconstruct the combinatorial background. For relatively weak background with less or no fluctuation near the resonance peak, the polynomial (or arbitrary) fitting is useful. However the fitting does not contain any physics information, and its correspondence to the background will not be satisfying especially for comparatively weak resonance signal with strong background in the fitting region. To avoid that, the background reconstruction needs to be processed with the methods that correctly utilize the physics information from experiment, such as the event-mixing method and the like-sign method.

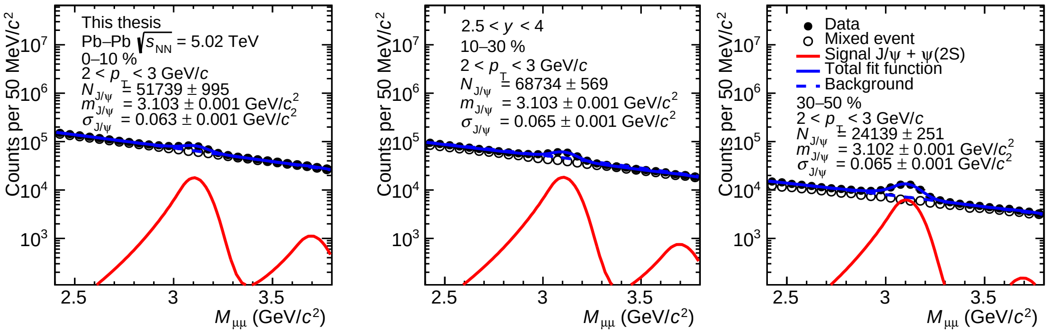

Figure 4.4: J/ψ raw yield extraction for different centrality interval, in the same p_T range.

The background, which is mostly combinatorial especially in central events, is well reproduced with the event-mixing technique, which consists of combining uncorrelated muon pairs taken from different events, with similar collision centrality and longitudinal vertex position (z). In any case, for the background function, a variable-width Gaussian (4 parameters, where the width is linear with the dimuon invariant mass [125]) could be used, either in the charmonium or bottomonium mass range. The total fit function is the result of the combination of the signal and background functions. Examples of fits to the dimuon invariant mass distributions are shown in Fig. 4.4 for the J/ψ, and in Fig. 4.6 for the $\Upsilon(1S)$.

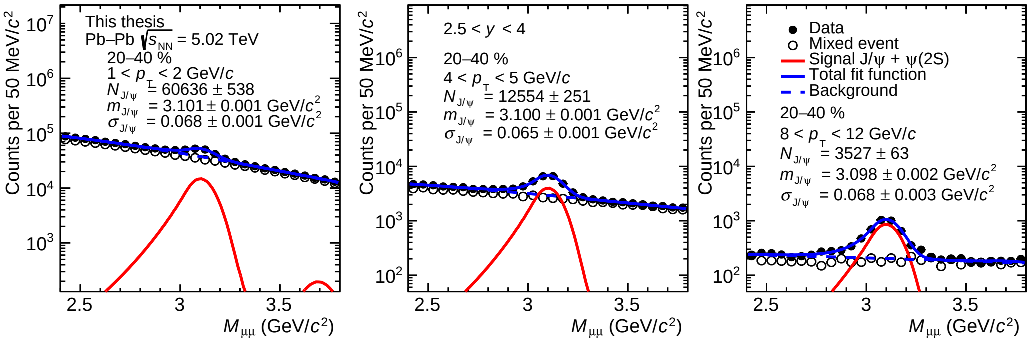

Figure 4.5: J/ψ raw yield extraction for different p_{T} ranges, in the same centrality interval.

Dimuons can be formed by two muon tracks from the same event, or by constructing a pair of muons from different events (mixed-event). Therefore, it leads to the possibility to obtain either: opposite sign ($+-$), positive sign ($++$) or negative sign ($--$) muon pairs, from mixed- or same-event. The advantage of using mixed-event is that, there are no limits in the number of formed muon pairs, unlike using the same-event. Since the μ^+ and μ^- have a different acceptance, it is necessary to apply a normalization (based on the like-sign muon pairs distributions) to the mixed-event spectra, if one needs to compare them to the raw same-event spectra. This method introduces the factor $\mathcal{F}$, which can be defined to normalize the mixed-event spectrum as

$$\mathcal{F} = \int 2R\sqrt{N^{++}_{\text{same}}N^{--}_{\text{same}}}\,\mathrm{d}M_{\mu\mu} \Big/ \int N^{+-}_{\text{mix}}\,\mathrm{d}M_{\mu\mu}, \tag{4.2}$$

where the integration limits are defined in a large $M_{\mu\mu}$ range, around the signal peak. R is calculated using negative, positive and opposite sign dimuons from mixed events, with the formula $R = N^{+-}_{\text{mix}}/(2\sqrt{N^{++}_{\text{mix}}N^{--}_{\text{mix}}})$. This factor, which can be slightly different than 1 for low masses, allows to take into account the acceptance difference between positive and negative muon tracks.

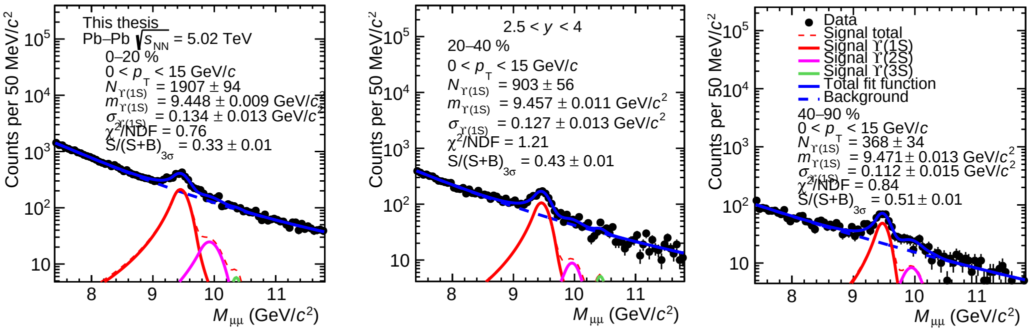

Figure 4.6: Integrated Υ(1S) raw yield extraction for different centrality intervals.

The background under the J/ψ peak is mostly combinatorial, however this is not the case under the Υ(1S) peak (where significant beauty pair production produces correlated background e.g. $gg \rightarrow b + \bar{b}$, $g \rightarrow b + \bar{b}$). Indeed, in the latter case around 30% of the background is not combinatorial, and thus cannot be reproduced by combining muon pairs from different events. Therefore, only in the J/ψ raw yield extraction the event-mixing is used. In this case, the normalised mixed-event spectra reproduces quite well the dimuon background of the same-event spectra under the peak, as suggested by Fig. 4.4.

The approach applied in the fit of the invariant mass spectra for the signal extraction, in which the ratio $\alpha(M_{\mu\mu})$ is obtained, is a (log) likelihood method, while for the extraction of v_n^{sig} in the dimuon v_n profile, a χ^2-fit is used. In order to take into account the binned fit, the option `"I"` corresponding to the integral of the function in bin, instead of the value at the bin center, has been applied. Each fit needs to be validated by requiring a good fit result (`status = 0`) and a good covariance-matrix status (`covMatrix = 3`).

The measured J/ψ and Υ(1S) integrated raw yield (for $0 < p_{\mathrm{T}} < 15$ GeV/c^2) are shown in Fig. 4.7 (left panel), as a function of the centrality. The uncorrected raw yield are obtained after fitting the dimuon invariant mass spectra for the different centrality intervals (see Fig. 4.4 and Fig. 4.6). Figure 4.7 (center panel) shows the significance $(\mathrm{S}/\sqrt{\mathrm{S+B}})$ as a function of p_{T} in different centrality intervals for the J/ψ, and in 0–90% for Υ(1S). The corresponding signal-over-background ratio (S/B) versus p_{T} is also presented in Fig. 4.7 (right panel).

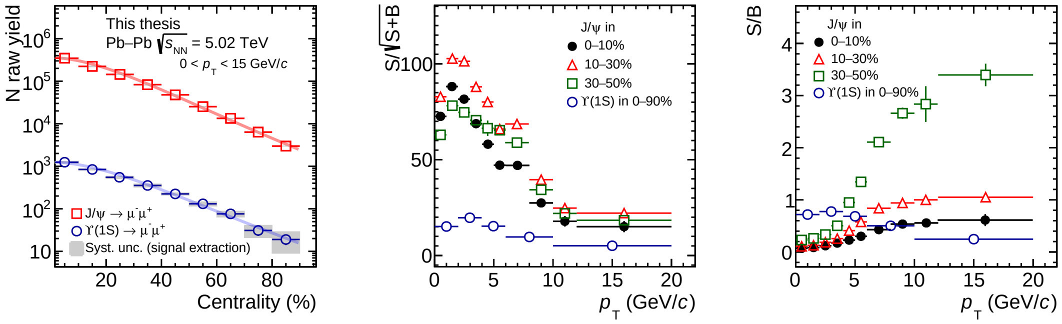

Figure 4.7: Left: Integrated quarkonium raw yield extracted (in 2015 + 2018 data sample), as a function of centrality. Center: Significance as a function of p_{T}. Right: signal-over-background ratio versus p_{T}.

The quarkonium production mesured through the raw yield for both J/ψ and Υ(1S) is maximum in central Pb–Pb collisions (where a hotter and bigger medium is created), and decrease quickly toward peripheral collisions. More than 10^5 J/ψ are extracted in very central Pb–Pb (0–10%) collisions, while about 10^3 Υ(1S) are measured in the same centrality interval. Looking to the significance of the signals, one can see that both J/ψ and Υ(1S) have maximum values at low-p_{T} around 2–3 Gev/c. The signal-over-background ratio for J/ψ is increasing toward higher p_{T}, starting from 0.1 at low-p_{T}, to the value of 0.6 for central Pb–Pb or around 3 for 30–50%, beyond 10 GeV/c. Despite the centrality integrated measurement of Υ(1S) (due to a low number of candidates), the S/B reaches its maximum at around $2 < p_{\mathrm{T}} < 4$ GeV/c, and decreases at high-p_{T}.

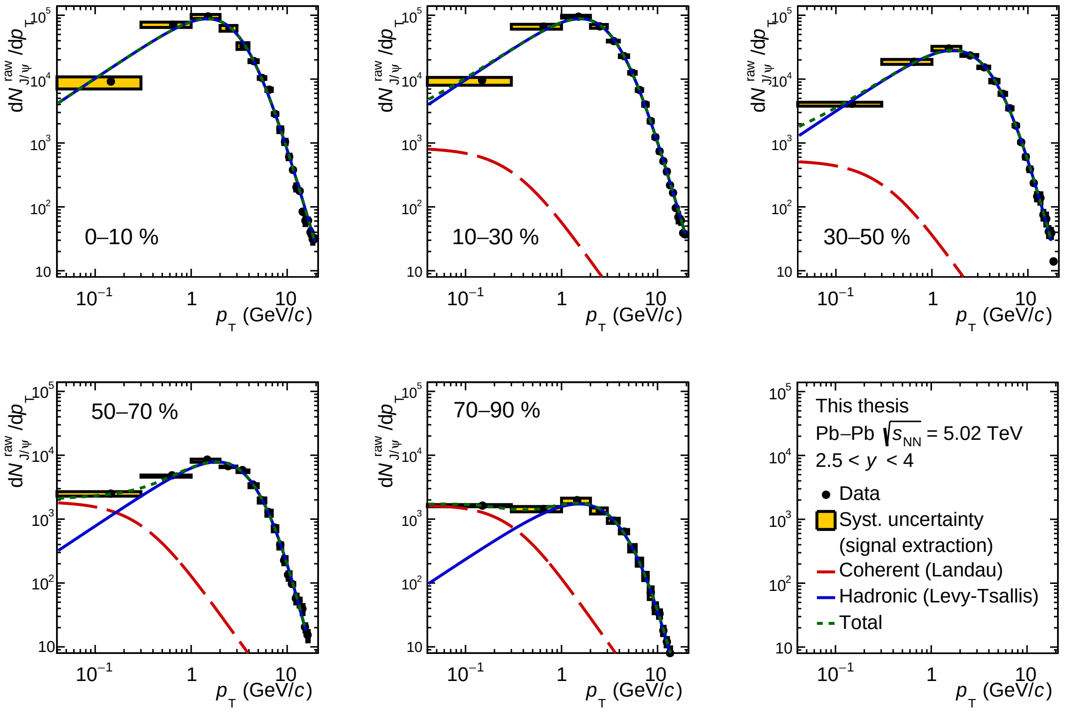

Figure 4.8: p_{T}-differential J/ψ raw yield spectra for various centrality intervals.

Figure 4.8 shows the p_{T}-differential J/ψ raw yield spectra, for various centrality intervals. The photoproducted J/ψ at very low-p_{T} lead to an excess in the raw yield spectra with respect to the expected hadronic production, it was already studied through R_{AA} measurements [127]. Initially, the photo-production of J/ψ is studied in ultra-peripheral Pb–Pb collisions (UPC), where the ions do not break, but emit γ radiations. The total production is dominated by the hadronic contribution which is fitted by a Levy-Tsallis function (blue curves). Otherwise the coherent J/ψ photo-production at very low-p_{T} (below 0.3 GeV/c) which is fitted by an arbitrary (Landau) function (red dotted curves), becomes significant in very peripheral Pb–Pb collisions. One can see that the hadronic contribution can be well studied with a good precision, in a large p_{T} range up to 20 GeV/c, and for various centrality intervals up to 70–90%.

As it was mentioned, this alternative J/ψ photo-production mechanism seems to be significant in peripheral hadronic collisions. The impact of this excess on azimuthal anisotropy measurement in Pb–Pb collisions will be studied later in a dedicated section when showing the results.

4.3 Azimuthal anisotropy measurements

This section will describe the J/ψ and Υ(1S) v_n extraction using the already defined scalar-product (SP) method, which has proven a better reliability, precision with respect to the event-plane method.

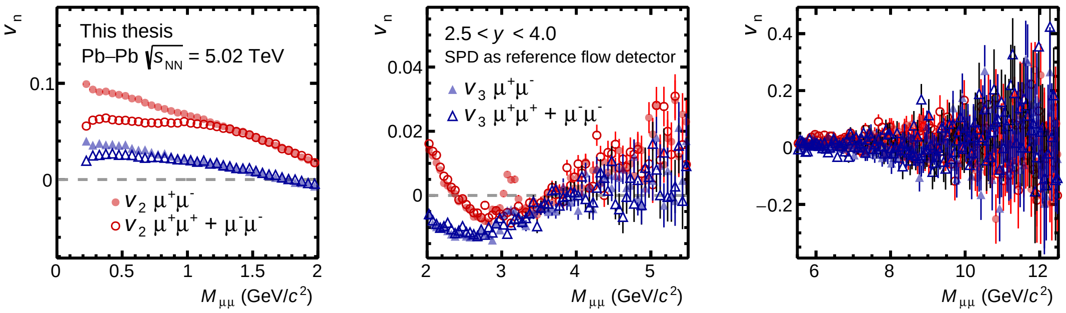

Figure 4.9: Dimuon v_n computed with the scalar product method for unlike- and like-sign muon pairs, as a function of $M_{\mu\mu}$, for low-masses (left), charmonium mass region (center), and bottomonium mass region (right).

Figure 4.9 shows the centrality and p_{T} integrated dimuon v_n computed using the SP method with the $\mathbf{Q}_{\mathrm{n}}$ vector obtained in the SPD, in different mass regions. This data illustrate the mass dependance of the anisotropic flow coefficients, which exhibit a strong variation around the charmonium mass region. One can also notice than the profiles of like-sign and unlike-sign muon pairs deviate at low masses due to in principle of different triggers performances, while the deviation around 3.1 GeV/c^2 seems caused by the presence of correlations originated by the J/ψ decays.

4.3.1 Overview of dimuon v_n extraction, the case of J/ψ

The anisotropic flow coefficient v_n for a set of particles, with an azimuthal angle φ, can be estimated with the already introduced relation:

$$v_n = \langle \cos[n(\varphi - \Psi_n)] \rangle \,, \tag{4.3}$$

which is derived from the dN/dφ decomposition in Fourier series, solely by using the orthogonality properties of trigonometric functions. The observed v_n is corrected event-by-event with the reference flow R_n factor, which is obtained by the product of event flow vectors computed with different detectors (SPD, V0A, V0C). Then, the flow coefficients are extracted from sequential fits to the dimuon invariant mass distribution, $M_{\mu\mu}$, and the v_n profile as a function of $M_{\mu\mu}$, which include the superposition of a J/ψ signal and a background contribution, using the function

$$v_{\mathrm{n}}(M_{\mu\mu}) = \alpha(M_{\mu\mu})\, v_{\mathrm{n}}^{\mathrm{J}/\psi} + [1 - \alpha(M_{\mu\mu})]\, v_{\mathrm{n}}^{\mathrm{bkg}}(M_{\mu\mu}). \tag{4.4}$$

Each value of $v_n(M_{\mu\mu})$ represents the mean over all particles (all muon pairs), over all events, in one invariant mass bin. Here, $v_{\mathrm{n}}^{\mathrm{J}/\psi}$ denotes the J/ψ v_2 or v_3, and

$\alpha(M_{\mu\mu})$ is the signal fraction defined as $S/(S+B)$. The latter is extracted from fits to the dimuon invariant mass distribution as described previously. The $v_{\rm n}^{\rm bkg}(M_{\mu\mu})$ corresponds to the dimuon background v_2 or v_3. The signal of the $\psi(2S)$ is not included in the fit of the $v_{\rm n}$ coefficients due to its marginal significance. The v_n of the dimuon background is fitted using polynomial functions (where its order depends of the $p_{\rm T}$ range, usually third order is for low $p_{\rm T}$, second order is intermediate $p_{\rm T}$ and first order for high $p_{\rm T}$).

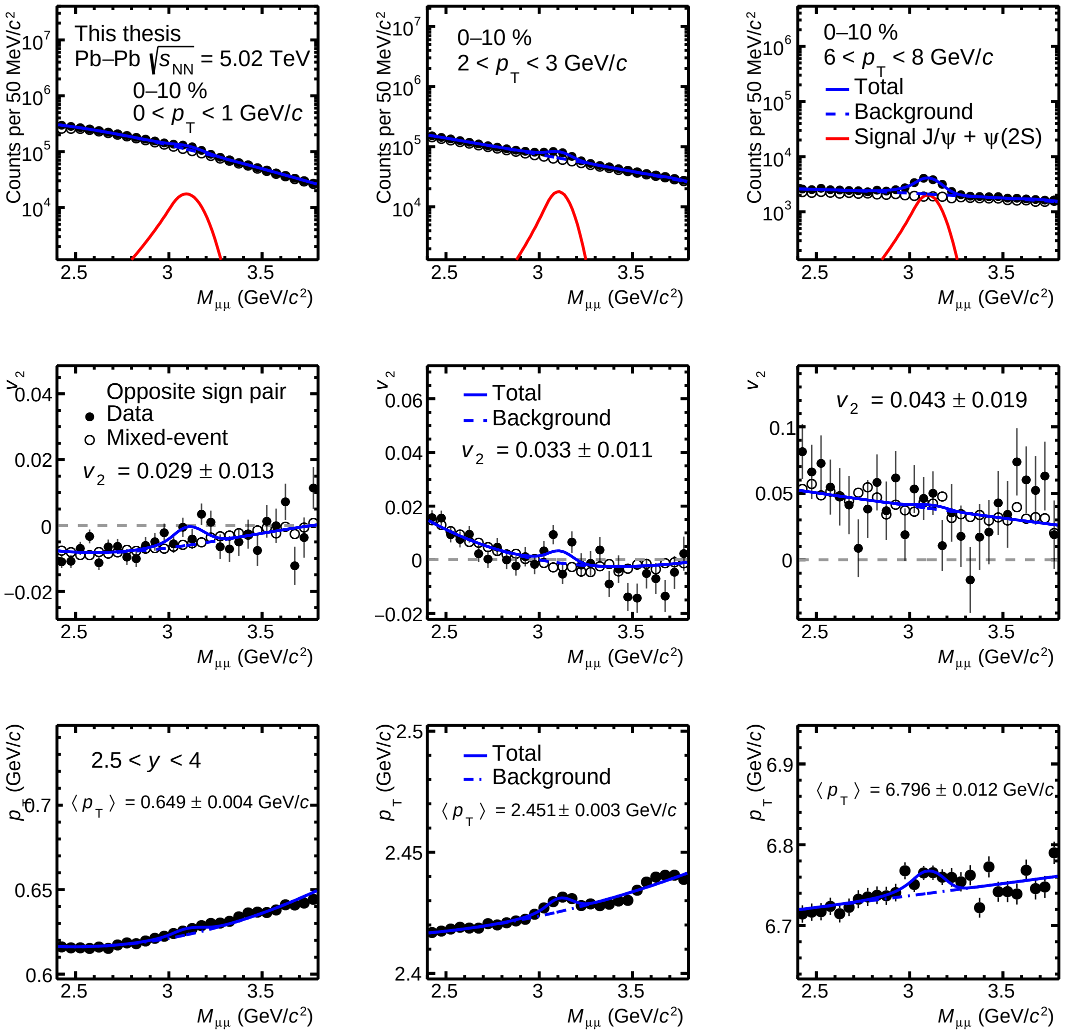

Figure 4.10: J/ψ v_2 extraction for different $p_{\rm T}$ range in 0–10%.

The $v_{\rm n}$ extraction method employed in this work is the same as the one described in detail in Ref. [92], where the $v_{\rm n}^{\rm bkg}(M_{\mu\mu})$ distribution is obtained using the event mixing technique. There, it was first demonstrated that the flow coefficients of the background can be obtained from the flow coefficients of the single muons used to form the background dimuons as

$$v_{\mathrm{n}}^{\mathrm{bkg}}(M_{\mu\mu}) = \frac{\langle v_{\mathrm{n}}^{(1)}\cos[\mathrm{n}(\varphi^{(1)}-\varphi)] + v_{\mathrm{n}}^{(2)}\cos[\mathrm{n}(\varphi^{(2)}-\varphi)]\rangle_{M_{\mu\mu}}}{\langle 1+2\sum\limits_{\mathrm{m}=1}^{\infty} v_{\mathrm{m}}^{(1)} v_{\mathrm{m}}^{(2)} \cos[\mathrm{m}(\varphi^{(1)}-\varphi^{(2)})]\rangle_{M_{\mu\mu}}}, \tag{4.5}$$

where $v_{\mathrm{n}}^{(1)}$ $(\varphi^{(1)})$ and $v_{\mathrm{n}}^{(2)}$ $(\varphi^{(2)})$ are the flow coefficients (azimuthal angles) of the two muons, respectively, and φ is the dimuon azimuthal angle. The brackets $\langle\cdots\rangle_{M_{\mu\mu}}$ denote an average over all dimuons belonging to the given $M_{\mu\mu}$ interval. Here, it is worth to note that the denominator in Eq. 4.5 represents the modification of the dimuon yields induced by the flow of single muons.

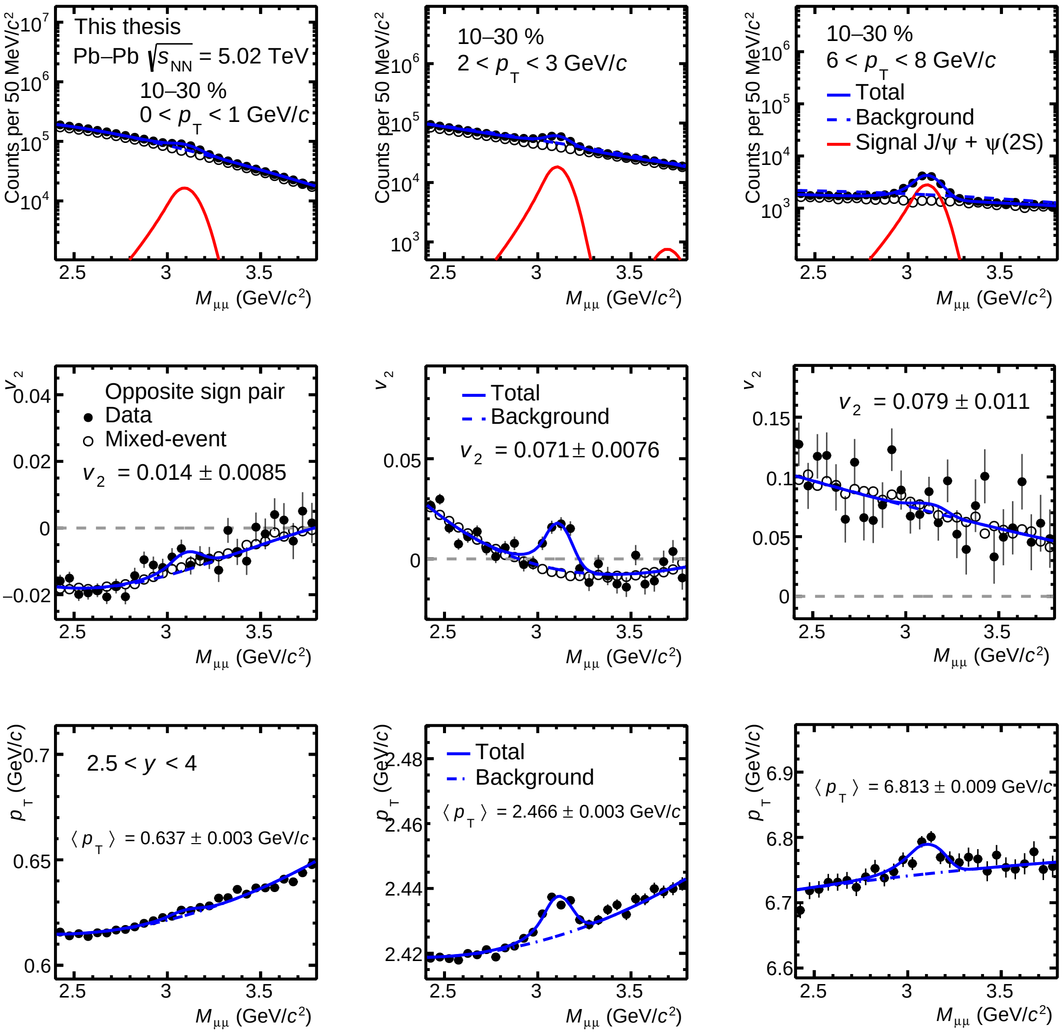

Figure 4.11: J/ψ v_2 extraction for different p_{T} range in 10–30%.

Then, when background dimuons are built using the event mixing technique, the numerator in Eq. 4.5 is given by

$$\left\langle \frac{\langle \mathbf{u_n}^{(1)}\mathbf{Q_n}^{(1),\mathrm{A}*}\rangle}{R_{\mathrm{n}}^{(1)}} \cos[\mathrm{n}(\varphi^{(1)}-\varphi)] + \frac{\langle \mathbf{u_n}^{(2)}\mathbf{Q_n}^{(2),\mathrm{A}*}\rangle}{R_{\mathrm{n}}^{(2)}} \cos[\mathrm{n}(\varphi^{(2)}-\varphi)] \right\rangle_{M_{\mu\mu}}. \tag{4.6}$$

Here, $\mathbf{u}_n^{(1)}$ and $\mathbf{u}_n^{(2)}$ are the unit vector of the two muons, $\mathbf{Q}_n^{(1),A}$ and $\mathbf{Q}_n^{(2),A}$ are the event flow vectors, reconstructed in detector A (the SPD), of the events containing the two muons, and $R_n^{(1)}$ and $R_n^{(2)}$ their respective event flow factors (corresponding to the denominator of Eq. 3.9). Since the event flow vectors of the mixed events are not correlated, the mixed-event dimuon yield is not modified by the flow of the single muons.

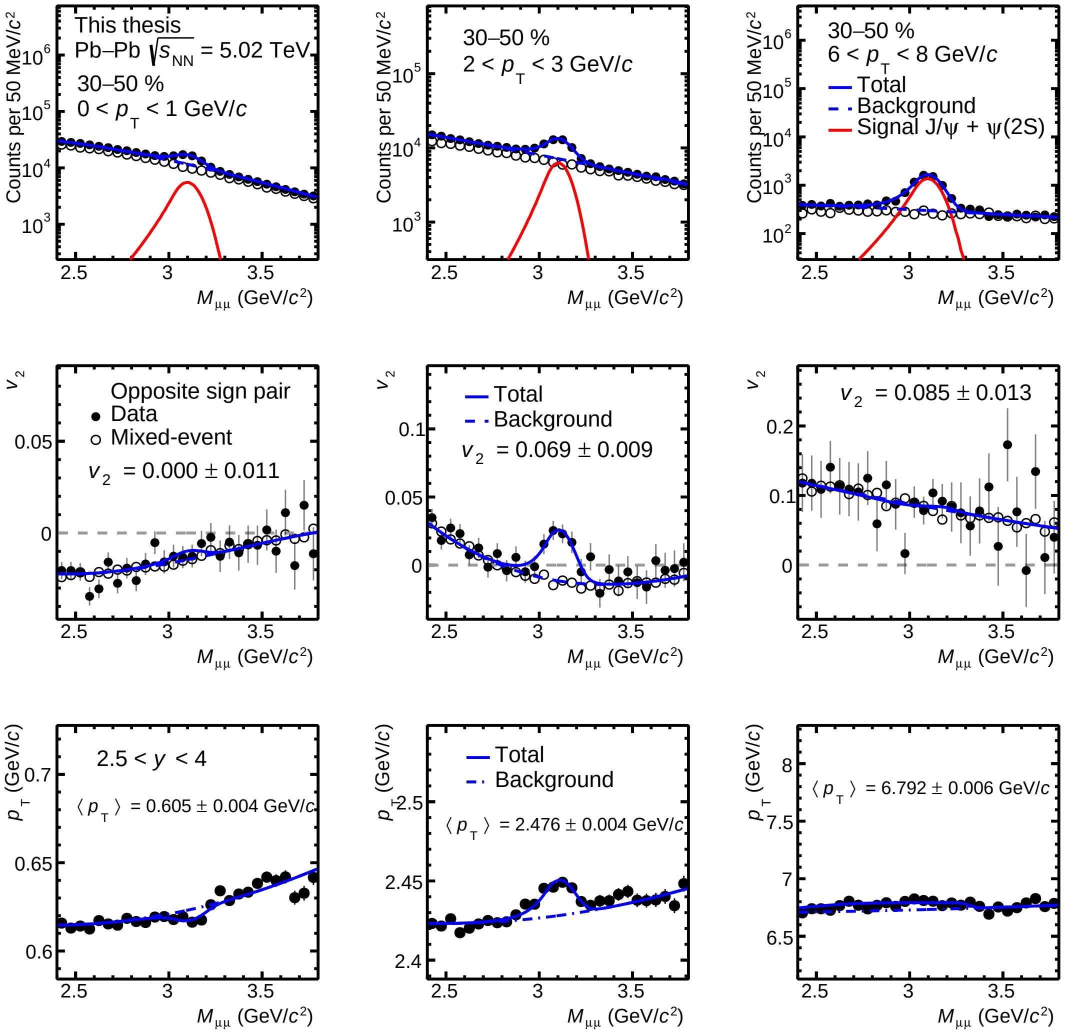

Figure 4.12: J/ψ v_2 extraction for different p_{T} range in 30–50%.

In the absence of correlated background (muons from correlated heavy flavor pairs) mostly the case in central collisions and at low-p_{T}, the background flow (v_n^{bkg}) is directly given by the mixed-event flow. However, at high-p_{T}, the hypothesis of $v_n^{\mathrm{corr}} \propto v_n^{\mathrm{mix}}$ is applied, in order to take into account this correlated dimuon background flow, hence the coefficients can be rewritten as

$$v_n(M_{\mu\mu}) = v_n^{J/\psi}\alpha(M_{\mu\mu}) + v_n^{\mathrm{mix}}(M_{\mu\mu})\frac{N_{+-}^{\mathrm{mix}}}{N_{+-}^{\mathrm{same}}} + v_n^{\mathrm{corr}}(M_{\mu\mu})\frac{N_{+-}^{\mathrm{corr}}}{N_{+-}^{\mathrm{same}}}, \tag{4.7}$$

where N_{mix} is the number of dimuons from mixed-events, N_{same} is the number of dimuons from the same-event, and N_{corr} is the unknown number of correlated muon pairs. The effect of the unknown flow contribution of the correlated background and residual mismatches between the same-event and mixed-event background flow, is considered as a systematic uncertainty (and is presented in the dedicated section later). In the default approach, the flow of the correlated background is assumed to be negligible, and thus the denominator of Eq. 4.5 is given by the ratio $N_{+-}^{\mathrm{bkg}}/N_{+-}^{\mathrm{mix}}$ between the number of background unlike-sign dimuons N_{+-}^{bkg} and the number of unlike-sign dimuons from mixed events N_{+-}^{mix}, which is obtained after a proper normalization involving like-sign dimuons as described in Ref. [92].

Examples of comparisons between normalized mixed-event spectra and raw same-event spectra for different p_{T} ranges in 0–10%, 10–30%, and 30–50% are shown in Fig. 4.10, Fig. 4.11, and Fig. 4.12, respectively. The dimuon invariant mass distributions correspond to the top panels, the corresponding dimuon v_2 profiles are located in the middle panels, and the $\langle p_{\mathrm{T}} \rangle$ extraction is shown in the bottom panels.

As mentioned previously, the dimuon mix- and same-event v_2 is computed for opposite sign muon pairs from the scalar product method using the SPD as reference detector ($\Delta\eta = 1.1$). The middle panels illustrated the J/ψ v_2 extraction using the fit of the dimuon v_2 profile, and by using the S/(S+B) ratio. The bottom panels show the fits of p_{T} versus $M_{\mu\mu}$, which give access to the raw $\langle p_T \rangle$ values in the corresponding centrality and p_{T} interval. Similar sequential fitting procedure than Eq. 4.4 is used in the extraction of $\langle p_T \rangle$ for the J/ψ signal, where the background used is a polynomial function. For each panel, the total (blue curves) and background (blue dotted curves) fit functions are plotted.

Taking now the third harmonic of the event flow vector ($\mathbf{Q_3}$ obtained in the SPD), and by dividing event-by-event the observed v_3 with the reference flow R_3 computed previously, one can access to the v_3 coefficient. The triangular flow takes its origin mainly from fluctuations of the initial energy density profile. Figure 4.13 shows the J/ψ v_3 extraction for different p_{T} ranges in 0–50%. The profile of dimuon v_3 versus invariant mass exhibits a similar shape that those of v_2, but with intrinsic lower values. For the first time, a significant J/ψ v_3 signal is observed in $2 < p_{\mathrm{T}} < 5$ GeV/c, for 0–50%, with a total significance of 5.1σ, as illustrated in the center panels in Fig. 4.13.

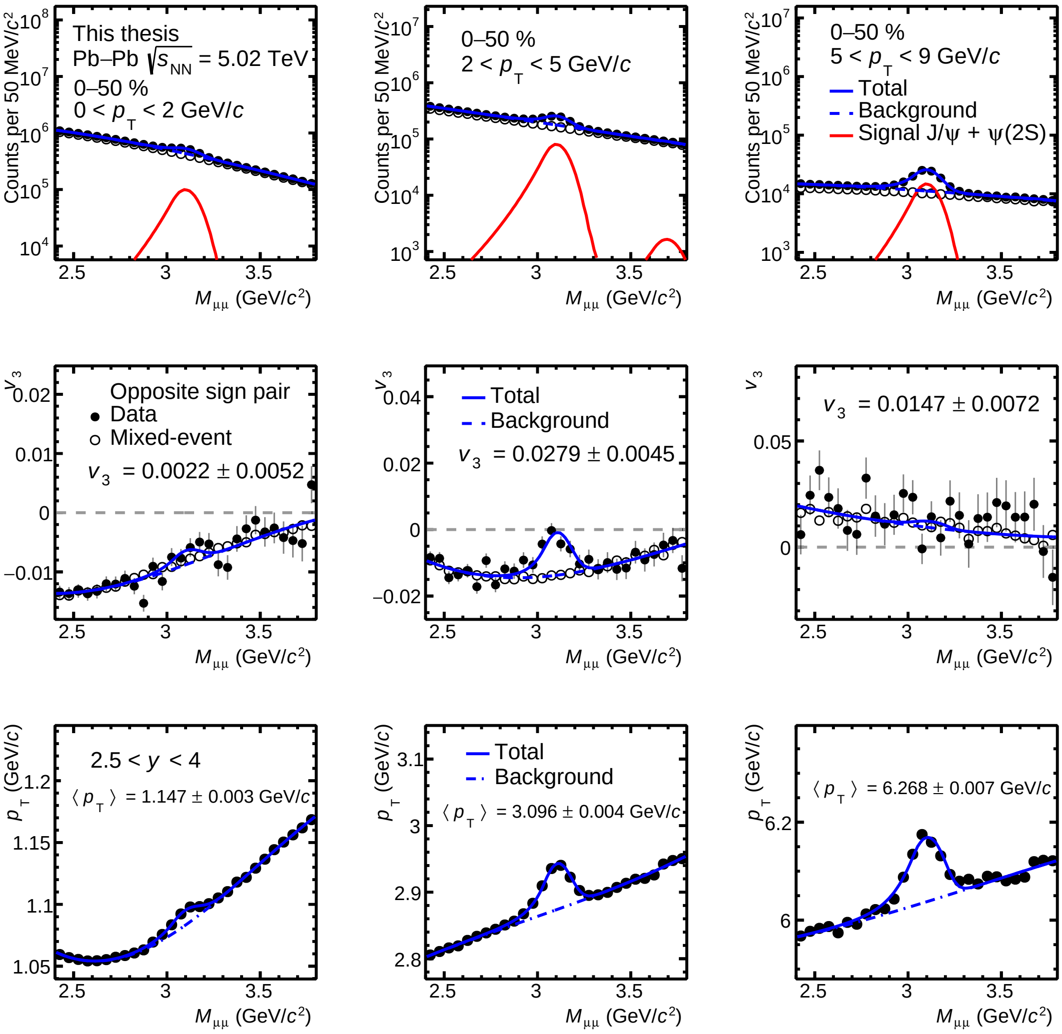

Figure 4.13: J/ψ v_3 extraction for different p_T range in 0–50%.

4.3.2 Υ(1S) v_2 extraction

The extraction of the Υ(1S) v_2 is performed similarly than for the J/ψ v_n, previously presented. A sequential fit on dimuon invariant mass and on dimuon v_2 profile versus $M_{\mu\mu}$, allows us to extract the Υ(1S) v_2 coefficient. In this bottomonium mass range, the background of the dimuon invariant mass is also fitted using a Variable-Width Gaussian (where width is linear with the mass), and gives satisfying results. The 1S, 2S, 3S signal peaks are fitted using the common Extended Crystall Ball functions.

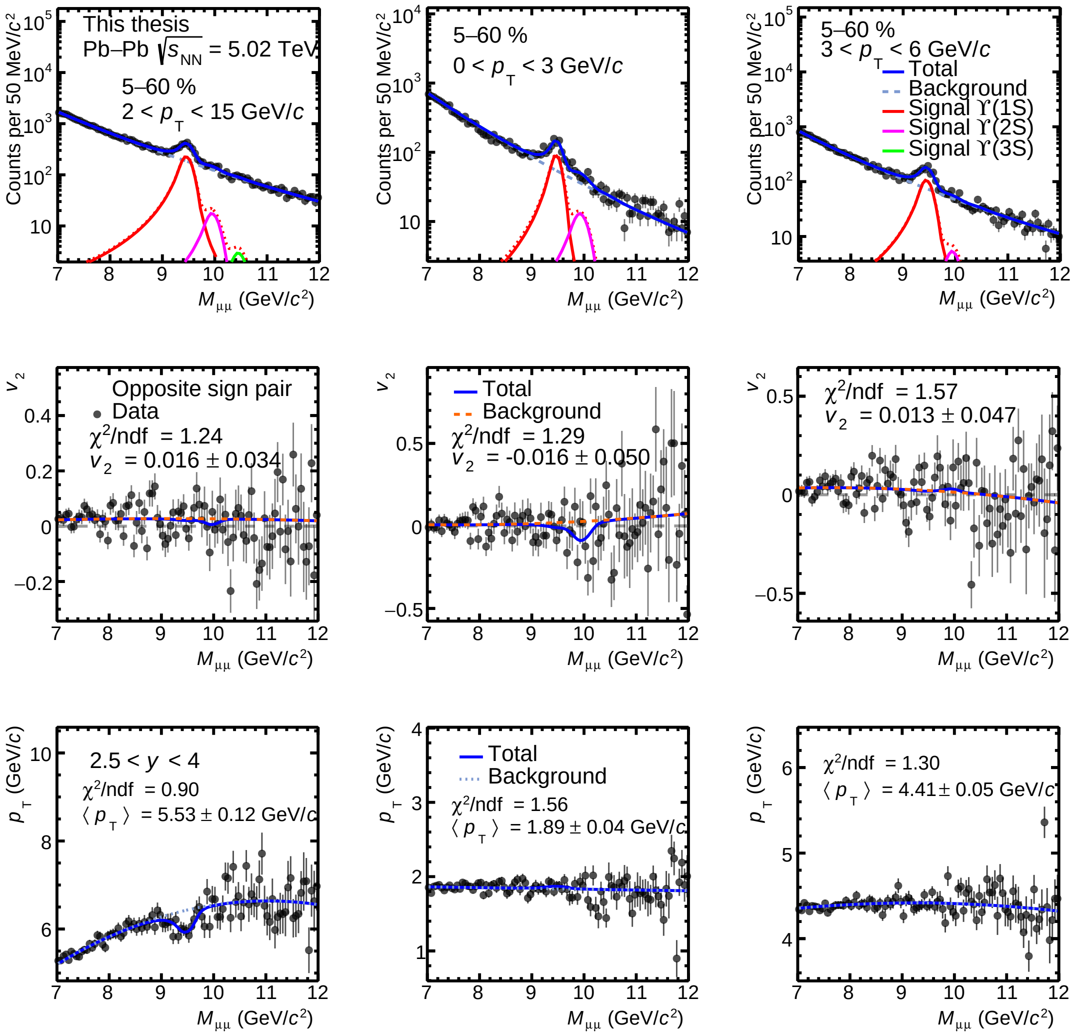

Figure 4.14: Υ(1S) v_2 extraction for different p_T range in 5–60%.

The event-mixing technique developed in Ref. [92] in order to fix v_2^{bkg} is not applied here due to the presence of significant correlated background. Nevertheless, based on the results from the application of this technique a second-order polynomial function is chosen as default $v_2^{\mathrm{bkg}}(M_{\mu\mu})$ parametrization. For consistency, and despite its low yield, the Υ(2S) is included in the fit by restricting the value of its v_2 coefficient within the range between -0.5 and 0.5. In practice, this inclusion has a negligible impact on the Υ(1S) fit results. The Υ(3S) signal is not included in the v_2 fit due to its marginal significance. The tail parameters of the signal functions are fixed from values obtained in Monte Carlo studies (described in the next section).

Figure 4.14 shows the Υ(1S) v_2 extraction in different p_{T} ranges. The choice of centrality or p_{T} interval is crucial in order to maximise the signal significance from one side, and from another side to remove region where v_2 values and R_2 factor are low, especially in very central and peripheral Pb–Pb collisions. Therefore, the 0–5% and 60–90% centrality intervals will be excluded in the v_2 extraction. For the centrality dependent measurement, the very low-p_{T} range ($0 < p_{\mathrm{T}} < 2$ GeV/c) is removed since the v_2 is expected to be very low. The values of $v_2^{\Upsilon(1\mathrm{S})}$ are found to be compatible with 0 in all studied cases, albeit with large uncertainties. Further systematic studies will be carried out in the next section, including the different choices of fitting functions for both raw yield and v_2 extraction.

4.4 Systematic and Monte Carlo studies

Monte Carlo (MC) simulations are an important ingredient for the measurement of quarkonium production, to study the selection variables, and to compute the detector acceptance and reconstruction efficiency corrections. In this section, first, the reconstruction efficiency of J/ψ and Υ(1S) using an embedded MC data sample of Pb–Pb collisions is presented. Secondly, the different sources of systematic uncertainties assigned to the $v_{\rm n}$ measurements are investigated. Indeed, several effects could induce systematic biases on the final results, and each of them need to be evaluated.

4.4.1 MC input signal shape

Simulations are used to reproduce the detector performances, which are based on a detailed description of the ALICE apparatus geometry and its detectors responses. In particular, for the different collision systems the generated particles were propagated through the detectors using the `GEANT3` transport package (the `GEANT4` package was found also to produce compatible results). MC simulations are used in this analysis to reproduce precisely the J/ψ or Υ(1S) decay to $\mu^+\mu^-$ and its measurement in the detector in terms of decay kinematics and topology (the excited states decays were also added). In the dimuon analysis, the acceptance and efficiency factors were computed using the embedding technique, where MC J/ψ or Υ(1S) particles are injected (using standard parametrizations) into the raw data of real minimum bias Pb–Pb events, and finally reconstructed. This method allows to account the variation of the reconstruction efficiency with the detector occupancy and, thus, the collision centrality.

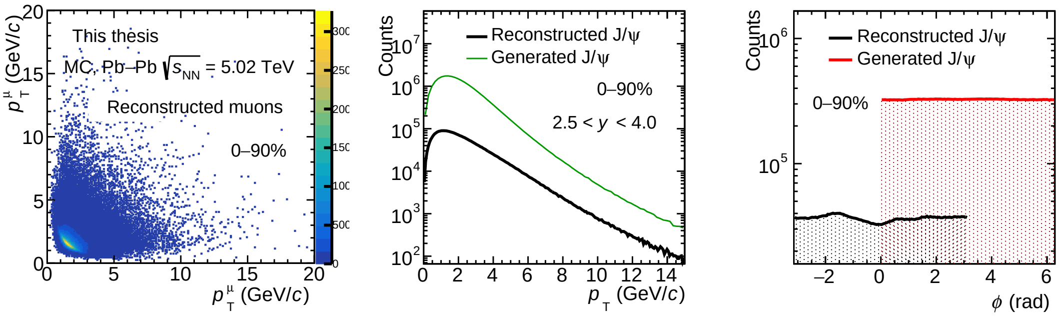

Figure 4.15: Left: 2D histogram of single muons $p_{\rm T}$ reconstructed from MC. Center: $p_{\rm T}$ spectra of generated and reconstructed J/ψ. Right: generated and reconstructed J/ψ azimuthal angle.

The same analysis cuts and selection on events (previously defined on real events) are also applied on these simulated events. General kinematic details concerning the generated and reconstructed J/ψ and its daughter muons are shown in Fig. 4.15. In particular, the two-dimensions histogram representing the single $p_{\rm T}$ for positive and negative muons is shown on the left panel, while a comparison between generated

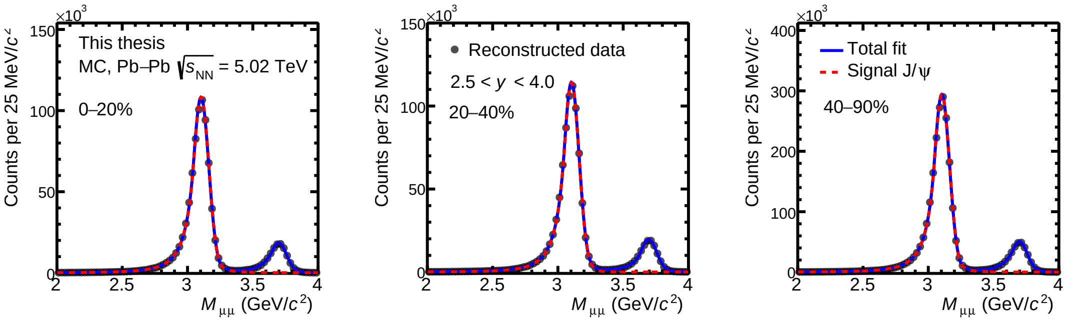

Figure 4.16: Signal of J/ψ reconstructed in the dimuon decay channel for different centrality intervals.

and reconstructed J/ψ $p_{\rm T}$ and azimuthal angle ϕ are plotted in the middle and right panel, respectively. The main effect inducing a φ dependence of acceptance and efficiency is the magnetic field bending tracks in y but not in x. Then, additional effects due to dead areas differences lead to significant variations in the reconstructed J/ψ azimuthal angle distribution with respect to the flat generated one, as illustrated in Fig. 4.15 (right panel). Since the generated J/ψ and Υ(1S) have a flat azimuthal distribution, no azimuthal anisotropy ($v_2 = 0$) will be expected from the decay system (and also no polarisation). However a bias originated from the detector can occurs during the reconstruction, and it will be estimated in a dedicated part as a systematic uncertainty.

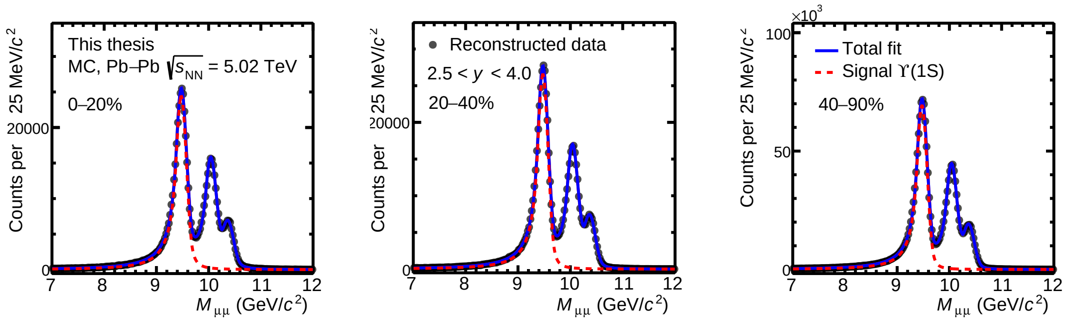

Figure 4.17: Signal of Υ(1S) reconstructed in the dimuon decay channel for different centrality ranges.

Keeping only the injected MC quarkonium decays, the tail parameters of the common Crystall Ball signal functions can be fixed from the fit results obtained using these simulated events. Here, the Fig. 4.16 and Fig. 4.17 show the reconstructed data and the signal fit (red dotted curves) in different centrality intervals for J/ψ and Υ(1S), respectively. The CB tail parameters were left free in the fit of the invariant mass of reconstructed J/ψ and Υ(1S), and their values do not deviate beyond 10% from central to peripheral collisions (see Appendix A for the values).

4.4.2 Acceptance and efficiency

The true number of extracted quarkonium in a specific p_{T}, centrality, or rapidity range is obtained after correcting the measured raw yield extracted by the detector acceptance and reconstruction efficiency factor $(A \times \varepsilon)$. The latter is defined as the ratio of reconstructed J/ψ or Υ(1S), over the number of generated one (which means at the beginning of the simulation) as

$$A \times \varepsilon = \frac{N_{\mathrm{rec}}(p_{\mathrm{T}}, y)}{N_{\mathrm{gen}}(p_{\mathrm{T}}, y)}. \tag{4.8}$$

The acceptance and efficiency factor allows to correct the raw measured values by the true detector response and performances (such as the status of electronics during the data taking or high voltage applied to the chambers). Several uncertainties can bias the result of this factor, in particular the choice of the parametrization function in the generation of J/ψ or Υ(1S), the muon trigger, tracking, and the matching between the two systems, which have in each case specific efficiency (these systematic biases on acceptance and efficiency were estimated to not produce deviations beyond 2% as a function of p_{T} or y).

In our case, the corrections for acceptance and efficiency will be only needed when v_{n} measurements are performed in a integrated way, corresponding to a large p_{T}, y or centrality intervals. In these cases, this procedure will be realised by associating a weight for each dimuon corresponding to the value of $\frac{1}{A\times\epsilon(p_{\mathrm{T}},y)}$, when the dimuon v_n profile is filled. The negative impact of this procedure is its slight increase in the final statistical uncertainty. Moreover, the correction of $A \times \varepsilon$ have significant impact on p_{T} distributions, then the extraction of uncorrected mean p_{T} ($\langle p_{\mathrm{T}}\rangle^{\mathrm{uncorr}}$) will produce reduced values. As a consequence of this correction, the $v_n(p_{\mathrm{T}})$ measurements will be solely shifted according to the value of $v_n(\langle p_{\mathrm{T}}\rangle^{\mathrm{uncorr}})$, to the value of $v_n(\langle p_{\mathrm{T}}\rangle)$. This correction leads simply to two different quantities, one measured at $\langle p_{\mathrm{T}}\rangle^{\mathrm{uncorr}}$ and the second one measured at $\langle p_{\mathrm{T}}\rangle$.

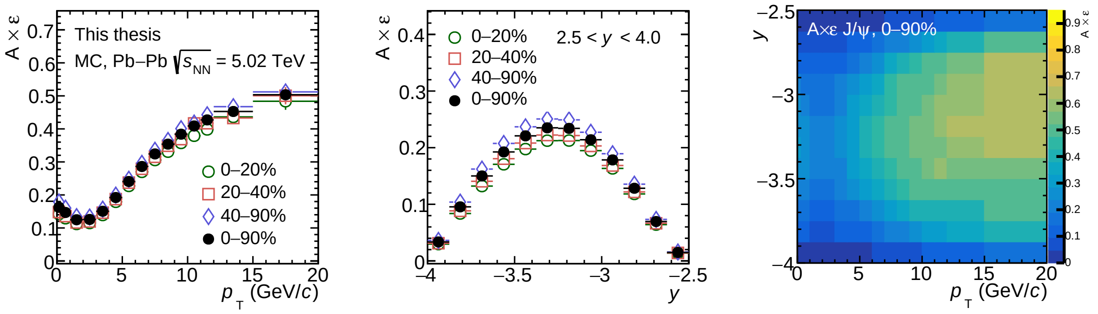

Figure 4.18: Acceptance times efficiency of J/ψ reconstructed in the dimuon decay channel, for different centrality intervals.

These simulations are performed on a run-by-run basis. A weight proportional to the number of `CMUL7` events is applied in order to take into account for the difference between the number of minimum bias and dimuon events. The p_T- and y-differential $A \times \varepsilon$ factor is computed for J/ψ and Υ(1S) in Fig. 4.18 and Fig. 4.19, respectively.

The p_T-differential J/ψ acceptance and efficiency (left panel in Fig. 4.18) reaches its lower values at around 0.1 for $p_T \sim$ 2–3 GeV/c, while it increases toward high p_T, at 0.5 for $p_T \sim$ 15 GeV/c. The variations seen as a function of rapidity show that the $A \times \varepsilon$ is maximal for the interval $-3.5 < y < -3$, while it decreases on the edges of the muon spectrometer. Please notice that here, the negative rapidity sign is arbitrary, since there are no preferred forward/backward direction due to the symmetric Pb–Pb collisions. Unsurprisingly, the 2D-map of acceptance times efficiency (right panel) shows that the maximal value is located at high-p_T and for the central rapidity region of the muon spectrometer. Contrary to the J/ψ, the $A \times \varepsilon$ of reconstructed Υ(1S) has a weakly p_T-dependence and globally larger values, in particular for the low-p_T region.

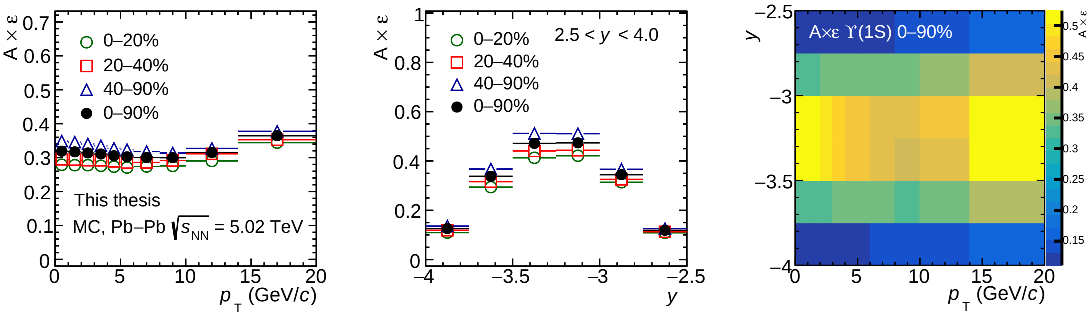

Figure 4.19: Acceptance times efficiency of Υ(1S) reconstructed in the dimuon decay channel, for different centrality intervals.

The centrality dependence of acceptance and efficiency for J/ψ and Υ(1S) is shown in Fig. 4.20 (left panel), while their dependence as a function of the run number is plotted in Fig. 4.20, in the center and right panel, respectively. The $A \times \varepsilon$ factor is found to be minimal for central collisions, while it increase toward peripheral Pb–Pb collisions (where detector occupancy decrease). One can see that the values of acceptance and efficiency, as well as its statistical uncertainty, varies run-by-run, simply because the status of the detector changes (due to high or low voltage applied to muon chambers and readout problems) from a run to another. As mentioned previously, the value of $A \times \varepsilon$ for J/ψ is found to be lower than those of Υ(1S), by approximately a factor 2.

Since its values fluctuates run-by-run, the final acceptance and efficiencies need to be weighted by the $A \times \varepsilon_i$ factor run per run (where i is the run number). Given that the centrality distribution of quarkonia is peaked towards central collisions (while it is flat in these simulations), because $c\bar{c}$ production follows the N_{coll} scaling, additional weight corresponding to this factor is also applied. The final weighted $A \times \varepsilon$ is then found lower than the previous one. Figure 4.21 shows these corrected values in open-square (J/ψ) and open-circle markers (Υ(1S)). These values and the p_T, y and centrality dependence are found to be compatible with other analyses related to quarkonium production. However, the acceptance and efficiency corrections

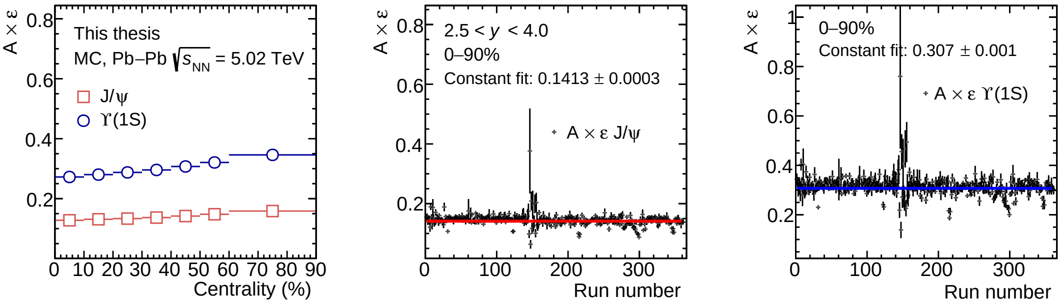

Figure 4.20: Acceptance times efficiency (uncorrected) of J/ψ and Υ(1S) as a function of centrality (left) and run index (center and right panels).

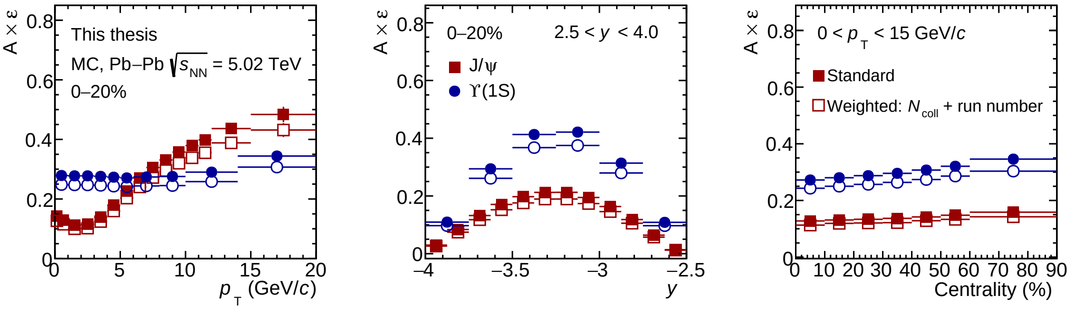

Figure 4.21: Final acceptance times efficiency of J/ψ and Υ(1S) as a function of p_{T} (left), rapidity (center) and centrality (right), without (full markers) and with (open markers) weighting procedure.

are needed for integrated measurements (e.g. cross-sections or R_{AA}) in large p_{T}, y or centrality intervals. Since, this thesis is measuring azimuthal anisotropy (which means a number of quarkonium reconstructed azimuthally), many corrections usually performed in standard analyses are not needed here in the final p_{T}-differential v_{n}.

4.4.3 Overview of systematic uncertainties

This section below describes the different sources of systematic uncertainties related to the final v_{n} coefficients, mainly for J/ψ and to a lesser extent for the Υ(1S).

Raw yield and v_{n} extraction

The systematic uncertainty originating from the signal extraction was studied by varying the signal and background function of the invariant mass distribution, the background flow function, the mass range, and the set of tail parameters used in the signal functions. The swapping between these different fit choices: signal functions $\otimes$ background functions $\otimes$ background flow functions $\otimes$ set of tail parameters $\otimes$ mass fit ranges, corresponds to a total of 48 different fits for the J/ψ v_n extraction (similar method is also applied for $\Upsilon(1\mathrm{S})$). For the J/ψ extraction, the dimuon background v_n is fixed using the mixed-event profile, and therefore reduces the statistical and the associated v_n uncertainty.

Figure 4.22 shows the results of these fits on J/ψ v_2 for 20–40% and $1 < p_\mathrm{T} < 2$ GeV/c, the left panel gives the variations as a function of the test, the center panel presents the corresponding distribution, in the right panel the distribution of number of raw J/ψ is plotted. Similarly the Fig. 4.23 and Fig. 4.24 show the results obtained for $\Upsilon(1\mathrm{S})$ v_2 and for the J/ψ v_3 (in different p_T ranges and centrality centrality intervals), respectively. The final v_n values and their statistical uncertainties were obtained as the average of the results of all the tests that are successful.

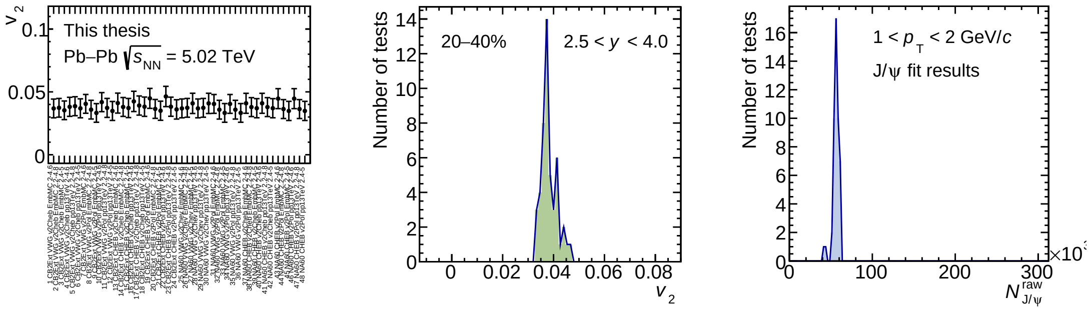

Figure 4.22: J/ψ v_2 systematic uncertainty from signal extraction in 20-40 % and $1 < p_\mathrm{T} < 2$ GeV/c, using the SP method (where v_2^{bgk} is fixed from mixed-event)

The signal function in the dimuon invariant mass spectra used to fit the different charmonium states : J/ψ, $\psi(2\mathrm{S})$ and the bottomonium states: Υ(1S,2S,3S), corresponds to the standard extended Crystall Ball (CB2) function (where fit parameters of excited states are scaled from the fundamental state 1S : mass $m_{1\mathrm{S}}$, width $\sigma_{1\mathrm{S}}$, to take into account the mass difference between 1S, 2S, ...). The standard NA60 function was also used to describe the signal in order to fit the J/ψ and $\psi(2\mathrm{S})$ peaks (its definition can be found in Appendix A).

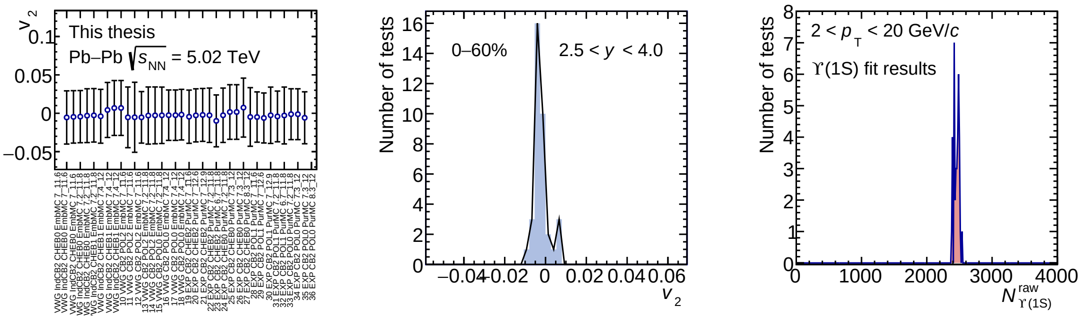

Figure 4.23: $\Upsilon(1\mathrm{S})$ v_2 systematic uncertainty from signal extraction in 0-60 % and $2 < p_\mathrm{T} < 20$ GeV/c, using the SP method

The invariant mass background shape is fitted with a Variable Width Gaussian (VWG) where the width is linear with $M_{\mu\mu}$. A fourth order Chebyshev polynomial, or a Double Decreasing Exponential (only for bottomonium mass region) were also used in the background fit of the invariant mass distribution.

The tail parameters included in the signal functions are fixed. In the CB2 functions, this set corresponds to 4 parameters (α, n, α', n'), which depend on p_{T}, y and centrality intervals. The tail parameters are extracted from the Embedding Monte Carlo reconstructed data, as illustrated in Fig. 4.16 and Fig. 4.17 where the fit on the signal are performed in three different centrality intervals (the obtained values are presented in Appendix A). Another set of tail parameters is taken from a p–p collision analysis at 13 TeV (where a peak with high S/B could be fitted). For the NA60 functions, the standard set of 9 tail parameters $(\alpha^l, p_1^l, p_2^l, p_3^l, \alpha^r, p_1^r, p_2^r, p_3^r))$ was also extracted from the Embedding Monte Carlo. The mass fit range was varied inside the window 2–5 GeV/c^2 for the J/ψ, corresponding to the ranges 2–4.6, 2.2–4.8 and 2.4–5 GeV/c^2. For the Υ(1S) states, these ranges correspond to 7–11.6, 7.2–11.8, 7.4–12 GeV/c^2.

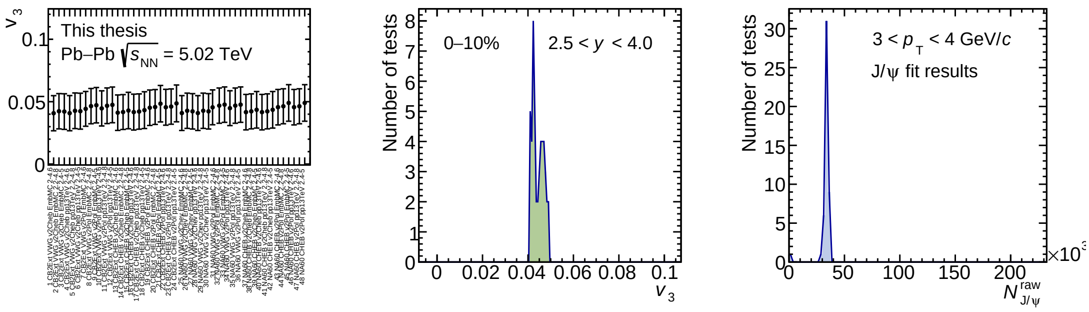

Figure 4.24: J/ψ v_3 systematic uncertainty from signal extraction in 0-10 % and $3 < p_{\mathrm{T}} < 4$ GeV/c, using the SP method

The binning of mass range is taken as 50 MeV/c^2. Without using the event mixing, or in case the mixed-event are fitted, the background flow function is chosen to be a standard polynomial function or a Chebyshev polynomial. For the J/ψ, the third order were used only for $p_{\mathrm{T}} < 5$ GeV/c. Then, the fit function is adjusted to second order at intermediate p_{T}, and finally for $p_{\mathrm{T}} > 9$ GeV/c the first order is sufficient since dimuon flow background seems linear. For the Υ(1S), as illustrated in Fig. 4.9 in the right panel, despite low dimuon candidates the background flow is almost flat, then a second order polynomial or Chebyshev functions is already sufficient, first or zero order can be used in specific cases, in particular for improving the χ^2/ndf).

As mentioned, using the event mixing the dimuon background flow is fixed using mixed event (fitted on v_n^{mix} and then fixed), which reproduces perfectly well the background flow in central collisions and at low-p_{T}. However, in non-central collisions and at high-p_{T} the emergence of correlated dimuon background need to be taken into account, and will lead to additional systematic uncertainty due to the choice of the scaling applied on v_n^{mix} (and will be discussed later).

One can mention a promising alternative extraction method for the quarkonium $v_{\rm n}$, which use the ${}_s\mathcal{P}$lot formalism [128]. This technique is based on an event-by-event extraction, and no-longer using sequential fit on both invariant mass and $v_{\rm n}$. An example of this method applied on J/ψ and Υ(1S) v_2 measurement is described in Appendix B.

The systematic uncertainty originating from the raw yield and v_2 extraction for Υ(1S) in 5–60% centrality, is found at 0.0161 in the $p_{\rm T}$ range 0–3 GeV/c, 0.0075 in the range 3–6 GeV/c, and 0.0060 in the range 6–15 GeV/c.

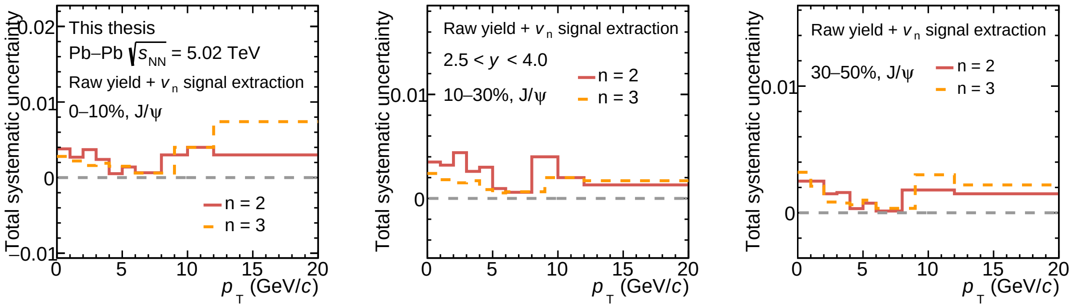

Figure 4.25: Total systematic uncertainty associated to the raw yield and $v_{\rm n}$ signal extraction on J/ψ v_2 and v_3, as a function of $p_{\rm T}$ for different centrality intervals

The final systematic uncertainties estimated coming from the signal extraction (invariant mass and dimuon $v_{\rm n}$ fit) for J/ψ v_2 and v_3 are shown in Fig. 4.25 for different centrality intervals as a function of $p_{\rm T}$. One can notice that these systematic uncertainties are higher for low $p_{\rm T}$, where the S/B is low, then have minimal values for intermediate $p_{\rm T}$, and finally increase for the high-$p_{\rm T}$ bins, where the $v_{\rm n}$ is not clearly visible from the $v_n^{\rm bkg}$ (despite S/B is high), and because the number of dimuon events is low. This systematic uncertainty will be considered to be part of the final and total systematic uncertainties.

Detector effects

The dimuon trigger and reconstruction depend on the muon chamber occupancy, and coupled to the flow of particles, could lead to a bias in the measured $v_{\rm n}$. This bias is originated from the detector occupancy, which can be azimuthally asymmetric, due to the flow of particles reaching the detector. The corresponding systematic uncertainty is obtained by injecting simulated quarkonium decays into real Pb–Pb events (the Embedding Monte Carlo). The $v_{\rm n}$ as a function of $p_{\rm T}$ is calculated using the usual SP method, by using the azimuthal angle of reconstructed quarkonium state (dimuon angle) and the event flow vector components (where the $\mathbf{Q}_n$ is taken from the real event itself), corrected by the R_n factor.

Although the generated J/ψ or Υ(1S) have a flat azimuthal distribution, one can study the reconstructed $v_{\rm n}$ as a function of $p_{\rm T}$ in order to estimate a residual bias originating from the detector. Figure 4.26 and Fig. 4.27 show the reconstructed J/ψ and Υ(1S) v_2, which are fitted using a constant function (since no particular

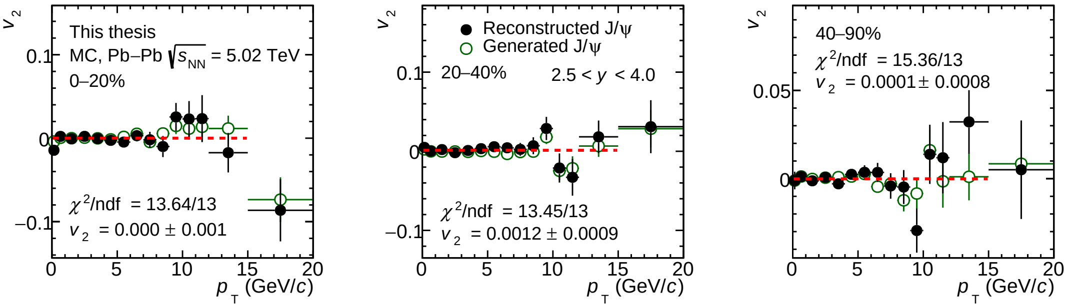

Figure 4.26: Effect of reconstruction efficiency on J/ψ v_2 as a function of p_T for different centrality intervals

p_T dependence was found), up to 15 GeV/c. Both generated and reconstructed v_2 (p_T) are measured to be very close to zero, in all centrality or rapidity intervals. Figure 4.28 shows the reconstructed J/ψ v_3 with a constant fit, which is measured also close to zero.

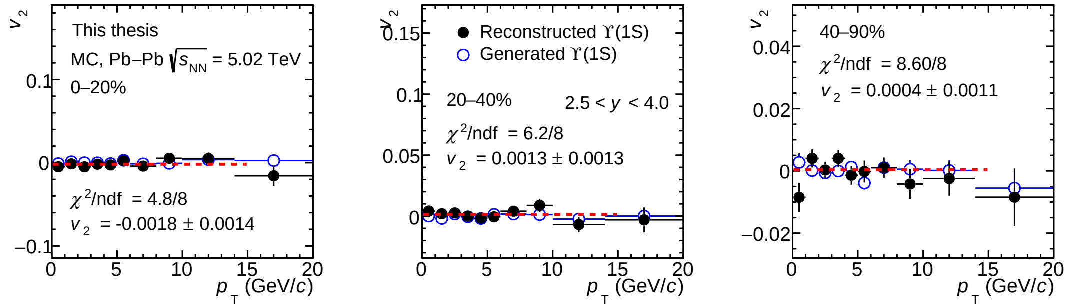

Figure 4.27: Effect of reconstruction efficiency on Υ(1S) v_2 as a function of p_T for different centrality intervals

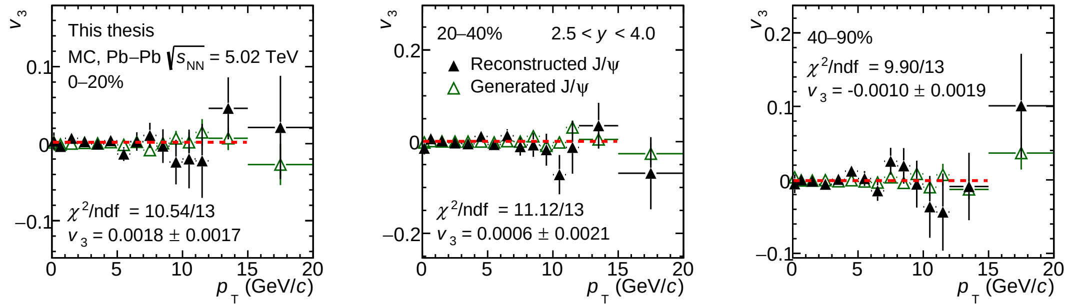

Figure 4.28: Effect of reconstruction efficiency on J/ψ v_3 as a function of p_T for different centrality intervals

When the fit result deviate more than 1σ, it is assigned as a systematic uncertainty, otherwise the statistical deviation will be chosen. Values are found to be maximal in central collisions (up to 0.0023 for J/ψ in 0–10%), and slightly decrease toward peripheral ones. The uncertainty is assumed to be the same in all considered $p_{\rm T}$ bins. For Υ(1S), the systematic uncertainty coming from this occupancy bias is estimated to be 0.0015 in the large centrality interval 5–60%. This systematic uncertainty will be part of the final total systematic uncertainty.

Centrality and R_n determination

The centrality determination is performed using the `V0M` estimator, and this choice could have a bias on v_n measurement, since the R_n factor is computed as a function of the centrality of the event. This possible bias on the v_n is estimated to be negligible in central collisions, but it can still be assumed to not deviate beyond 1%. Nevertheless, moving to non-central and peripheral collisions, this bias on the centrality determination is estimated to be around 2-3%. Basically, these values are obtained simply by selecting different estimators (here, named `V0plus05` and `V0minus05`), and taking the difference between their distributions. The centrality distributions obtained using the `V0` estimator of minimum bias and unlike-sign dimuon (`CMUL`) triggered events are shown in the left panel of Fig. 4.29.

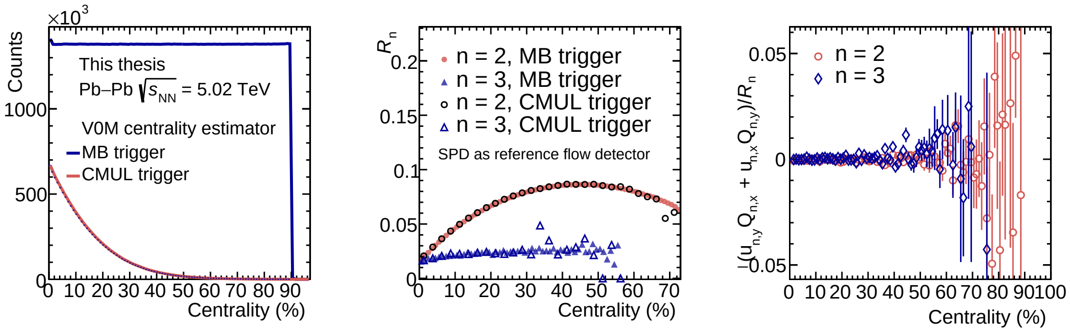

Figure 4.29: Left: Centrality distribution for `MB` and `CMUL` (unlike sign dimuon) events. Center: Centrality dependence of R_n factors for `MB` and `CMUL` events. Right: Centrality dependence of the cross-term products between $u_{n,x}$ and $Q_{n,y}$, using SPD as reference flow detector.

The computed R_n distributions for $n = 2, 3$ using either `MB` events or dimuon events, are shown in the center panel of Fig. 4.29. The deviation seems visible after 50–60% for $n = 2$, while it becomes significant around 30–40% for $n = 3$. This effect could possibly have a bias on v_n measurement, since the event flow vector $\mathbf{Q}_n$ is calibrated using `MB` events, while the signal extraction is realised with dimuon events. The relative ratio (between `MB` and `CMUL` distributions) corresponds to a bias that do not exceed 1% for R_2 and 2-3% for R_3. Alternatively searching for centrality dependence of non-flow effects, one can see in Fig. 4.29 (right panel) that no large deviations are visible up to 50–60% in the cross-term products between $u_{n,x}$ and $Q_{n,y}$.

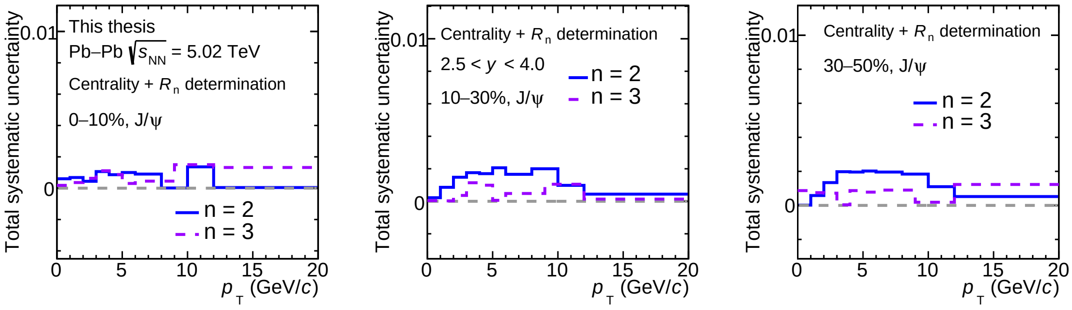

Figure 4.30: Total systematic uncertainty associated to centrality and R_n determination on J/ψ v_2 and v_3, as a function of p_T for different centrality intervals

The final systematic uncertainties originated from the centrality and R_n determination are shown in absolute values as a function of p_T in Fig. 4.30, for different centrality intervals (since these values are evaluated in % of v_n, this figure is not useful but just plotted to give an order of magnitude). This systematic uncertainty will be part of the final total systematic uncertainty.

Residual non-flow effects

Non-flow is usually the term which refers to few particle corrections (from jets or resonances). Basically the non-flow effects are strongly suppressed simply because the 3-sub-event method is used, which involves large pseudo-rapidity gaps (SPD used to measured tracklets, V0A and V0C for the energy deposited, and the muon spectrometer for measuring J/ψ). However, an estimate of these effects can be performed using the cross-term products between $\mathbf{u}_n$ and $\mathbf{Q}_n$ components. This study is realised in different p_T ranges versus $M_{\mu\mu}$ in Fig. 4.31 (J/ψ) and Fig. 4.32 (Υ(1S)), and finally as a function of p_T in Fig. 4.33 for different mass regions (low masses, J/ψ sector, Υ(1S) sector).

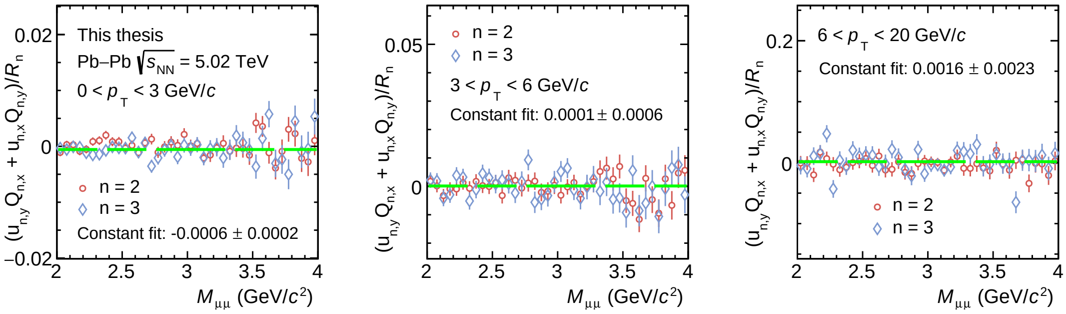

Figure 4.31: $M_{\mu\mu}$ dependence of the cross-term products $\mathbf{u}_{n,x}$ and $\mathbf{Q}_{n,y}$ (using SPD as reference flow detector) for different p_T ranges, in the J/ψ mass region.

The cross-product profiles can be fitted using a constant function to obtain an order of magnitude of its variation in the mass or p_{T} range considered. When this contribution deviate from zero more than 1σ, then this contribution is assigned as systematic uncertainty, if not, since this measurement is also statistically limited (because it is dimuon events), no systematic uncertainty are assigned on this p_{T} or centrality range.

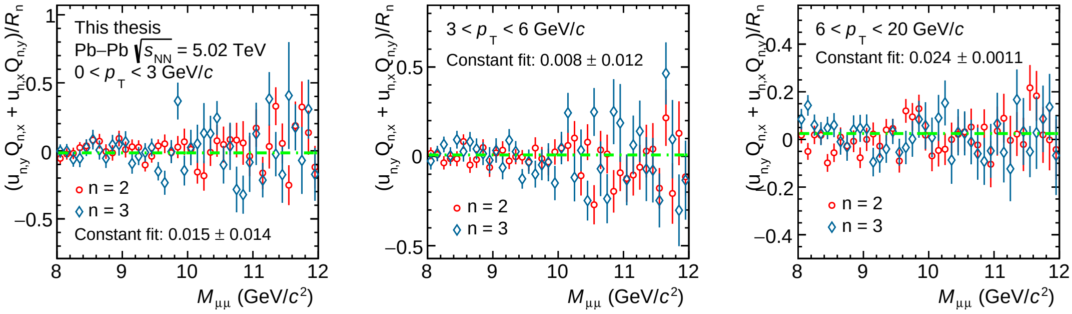

Figure 4.32: $M_{\mu\mu}$ dependence of the cross-term products $\mathbf{u}_{n,x}$ and $\mathbf{Q}_{n,y}$ (using SPD as reference flow detector) for different p_{T} ranges, in the Υ(1S) mass region.

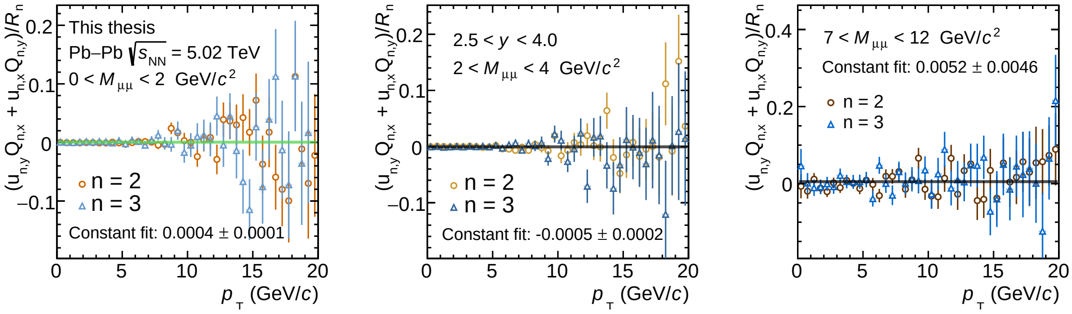

Figure 4.33: p_{T}-dependence of the cross-term products between $\mathbf{u}_{n,x}$ and $\mathbf{Q}_{n,y}$ (using SPD as reference flow detector) for different mass regions.

One can mention that, the difference between the cross-term products performed here are used to determine the non-flow effects originated from the correlations of J/ψ with other particles, while the cross-term products of $\mathbf{Q}_{n,x}$ and $\mathbf{Q}_{n,y}$ (from different or same detectors) also allow to estimate the systematic biases due to the non-uniform azimuthal acceptance, which are not classified as non-flow effects.

The goal is to estimate the bias originated from the non-flow contribution in the v_{n} extraction. The results show that in all p_{T} or mass ranges, the non-flow effects are estimated bin-per-bin and found to be around 1–2% of the v_{n} depending of the p_{T} range. This systematic uncertainty will be part of the final total systematic uncertainty.

Correlated background and event mixing

The event mixing, which reproduces the combinatorial background (originated from uncorrelated muon pairs) perfectly well the background flow in central collisions and at low-p_{T}, allows to fix the dimuon background v_{n} using mixed-event distributions. However, in non-central collisions and at high-p_{T} the emergence of correlated dimuon background leads to an unknown contribution, which could produce a bias on final v_{n} measurement. Hence, it produces an additional systematic uncertainty due to the value of the scaling (β) applied on v_n^{mix} (see Eq. 4.7), the later is left free in the fit when the ratio $\frac{N^{\mathrm{mix}}}{N^{\mathrm{same}}}$ deviates from one.

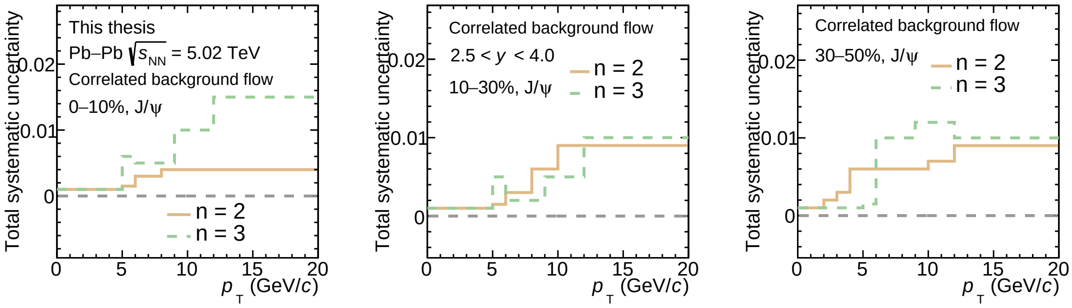

Figure 4.34: Total systematic uncertainty associated to the correlated background shape on J/ψ v_2 and v_3, as a function of p_{T} for different centrality intervals

This systematic uncertainty is estimated by taking the difference of the v_{n} values obtained with and without the scaling correction ($\beta \neq 0$ or $\beta = 0$), which is originated from the fact that the mix-event spectra do not fit perfectly well the same-event spectra at high-p_{T}. Taking the previous Eq. 4.7, and replacing the unknown v_n^{corr} by a free parameter β in the fit (which reflects the proportionality with v_n^{mix}), one can rewrite the formula as

$$v_{\mathrm{n}}(M_{\mu\mu}) = v_{\mathrm{n}}^{\mathrm{sig}}\alpha(M_{\mu\mu}) + v_{\mathrm{n}}^{\mathrm{mix}}(M_{\mu\mu})\Big(\frac{N_{\mathrm{mix}}}{N_{\mathrm{same}}} + \beta(1 - \frac{N_{\mathrm{mix}}}{N_{\mathrm{same}}})\Big). \tag{4.9}$$

Figure 4.34 shows the values of this uncertainty, which are negligible for very low-p_{T} bin but become significant for both v_2 and v_3 when p_{T} goes beyond 5–6 GeV/c, and it is even more pronounced moving toward peripheral collisions.

Summary of systematic uncertainty

The total absolute values of the systematic uncertainty will be assigned at each measured v_{n} for the different p_{T}, y or centrality bin. The obtained final values are plotted in Fig. 4.35 for J/ψ v_2 and in Fig. 4.36 for the J/ψ v_3 measurements, as a function of p_{T}. The extraction is performed in three different centrality intervals, from central Pb–Pb collisions 0–10%, to 10–30%, to non-central 30–50%.

Even if the systematic uncertainties coming from correlated background flow seems large at high-p_{T}, the few last p_{T} ranges are big (since low number of dimuons

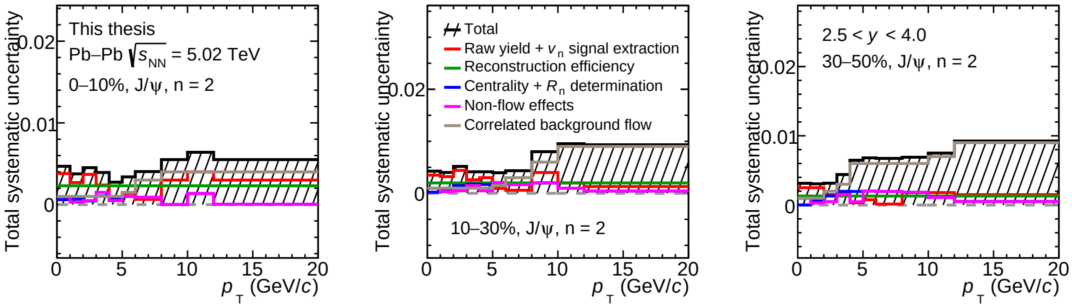

Figure 4.35: Summary of J/ψ v_2 total systematic uncertainty as a function of p_T for different centrality intervals

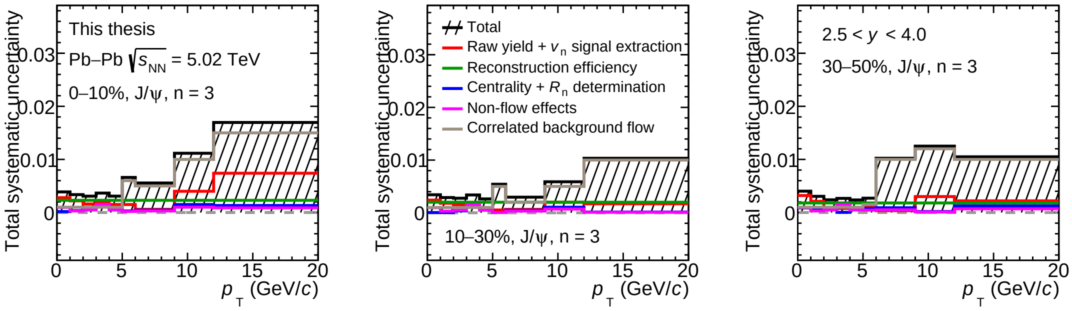

Figure 4.36: Summary of J/ψ v_3 total systematic uncertainty as a function of p_T for different centrality intervals

are counted), and the statistical uncertainties on v_n in these high-p_T bins are also very large compared to the systematic uncertainties found. Except in jet study, the major phenomena related to QGP occurs at low p_T (below 5 GeV/c), and in this case the dominant systematic uncertainties originate from the raw yield and v_n signal extraction.

The total systematic uncertainties for the centrality-differential J/ψ v_n measurement are shown in Fig. 4.37 and Fig. 4.38. One can mention that, at low p_T ($0 < p_T < 5$ GeVc) and in central collisions, the dominant systematic uncertainty originates from the signal extraction. While at high p_T ($5 < p_T < 20$ GeVc) the dominant one is coming from the correlated background flow, one can still mention that statistical uncertainties are also larger for high p_T bins. One can mention that here, the systematic uncertainty estimated from reconstruction efficiency varies from a centrality to another, and decreases toward peripheral collisions.

Concerning the total systematic uncertainties of the Υ(1S) v_2, in the p_T ranges 0 to 3, 3 to 6, and 6 to 15 GeV/c, and for the centrality interval 5–60%, the raw yield and v_n extraction (evaluated at 0.0161, 0.0075, and 0.0060) are included, the occupancy or reconstruction efficiency (0.0015 with no p_T dependence) also added, and those from the R_n determination and non-flow (around 2%). Since the event

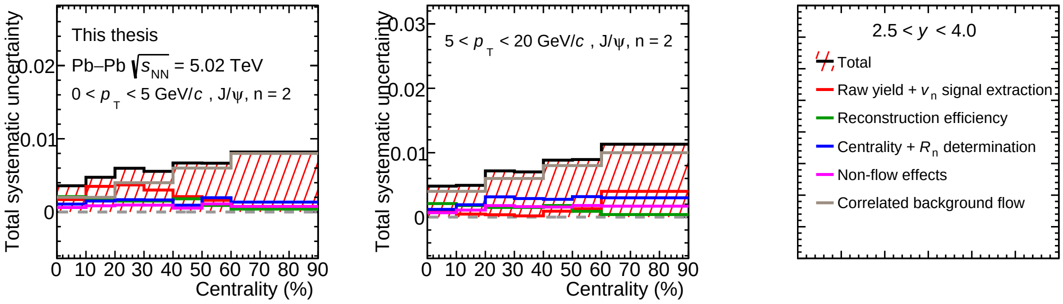

Figure 4.37: Summary of J/ψ v_2 total systematic uncertainty as a function of centrality for $p_T < 5$ GeV/c and $p_T > 5$ GeV/c

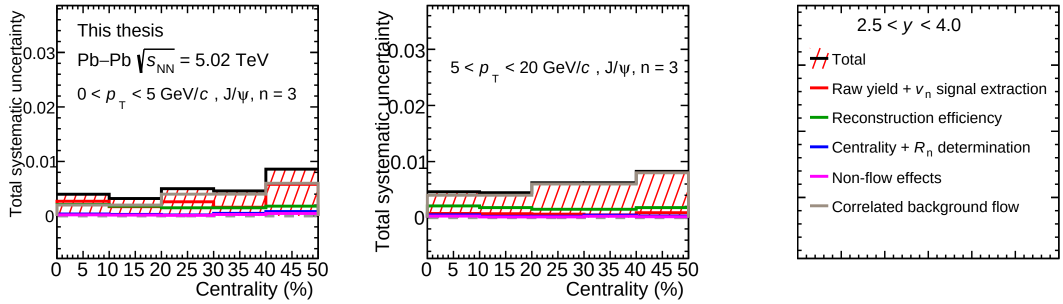

Figure 4.38: Summary of J/ψ v_3 total systematic uncertainty as a function of centrality for $p_T < 5$ GeV/c and $p_T > 5$ GeV/c

mixing technique is not used for the Υ(1S), no additional systematic uncertainty are added on this measurement.

As illustrated for example the Fig. 4.35, the final total systematic uncertainties are given by the quadratic sum of the different contributions, and will be then represented as boxes around the final data points. Thanks to the detector performances and to the large Pb–Pb data sample recorded (during the full Run 2), in all studied p_{T} ranges, y bins or centrality intervals, the systematic uncertainties do not exceed the statistical ones, down to $p_{\mathrm{T}} = 0$ GeV/c, which leads to precise J/ψ v_{n} values, and a first Υ(1S) v_2 measurement.

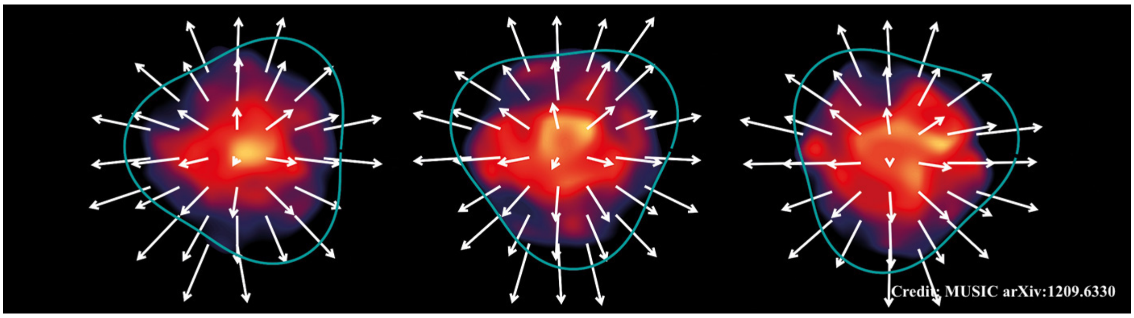

Chapter 5

Results and discussions

In this chapter, the results of J/ψ v_{n} and Υ(1S) v_2 are presented, and the comparisons with model calculations will be discussed. The first section concerns the final J/ψ v_2 and v_3 measurements, in which the p_{T}-differential v_{n} and the ratio v_3/v_2 will be shown. Further results about the centrality and rapidity dependence of J/ψ v_{n}, and the J/ψ v_2 in peripheral Pb–Pb at very low p_{T} will be also investigated. A comparison of these results with the current theoretical models will be discussed. In a second section, the Υ(1S) v_2 will be presented in p_{T}- and centrality-differential measurements, and then compared with theoretical models. Finally, further investigations using the number of constituent quark scaling will be performed in order to bring new aspects on open-heavy flavor v_{n}.

Contents

5.1 J/ψ v_n results and interpretations

5.1.1 p_T-differential v_n

Figure 5.1 shows the J/ψ v_2 results as a function of p_T for different centrality intervals (0–10%, 10–30%, 30–50%). A positive v_2 is observed in non-central Pb–Pb collisions over a quite large p_T range (from 0 to ∼12 GeV/c). In non-central collisions, the v_2 (which should be proportional to $\kappa_2\epsilon_2$ [32]) is found to be compatible with zero around p_T = 0 GeV/c, then it increases to reach maximal values at around 0.1, between 4 and 8 GeV/c. In central collisions, the v_2 exhibits a weak p_T dependence, with lower maximal values. Toward high-p_T values, the v_2 seems to decrease or saturate with slightly positive values. However, the statistical uncertainties beyond 10 GeV/c are large, and thus do not allow us to draw firm conclusions.

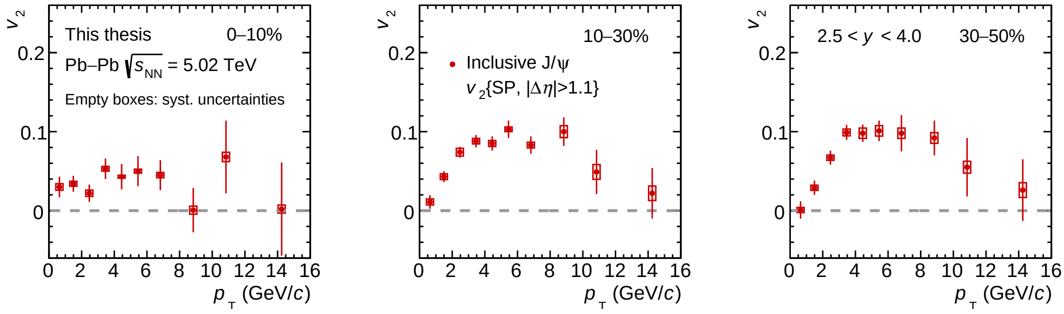

Figure 5.1: p_T-differential J/ψ v_2 for different centrality ranges. Empty boxes show the uncorrelated uncertainties, while the error bars the statistical uncertainties.

Figure 5.2 presents the J/ψ v_3 results as a function of p_T in the same centrality intervals than for the v_2. The v_3 originates from fluctuations of the initial energy density distribution and is less intuitive than the v_2. However, the proportionality between triangular flow and the eccentricity is still true ($v_3 \propto \kappa_3\epsilon_3$ [32]). The v_3 is measured to be lower than the J/ψ v_2 in a large p_T range up to 14 GeV/c.

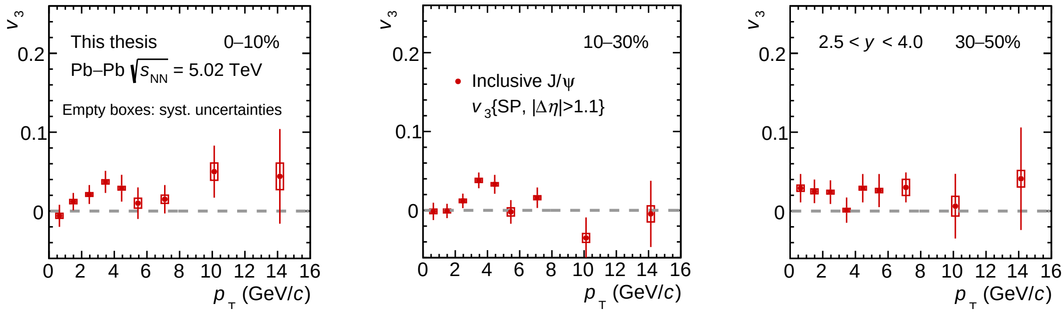

Figure 5.2: p_T-differential J/ψ v_3 for different centrality ranges. Empty boxes ares the uncorrelated uncertainties, while the error bars show the statistical uncertainties.

In the 0–50% centrality range, the triangular flow coefficient is measured to be larger than zero ($v_3 = 0.0250 \pm 0.0045$ (stat.) $\pm$ 0.0020 (syst.) in $2 < p_{\mathrm{T}} < 5$ GeV/c) corresponding to a significance of 5.1σ, calculated adding quadratically the statistical and systematic uncertainties. At low and intermediate p_{T}, the J/ψ v_2 values increase from central to non-central collisions, while it does not seem as clear for the v_3. The measurement of a positive v_3 indicates that the initial state energy-density fluctuations, the dominant source of v_3, are reflected also in the anisotropic flow of charm quarks.

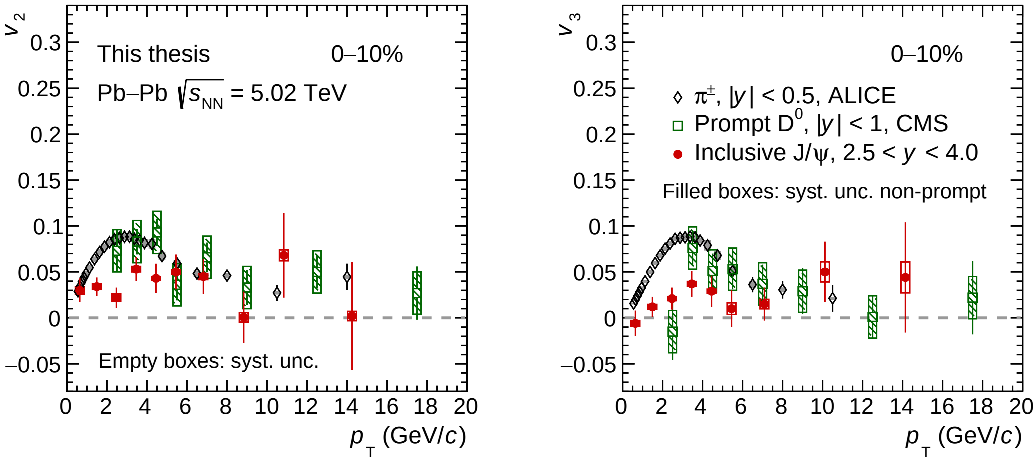

Figure 5.3: Comparison of J/ψ v_2 and v_3 to $\pi^{\pm}$ and prompt D^0 (published data), as a function of p_{T} for the 0–10% centrality interval.

To understand how significant the J/ψ v_{n} are, one can compare the results to $\pi^{\pm}$ v_{n}. Since pions are the lightest mesons produced, and in the hydro picture of the QGP the $\pi^{\pm}$ flow is expected to be the largest one (at a given p_{T}), with respect to the other mesons which are heavier. Since the published $\pi^{\pm}$ v_{n} measurements [34] were performed per 10% centrality intervals (except between 0–10% which is per 5%), the data have been re-weighted using Eq. (5.1), according to their corrected p_{T} spectra, and then merged in order to form the 0–10%, 10–30%, 30–50% centrality intervals, the standard weighting formula is

$$v_n(p_{\mathrm{T}}) = \sum_i w_i \cdot v_n^{(i)}(p_{\mathrm{T}}) \Big/ \sum_i w_i. \tag{5.1}$$

The J/ψ v_{n} can also be compared to the open-charm data, which can provide an intermediate comparison between light flavor and closed charm. Three regimes need to be considered in this comparison with the D mesons, the hydro at low p_{T} which imply a mass ordering (where the mass matters), the recombination by coalescence at intermediate-p_{T} (where the quark content matters), and the fragmentation occurring at high-p_{T} (where the energy loss matters). The J/ψ v_{n} results are compared with the midrapidity v_2 measurements for charged pions by ALICE [34] and prompt D mesons by CMS [129]. Figure 5.3, Fig. 5.4, and Fig. 5.5 show the p_{T}-dependent inclusive J/ψ v_2 and v_3 coefficients measured at forward rapidity, compared with the charged pion and D meson data in the three different centrality intervals.

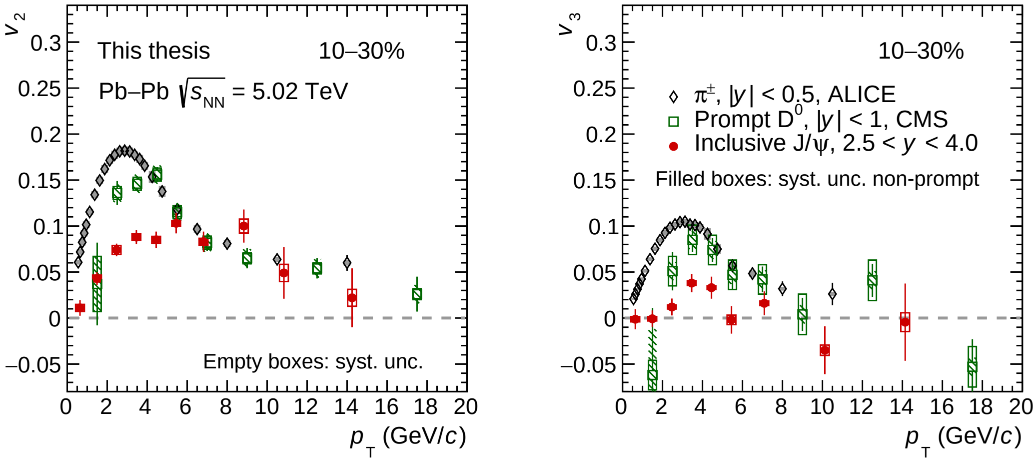

Figure 5.4: Comparison of J/ψ v_2 and v_3 to $\pi^{\pm}$ and prompt D^0 ([34, 129]), as a function of $p_{\rm T}$ for the 10–30% centrality interval.

The behavior of an increase in v_2 from central to non-central collisions is qualitatively similar to the one observed for $\pi^{\pm}$ and D mesons in the same $p_{\rm T}$ ranges. As also noted previously [92], a clear mass hierarchy of the v_2 values is seen in the low-$p_{\rm T}$ region ($p_{\rm T} <$ 3 GeV/c) for the light hadrons and D mesons measured at midrapidity and inclusive J/ψ, with the J/ψ exhibiting the lowest elliptic flow. The mass ordering is a property originated directly from hydro, and it is understood by considering that thermalized particles with different masses evolving in a common velocity field will correspond to different $p_{\rm T}$, which turns into a mass hierarchy in the $v_2(p_{\rm T})$ at a given $p_{\rm T}$. Here, it is important to note that in the considered η range, the η dependence of the v_2 at a given $p_{\rm T}$ is expected to be negligible, as shown by the CMS measurement for charged particles [130].

At high $p_{\rm T}$ ($p_{\rm T} > 8$ GeV/c), the v_2 coefficients from all species converge into a single curve suggesting that, in this kinematic range, the anisotropy for all particles arises dominantly from path-length dependent energy-loss effects [131]. However, in the case of the much heavier J/ψ, one may also consider that the hydrodynamic flow, which arises from a common velocity field, may still contribute significantly even at high $p_{\rm T}$, as can be expected from the particle mass dependence of the $p_{\rm T}$ range where the flow reaches its maximum.

The mass hierarchy observed for v_2 holds also in the case of v_3. Together with the J/ψ v_2, these observations provide a strong support for the hypothesis of charm quark being, at least partially, kinetically equilibrated in the dense and deconfined QGP medium.

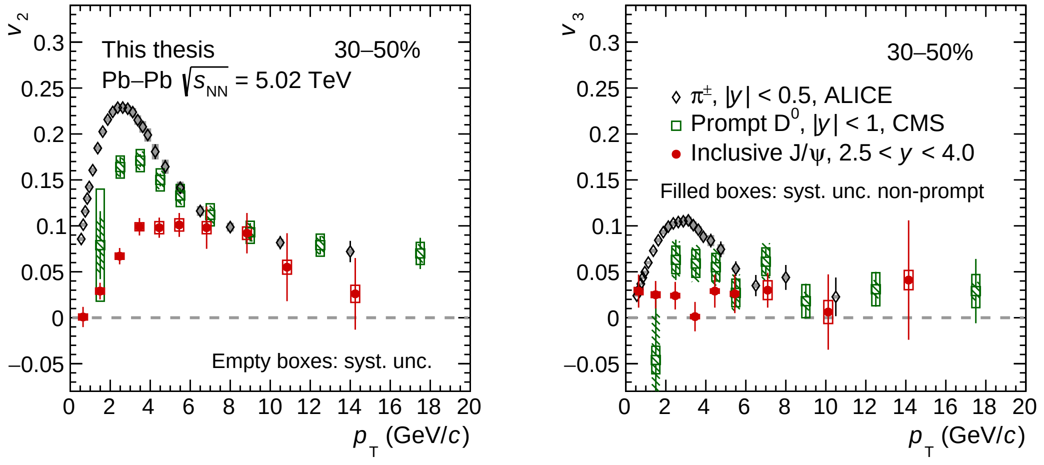

Figure 5.5: Comparison of J/ψ v_2 and v_3 to $\pi^{\pm}$ and prompt D^0 (published data), as a function of p_{T} for the 30–50% centrality interval.

5.1.2 p_{T}-differential v_3/v_2 ratio

The medium response to the initial state anisotropy (ϵ_n), which is transformed into the v_{n} (i.e. $v_n \propto \kappa_n \epsilon_n$), strongly depends on the macroscopic properties of the fireball (like the temperature dependent equation of state and the shear and bulk viscosity). The ratio of the triangular to elliptic flow coefficients, v_3/v_2 is an interesting quantity because it is a way to characterize the response of the system, and whether this response is independent of the particle type (when comparing v_3/v_2 for various particles the $\varepsilon_3/\varepsilon_2$ cancel). The ratio v_3/v_2, as a function of p_{T} is shown in the left panel of Fig. 5.6 for the inclusive J/ψ at forward rapidity. In

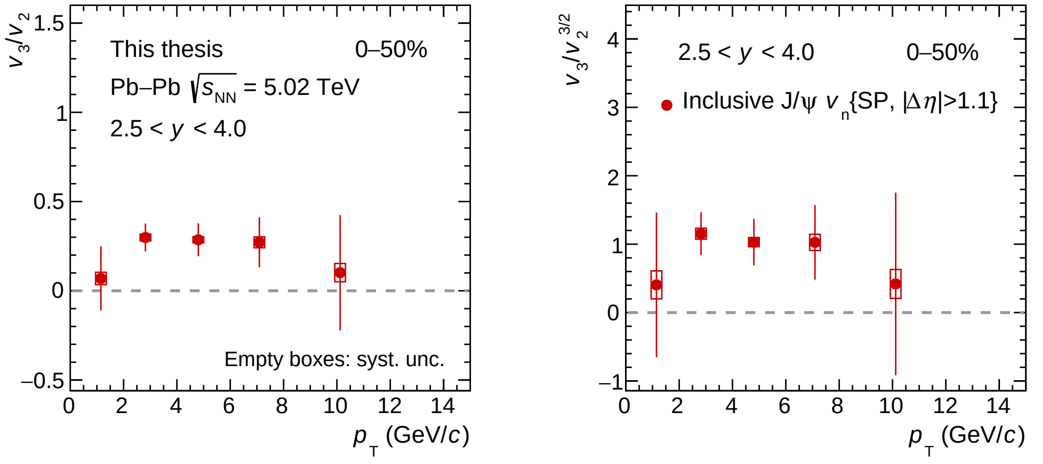

Figure 5.6: p_{T}-differential J/ψ v_3/v_2 and $v_3/v_2^{3/2}$ in 0–50%.

this ratio, the statistical uncertainties are considered to be uncorrelated due to the weak correlation between the orientation of the $\mathbf{Q}_2$ and $\mathbf{Q}_3$ flow vectors [132], while the systematic uncertainties related to $\alpha(m_{\mu\mu})$ and to the reconstruction efficiency, cancel in the ratio.

At RHIC [133, 134] and LHC [135, 136], it was observed that the flow coefficients of light particles from different harmonics follow a power-law scaling as $v_{\mathrm{n}}^{1/\mathrm{n}} \propto v_{\mathrm{m}}^{1/\mathrm{m}}$ up to about 6 GeV/c, for most centrality ranges, but the 0–5%, independently of the harmonics n and m. The ratio $v_3/v_2^{3/2}$ in the right panel of Fig. 5.6 illustrates such a scaling. The J/ψ v_3/v_2 results are compared to D mesons and charged pions at midrapidity in Fig. 5.7 (left panel). The same hierarchy observed for the individual v_2 and v_3 measurements is also observed in the v_3/v_2 ratio, which suggests that higher harmonics are damped faster for heavy quarks than for the light ones. Furthermore, the $v_3/v_2^{3/2}$ for pions, D and J/ψ mesons tend to converge, although the J/ψ values are systematically lower than the ones of pions.

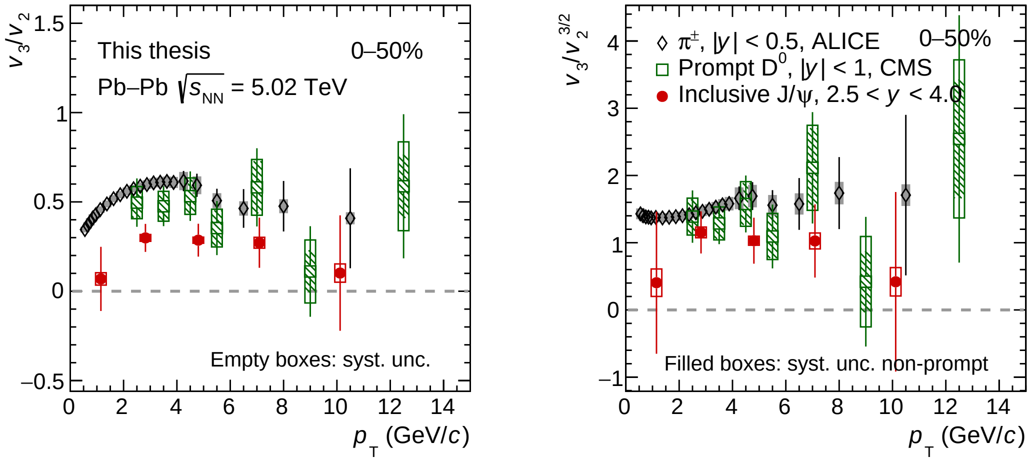

Figure 5.7: Comparison of J/ψ v_3/v_2 and $v_3/v_2^{3/2}$ as a function of p_{T} in 0–50%, with $\pi^{\pm}$ and prompt D^0 published data.

5.1.3 Centrality and rapidity dependence of the v_{n}

In large systems such as Pb–Pb collisions, the light flavor v_2 and v_3 exhibits a strong centrality (or multiplicity) dependence [35, 137], and an ordering of $v_2 > v_3$ is observed (details can be found in Sec. 1.5) except for the very central collisions, where $v_2 \approx v_3$ (caused by the event-by-event fluctuations of the energy density profile, which generate anisotropy). However, this system size dependence is not fully understood for the heavy flavor sector.

The centrality dependence of the J/ψ results are compared with that of flow coefficients of charged pions for a p_{T} value similar to the corrected J/ψ $\langle p_{\mathrm{T}} \rangle$, published by ALICE in Ref. [34]. Figure 5.8 shows the centrality dependence of the inclusive J/ψ and $\pi^{\pm}$ v_2 for low-p_{T} intervals, while the Fig. 5.9 shows high-p_{T} ones.

In addition, the ratio $v_2^{\pi}/v_2^{\mathrm{J}/\psi}$ is computed and shown in the right panels of these figures. Similar measurements are performed and presented for J/ψ v_3 in Fig. 5.10 and Fig. 5.11. Here, due to the large integrated p_{T} range, the v_{n} coefficients are corrected for the J/ψ detector acceptance and reconstruction efficiency. Each dimuon pair is weighted using the inverse of the p_{T} and y dependent $A \times \varepsilon$ factor before filling the invariant mass and $v_{\mathrm{n}}(M_{\mu\mu})$ distributions.

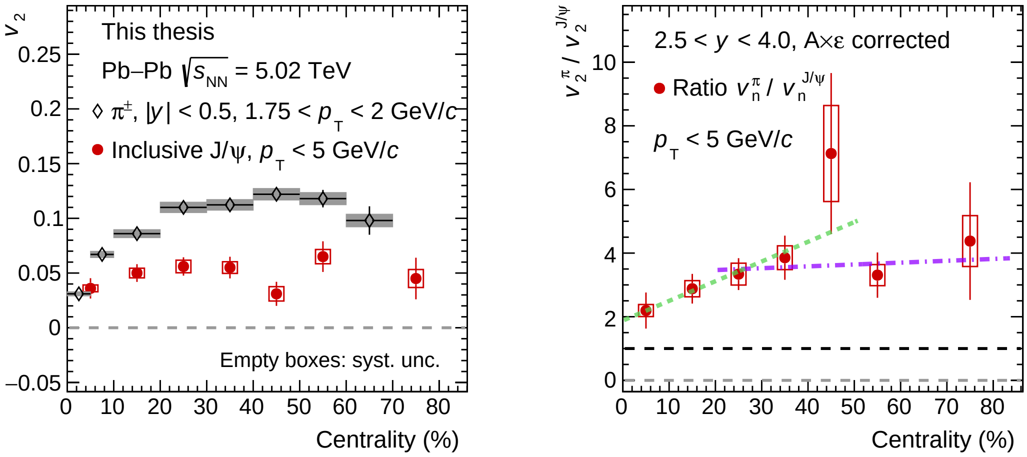

Figure 5.8: Centrality dependence of J/ψ v_2 for $p_{\mathrm{T}} < 5$ GeV/c. The data are compared to $\pi^{\pm}$ selected in a p_{T} range ($1.75 > p_{\mathrm{T}} > 2$ GeV/c) similar to the $\langle p_{\mathrm{T}} \rangle$ of J/ψ. Linear fits are performed on the 0–50% (green dotted line) and 20–80% (magenta dotted line) data.

Both at low p_{T} ($1.75 < p_{\mathrm{T}} < 2$ GeV/c) and high p_{T} ($6 < p_{\mathrm{T}} < 7$ GeV/c), the v_2 of $\pi^{\pm}$ increases from central to semi-central collisions, reaching a maximum at 40–50% centrality, and then decreases towards peripheral collisions. For the J/ψ at low p_{T} ($0 < p_{\mathrm{T}} < 5$ GeV/c), while the centrality trend is qualitatively similar, the maximum (or even saturation) of v_2 seems to be reached for more central collisions than for the pions. This is more clearly emphasized by the increasing trend of the ratio $v_2^{\pi}/v_2^{\mathrm{J}/\psi}$, from central to peripheral collisions (this ratio deviates from unity by a significance of 8.5σ). Since in the framework of transport models the $c\bar{c}$ production follows the variation of the energy density, then this increasing trend of $v_2^{\pi}/v_2^{\mathrm{J}/\psi}$ could be understood by the increasing fraction of regenerated J/ψ at low p_{T} when moving from peripheral to central collisions.

Alternatively, and independently of the regeneration scenario, the increase of the $v_2^{\pi}/v_2^{\mathrm{J}/\psi}$ from central to peripheral collisions, could also be understood in terms of partial or later thermalization of the charm quarks compared to light quarks. Indeed, the heavy quark needs a longer time in the medium to develop its flow compared to light quark. The decrease in energy density and lifetime of the system is counterbalanced by the increase of the initial spatial anisotropy towards peripheral collisions. Therefore, the v_2 of the J/ψ (mainly regenerated) will reach its maximum at more central collisions compared to light particles because charm quarks require

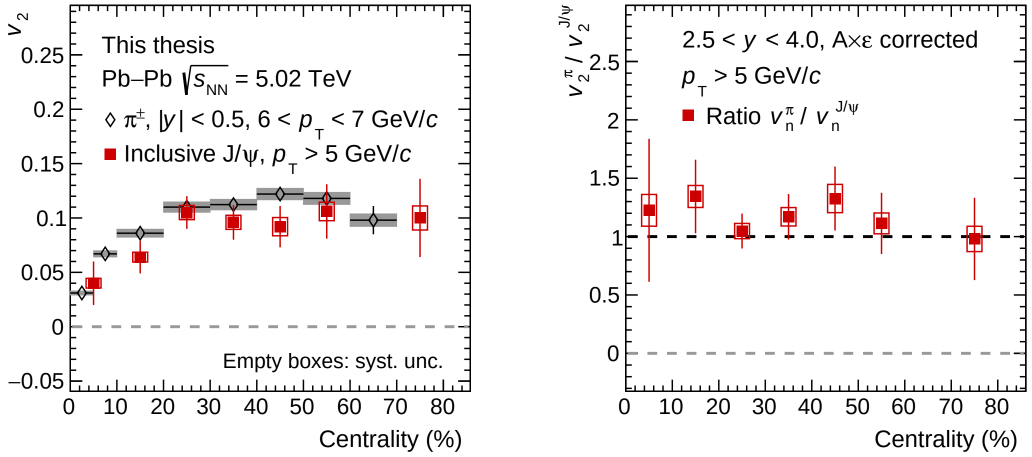

Figure 5.9: Centrality dependence of J/ψ v_2 for $p_{\rm T} > 5$ GeV/c. The data are compared to $\pi^{\pm}$ selected in a $p_{\rm T}$ range ($6 > p_{\rm T} > 7$ GeV/c) similar to the $\langle p_{\rm T} \rangle$ of J/ψ.

larger energy densities to develop flow [65, 138–140].

At high $p_{\rm T}$, J/ψ mesons (corresponding to $p_{\rm T} > 5$ GeV/c) and charged pions ($6 < p_{\rm T} < 7$ GeV/c) seem to exhibit the same centrality dependence, although the v_2 coefficients are systematically lower for the J/ψ mesons than for the pions. Such a similar centrality dependence could indicate a similar mechanism at the origin of the flow for both J/ψ mesons and pions at high $p_{\rm T}$. Also, the $\pi^{\pm}$ v_2 at high $p_{\rm T}$ is understood to originate from a parton energy loss.

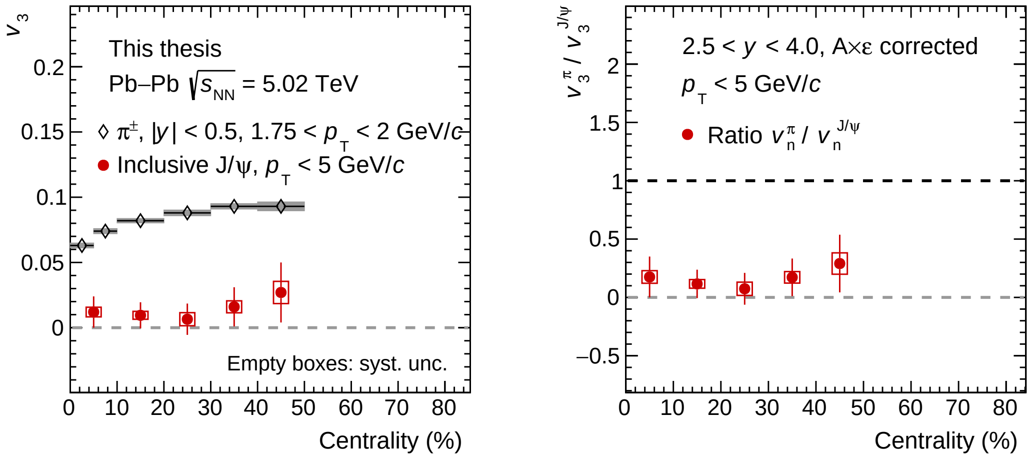

Figure 5.10: Centrality dependence of J/ψ v_3 for $p_{\rm T} < 5$ GeV/c. The data are compared to $\pi^{\pm}$ selected in a $p_{\rm T}$ range ($1.75 > p_{\rm T} > 2$ GeV/c) similar to the $\langle p_{\rm T} \rangle$ of J/ψ.

Figure 5.10 shows that the centrality dependence of the v_3 coefficient at low p_T is less pronounced than that of the v_2 for both pions and J/ψ, as expected since initial state fluctuations only weakly depend on centrality. Also, the J/ψ v_3 is smaller relative to the one of charged pions, in both p_T intervals considered.

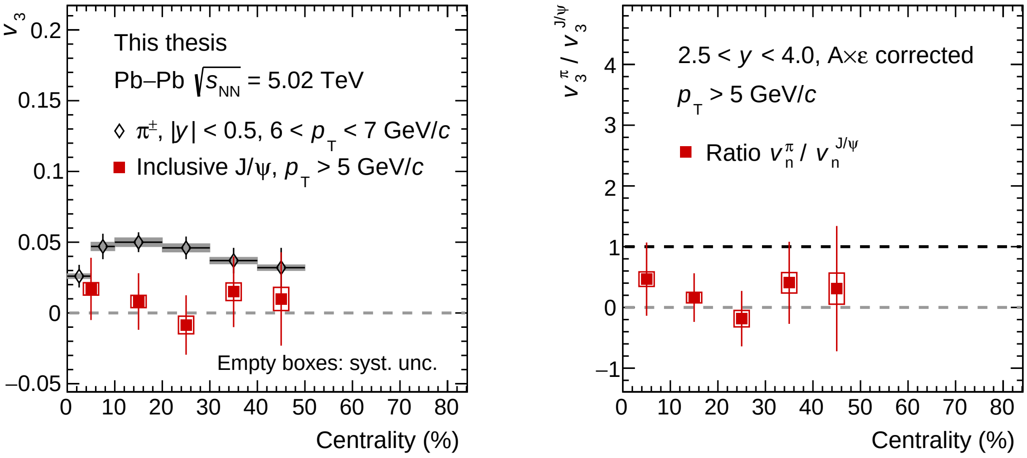

Figure 5.11: Centrality dependence of J/ψ v_3 for $p_\mathrm{T} > 5$ GeV/c. The data are compared to $\pi^\pm$ selected in a p_T range ($6 > p_\mathrm{T} > 7$ GeV/c) similar to the $\langle p_\mathrm{T} \rangle$ of J/ψ.

Since the measured v_2 of the reconstructed J/ψ depends on the p_T distribution, which could vary with the collision centrality, the $\langle p_\mathrm{T} \rangle$ or $\langle p_\mathrm{T} \rangle^{\mathrm{uncorr}}$ of J/ψ should be also studied. Figure 5.12 shows the variations of the J/ψ $\langle p_\mathrm{T} \rangle$ extracted after a correction on each dimuon candidate with the acceptance and efficiency ($A \times \varepsilon$) factor. It is important to understand if the origin of the variation of v_2 is from a modification of the $\langle p_\mathrm{T} \rangle$ or a real modification as a function of the number of participants in the Pb–Pb collision. For low-p_T J/ψ, the variation of $\langle p_\mathrm{T} \rangle$ is contained between 1.9 and 2.1 GeV/c, which is referring to a v_2 included in the range 0.06–0.07 (for the 10–50% centrality interval). For high-p_T J/ψ, the $\langle p_\mathrm{T} \rangle$ varies between 6.4 and 6.7 GeV/c, corresponding to a v_2 of about 0.1, also with small variations. Moreover, it is worth to notice that the monotonic increase of $\langle p_\mathrm{T} \rangle$ toward peripheral collisions, is a consequence of the smaller suppression observed at low p_T in central collisions, which hints a strong contribution from (re)combination processes. Concerning the most peripheral bin of $\langle p_\mathrm{T} \rangle$, its value should be contaminated by the photo-production of J/ψ (for $0 < p_\mathrm{T} < 0.3$ GeV/c, which are not removed here). The result of this contamination is simply that it reduces the value of $\langle p_\mathrm{T} \rangle$ by at least for 4% (percentage estimated from [141]) in this most peripheral centrality interval.

In the common picture of transport models (which will be described later), it is expected than the energy density of the created medium exhibits a rapidity dependence, where the number of initially produced charm quarks is larger at mid-rapidity than at forward rapidity. In this picture, the regenerated J/ψ largely contribute to

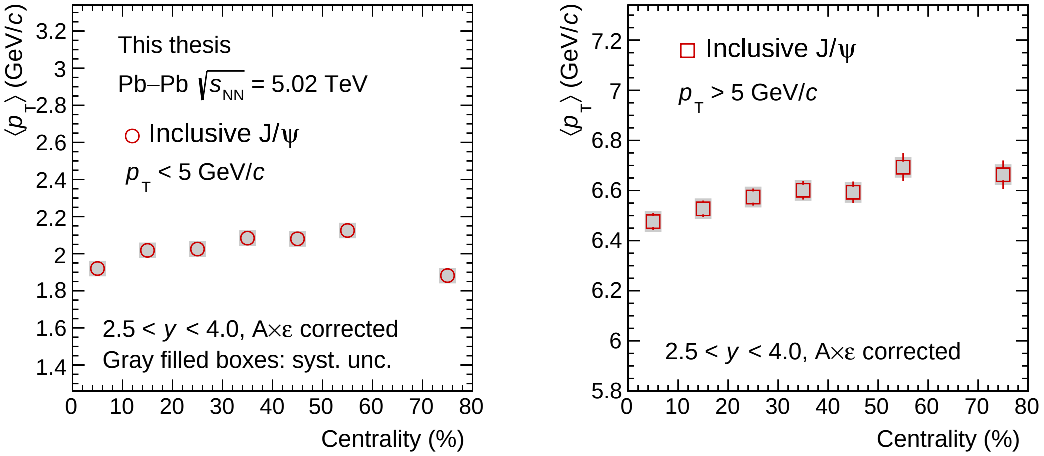

Figure 5.12: Centrality dependence of the $\langle p_{\mathrm{T}} \rangle$ extracted after the acceptance and efficiency correction, for low p_{T} (left) and high p_{T} (right) inclusive J/ψ.

the v_2 measured, one could expect that the v_2 exhibits also a dependence as a function of rapidity. On the other hand, in the picture of statistical hadronization model (SHM), J/ψ production is expected to solely originate from regenerated J/ψ, since there is no primordial contribution in this model. Thus, in this case the J/ψ elliptic flow should not be expected to acquire an energy density (or rapidity) dependence.

Figure 5.13 (left) shows the J/ψ v_2 measured both at forward rapidity and at mid-rapidity in the dimuon and dielectron decay channel, respectively. The mid-rapidity

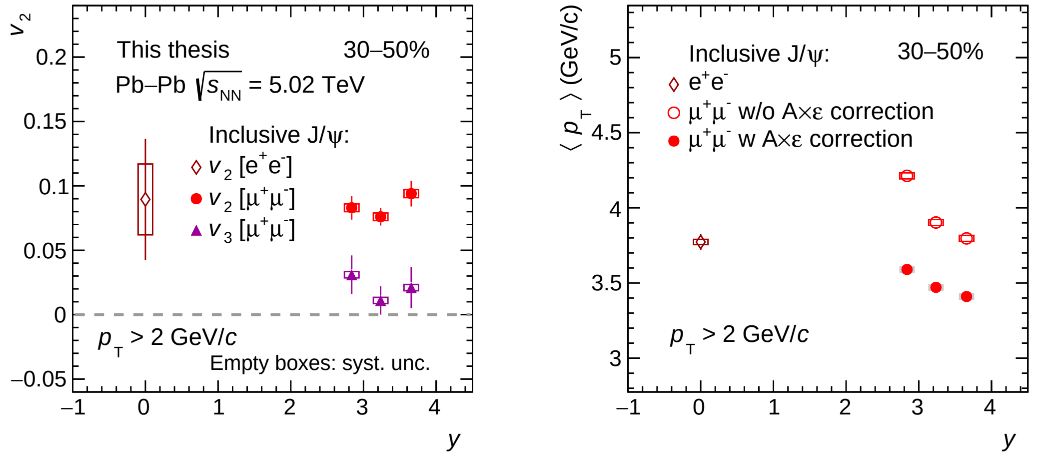

Figure 5.13: J/ψ v_n as a function of rapidity y (corrected for $A\times\varepsilon$), for the centrality range 30-50 % and $2 < p_{\mathrm{T}} < 20$ GeV/c. Thanks to the dielectrons analyzers, the mid-rapidity v_2 value is shown.

value is also extracted with the SP method where the V0A detector is used to obtain the $\mathbf{Q}_2$, and the ITS-TPC for measuring the dielectrons. Both results are presented using events with a centrality corresponding to 30–50% and $2 < p_T < 20$ GeV/c. Forward rapidity v_2 values are plotted with the acceptance and efficiency correction because it is an integrated measurement. One can also notice that the $v_2(p_T)$ is independent of energy density, while it is not the case for the $v_2(y)$ [142].

Since R_n is lower in the central collisions, 0–30% are excluded. Moreover, the p_T range corresponding to 0-2 GeV/c was also excluded, due to low values of v_2 and v_3. The pseudo-rapidity gap between TPC and the V0A detector is around $\Delta\eta = 0.8$, while in our case the gap between SPD and the muon spectrometer corresponds to $\Delta\eta = 1.1$. The effect of the decorrelation of the symmetry plane angles corresponding to ψ_n (for $n = 2, 3$) between mid- and forward-pseudorapidity has been estimated to be less than 1% and 3% for v_2 and v_3, respectively [143, 144]. In addition, the corrected $\langle p_T \rangle$ and the $\langle p_T \rangle^{\text{uncor}}$ of the reconstructed J/ψ are shown in the right panel of Fig. 5.13, which decrease slightly going toward forward rapidities (from 3.8 to 3.3 GeV/c). This comparison could be useful in order to discriminate if the origin of the variation of v_2 is from a modification of $\langle p_T \rangle$, or a real modification of v_2 as a function of the rapidity. In our case these displacements of $\langle p_T \rangle$ correspond to small variations of v_2 (few percents).

5.1.4 Comparison to previous analyses

This section focuses on the comparison between this analysis and older J/ψ v_2 analyses in Pb–Pb collisions. The previous analyses were realized in Pb–Pb collisions at $\sqrt{s_{\text{NN}}} = 2.76$ TeV [82], and at $\sqrt{s_{\text{NN}}} = 5.02$ TeV with only the 2015 data sample [79] (without the 2018 data which complete the full Run 2).

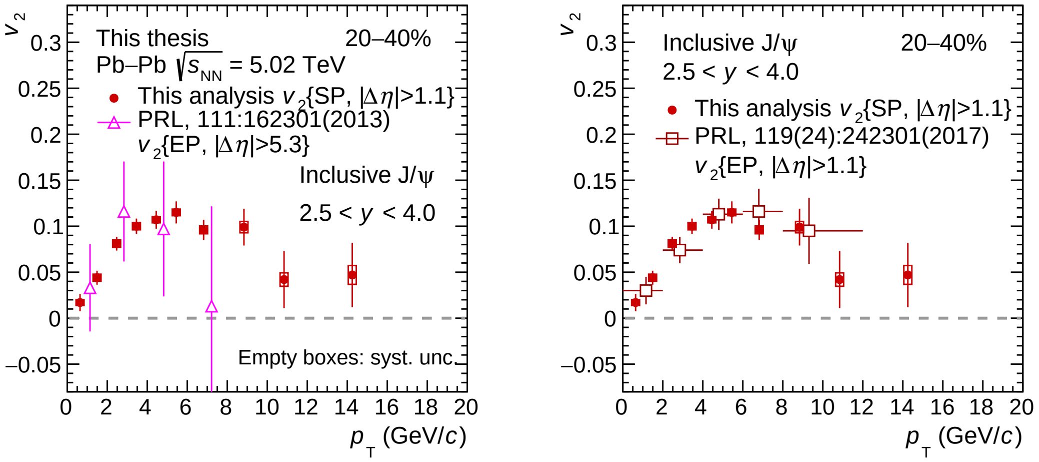

Figure 5.14: Comparison of J/ψ v_2 in 20–40% with the previous published data.

Figure 5.14 shows the values of J/ψ v_2 measured in this analysis compared to the values of J/ψ v_2 measured at $\sqrt{s_{\text{NN}}} = 2.76$ TeV in Pb–Pb collisions (using Run 1 data, in 2011) extracted using the event-plane method (see [82] for details).

The comparison illustrates the agreement between values found in the two analyses. Moreover, it is also compatible with a negligible variation of v_2 as a function of the beam energy, which is compatible with the negligible variations observed for the light particles. Figure 5.14 (right panel) shows the data comparison using the older analysis performed at 5.02 TeV. The results obtained here are found to be in agreement with the previous published results. Although residual differences could be present because the values were extracted using the event-plane method, the v_2 values for both analyses are compatible. The real improvements of these results with respect to the previous analyses shown in Fig. 5.14, is that both SP and event-mixing method in the extraction procedures were used, which lead to reduced statistical uncertainties.

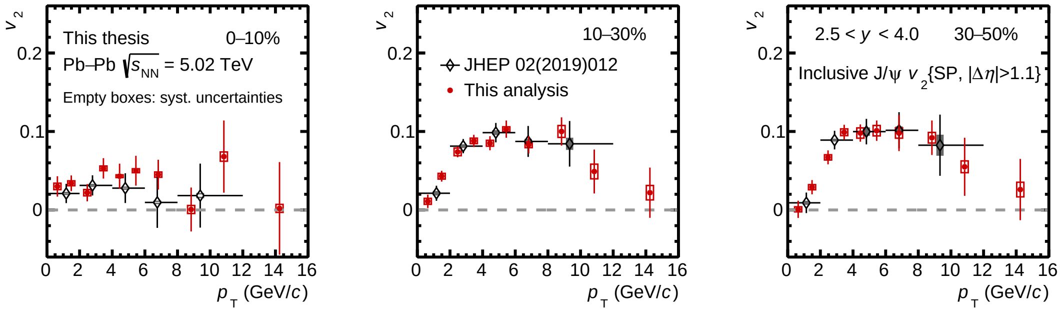

Figure 5.15: Comparison of J/ψ v_2 (using SP method and event-mixing) with the previous analysis (using only the 2015 Pb-Pb data sample).

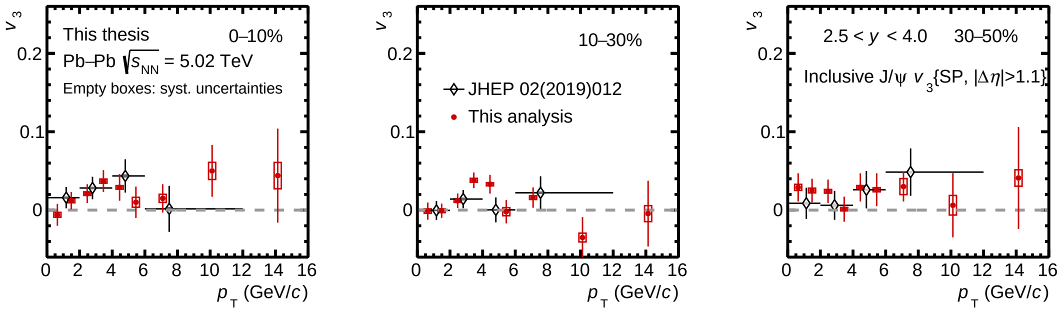

Figure 5.16: Comparison of J/ψ v_3 (using SP method and event-mixing) with the previous analysis (using only the 2015 Pb-Pb data sample).

The values of J/ψ v_n obtained using the SP method coupled with the event mixing procedure (as described in the previous Chapter 4) are presented in the three centrality classes in Fig. 5.15 and Fig. 5.16, and compared with a previous analysis (based only on 2015 data sample [92]) of J/ψ v_n using also the same extraction procedures. A good agreement is found between both analyses, for all the available p_T and centrality intervals. In this thesis, the global statistical uncertainties are reduced, the p_T coverage is extended up to the last range 12-20 GeV/c, and the number of $p_{\rm T}$ intervals is increased, simply because this analysis use the full Run 2 data sample.

5.1.5 Comparison to current theoretical models

Figure 5.17 (left panel), shows the inclusive J/ψ v_2 as a function of $p_{\rm T}$ in the 20–40% centrality interval, and the data are compared to the microscopic transport calculations by Du et al. [64, 83]. In this model, the J/ψ are created both from the primordial hard partonic interactions but also from the recombination of thermalized charm quarks in the medium, which accounts for roughly 50% of all J/ψ at low $p_{\rm T}$. The fraction of regenerated J/ψ is higher at low $p_{\rm T}$, while it decrease quickly toward high $p_{\rm T}$. Non-prompt J/ψ mesons, created in the weak decays of beauty hadrons, are also included in the model. The amplitude of the inclusive J/ψ v_2 in the calculations is in good agreement with the experimental measurements for $p_{\rm T} <$ 4 GeV/c. However, the overall trend of the model calculation does not describe the data well, especially in the intermediate $p_{\rm T}$ range, $4 < p_{\rm T} < 10$ GeV/c, where the J/ψ flow is largely underestimated.

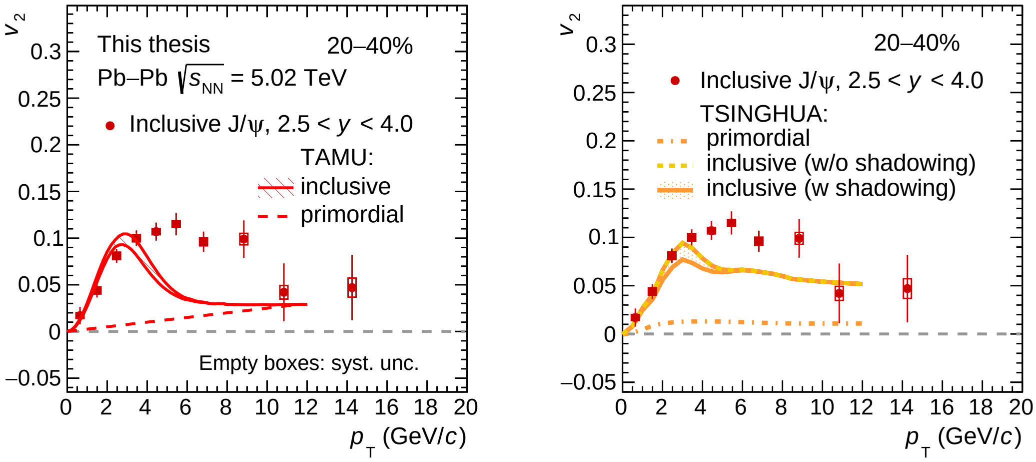

Figure 5.17: Comparison of J/ψ v_2 with theoretical calculations, in the 20–40% centrality interval.

The primordial J/ψ component, which is sensitive mainly to path length dependent effects, like survival probability, exhibits a monotonically increasing trend from low towards high $p_{\rm T}$, with this mechanism becoming the dominant source of the anisotropic flow for $p_{\rm T}$ larger than 8 GeV/c. Path length dependent energy loss, widely seen as a major source of anisotropy at large $p_{\rm T}$, is not implemented for J/ψ mesons in this calculation. It is worth noting that this model provides a qualitative good description of the centrality and transverse momentum of the J/ψ nuclear modification factor [78, 141].

For simplicity, the transport model TAMU assumes the primordial part to be constant in the $R_{\rm AA}(p_{\rm T})$ of J/ψ, which reflects our currently limited knowledge about the $p_{\rm T}$ dependence of the dissociation rates, formation time effects, etc... The total $R_{\rm AA}$ or the total v_2 can be decomposed in a regeneration component (which is evaluated with a blast-wave ansatz in the fireball evolution at sequential freeze-out times), and a suppressed primordial component (as obtained from a Boltzmann transport equation without gain term).

Figure 5.17 and Fig. 5.18 (right panels) show the comparison between a second transport model (TSINGHUA) calculations [145] and the data. In this model, the J/ψ v_2 takes also its origins from a primordial and regenerated component, nevertheless the implementation of the system evolution, the spectral properties of charmonia, the regeneration and suppression terms in the Boltzmann equation are implemented differently, and thus lead to different v_2. The shadowing effect is also included in this transport model, leading to significant uncertainties at $p_{\rm T}$ around 3 GeV/c. Moreover, an additional effect could help to describe a higher v_2 at intermediate and high $p_{\rm T}$, it is an effect to a strong magnetic field in the early stage of the medium expansion ("with non-collective" curve), created principally by proton spectators which generate an electric charge asymmetry.

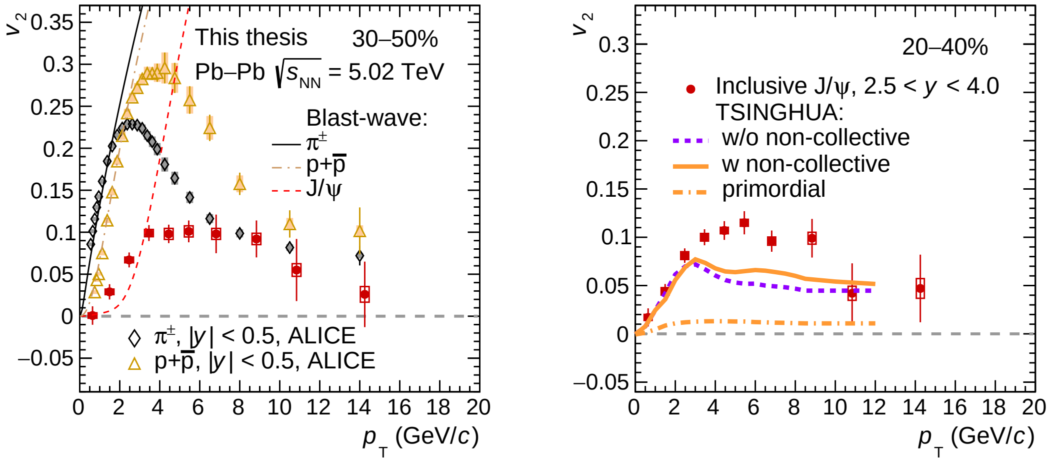

Figure 5.18: Model comparisons with the J/ψ v_2 as a function of $p_{\rm T}$ for the 20–40% centrality interval.

A simultaneous blast-wave fit to particle yields and v_2 using a compact formula for the calculation of $v_2(p_{\rm T})$ [146] for an elliptic freeze-out surface (which follows from the Cooper-Frye ansatz without further assumptions), could be used to predict the J/ψ v_2. Figure 5.18 shows the blast-wave fit results for pions, protons, and the scaled J/ψ v_2 curve. The obtained fits correspond to the parameters $\rho_0 = 1.04$, $\rho_2 = 0.09$, $R_x/R_y = 0.83$, and a pseudo critical temperature (freeze out) of $T_{pc} = 155$ MeV. Here, ρ_0 and ρ_2 are the parameters of the radial velocity profile

$$\rho(\hat{r},\hat{\phi}) = \hat{r}(\rho_0 + \rho_2\cos(2\phi_b)), \tag{5.2}$$

$$\phi_b(\hat{\phi}) = \arctan\left(\frac{R_x}{R_y}\tan\hat{\phi}\right) + [\frac{\hat{\phi}}{\pi} + \frac{1}{2}]\pi, \tag{5.3}$$

where R_x and R_y are the radii of the ellipse along the x and y axes, respectively. ϕ_b is the azimuthal angle of the emitted particle, and $[x]$ denotes the greatest integer less than or equal to x. The corresponding expression for $v_2(p_{\mathrm{T}})$ is obtained as the average of $\cos(2\phi_b)$ over the azimuthal particle distribution $\mathrm{d}N/\mathrm{d}p_{\mathrm{T}}$.

Basically, the blast-wave model describes the p_{T} distributions at the kinetic freeze-out of particles produced from a source in thermal equilibrium which undergoes a collective radial expansion. One can expect that the recombination of c quarks to form J/ψ occurs at higher temperature than the critical one, then the kinetic freeze-out hyper-surface of regenerated J/ψ will be expected to be much more elliptical than in later stages. In principle, the validity of this fit occurs only for low-p_{T} spectra and v_2 coefficients ($p_{\mathrm{T}} < 2$ GeV/c for light hadrons), where the hydrodynamic description can be applied. Here, the obtained curve for the J/ψ v_2 suggests that the parameters extracted from blast-wave fits (ρ_0, ρ_2, R_x/R_y) on pions and protons, should be slightly different in order to better describe the J/ψ flow.

5.1.6 Very low-p_{T} J/ψ v_2

The photo-production of J/ψ at very low p_{T} ($p_{\mathrm{T}} < 0.3$ GeV/c), with photons emitted from the two Pb nuclei, was expected to be the main production mechanism in ultra-peripheral collisions (UPC), where the two Pb ions do not break [147]. Typically, in UPC events the virtual photon (γ^*) emitted by one Pb may fluctuate into $c\bar{c}$ pairs, and then scatter off (with a single pomeron exchange) on the other Pb, and emerge as J/ψ.

Recently, an excess in the J/ψ production was observed at very low-p_{T} in peripheral hadronic Pb–Pb collisions at the LHC [127], where an enhancement of the R_{AA} up to 10 was observed, for p_{T} below 0.3 GeV/c. Up to now, this J/ψ excess in hadronic Pb–Pb cannot be explained by hadronic production with the currently known cold and hot medium effects. Hence, the photoproduction could be a significant J/ψ production mechanism in peripheral Pb–Pb collisions.

Figure 5.19 shows the p_{T} distribution of dimuons in various centrality intervals, selections on $M_{\mu\mu}$ were applied inside and outside the J/ψ mass range, in order to study the background (with photon decaying into dimuon). The significance of the J/ψ excess (fitted in red curves) is marginal for central and non-central collisions compared to the hadronic contribution, however it becomes significant beyond ~30% of centrality (with significance higher than 3σ). The J/ψ excess is denoted as the non-hadronic production represented by the photoproduction (coherent and incoherent part). In 70–90% centrality interval, most of the J/ψ with $p_{\mathrm{T}} < 0.3$ GeV/c in Pb–Pb collisions are expected to be produced by photoproduction (significance of the J/ψ excess is around 15σ).

The conventional anisotropy observed in Pb–Pb arises from the anisotropy of the initial collision geometry that get transformed through strong parton-medium interactions. In principle, the v_2 of all particles species (including J/ψ) originate from hadronic production converges to 0, when p_{T} goes to 0. It was expected by some theorists [148] that some interference between J/ψ photoproduction amplitudes on ions moving in opposite direction could lead to additional modulations in the azimuthal particle distribution, an then to non zero v_2. This anisotropy related to

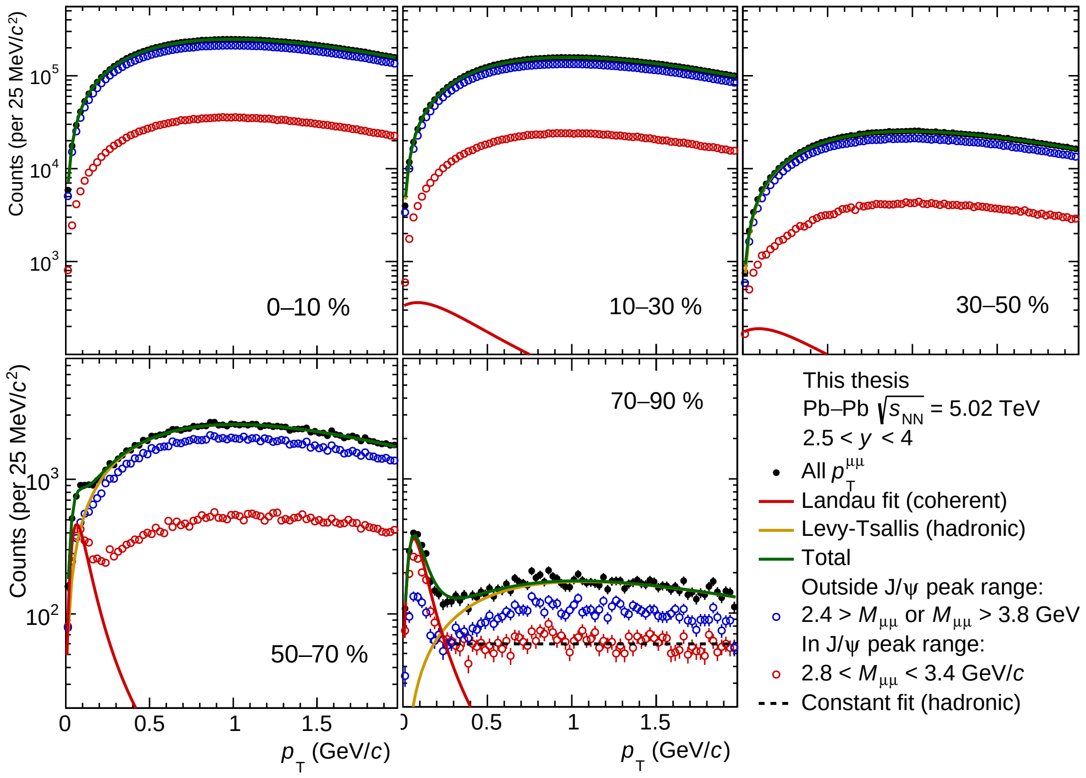

Figure 5.19: Low-p_T p_T distribution in the J/ψ mass region. Data are fitted with common Levy-Tsallis (hadronic) and Landau (coherent) functions.

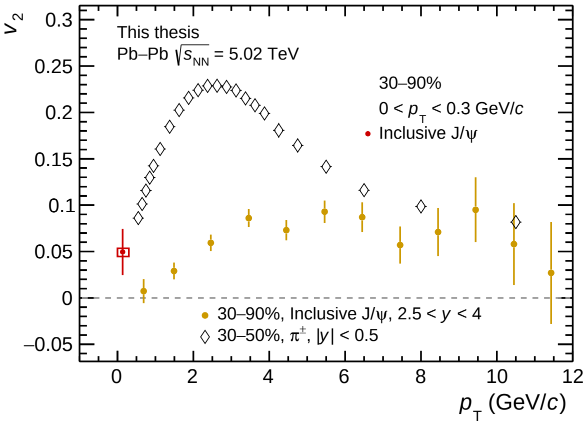

Figure 5.20: Extraction of J/ψ v_2 at very low-p_T p_T in 30–90% centrality interval, corresponding to non-central and peripheral Pb–Pb collisions.

the coherent J/ψ originates from the asymmetric density profiles of the emitters convoluted with the interference effects. It was also suggested that the J/ψ angular distributions measurement with respect to the reaction plane in different centrality classes could provide an additional handle to distinguish coherently produced J/ψ from ones produced in hadronic interactions.

Figure 5.20 shows the measured J/ψ v_2 at very low p_T ($p_T < 0.3$ GeV/c) in a large centrality interval corresponding to 30–90%. Similar measurement is obtained for 50–90%, while it is statistically limited for 70–90%. One has to notice that this peripheral Pb–Pb region is also corresponding to low R_n values (which are poorly determined). This v_2 of photoproduced J/ψ is found to be positive by 1.9 σ but no strong statements on the possible non-zero value can be drawn due to the large uncertainties. This measurement is worth to be pursued in the futur, especially with the expected increase in integrated luminosity for the Run 3.

5.2 First results of $\Upsilon(1S)$ v_2

This section is focuses on the presentation of the results of the $\Upsilon(1S)$ v_2 in Pb–Pb collisions at 5.02 TeV, using the full Run 2 data set.

5.2.1 p_T- and centrality-differential v_2

Figure 5.21 (left panel) shows the $\Upsilon(1S)$ v_2 coefficient as a function of p_T in the 5–60% centrality interval. The central (0–5%) and peripheral (60–100%) collisions are not considered as the eccentricity of the initial collision geometry is small for the former and the signal yield is low in the latter. The p_T intervals are 0–3, 3–6, and 6–15 GeV/c and the points are located at the average p_T of the reconstructed $\Upsilon(1S)$ uncorrected for detector acceptance and efficiency. The $\Upsilon(1S)$ v_2 values in the three p_T intervals are found to be lower, albeit with large uncertainties, compared to those of the inclusive J/ψ measured in the same centrality and p_T intervals.

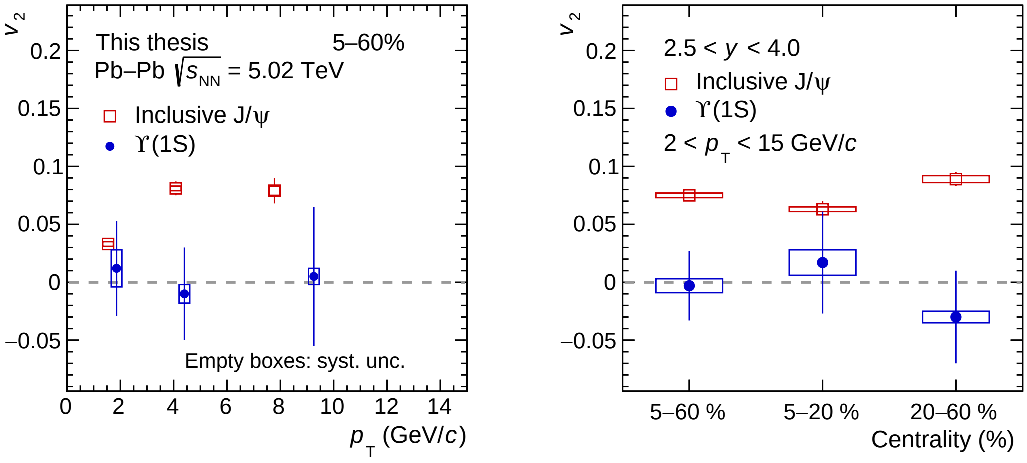

Figure 5.21: Left: $\Upsilon(1S)$ v_2 as a function of p_T in 5–60%, compared to the J/ψ data. Right: $\Upsilon(1S)$ v_2 for three centrality intervals, compared to the J/ψ data.

Although expected, the Υ(1S) v_2 is compatible with 0, and it is the first measured particle at the LHC for which v_2 is zero.

Given that any v_2 originating either from recombination or from path-length dependent dissociation vanishes at zero p_{T}, the observed difference between Υ(1S) and J/ψ v_2 is quantified by performing the p_{T}-integrated measurement excluding the low p_{T} range. Figure 5.21 (right panel) presents the Υ(1S) v_2 coefficient integrated over the transverse momentum range $2 < p_{\mathrm{T}} < 15$ GeV/c for three centrality intervals compared with that of the inclusive J/ψ. The Υ(1S) v_2 is found to be $-0.003 \pm 0.030(\mathrm{stat}) \pm 0.006(\mathrm{syst})$ in the $2 < p_{\mathrm{T}} < 15$ GeV/c and 5–60% centrality interval. This value is lower than the corresponding J/ψ v_2 by 2.6σ.

This observation, coupled to the different measured centrality and p_{T} dependence of the Υ(1S) and J/ψ suppression in Pb–Pb collisions at the LHC [78, 88], can be interpreted within the models used for comparison as a sign that unlike Υ(1S), J/ψ production has a significant regeneration component. Nevertheless, no firm conclusions can be drawn, given that currently the transport models cannot explain the significant J/ψ v_2 for $p_{\mathrm{T}} > 4$ GeV/c observed in the data.

5.2.2 Comparison to current theoretical models

Figure 5.22 shows the Υ(1S) v_2 coefficient as a function of p_{T} in the 5–60% centrality interval, compared with available theoretical calculations. The results are compatible with zero and with the small positive values predicted by the models within uncertainties.

The KSU-BBJS model (Fig. 5.22, right panel) is a hydro-dynamical model which only considers the path-length dependent dissociation of initially-created bottomonia inside the QGP medium [90]. The TAMU model (Fig. 5.22, left panel) incorporates, in addition, a small regeneration component originating from the recombination of (partially) thermalized bottom quarks [83]. Given that the regeneration component produces practically negligible contribution to the total Υ(1S) v_2, the differences between the KSU-BBJS and TAMU models are marginal.

For the Υ(2S), due to lower binding energies or radius, in TAMU the regeneration component is predicted to be larger compared to the ground state, as suggested by the green curves in Fig. 5.22 (left panel). Recently, CMS has presented the first measurement of Υ(2S) v_2 [149], which is also compatible with 0 (albeit large uncertainties). For the future Run 3, this Υ(2S) flow measurement should bring additional constraints on transport and hydrodynamical models for bottomonia, which have now produced a large variety of calculations [150–152].

Figure 5.22 (right panel) shows also a simultaneous blast-wave fit [153] to particle (only pions and protons) yields and v_2, then the scaled curve for Υ(1S) v_2 is plotted. Over the full available p_{T} range, the Υ(1S) v_2 data is described by the prediction based on the fit to lighter particles. This prediction shows that, due to the large Υ(1S) mass, a sizable v_2 is only expected at transverse momenta above 10 GeV/c.

It is worth noting that although the quoted model predictions are for mid-rapidity, they remain valid also for the rapidity range of the measurement within the

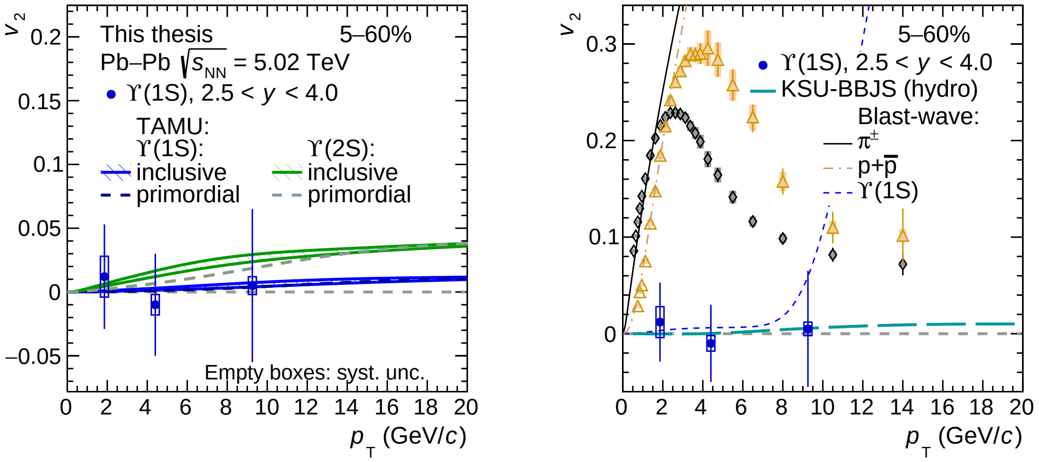

Figure 5.22: Model comparisons with the Υ(1S) v_2 results as a function of p_T in the 5–60% centrality interval.

theoretical uncertainties. Indeed the fractions of regenerated and initially-produced Υ(1S) are very close at mid- and forward rapidities [83]. In addition, the QGP medium evolution is also similar between mid- and forward rapidities, given the weak rapidity dependence of the charged-particle multiplicity density [154]. The presented Υ(1S) v_2 result is coherent with the measured Υ(1S) suppression in Pb–Pb collisions [88], as the level of suppression is also fairly well reproduced by the KSU-BBJS model and the TAMU model including or excluding a regeneration component.

Therefore, the result is in agreement with a scenario in which the predominant mechanism affecting Υ(1S) production in Pb–Pb collisions at LHC energies is the dissociation limited to the early stage of the collision. It is interesting to note that the presented Υ(1S) v_2 results are reminiscent of the corresponding charmonia measurements in Au–Au collisions at RHIC [155], where so far non-observation of significant v_2 is commonly interpreted as a sign of a small regeneration component from recombination of thermalized charm quarks at lower RHIC energies.

5.3 Investigating the coalescence mechanism

This section presents a study of the open-charm and open-beauty meson v_n based on the hidden charm (J/ψ) and beauty (Υ(1S)) results already presented in this manuscript. This work was initiated by other analyzers and it was first presented in our paper [156].

5.3.1 Light and heavy-quark v_n distribution

Basically, the hadronization via quark coalescence considers that the relevant degrees of freedom are not free partons but massive valence quarks. Gluons are assumed to have converted to quarks, therefore there are no dynamical gluons considered. This quark coalescence mechanism enhances the hadron v_2 at large p_T relative to that of partons at the same transverse momentum [157]. The saturation and eventual decrease of v_2 at high-p_T has been also demonstrated as a consequence of finite inelastic parton energy loss [158, 159].

Besides particle spectra, coalescence is also applicable to anisotropic flow. The flow of light and strange particles was shown to approximately scale with the number of constituent quarks (NCQ scaling) at both RHIC and LHC energies [160, 161]. This was typically interpreted to arise naturally in hadronization scenarios based on quark coalescence in which the flow of bound mesons and baryons depends solely on the collective flow of light and strange quarks (assumed to be identical) and the number of valence quarks [157, 162]. The comparison between pions, D meson, and J/ψ v_n are consistent with the number of constituent quark (NCQ) scaling, which tells that if hadrons inherit flow developed at quark level in the deconfined phase, then $v(qqq)/3 = v(qq)/2$.

In this formalism, one can define the azimuthal distributions of produced pions using the common Fourier series [163]. Within the assumption that the meson distribution function is a convolution between the two single quark distributions, ignoring the normalization, and taking $\Psi_\mathrm{RP} = 0$, one can obtain for example the pion (π^+) v_n distribution as

$$\begin{aligned}
v_n^{\pi^+} &= \int\int\int \mathrm{d}\varphi^u \mathrm{d}\varphi^{\bar{d}} \mathrm{d}\varphi^{\pi^+} \cos(2\varphi^{\pi^+})\Big(1 + 2v_n^u \cos(2\varphi^u)\Big) \\
&\qquad\qquad \times \Big(1 + 2v_n^{\bar{d}} \cos(2\varphi^{\bar{d}})\Big)\delta(\varphi^{\pi^+} - \varphi^u)\delta(\varphi^{\pi^+} - \varphi^{\bar{d}}) \\
&= \int \mathrm{d}\varphi^{\pi^+} \cos(2\varphi^{\pi^+})\Big(1 + 2v_n^u \cos(2\varphi^u)\Big)\Big(1 + 2v_n^{\bar{d}} \cos(2\varphi^{\bar{d}})\Big) \\
&\approx \int \mathrm{d}\varphi^{\pi^+} \cos(2\varphi^{\pi^+})(2v_n^u + 2v_n^{\bar{d}}) \cos(2\varphi^{\pi^+}) \\
&= v_n^u + v_n^{\bar{d}}.
\end{aligned} \tag{5.4}$$

Here, the δ functions are there to enforce coalescence, and the higher-order term $v_n^u v_n^{\bar{d}}$ has been ignored, assuming $v_n \ll 1$. In the case of charmed hadrons, the NCQ scaling assuming a flavor independent flow would obviously not work due to the large observed differences between the flow of light-flavor particles, D and J/ψ mesons. However, one can extend this scaling by assuming that the much heavier charm quark has a different flow magnitude [164] and that it can be derived from the flow of the J/ψ via the usual NCQ formula,

$$v_\mathrm{n}^{\mathrm{J}/\psi}(p_\mathrm{T}^{\mathrm{J}/\psi}) = 2 \cdot v_\mathrm{n}^\mathrm{c}(p_\mathrm{T}^{\mathrm{J}/\psi}/2). \tag{5.5}$$

Then, if the momentum conservation is satisfied, it is straightforward to show that the flow of the D meson can be constructed as the sum of the flow coefficients for light ($q = u$ or d) and charm quarks as

$$v_\mathrm{n}^\mathrm{D}(p_\mathrm{T}^\mathrm{D}) = v_\mathrm{n}^\mathrm{q}(p_\mathrm{T}^\mathrm{q}) + v_\mathrm{n}^\mathrm{c}(p_\mathrm{T}^\mathrm{c}), \tag{5.6}$$

where p_T^q and p_T^c are the p_T of the light and charm quarks, respectively, corresponding to the D-meson p_T, p_T^D. The light quark flow is obtained by interpolating the measured charged pion flow using $v_\mathrm{n}^\pi(p_\mathrm{T}^\pi) = 2 \cdot v_\mathrm{n}^\mathrm{q}(p_\mathrm{T}^\pi/2)$.

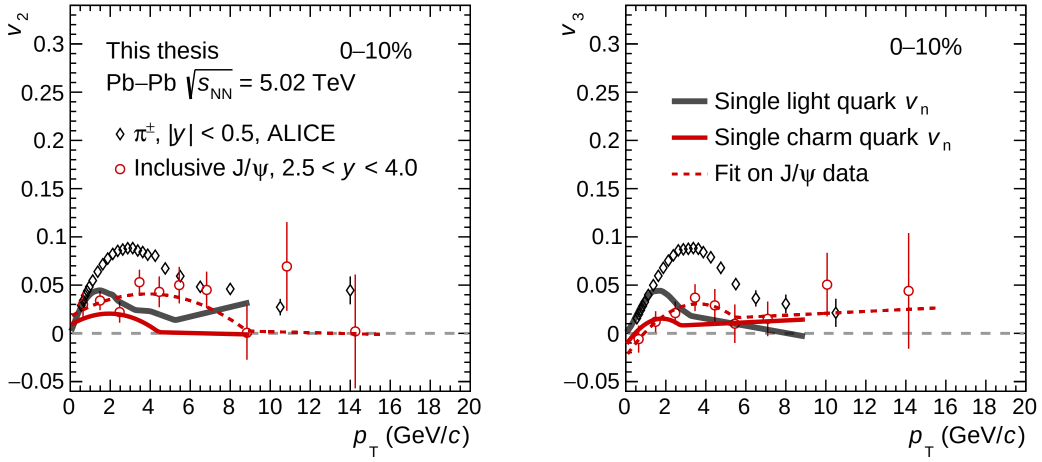

Figure 5.23: Single light and charm quark v_2 (left) and v_3 (right) distribution as a function of p_T, extracted from $\pi^{\pm}$ and J/ψ v_n, for the 0–10% centrality interval.

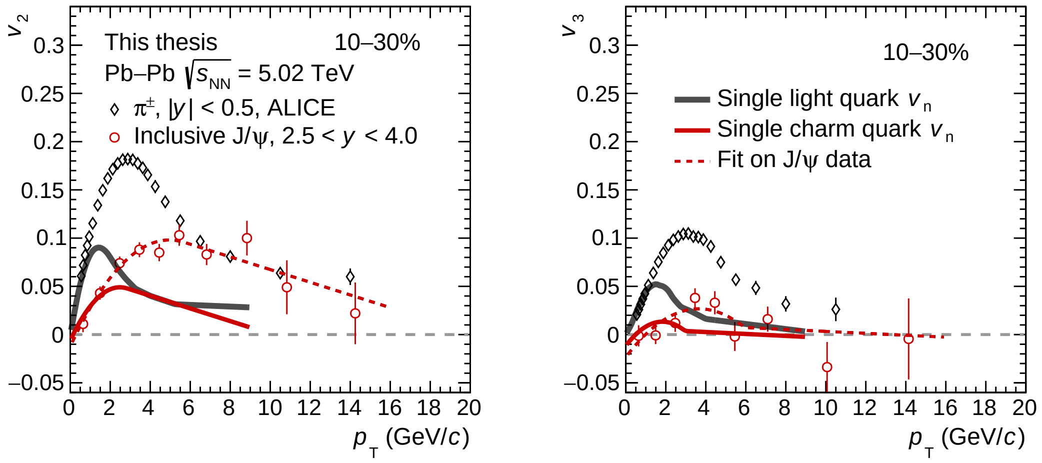

Figure 5.24: Single light and charm quark v_2 (left) and v_3 (right) distribution as a function of p_T, extracted from $\pi^{\pm}$ and J/ψ v_n, for the 10–30% centrality interval.

Figure 5.23, Fig. 5.24, and Fig. 5.25 show the single light and charm quark v_2 (left panels) and v_3 (right panels) as a function of p_T, for the 0-10%, 10-30%, and 30-50% centrality intervals, derived from the measured pions and J/ψ v_n, assuming the above described procedure. The red dashed curves show fits to the J/ψ v_n employing an ad-hoc function (a third order polynomial at low p_T and a linear function at high p_T) used to extract the flow of charm quarks needed to obtain the scaled D-meson flow according to Eq. (5.6). Then, the obtained black and red curves corresponding to the single light and charm quark flow will be used in order to construct the D meson v_n, where different assumptions can be formulated on the p_T sharing fraction

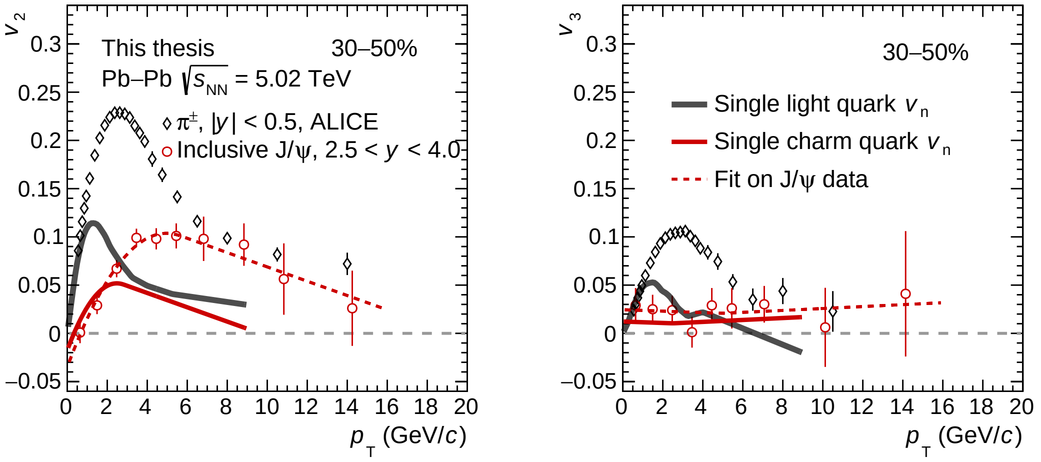

Figure 5.25: Single light and charm quark v_2 (left) and v_3 (right) distribution as a function of p_{T}, extracted from $\pi^{\pm}$ and J/ψ v_n, for the 30–50% centrality interval.

between the light and the charm quark.

5.3.2 Scaled D meson v_{n}

Figure 5.26, Fig. 5.27, and Fig. 5.28, show a comparison of the D-meson v_2 and v_3 as a function of p_{T}, derived assuming the above described procedure, to the measured D-meson v_{n} from CMS [129]. This approach is based on the simple quark coalescence mechanism where the relevant degrees of freedom are only the light and charm quarks.

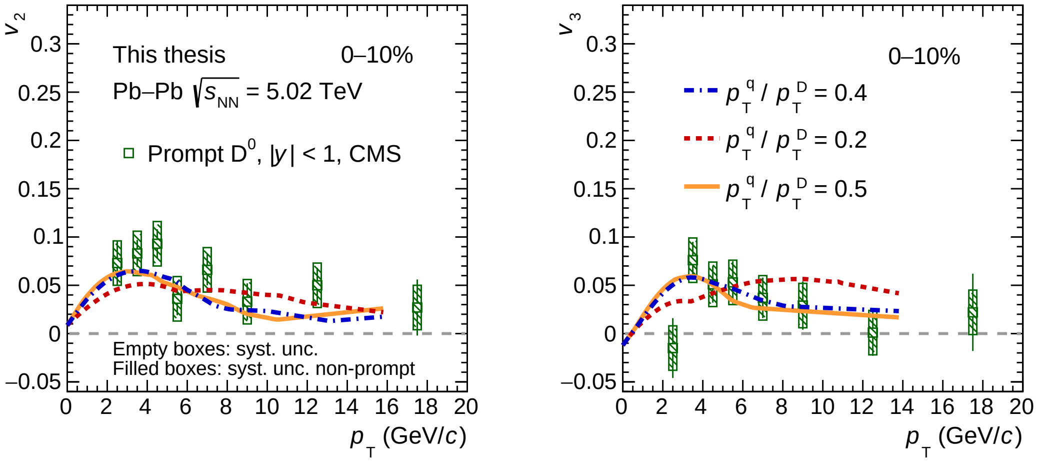

Figure 5.26: Scaled D meson v_2 (left) and v_3 (right) distribution as a function of p_{T}, constructed from $\pi^{\pm}$ and J/ψ v_n, for the 0–10% centrality interval.

The scaled D-meson flow is found to be very sensitive to the fraction of p_{T} carried by each of the constituent quarks. In coalescence-like models, constituent quarks must have equal velocities which leads to a sharing of the D-meson p_{T} proportional to the effective quark masses. This implies that by far the largest fraction of p_{T} should be carried by the charm quark.

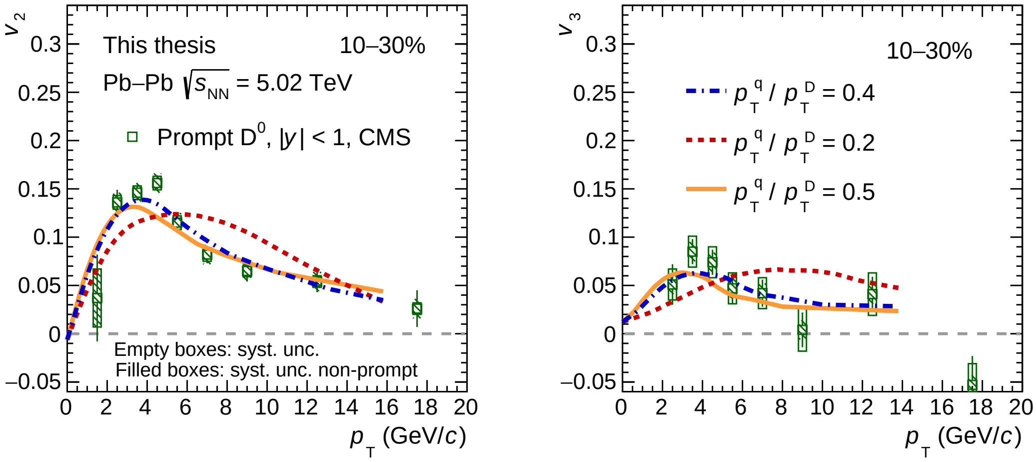

Figure 5.27: Scaled D meson v_2 (left) and v_3 (right) distribution as a function of p_{T}, constructed from $\pi^{\pm}$ and J/ψ v_n, for the 10–30% centrality interval.

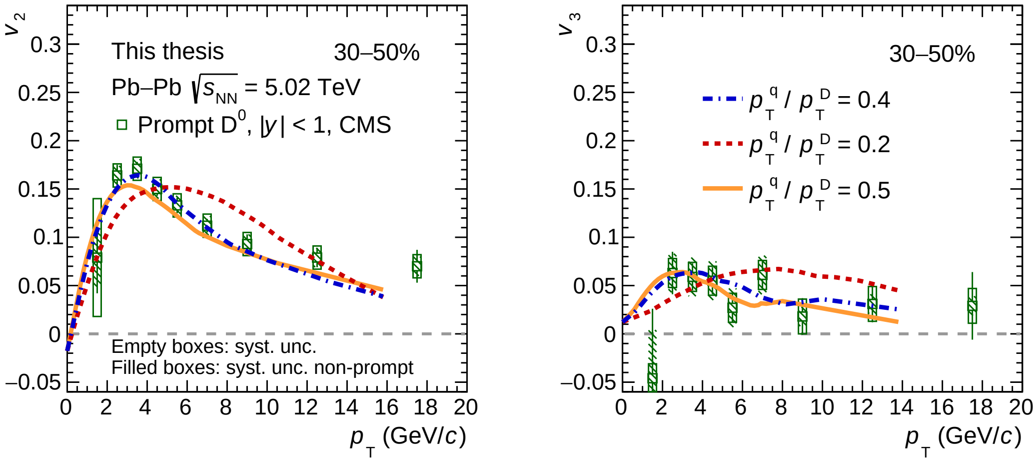

Figure 5.28: Scaled D meson v_2 (left) and v_3 (right) distribution as a function of p_{T}, constructed from $\pi^{\pm}$ and J/ψ v_n, for the 30–50% centrality interval.

Based on the simplistic and naive approach described here, a p_{T} sharing between light and charm quarks [164, 165] where the ratio $p_{\mathrm{T}}^{\mathrm{q}}/p_{\mathrm{T}}^{\mathrm{D}} = 0.2$ (red dotted curve), is clearly disfavored by the data. Surprisingly, it was found that a good description of the D-meson flow measurements, as illustrated by the blue dotted and orange curves in Fig. 5.26, Fig. 5.27, and Fig. 5.28, is obtained when the light quark carries a relatively large fraction of the D-meson p_T.

The best agreement with the D-meson CMS data is obtained when the light-quark p_T fraction has a value of $p_\mathrm{T}^\mathrm{q}/p_\mathrm{T}^\mathrm{D} = 0.4$ (blue dotted curve), but a rather good description of the data is observed also when assuming that the light and charm quarks share equally the D-meson p_T (green curve). Within uncertainties, the scaling seems to work well for both v_2 and v_3 over the entire covered p_T range and in all centrality intervals.

5.3.3 Scaled B meson v_2

Similarly, the B-meson v_2 can be constructed using pions and $\Upsilon(1\mathrm{S})$ v_2 data. The same coalescence mechanism approach implies that by far the largest fraction of p_T should be carried by the beauty quark. The $\Upsilon(1\mathrm{S})$ v_2 results are fitted using the same ad-hoc functions described by a second order polynomial at low p_T, and first order polynomial at high p_T. The B-meson v_2 is build from light and beauty quark flow, by assuming different fraction of $p_\mathrm{T}^\mathrm{q}/p_\mathrm{T}^\mathrm{B}$. Figure 5.29 shows the results of single light and beauty quark flow (left panel), and the scaled B-meson v_2 plotted with different p_T sharing fraction.

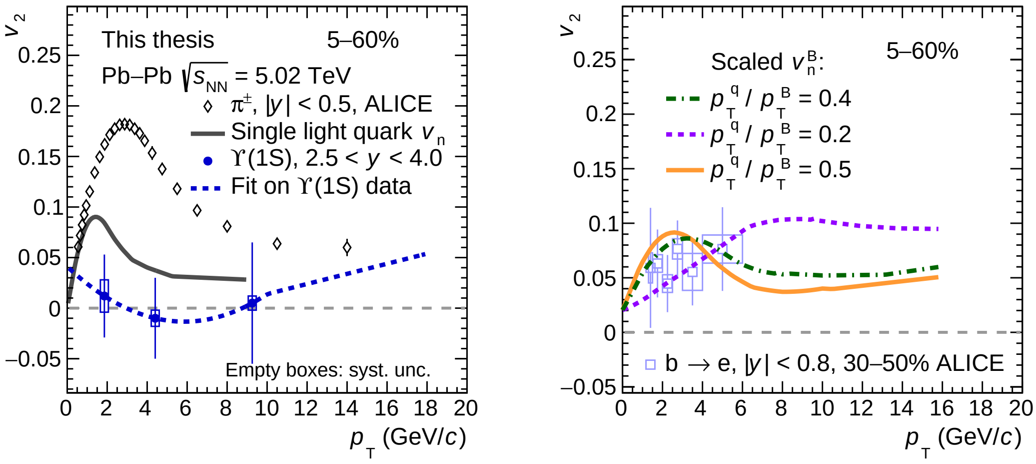

Figure 5.29: Scaled B meson v_2 (right) distribution as a function of p_T, constructed from $\pi^\pm$ and $\Upsilon(1\mathrm{S})$ v_2, for the 5–60% centrality interval.

Given that no B meson v_2 data are yet available, one decides simply to compare the obtained scaled curves to the recent result of the v_2 of electrons from b-hadron decays at midrapidity, extracted in 30–50% [166], which are different than those only originated from B-mesons. This exploratory work is not supposed to draw any firm conclusions or even predictions. Despite that large uncertainties are associated to the current $\Upsilon(1\mathrm{S})$ v_2 data (and the number of p_T bins is not sufficient to perform a reasonable fit), the scaled B-meson v_2 which corresponds to a coalescence scenario between a flowing light quark and a beauty quark (which seems to not flow), reproduces rather well the magnitude of the v_2 of electron from b-hadron decays (even taking the assumption of constant fit for $\Upsilon(1S)$ v_2).

5.4 Global picture: from light, to charm, to beauty flavor

At low or intermediate p_T, the v_2 of electrons from B meson decays and the $\Upsilon(1S)$ v_2 are both expected to be lower than the v_2 of closed charm (J/ψ) and open charm (D mesons), which are themselves measured to be lower than the v_2 of light flavor particles. In a certain sense these beauty elliptic flow measurements close the measurement concerning the flow of particles with different masses and flavors, from the lightest at a maximal v_2, to the charm, and to heaviest and beauty at a minimal v_2. Figure 5.30 shows the compilation of the v_2 measurements in non-central Pb–Pb collisions for different particle species.

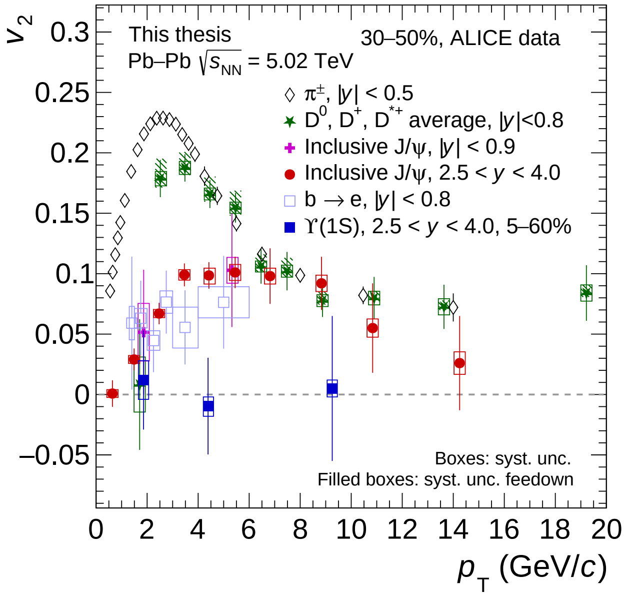

Figure 5.30: Comparison of v_2 of different particles in non-central Pb–Pb collisions, from the lightest to the heaviest one (based on full ALICE published measurements, $\pi^{\pm}$ from [34], D from [167], $b \to e$ from [166]).

Therefore, the following points can be formulated:

- At low p_T ($p_T < 3$ GeV/c): the mass ordering visible is consistent with hydrodynamics, which suggests that the (partially) thermalized heavy and light quark evolve in a common velocity field.

- At intermediate p_{T} ($3 < p_{\mathrm{T}} < 6$ GeV/c): the mass hierarchy already observed between light and charm flavor is extended to beauty flavor. Figure 5.30 suggests that $v_2^{\pi} > v_2^{D} > v_2^{\mathrm{J}/\psi} \gtrsim v_2^{b\rightarrow e} > v_2^{\Upsilon(1\mathrm{S})}$. For D meson, this ordering is in agreement with the scenario of heavy quark hadronization via coalescence with a flowing light quark. For J/ψ, as for low p_{T}, the measurement strongly supports the picture where two charm quarks (partially) thermalized and potentially flowing with the medium, recombine to form a J/ψ. While for Υ(1S), the measurement is consistent with $v_2^{\Upsilon(1\mathrm{S})} \approx 0$, and with the scenario where the beauty quarks do not seem to acquire flow from the medium.

- At high p_{T} ($p_{\mathrm{T}} > 6$ GeV/c), the picture is consistent with an universal path-length dependent energy loss mechanism for light and heavy quarks, which tends to group all v_2 into a single branch.

Figure 5.31 tries to illustrate in a very simplified picture, the sensitivity of different mesons (previously plotted in Fig. 5.30) to different stages of the collision, because J/ψ and Υ(1S) can be classified via their dissociation (or recombination) temperature and their binding energy. In this continuity, the D meson and pions can also be classified because of their different hadronic interaction cross section and also their binding radius. On the right panel, the simplistic evolution of the temperature of the QGP phase and its corresponding v_2 is plotted (based on results from [168] for T, and [169] for the momentum anisotropy), the suggested time intervals for the different meson sensitivities are also shown (in color bands).

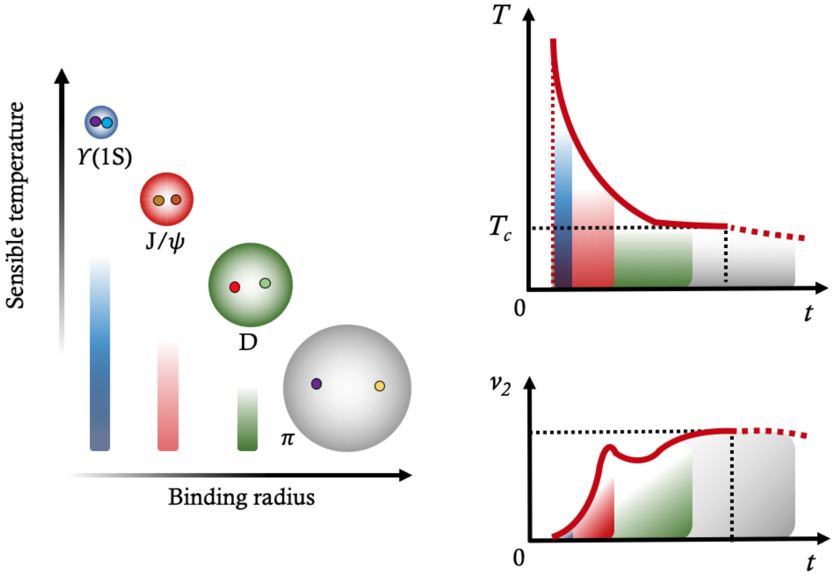

Figure 5.31: Sketch of the different mesons from light, to charm, to beauty flavor, and the time evolution of the QGP temperature and v_2 (very simplified picture).

Many complaints can be formulated to this simplified picture that addresses only one aspect of how mesons couple to the medium. Also, pions keep interacting hadronically and developing flow beyond $T_{\mathrm{c}} \approx 160$ MeV, and until the freeze-out temperature ($T_{\text{fo}} = 100$ MeV). However, what emerges from this sketch is the different time windows where each meson is expected to acquire flow from the medium evolution. Therefore, the Υ(1S) has the smallest time interval to develop flow from the medium, while J/ψ which acquires flow mainly from the recombination of partially thermalized charm quarks, probes a longer time interval. The D-meson resulting of the hadronization of a c and a light quark has an even longer time window to acquires flow, while the pions inherits its flow at the hadronization of the medium constituents and beyond. One can notice that the result of electrons from b-hadron decays should take place somewhere between those of Υ(1S) and J/ψ. This simplistic description could help in the understanding of the different magnitudes of v_2 at intermediate p_{T} as seen in the Fig.5.30.

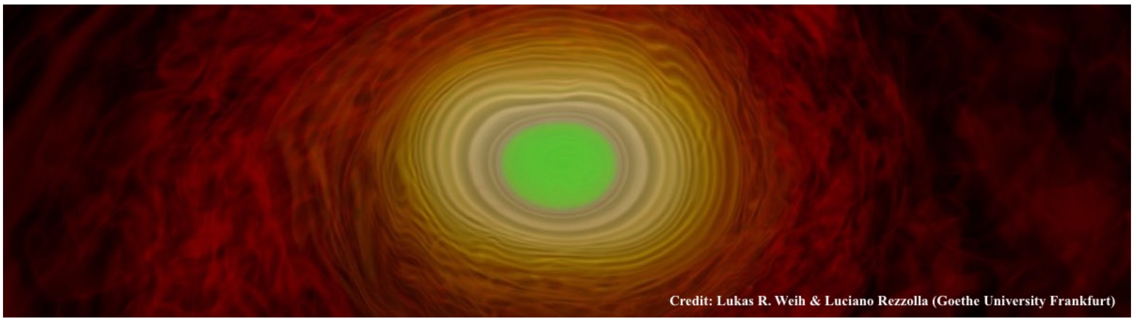
Credit: Lukas R. Weih & Luciano Rezzolla (Goethe University Frankfurt)

Conclusion and outlook

In this thesis manuscript, the inclusive J/ψ and Υ(1S) azimuthal anisotropy measurements performed at forward rapidity using the scalar product method were presented in Pb–Pb collisions at $\sqrt{s_{\rm NN}} = 5.02$ TeV with ALICE at the LHC. These results use available data from the full Run 2, and allow to describe more precisely the competition between the suppression and regeneration mechanisms involved in the charmonium and bottomonium production, originated by the presence of an extremely hot and dense nuclear matter. Since charm and bottom quarks are produced in the initial stages of the collision, it follows that quarkonium measurements offer us a unique access to the general properties of the QGP during its whole evolution.

In non-central Pb–Pb collisions, the J/ψ v_2 values are found to be positive up to the last $p_{\rm T}$ interval corresponding to $12 < p_{\rm T} < 20$ GeV/c and reach a maximum of approximately 0.1 around a $p_{\rm T}$ of 5 GeV/c. The J/ψ v_3 values at forward rapidity reach 0.04 around a $p_{\rm T}$ of 4 GeV/c and are positive in the 0–50% centrality interval for $2 < p_{\rm T} < 5$ GeV/c with a significance of 5.1 standard deviations. The mass hierarchy observed for v_2, $v_2^{\pi} > v_2^{D} > v_2^{{\rm J}/\psi}$ in the low-$p_{\rm T}$ range, as visible in Fig. 5.30, seems to also hold in the case of v_3 and will be the subject of more detailed studies with the Run 3 and Run 4 data. At high $p_{\rm T}$, the v_2 for all particles converge to similar values, suggesting that path-length dependent effects become dominant there. The measured J/ψ v_3/v_2 ratios exhibits the same hierarchy indicating that higher harmonics are damped faster for charmonia compared to lighter particles. The agreement found at low-$p_{\rm T}$ between J/ψ v_2 data compared to microscopic transport models favors the scenario which suggests that at LHC energy, almost all the initially created J/ψ are dissociated in the medium and a recombination of c and $\bar{c}$ quarks (regeneration) dominates the J/ψ production. However, the discrepancies visible at intermediate $p_{\rm T}$ suggest missing mechanisms in the current transport models trying to explain this v_2.

The $p_{\rm T}$-integrated v_2 coefficient in a low ($p_{\rm T} < 5$ GeV/c) and a high-$p_{\rm T}$ ($p_{\rm T} > 5$ GeV/c) region is in both cases dependent on centrality and reaches a maximum value of about 0.1, while the v_3 has no clear centrality dependence. Both J/ψ v_2 and v_3 coefficients, either at low-$p_{\rm T}$ or at high-$p_{\rm T}$ are found to be lower than the ones of charged pions at a $p_{\rm T}$ similar to the J/ψ average $p_{\rm T}$. At low $p_{\rm T}$, the ratio of the charged pions v_2 to those of $p_{\rm T}$-integrated J/ψ increase from central to peripheral collisions, compatible with a scenario in which charm quarks thermalize later than the light ones. At high $p_{\rm T}$, this ratio is compatible with unity without any statistically significant centrality dependence.

Using an extension of the well known number of constituent quark scaling, the measured charged pion and J/ψ v_n can be used as proxies in order to derive the D-meson v_2 and v_3 as a combination of the flow of light and charm quarks. Within this procedure, it is surprising to observe that the measured D meson v_2 and v_3 can be described if one considers that the light and charm quarks share similar fractions of the D-meson p_T, which is counterintuitive in a coalescence approach. The fact that such a simple scaling works suggests that the flow of charmonia and open charm mesons can be effectively explained assuming a common underlying charm quark flow in addition to the flow of light quarks.

The measurements presented show once again the intriguing results about the J/ψ flow story. It is a real challenge for theorists to be able to explain both the R_AA and v_2. In the future, and in particular during the Run 3, thanks to the major ALICE upgrades, the addition of the MFT detector to the Muon Spectrometer will allow us to discriminate prompt and non-prompt J/ψ on a large p_T range. The MFT will enable the separation of the prompt and non-prompt J/ψ contributions to the measured flow coefficients, thus providing valuable information on both the charmonium and open beauty hadron production dynamics. Moreover, the future increase of J/ψ candidates will allow to further constrain the theoretical calculations, first at low p_T to confirm the contribution of regenerated J/ψ, and secondly at high p_T where an universal path-length dependent energy loss is expected to produce similar v_n for any particle species (see Fig. 5.30).

The event-by-event fluctuations of v_2 are influenced by initial state fluctuations (mainly due to random positions of the colliding nucleons) at low p_T, and also by the variations of particle energy loss at high p_T. The magnitude of event-by-event fluctuations of flow harmonics from heavy-flavor quarks is not well understood, and it should be accessed via multiparticle correlation techniques involving four particles and more ($v_2\{n\}$, with $n \geq 4$, e.g. $v_2\{4\}$ means a correlation of the J/ψ with 3 other charged particles). To further investigate the origin of v_2 fluctuations, for example, it has been predicted that the ratio $v_2\{4\}/v_2\{2\}$ for high-p_T heavy-flavor particles is sensitive to energy loss fluctuations [163]. In the future, this kind of measurement for the J/ψ, compared to those of light flavor hadrons, and to those of prompt D^0 (already mesured [170]), should allow to bring new constraints on energy loss calculations.

The first measurement of the Υ(1S) v_2 coefficient in Pb–Pb collisions at $\sqrt{s_\mathrm{NN}} =$ 5.02 TeV is also presented in this manuscript. The measurement is performed in the 5–60% centrality interval within $0 < p_\mathrm{T} < 15$ GeV/c range at forward rapidity. The v_2 coefficient is compatible with zero and with the model predictions within uncertainties. Despite results are presented with large statistical uncertainties, the values are in agreement with a scenario where the $b\bar{b}$ bound state formation is limited to the first stages of the collision, when the temperature is extremely high and the created matter has not yet developed its collective flow. Excluding low p_T ($0 < p_\mathrm{T} <$ 2 GeV/c), Υ(1S) v_2 is found to be 2.6σ lower with respect to that of inclusive J/ψ. This measurement allows to extend the current mass hierarchy of v_2 to the beauty flavor, and to the heaviest particle measured, as $v_2^{\pi} > v_2^{D} > v_2^{\mathrm{J}/\psi} \gtrsim v_2^{b\rightarrow e} > v_2^{\Upsilon(1\mathrm{S})}$

visible in Fig. 5.30. The presented measurement opens the way for further studies of bottomonium flow using the future data samples from the LHC Runs 3 and 4 with an expected ten-fold increase in the number of Υ candidates [36].

Appendix A

Signal and background fit functions

Signal functions

The signal mass distribution is modelled with a extended Crystal Ball (CB) function represented by a Gausian core and two tails. The function takes seven parameters $f_{\mathrm{CB}}(N, \bar{x}, \sigma, \alpha, n, \alpha', n')$ corresponding to: a normalisation factor, a mean value, a width, and four tail parameters. This signal function can be defined as

$$f_{\mathrm{CB}} = N \cdot \begin{cases} \left(\frac{n}{|\alpha|}\right)^{n} \exp(-\frac{1}{2}|\alpha|^2)\Big(\left(\frac{n}{|\alpha|} - |\alpha| - X\right)^{-n}\Big), & \text{if } X < -\alpha \\ \exp\left(-\frac{1}{2}X^2\right), & \text{if } \alpha' > X > -\alpha \\ \left(\frac{n'}{|\alpha'|}\right)^{n'} \exp(-\frac{1}{2}|\alpha'|^2)\Big(\left(\frac{n'}{|\alpha'|} - |\alpha'| + X\right)^{-n'}\Big), & \text{if } X \geq \alpha' \end{cases} \tag{A.1}$$

with the introduced variable $X = (x - \bar{x})/\sigma$. The tail parameters of this function are fixed from MC or from pp data. In the following table, an example of these tail parameters for J/ψ and Υ(1S) signal in three different Pb–Pb centrality intervals, obtained after MC simulations, are presented.

J/ψ tails parameters: [α, n, α', n']

0-20%	20-40%	40-90%
[0.95, 3.81, 2.23, 1.77]	[0.93, 4.19, 2.13, 1.93]	[0.96, 3.78, 2.29, 2.11]

Υ(1S) tails parameters: [α, n, α', n']

0-20%	20-40%	40-90%
[0.90, 2.17, 1.83, 2.04]	[0.93, 2.14, 1.96, 2.10]	[0.95, 2.13, 2.03, 2.25]

In this context the excited states are also modelled by the same signal functions with different fixed tail parameters. Hence, the total signal function will be the sum of all independent CB functions. However, one can noticed that the function parameter of exctited states are often scaled (related to their mass ratio) to the obtained fit parameters of the 1S ground state.

An alternative signal function could be used in the fit of J/ψ mass distribution, which is originated from the NA60 experiment. This function has eleven parameters as $f_{\mathrm{NA60}}(N, \bar{x}, \sigma, \alpha^l, p_1^l, p_2^l, p_3^l, \alpha^r, p_1^r, p_2^r, p_3^r)$, which correspond to the normalisation factor, the mean and the width of the Gaussian core, and eight tail parameters. The function is defined as

$$f_{\mathrm{NA60}} = N \cdot \begin{cases} \exp(-\frac{1}{2}(X^2/(1+p_1^l(\alpha^l - X)^{p_2^l - p_3^l\sqrt{\alpha^l - X}})^2), & \text{if } X < \alpha^l \\ \exp\left(-\frac{1}{2}X^2\right), \quad \text{if } \alpha^l < X < -\alpha^r & \\ \exp(-\frac{1}{2}(X^2/(1+p_1^r(X - \alpha^l)^{p_2^r - p_3^r\sqrt{X-\alpha^r}})^2), & \text{if } X > \alpha^r \end{cases} \tag{A.2}$$

where $X = (x - \bar{x})/\sigma$ is the same variable previously defined.

Background functions

The background function of the mass distribution has several possible definition. In this thesis, the variable width Gaussian is used, this function contains four parameter as $f_{\mathrm{VWG}}(N, \bar{x}, \alpha, \beta)$, which correspond to the normalisation factor, the mean and the width Gaussian parameter, and a last parameter describing the linear mass dependence. The function is defined as

$$f_{\mathrm{VWG}} = N \cdot \exp(-\frac{1}{2}X^2) \tag{A.3}$$

where $X = (x - \bar{x})/\sigma$ and the mass dependant width $\sigma = \alpha + \beta(x - \bar{x})/\bar{x}$. In the quadratic variable width version, the definition of the width parameter is modified by adding a quadratic term proportional to a third parameter γ as $\sigma = \alpha + \beta(x - \bar{x})/\bar{x} + \gamma(x - \bar{x})^2/\bar{x}^2$..

The Chebyshev polynomial functions (up to order 5) could be also used in order to describe the background mass distribution. It can be formulated from the recurrence relation as

$$T_0(x) = 1, \qquad T_1(x) = x, \qquad T_{n+1}(x) = 2xT_n(x) - T_{n-1}(x), \tag{A.4}$$

where the ordinary generating function can be expressed as

$$\sum_{n=0}^{\infty} T_n(x)t^n = \frac{1 - tx}{1 - 2tx + t^2}. \tag{A.5}$$

Alternatively, standard polynomial functions are also used in the background fit. The common double exponential could also used in the fit of the background mass distribution. This later is commonly used in the bottomonium mass sector.

Appendix B

Alternative extraction: $_{s}\mathcal{P}$lot

Event-by-event invariant mass analysis

To handle an event-by-event signal extraction and no longer with histograms as above in this manuscript, one could use the $_{s}\mathcal{P}$lot `ROOT` package [128]. This technique was initially used to statistically subtract the background contribution from the signal sample, which was then weighted to reproduce the kinematic variables of the signal candidates. The use of $_{s}\mathcal{W}$eights relies on the assumptions of the $_{s}\mathcal{P}$lot formalism, namely that the parameterising variables are uncorrelated to the fit variables.

As example, we consider the measurement of the Υ(1S) elliptic flow v_2 at the LHC. In this case the discriminating variable is the invariant mass m, while the variable of interest is the $\cos\Delta\phi = \cos 2(\phi_{\Upsilon} - \phi_{ref})$. The angle ϕ_{Υ} represents the azimuthal angle of the Υ(1S) candidate and the reference angle ϕ_{ref} is the standard symmetry plane, which can be defined as zero (in our case of generated event). In order to demonstrate the approach, we generate toy data with a model for the underlying probability distributions. Since we are focusing on the statistical aspect and not the systematic uncertainties inherent of any fitting procedure with incomplete knowledge of the true underlying distributions, we consider the model used for the data generation as the fit model, and fix the model parameters (apart from the signal and the background yield). The signal mass distribution is modelled with a Crystal Ball function (with only one tail)

$$f_{\text{CB}}(x; M, \sigma, \alpha, n) = \begin{cases} \dfrac{\left(\frac{n}{|\alpha|}\right)^n e^{-\frac{1}{2}\alpha^2}}{\left(\frac{n}{|\alpha|} - |\alpha| - \frac{x-M}{\sigma}\right)^n}, & \text{if } \frac{x-M}{\sigma} < -|\alpha| \\ \exp\left(-\frac{1}{2}\left(\frac{x-M}{\sigma}\right)^2\right), & \text{if } \frac{x-M}{\sigma} \geq -|\alpha|. \end{cases} \tag{B.1}$$

The Gaussian width is chosen to be $\sigma = 0.13$ GeV/c^2, the parameter $\alpha = 0.82$ and the power-law tail $n = 2.44$. These values are typical for LHC energies and are taken from Ref. [88].

The azimuthal distribution of the signal is drawn from an event-by-event flow distribution according to the common formula from [171], in our case only the highest harmonic $n = 2$ is kept

$$f(\Delta\phi) = 1 + 2v_2 \cos(\Delta\phi). \tag{B.2}$$

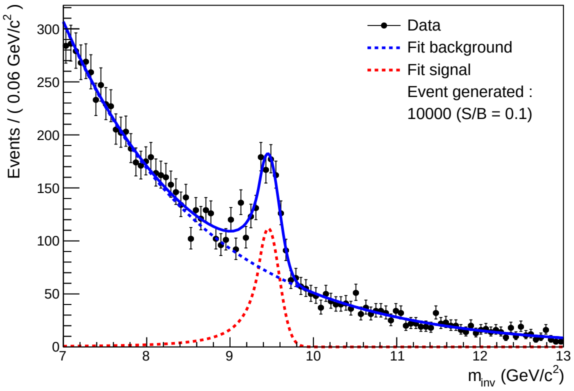

Figure B.1: The invariant mass distribution with the background and signal components from the log-likelihood fit superimposed.

The v_2 of the signal is generated with a value of 0.01. We consider candidates in a invariant mass range of $m \in [7, 13]$ GeV/c^2. A simple exponential distribution is assumed for the background distribution as function of invariant mass $\propto e^{-\lambda m}$ with lambda fixed to -0.6. For the background azimuthal anisotropy, a constant v_2 value of 0.03 is assumed. The toy data is generated with a signal over background over the full invariant mass range of 0.1. After the generation, a unbinned log-likelihood fit to the data with `RooFit` is done. The generated data and the fit with the background and the signal component are shown in Fig. B.1.

After the fit is performed, ${}_s\mathcal{W}$eights are retrieved and used to extract the v_2 as average over all events. The resulting distributions compared to the generated input distribution is shown and the pulls w.r.t. this distribution in Fig. B.2 for the observable of interest are shown. The input distributions are reproduced within the statistical uncertainties of the fit.

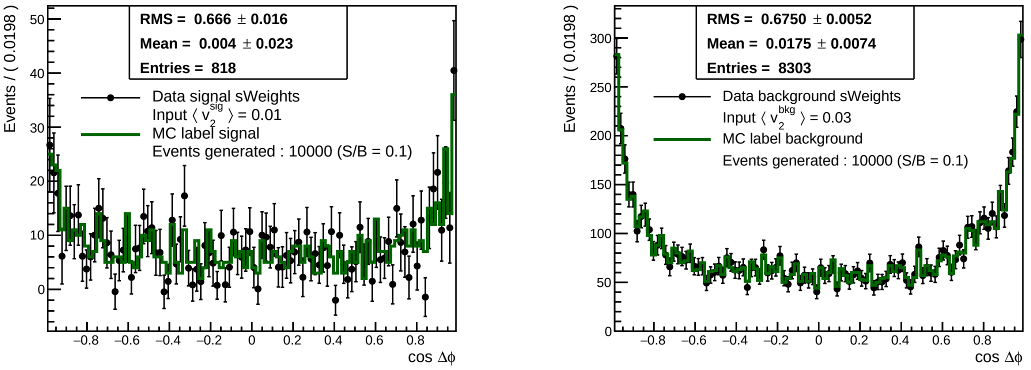

Figure B.2: Visualization of the $\cos \Delta\phi$ distribution signal and background respectively. The mean value correspond to the first moment of the distribution and in this case is represent the v_2 accompanied of his statistical uncertainty.

For the smallest data set investigated, the mean value of the true distribution that is put in amounts to 0.01, the mean value of the fitted signal component amounts to 0.004± 0.023. The background yields to a larger statistical uncertainty. In this part, the background flow is generated following a constant distribution as function of mass, and it represent a specific case in the v_2 extraction.

The case of mass dependent background flow: full 2-dimensional fit

In general, the background azimuthal anisotropy under the signal peak and in its vicinity can have significant mass dependence. This mass dependence can originate from different sources, the background composition as well as changing kinematics affecting the elliptic flow of specific background components. If the v_n measurement based on an invariant mass analysis depends strongly on the value of the background flow, the ${}_s\mathcal{W}$eights can yield to biases in the extraction. These biases can be avoided by a unbinned multidimensional 2D log-likelihood fit on the invariant mass distribution versus the event by event flow distribution. In the following, we develop an simple case and compare with the outcome of the pure ${}_s\mathcal{W}$eights method presented in the previous paragraph. In our example the fits work because there is a unique probability distribution for signal and background component, in a most common cases this is not perfectly reproducible due to large kinematic and centrality bins as well as event-by-event fluctuations.

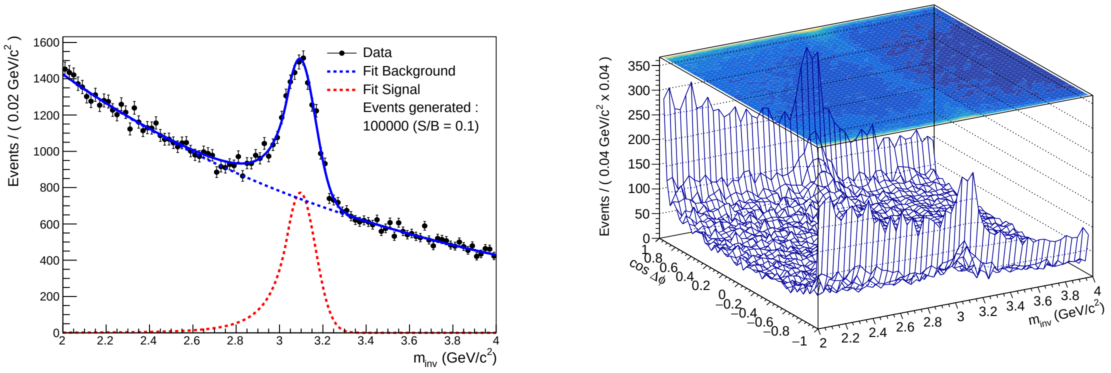

Figure B.3: (left) The invariant mass distribution with the background and signal components from the log-likelihood fit superimposed, in the J/ψ mass region. (right) Visualization of the $\cos\Delta\phi$ vs. invariant mass distribution in the J/ψ mass region, with signal and background events generated.

In the case of J/ψ v_2 measurements, the background flow has been observed by ALICE to depend significantly on invariant mass [92]. In order to demonstrate the methodology, this example case is chosen. The signal and background events are generated following the distribution (B.2) with different mean v_2 corresponding to 0.1 for signal and 0.02 for background. For the background, the v_2 in (B.2) is parametrized as a function of mass with second order polynomial of the following form: $v_2(m) = a \cdot (m - m_0)^2 + b \cdot (m - m_0) + c$ where m_0 is the reference mass (here the J/ψ mass) with $a = 0.01, b = -0.01, c = 0.01$. The fitting model is equal to the generation model, where the fit parameter as function of invariant mass for the background are left free in the fit.

In the procedure, a 1D fit on the mass axis is performed first. In a second step, the $_s\mathcal{W}$eights are used to initialize the fit parameters in the $\cos(\Delta\phi)$ dimension. The 2D fit is performed using the product of the mass dependent function and $\cos\Delta\phi$ dependent function:

$$f(m, \cos\Delta\phi) = \sum_{s=0}^{N_s} w_s \cdot g_s(m) \cdot h_s(\cos\Delta\phi) \tag{B.3}$$

where N_s is the total number of species to introduce in the fit, s is the species, in our case their are only one signal and background component, w_s is the weight corresponding to the number of s events. The g_s and h_s are the functions corresponding to the invariant mass dependence and the $\cos(\Delta\phi)$ dependence corresponding to azimuthal correlations. For the v_2 measurement, we are only interested in the first moment of the final $\cos(\Delta\phi)$ distribution. Corresponding to the fit parameters, first

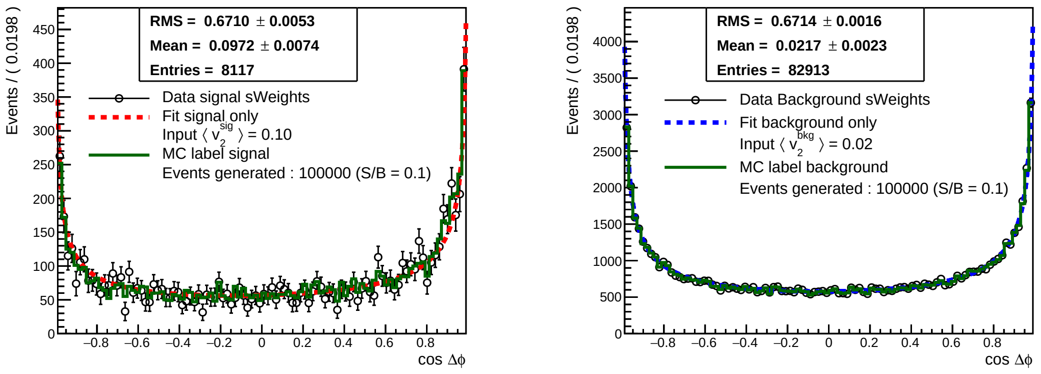

Figure B.4: Visualization of the $\cos\Delta\phi$ distribution signal and background respectively. (Left) The signal component are fitted in red corresponding to all signal candidates. (right) The background component is fitted in blue. The mean value of the $_s\mathcal{W}$eights data computed correspond to the $\langle v_2 \rangle$ for signal or background. Here, 10000 and 90000 signal and background events are generated from MC.

To find the appropriate probability distribution as a function of $\cos\Delta\phi = \zeta(\Delta\phi) = \zeta$ where $\zeta \in]-1; 1[$ that it will be used in the final fit, it is needed to change the variable that it used in the generation in (B.2). Applying the derivative of (B.2) to be able to change variable by ζ, it will give us the probability density function :

$$P(\zeta) = \frac{1 + 2v_2 \cdot \zeta}{2\sqrt{1-\zeta^2}} \tag{B.4}$$

which correspond to the $\cos\Delta\phi$ fit for signal and background component (need to replace the parameter by v_2^{sig} and $v_2^{\mathrm{bkg}}(m_{\mu\mu})$ shown with the $_s\mathcal{W}$eights computed data in Figure B.4.

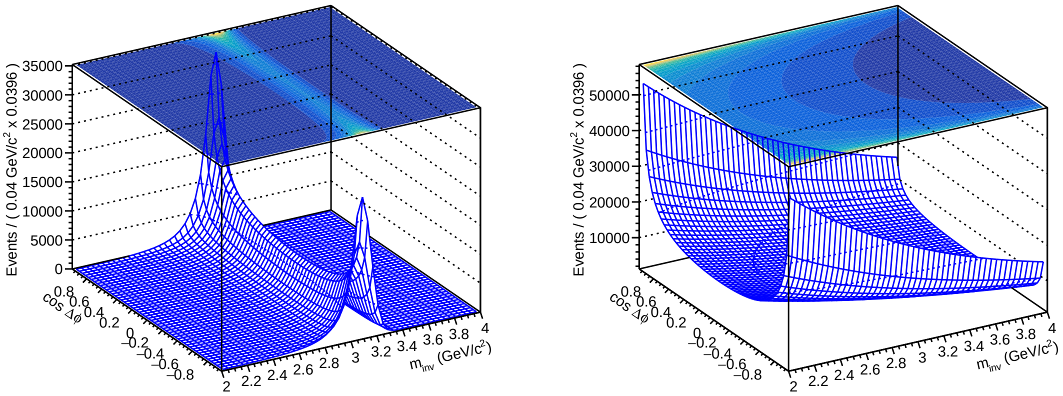

Figure B.5: Visualization of the signal and background model on the $\cos\Delta\phi$ vs. invariant mass distribution.

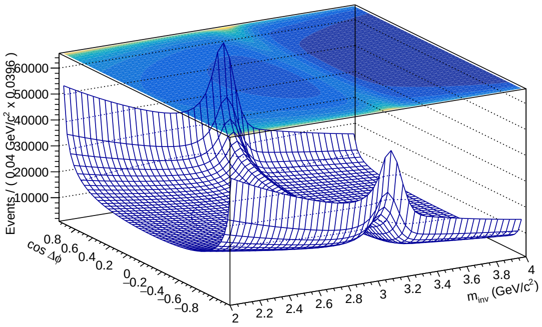

Figure B.6: Visualization of the model fitted on data generated which correspond to distribution signal and background component.

Appendix C

Prompt and non-prompt J/ψ v_n

At forward rapidity, the ALICE experiment does not have, yet, the capability to separate prompt and non-prompt J/ψ. At midrapidity, the two contributions can be separated but it is currently limited by statistics. The situation will clearly improve for ALICE in Runs 3 and 4 of the LHC due to the ongoing upgrades (addition of a silicon tracker in front of the muon spectrometer and faster readout).

One could estimate the difference between the v_n of prompt J/ψ (v_n^{prompt}) and the v_n of inclusive J/ψ (v_n) given the fraction f_B of non-prompt J/ψ over inclusive J/ψ and an hypothesis of the v_n of non-prompt J/ψ ($v_n^{\text{non-prompt}}$). The value of f_B can be taken from LHCb measurements [172]. The situation is more complicated for $v_n^{\text{non-prompt}}$ because the current measurements by ATLAS [173] and CMS [174] have large uncertainties and/or are limited to high p_T and to midrapidity only. The prompt contribution to the v_n is estimated as

$$v_n^{\text{prompt}} = \frac{v_n - f_B\, v_n^{\text{non-prompt}}}{1 - f_B}. \tag{C.1}$$

Recent ALICE results on the v_2 of electrons from the decay of beauty hadrons favour the lower values of $v_2^{\text{non-prompt}}$ [166]. With our best knowledge of $v_2^{\text{non-prompt}} \approx 0.04$, the difference between prompt and inclusive J/ψ v_2 is found to be small (see Appendix C for details).

For example CMS reports in 10–60% centrality at 2.76 TeV $v_2^{\text{non-prompt}} = 0.032 \pm 0.027$ (stat) ± 0.032 (syst) for $3 < p_\mathrm{T} < 6.5$ GeV/c and $1.6 < |y| < 2.4$, and $v_2^{\text{non-prompt}} = 0.096 \pm 0.073$ (stat) ± 0.035 (syst) for $6.5 < p_\mathrm{T} < 30$ GeV/c and $|y| < 2.4$) [174]. ATLAS reports at 5.02 TeV, $v_2^{\text{non-prompt}} \approx 0.035 \pm 0.02$ (stat) ± 0.01 (syst), $v_2^{\text{non-prompt}} \approx 0.04 \pm 0.02$ (stat) ± 0.01 (syst), and $v_2^{\text{non-prompt}} \approx 0.08 \pm 0.035$ (stat) ± 0.02 (syst), for $p_\mathrm{T} > 9$ GeV/c in the centrality classes 0–20%, 20–40%, and 40–60%, respectively [175]. Recent ALICE results on the v_2 of electrons from the decay of beauty hadrons favour the lower values of $v_2^{\text{non-prompt}}$ [166].

The table C.1 shows the difference between v_2^{prompt} and v_2^{inc}, at forward rapidity for 10–30% centrality, under several (extreme) hypotheses of $v_2^{\text{non-prompt}}$. With our best knowledge of $v_2^{\text{non-prompt}} \approx 0.04$ the difference between prompt and inclusive J/ψ v_2 is small.

Table C.1: Centrality 10–30%, difference between v_2^{prompt} and v_2^{inc}

p_{T} (GeV/c)	v_2^{inc}	f_B	$v_2^{\mathrm{npro}} = 0.10$	$v_2^{\mathrm{npro}} = 0.04$	$v_2^{\mathrm{npro}} = 0.00$
0.64	0.011 ± 0.009	0.0690	-0.007	-0.002	0.001
1.49	0.043 ± 0.007	0.0772	-0.005	0.000	0.004
2.47	0.074 ± 0.007	0.0883	-0.003	0.003	0.007
3.46	0.088 ± 0.008	0.1011	-0.001	0.005	0.010
4.45	0.085 ± 0.009	0.1154	-0.002	0.006	0.011
5.45	0.103 ± 0.011	0.1312	0.000	0.010	0.016
6.82	0.083 ± 0.011	0.1548	-0.003	0.008	0.015
8.84	0.100 ± 0.018	0.1926	-0.000	0.014	0.024
10.84	0.049 ± 0.028	0.2327	-0.015	0.003	0.015
14.25	0.022 ± 0.032	0.3035	-0.034	-0.008	0.010

Appendix D

Résumé en français

Chapter 1: introduction à la physique nucléaire de haute énergie

La matière peut être décrite par un assemblage de particules élémentaires et de leurs interactions fondamentales. Les hadrons tels que les protons et neutrons, sont composés de quarks et de gluons. Les premiers servent de briques élémentaires de matière, et les seconds agissent comme une forte glue entre les quarks. À basse énergie, cette interaction forte qui est représentée par l'échange de gluons entre les quarks permet de maintenir la cohésion du noyau atomique. La chromodynamique quantique (QCD) est la théorie qui décrit cette interaction en associant des charges de couleur aux quarks et gluons. À très haute énergie (ou très petites distances), QCD prédit que le couplage de l'interaction forte diminue et les quarks et les gluons ne sont plus confinés au sein des hadrons, cet état se nomme le plasma de quarks et de gluons (QGP).

Du fait des conditions extrêmes de température et de densité d'énergie atteintes, l'Univers primordial a probablement connu un tel état. Sur Terre, il est possible de recréer expérimentalement un tel état de la matière en réalisant des collisions d'ions lourd ultra-relativistes. Il existe différentes sondes pour étudier un tel milieu. Celles dites "douces", produites à la fin du refroidissment qui coïncide au mécanisme d'hadronisation, et permettent de mieux connaître les propriétés générales du système, et puis celles dites "dures", créés dans les premiers moments de la collision, et qui permettent de sonder les propriétées microscopique du milieu durant toute son évolution. Une des propriétés intriguante du QGP est son comportement hydrodynamique, étudié grâce au mesures d'écoulement anisotropique dans le plan transverse, tels que le flot elliptique (v_2) et triangulaire (v_3). Le v_2 est assimilé aux intenses gradients de pression présents et à la géométrie intiale de la collision des deux ions lourds, tandis que le v_3 est associé aux fluctuations de la densité d'énergie déposée par la collision. Cette thèse a pour but d'étudier la production azimuthale (en mesurant v_2 ou v_3) de deux sondes dures, correspondant à des paires liées de quarks lourds ($Q\bar{Q}$) créés dans les premiers instants d'une collisions d'ions lourds ultra-relativistes. La première est le J/ψ ($c\bar{c}$), et la deuxième est l'Υ(1S) ($b\bar{b}$).

En traversant le QGP, la paire quark/anti-quark ($Q\bar{Q}$) serait écrantée par les nombreux quarks et gluons (suppression des quarkonia). Comme différents états quarkonia ont différentes énergies de liaison, la probabilité de dissociation de chaque état sera différente (suppression séquentielle). Au LHC, Υ(1S) ($b\bar{b}$) et J/ψ ($c\bar{c}$) sont complémentaires, les premiers sont plus aptes pour étudier la suppression séquentielle, alors que les seconds permettent d'étudier la régénération (création de quarkonia par recombinaison de quarks lourds). En absence de toute interaction entre le QGP et la paire $Q\bar{Q}$, l'émission de quarkonia devrait se faire de façon isotrope. Si au contraire la paire $Q\bar{Q}$ intéragit avec les autres charges de couleurs du QGP, alors les quarks lourds entament une thermalisation dans le milieu et acquièrent ses propriétés hydrodynamiques, notament son écoulement anisotropique.

Ainsi, la mesure d'une anisotropie dans la production azimuthale des quarkonia révèle une direction d'émission privilégié de la paire $Q\bar{Q}$ dans l'évolution du système. Cela peut être associé à l'écoulement anisotropique du milieu, et ainsi traduirait le degré de thermalisation des quarks lourds dans le QGP. Cependant, la production de quarkonia dans les collisions d'ions lourds peut également être modifiée par d'autres effets qui sont présents dès l'état initial de la collision et qui ne sont pas liés à la formation du QGP. Ces effets sont pris en compte dans les modèles de transport microscopique qui décrivent le comportement des paires de quarks lourds au sein du milieu chaud et dense composé de quarks et gluons.

Chapter 2: dispositif expérimental

ALICE (A Large Ion Collider Experiment) est une des quatres grandes expériences utilisant les faisceaux du LHC situé au CERN. ALICE est dédié à l'étude de l'interaction forte aux hautes énergies, et plus particulièrement à la mesure des propriétés du plasma de quarks et de gluons créé lors des collisions d'ions lourds ultra-relativiste. Les détecteurs composant ALICE peuvent être décomposé en deux sous-ensemble ceux centraux autour du point d'interaction des faisceaux (IP), et ceux placés vers l'avant (ou l'arrière).

Les premiers sont composés principalement d'un système de trackers intérieurs (ITS) très proche de l'IP, englobé par une grande chambre de projection temporelle (TPC), puis entouré par des calorimètres électromagnétiques (EmCal). Ainsi, l'ITS (divisé en trois sous-parties SPD, SDD, SSD) permet de reconstruire avec précision les différents vertex d'où provient les traces des particles chargés, celles-ci sont tracées sur plusieurs niveaux ce qui permet de reconstruire leurs trajectoires. Il permet aussi de determiner les propriétés générales de l'événement comme le nombre de particles produites (multiplicité) ou l'angle du plan de la réaction représentant une direction privilégié des particules émises (ou vecteur flot de l'événement: $\mathbf{Q}_n$). La TPC permet l'identification des hadrons à l'aide des mesure de $\mathrm{d}E/\mathrm{d}x$ (l'énergie perdu par unité de distance) laissé par les différentes traces. L'EmCal quant à lui permet la mesure des propriétés des photons et aussi dans une plus faible portion participe à la reconstruction des jets (gerbe hadronique composée de quarks et gluons, issue de la matérialisation de l'énergie due à l'annihilation entre particule/antiparticule)

La seconde catégorie de détecteurs, concerne principalement les détecteurs V0, ZDC, et le spectromètre à muons. Les scintillateurs appellés V0A et V0C, placés de part et d'autre de l'IP, et permettent de mesurer le plan de la réaction, la centralité et la multiplicité de l'évenement. Un calorimètre à zéro degré (ZDC) placé le long de l'axe du faisceau à 112,5m de l'IP, aide à enlever des contamination électromagnétiques et les événements non considérés comme collisions entre constituants des faisceaux. Le spectromètre à muons placé vers l'avant de l'IP permet quant à lui de reconstruire les traces de muons, les propriétés des quarkonia (J/ψ, ψ(2S), Υ,...) et des bosons électrofaibles (Z,W). Un absorbeur hadronique situé entre l'IP et le spectromètre à muons permet de réduire drastiquement la contamination due aux hadrons chargés et aux muons venant de la désintégration des protons et kaons. Le spectromètre est composé de 5 stations de tracking (10 plans de détection), un grand aimant dipolaire (où $\int B\mathrm{d}z = 3$ Tm) pour courber les trajectoires, un filtre passif d'une épaisseur de 1,2 m suivant de 4 chambres plates résistives utilisées comme système de déclenchement pour l'acquisition des données, et ainsi permettre la reconstruction de l'événement.

Chapter 3: selection et calibration des événements

Les données utilisés dans cette thèse correspondent aux collisions Pb–Pb enregistrées lors du Run 2 au LHC (en 2015 puis en 2018). La reconstruction des événement Pb–Pb dans ALICE est réalisé en utilisant un logiciel `AliRoot`, basé sur le logiciel `ROOT` qui permet de stocker, traiter et analyser un grand volume de données. La sélection des bon événements Pb–Pb est réalisée en tenant compte de critères stricts qui permettent d'obtenir un échantillon de données prêt à être analysé. Des critères additionnel dans la sélection des événements peuvent être appliqué suivant le type de chaque analyse. Dans le cas des analyses cherchant à mesurer l'écoulement anisotropique, les propriétés générales des événements Pb–Pb doivent être calibrés, pour notamment supprimer les dépendances en fontion de la position z des vertex, de la centralité de la collision, et de corriger les biais à cause de la non-uniformité de l'acceptance azimuthale des détecteurs utilisés pour les mesures de multiplicité. Les événements ayant un z_{vertex} au dehors de [-10;+10]cm sont enlevés, pour coincider avec l'acceptance du détecteur à pixel en silicium (SPD) de l'ITS. De même pour la centralité de la collision qui doit être comprise dans l'intervalle [0;90]%. Les corrections sont appliqués de manière iterative, run par run, en fonction de z_{vertex} et de la centralité, sur le vecteur flot de l'événement ($\mathbf{Q}_n$).

Chapter 4: analyse de données

La calibration s'est réalisée sur un grand nombre d'événements Pb–Pb à biais minimum, leur nombre ne dépend pas de la centralité de la collision, ce qui permet d'éffectuer les étapes de corrections plus aisément. Une faible portion d'en eux contiennent des traces de muons reconstruits dans le spectromètre à muons, le nombre d'événements avec muons diminue rapidement plus les collisions deviennent non-centrale ou périphériques, et c'est sur cet échantillon de données que se base l'analyse.

Les quarkonia J/ψ et Υ(1S) sont des particules rares mesurées dans le cannal de désintégration dimuon. Les traces des muons sont reconstruites dans l'acceptance du spectromètre. L'étude des spectres de masse invariante $M_{\mu\mu}$ permet de déterminer le nombre de quarkonia. La mesure des coefficients v_{n} est réalisé en appliquant une méthode de corrélation à 2 particules, en utilisant à la fois les propriétés du vecteur $\mathbf{Q}_n$ pour le flot de l'événement et ceux issus des dimuons (associés aux quarkonia). Ainsi, un coefficient v_{n} est obtenu pour chaque pair dimuon, puis ils sont moyennés sur toutes les paires et puis tous les événements, il en résulte un profil de v_{n} en fonction de $M_{\mu\mu}$. Un fit séquentiel à la fois du spectre de masse invariante et du profil v_{n} $(M_{\mu\mu})$ permet d'obtenir la valeur v_{n} du signal J/ψ ou Υ(1S). L'extraction des anisotropies azimuthales (ou coefficients v_{n}) est réalisée dans de multiple intervalles d'impulsion transverse (p_{T}) et de centralité, pour le J/ψ et Υ(1S). Des études approffondies permmettent d'évaluer les incertitudes systématiques sur chaque mesure du signal v_{n}.

Chapter 5: résultats et discussions

Les mesures montrent des coefficients v_2 du J/ψ positifs dans les collisions Pb–Pb non centrales pour un domaine large en p_{T}, jusqu'à 14 GeV/c. Le v_2 est proche de 0 à bas p_{T}, puis augmente rapidement en passant par un maximum à 0.1 autour de 3–4 GeV/c, et enfin il semble converger vers des valeurs similaires que ceux autres hadrons plus légers. Le coefficient v_3 du J/ψ est mesuré positif avec une significance supérieure à 5σ dans l'intervalle de centralité 0–50%, et $2 < p_{\mathrm{T}} < 5$ GeV/c, autrement il est toujours plus faible que le v_2. À bas p_{T} (< 5 GeV/c), un ordre est visible entre différentes particules respectant $v_{2,\pi} > v_{2,\mathrm{D}} > v_{2,\mathrm{J}/\psi}$, et qui semble être aussi le cas pour le v_3. Enfin, les mesures différentielles en centralité pour $p_{\mathrm{T}} < 5$ GeV/c montrent une augmentation quasi-linéaire dans le ratio $v_2^{\pi}/v_2^{\mathrm{J}/\psi}$ jusqu'à 40–50%, à l'inverse ce ratio est compatible avec 1 sur toute la gamme de centralité pour $p_{\mathrm{T}} > 5$ GeV/c. Cette mesure suggère un comportement similaire aux pions à haut p_{T}, alors qu'à bas p_{T} où la production du J/ψ est dominé par la régénération, le comportement diffère, entre autre dû à une thermalization des quarks c dans le milieu en évolution. La mesure du v_2 de Υ(1S) est compatible avec zéro pour $2 < p_{\mathrm{T}} < 15$ GeV/c dans l'intervalle de centralité 5–60%. La mesure différentielle en p_{T} confirme aussi des valeurs compatiblent avec zéro, et avec les modèles de transport qui décrivent le comportement de la paire de quarks lourds $b\bar{b}$, prédisant un très faible v_2 pour l'Υ(1S).

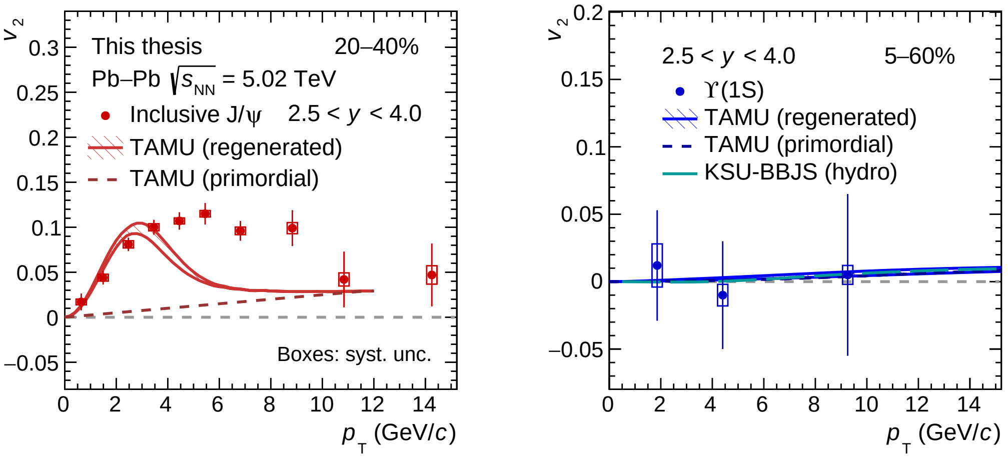

Figure D.1: Comparaison des v_2 du J/ψ (left) et de l'Υ(1S) (right) dans les collisions Pb–Pb non-central, avec différents modèles théoriques qui incluent différentes fractions de régénération et/ou suppression.

Les modèles microscopiques de transport prédisent une intense supression, accompagnée d'une forte recombinaison des quarks c, et donc une régénération du J/ψ. Cela mène à une anisotropie azimuthale positive dans la production du J/ψ dans les collisions Pb–Pb, principalement aux basses impulsions transverses. Ainsi, on peut voir sur la Figure D.1 (gauche) que le modèle de transport est en accord avec les données mesurées jusqu'à $p_{\mathrm{T}} < 4$ GeV/c, tandis que pour $5 < p_{\mathrm{T}} < 10$ GeV/c certains ingrédients semblent manquer dans le modèle pour pouvoir décrire correctement les valeurs du v_2 du J/ψ. Pour l'Υ(1S), l'état quarkonium le plus lourd et le plus lié, celui-ci serait produit en très petite quantité dans les collisions Pb–Pb au LHC comparé au J/ψ (~30 fois moins), et donc la régénération aurait un impact très faible sur sa production. De plus, au vu des températures très élevés demandées pour dissocier cet état, la suppression $b\bar{b}$ ne pourrait être réalisée qu'aux tous premiers instants de l'évolution du QGP, où celui-ci n'a pas encore développé son écoulement anisotrope. Sur la Figure D.1 (droite) on peut voir que, à la fois les modèles de transport et ceux se basant uniquement sur l'hydrodynamique du milieu permettent de décrirent les données mesurées du v_2 de l'Υ(1S).

Chapter 6: conclusion et perspectives

Cette thèse à eu pour but de mesurer les anisotropies azimuthales des paires liées de quarks lourds produites dans les collisions Pb–Pb au LHC, en particulier celles du J/ψ et de l'Υ(1S).

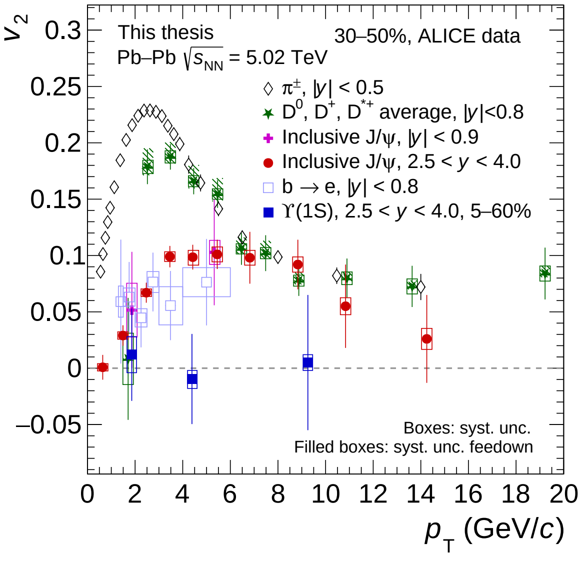

Figure D.2: Comparaison du v_2 de différente particules dans les collisions Pb–Pb non-centrales, de la plus lègère (π) à la plus lourde (Υ(1S)).

La mesure des v_{n} coefficients du J/ψ apporte de nouvelles évidences de la régénération du J/ψ dans les collisions Pb–Pb au LHC. Les mesures de v_2 du J/ψ et de l'Υ(1S) permettent de contraindre d'avantage les modèles de transport microscopique décrivant le comportement de la paire $c\bar{c}$ ou $b\bar{b}$ dans le milieu chaud et dense créé au LHC, qui s'apparente au QGP. De plus, la mesure du v_2 de l'Υ(1S) clôture en quelque sorte l'ensemble des mesures de v_2 pour différente particules, car l'Υ(1S) représente la particule la plus lourde mesurée. Les pions, considérés comme les hadrons les plus légers et les plus produits dans les collisions Pb–Pb possèdent les valeurs les plus élevées de v_2, ensuite plus la particule mesurée possède une masse élevée, plus son v_2 sera petit comparé à celui des pions. Ainsi, on peut voir sur la Figure D.2 que $v_2^{\pi} > v_2^{D} > v_2^{\mathrm{J}/\psi} \gtrsim v_2^{b\rightarrow e} > v_2^{\Upsilon(1\mathrm{S})} \approx 0$ semble être vrai pour des impulsions transverses de l'ordre de 3–5 GeV/c.

On peut remarquer que la mesure réalisée sur les J/ψ est inclusive, ce qui veut dire qu'elle prend en compte les J/ψ prompts (issus de la production direct $c\bar{c}$ et de la recombination dans le milieu) et non-prompts (c'est à dire issus de la désintégration d'un méson B). Avec les nouvelles données attendues du Run 3, ces deux mécanismes de production pourront être séparés dans le spectromètre à muons, grâce notamment à l'ajout du MFT, qui permettra la séparation entre les vertex primaires (J/ψ prompts) et ceux déplacés (correspondant aux J/ψ non-prompts). De plus, les prochaines prises de données issues du Run 3 bénéficieront aux deux mesures présentés dans cette thèse, en particulier pour augmenter le nombre de candidats J/ψ et aussi et surtout Υ(1S), dans l'extraction de leurs anisotropies azimuthales, caractérisées par les v_{n}. Ces nouvelles mesures, plus précises, permettront à terme de contraindre d'avantage leurs mécanismes de production, de $p_{\mathrm{T}} = 0$ GeV/c jusqu'à 20 GeV/c, dans les collisions Pb–Pb au LHC.

Bibliography

[1] E. D. Bloom, D. H. Coward, H. DeStaebler, J. Drees, G. Miller, L. W. Mo, R. E. Taylor, M. Breidenbach, J. I. Friedman, G. C. Hartmann, and H. W. Kendall. High-energy inelastic $e - p$ scattering at 6° and 10°. *Phys. Rev. Lett.*, 23:930–934, Oct 1969.

[2] Ian J R Aitchison and Anthony J G Hey. *Gauge theories in particle physics: a practical introduction; 4th ed.* CRC Press, Boca Raton, FL, 2013.

[3] F. Halzen and Alan D. Martin. *QUARKS AND LEPTONS: AN INTRODUCTORY COURSE IN MODERN PARTICLE PHYSICS.* 1 1984.

[4] F. Englert and R. Brout. Broken symmetry and the mass of gauge vector mesons. *Phys. Rev. Lett.*, 13:321–323, Aug 1964.

[5] Peter W. Higgs. Broken symmetries and the masses of gauge bosons. *Phys. Rev. Lett.*, 13:508–509, Oct 1964.

[6] Michael E Peskin and Daniel V Schroeder. *An introduction to quantum field theory.* Westview, Boulder, CO, 1995. Includes exercises.

[7] Walter Greiner, Stefan Schramm, and Echkart Stein. *Quantum chromodynamics; 3rd ed.* Springer, Berlin, 2007.

[8] M. Tanabashi et al. Review of Particle Physics. *Phys. Rev.*, D98(3):030001, 2018.

[9] John Collins. *Foundations of Perturbative QCD.* Cambridge Monographs on Particle Physics, Nuclear Physics and Cosmology. Cambridge University Press, 2011.

[10] David J. Gross and Frank Wilczek. Asymptotically free gauge theories. i. *Phys. Rev. D*, 8:3633–3652, Nov 1973.

[11] J. D. Bjorken. Highly Relativistic Nucleus-Nucleus Collisions: The Central Rapidity Region. *Phys. Rev. D*, 27:140–151, 1983.

[12] MADAI Collaboration. Models and Data Analysis Initiative .

[13] Rainer J. Fries. Early Time Evolution of High Energy Heavy Ion Collisions. *J. Phys. G*, 34:S851–854, 2007.

[14] Edward Shuryak. Theory of hadron plasma. *Sov. Phys JET*, 47(2:212–219, Feb 1978.

[15] Patrick Hanus, Aleksas Mazeliauskas, and Klaus Reygers. Entropy production in pp and Pb-Pb collisions at energies available at the CERN Large Hadron Collider. *Phys. Rev. C*, 100(6):064903, 2019.

[16] Anton Andronic, Peter Braun-Munzinger, Krzysztof Redlich, and Johanna Stachel. Decoding the phase structure of QCD via particle production at high energy. *Nature*, 561(7723):321–330, 2018.

[17] Jaroslav Adam et al. Enhanced production of multi-strange hadrons in high-multiplicity proton-proton collisions. *Nature Phys.*, 13:535–539, 2017.

[18] Adam Bzdak, Shinichi Esumi, Volker Koch, Jinfeng Liao, Mikhail Stephanov, and Nu Xu. Mapping the Phases of Quantum Chromodynamics with Beam Energy Scan. *Phys. Rept.*, 853:1–87, 2020.

[19] S. A. Bass, M. Gyulassy, Horst Stoecker, and W. Greiner. Signatures of quark gluon plasma formation in high-energy heavy ion collisions: A Critical review. *J. Phys. G*, 25:R1–R57, 1999.

[20] W. Israel and J.M. Stewart. Transient relativistic thermodynamics and kinetic theory. *Annals of Physics*, 118(2):341–372, 1979.

[21] Matthew Luzum and Paul Romatschke. Conformal Relativistic Viscous Hydrodynamics: Applications to RHIC results at $\sqrt{\mathbf{s_{NN}}} = \mathbf{200}$ GeV. *Phys. Rev.*, C78:034915, 2008. [Erratum: Phys. Rev.C79,039903(2009)].

[22] Paul Romatschke. New Developments in Relativistic Viscous Hydrodynamics. *Int. J. Mod. Phys.*, E19:1–53, 2010.

[23] Texas A&M University Robert E. Tribble. NSAC Subcommittee Report: Implementing the 2007 Long Range Plan. *http://science.energy.gov/np/nsac/reports/*, 2013.

[24] P. Kovtun, Dan T. Son, and Andrei O. Starinets. Viscosity in strongly interacting quantum field theories from black hole physics. *Phys. Rev. Lett.*, 94:111601, 2005.

[25] Sergei A. Voloshin, Arthur M. Poskanzer, and Raimond Snellings. Collective phenomena in non-central nuclear collisions. *Landolt-Bornstein*, 23:293–333, 2010.

[26] Chun Shen and Li Yan. Recent development of hydrodynamic modeling in heavy-ion collisions. *Nucl. Sci. Tech.*, 31(12):122, 10 2020.

[27] S. Z. Belenkij and L. D. Landau. Hydrodynamic theory of multiple production of particles. *Nuovo Cim. Suppl.*, 3S10:15, 1956.

[28] A. A. Amsden, G. F. Bertsch, F. H. Harlow, and J. R. Nix. Relativistic hydrodynamic theory of heavy-ion collisions. *Phys. Rev. Lett.*, 35:905–908, Oct 1975.

[29] Jean-Yves Ollitrault. Anisotropy as a signature of transverse collective flow. *Phys. Rev.*, D46:229–245, 1992.

[30] S. Voloshin and Y. Zhang. Flow study in relativistic nuclear collisions by Fourier expansion of Azimuthal particle distributions. *Z. Phys.*, C70:665–672, 1996.

[31] Nicolas Borghini, Phuong Mai Dinh, and Jean-Yves Ollitrault. Flow analysis from multiparticle azimuthal correlations. *Phys. Rev. C*, 64:054901, Sep 2001.

[32] Derek Teaney and Li Yan. Triangularity and Dipole Asymmetry in Heavy Ion Collisions. *Phys. Rev.*, C83:064904, 2011.

[33] Ulrich W. Heinz, John Scott Moreland, and Huichao Song. Viscosity from elliptic flow: The Path to precision. *Phys. Rev. C*, 80:061901, 2009.

[34] S. Acharya et al. Anisotropic flow of identified particles in Pb-Pb collisions at $\sqrt{s}_{\mathrm{NN}} = 5.02$ TeV. *JHEP*, 09:006, 2018.

[35] Shreyasi Acharya et al. Investigations of Anisotropic Flow Using Multiparticle Azimuthal Correlations in pp, p-Pb, Xe-Xe, and Pb-Pb Collisions at the LHC. *Phys. Rev. Lett.*, 123(14):142301, 2019.

[36] Z. Citron et al. Future physics opportunities for high-density QCD at the LHC with heavy-ion and proton beams. In *HL/HE-LHC Workshop: Workshop on the Physics of HL-LHC, and Perspectives at HE-LHC Geneva, Switzerland, June 18-20, 2018*, 2018.

[37] Bjoern Schenke, Prithwish Tribedy, and Raju Venugopalan. Fluctuating Glasma initial conditions and flow in heavy ion collisions. *Phys. Rev. Lett.*, 108:252301, 2012.

[38] Aleksi Kurkela, Aleksas Mazeliauskas, Jean-François Paquet, Sören Schlichting, and Derek Teaney. Matching the Nonequilibrium Initial Stage of Heavy Ion Collisions to Hydrodynamics with QCD Kinetic Theory. *Phys. Rev. Lett.*, 122(12):122302, 2019.

[39] Charles Gale, Sangyong Jeon, Björn Schenke, Prithwish Tribedy, and Raju Venugopalan. Event-by-event anisotropic flow in heavy-ion collisions from combined Yang-Mills and viscous fluid dynamics. *Phys. Rev. Lett.*, 110(1):012302, 2013.

[40] Michael L. Miller, Klaus Reygers, Stephen J. Sanders, and Peter Steinberg. Glauber modeling in high energy nuclear collisions. *Ann. Rev. Nucl. Part. Sci.*, 57:205–243, 2007.

[41] Constantin Loizides, Jason Kamin, and David d'Enterria. Improved Monte Carlo Glauber predictions at present and future nuclear colliders. *Phys. Rev. C*, 97(5):054910, 2018. [Erratum: Phys.Rev.C 99, 019901 (2019)].

[42] Edmond Iancu and Raju Venugopalan. *The Color glass condensate and high-energy scattering in QCD*, pages 249–3363. 3 2003.

[43] Francois Gelis, Edmond Iancu, Jamal Jalilian-Marian, and Raju Venugopalan. The Color Glass Condensate. *Ann. Rev. Nucl. Part. Sci.*, 60:463–489, 2010.

[44] Marlene Nahrgang, Jörg Aichelin, Pol Bernard Gossiaux, and Klaus Werner. Heavy-quark dynamics in a hydrodynamically evolving medium. *EPJ Web of Conferences*, 171:04003, 2018.

[45] V. Greco, H. van Hees, and R. Rapp. Heavy Quark Dynamics in the QGP. *AIP Conf. Proc.*, 1422(1):117–126, 2012.

[46] P. Crochet and P. Braun-Munzinger. Investigation of background subtraction techniques for high mass dilepton physics. *Nucl. Instrum. Meth. A*, 484:564–572, 2002.

[47] Guy D. Moore and Derek Teaney. How much do heavy quarks thermalize in a heavy ion collision? *Phys. Rev. C*, 71:064904, 2005.

[48] Hendrik van Hees and Ralf Rapp. Thermalization of heavy quarks in the quark-gluon plasma. *Phys. Rev. C*, 71:034907, 2005.

[49] Shanshan Cao, Guang-You Qin, and Steffen A. Bass. Heavy-quark dynamics and hadronization in ultrarelativistic heavy-ion collisions: Collisional versus radiative energy loss. *Phys. Rev. C*, 88:044907, 2013.

[50] Weiyao Ke, Yingru Xu, and Steffen A. Bass. Linearized Boltzmann-Langevin model for heavy quark transport in hot and dense QCD matter. *Phys. Rev. C*, 98(6):064901, 2018.

[51] K. Werner, Iu. Karpenko, T. Pierog, M. Bleicher, and K. Mikhailov. Event-by-event simulation of the three-dimensional hydrodynamic evolution from flux tube initial conditions in ultrarelativistic heavy ion collisions. *Phys. Rev. C*, 82:044904, Oct 2010.

[52] Marlene Nahrgang, Jörg Aichelin, Steffen Bass, Pol Bernard Gossiaux, and Klaus Werner. Heavy-flavor observables at RHIC and LHC. *Nucl. Phys. A*, 931:575–580, 2014.

[53] Matteo Cacciari and Einan Gardi. Heavy quark fragmentation. *Nucl. Phys. B*, 664:299–340, 2003.

[54] R. J. Fries, Berndt Muller, C. Nonaka, and S. A. Bass. Hadronization in heavy ion collisions: Recombination and fragmentation of partons. *Phys. Rev. Lett.*, 90:202303, 2003.

[55] Laura Tolos and Juan M. Torres-Rincon. D-meson propagation in hot dense matter. *Phys. Rev. D*, 88:074019, 2013.

[56] V. Ozvenchuk, J. M. Torres-Rincon, P. B. Gossiaux, J. Aichelin, and L. Tolos. d-meson propagation in hadronic matter and consequences for heavy-flavor observables in ultrarelativistic heavy-ion collisions. *Phys. Rev. C*, 90:054909, Nov 2014.

[57] N. Brambilla et al. Heavy quarkonium: progress, puzzles, and opportunities. *Eur. Phys. J.*, C71:1534, 2011.

[58] Helmut Satz. Quarkonium Binding and Dissociation: The Spectral Analysis of the QGP. *Nucl. Phys. A*, 783:249–260, 2007.

[59] S. Digal, P. Petreczky, and H. Satz. Quarkonium feed down and sequential suppression. *Phys. Rev.*, D64:094015, 2001.

[60] Frithjof Karsch. Deconfinement and quarkonium suppression. *Eur. Phys. J. C*, 43:35–43, 2005.

[61] Alexander Rothkopf. Heavy Quarkonium in Extreme Conditions. 2019.

[62] Peter Petreczky, Chuan Miao, and Agnes Mocsy. Quarkonium spectral functions with complex potential. *Nucl. Phys. A*, 855:125–132, 2011.

[63] A. Andronic, P. Braun-Munzinger, K. Redlich, and J. Stachel. The statistical model in Pb-Pb collisions at the LHC. *Nucl. Phys.*, A904-905:535c–538c, 2013.

[64] Xiaojian Du and Ralf Rapp. Sequential Regeneration of Charmonia in Heavy-Ion Collisions. *Nucl. Phys.*, A943:147–158, 2015.

[65] A. Beraudo et al. Extraction of Heavy-Flavor Transport Coefficients in QCD Matter. *Nucl. Phys. A*, 979:21–86, 2018.

[66] Nora Brambilla, Viljami Leino, Peter Petreczky, and Antonio Vairo. Lattice QCD constraints on the heavy quark diffusion coefficient. *Phys. Rev. D*, 102(7):074503, 2020.

[67] Jaroslav Adam et al. Azimuthal anisotropy of charged jet production in $\sqrt{s_{\rm NN}}$ = 2.76 TeV Pb-Pb collisions. *Phys. Lett. B*, 753:511–525, 2016.

[68] Marlene Nahrgang, Jörg Aichelin, Pol Bernard Gossiaux, and Klaus Werner. Influence of hadronic bound states above T_c on heavy-quark observables in pb + pb collisions at the cern large hadron collider. *Phys. Rev. C*, 89:014905, Jan 2014.

[69] Marlene Nahrgang, Jörg Aichelin, Pol Bernard Gossiaux, and Klaus Werner. Toward a consistent evolution of the quark-gluon plasma and heavy quarks. *Phys. Rev. C*, 93:044909, Apr 2016.

[70] Matteo Cacciari, Mario Greco, and Paolo Nason. The P(T) spectrum in heavy flavor hadroproduction. *JHEP*, 05:007, 1998.

[71] Matteo Cacciari, Stefano Frixione, and Paolo Nason. The p(T) spectrum in heavy flavor photoproduction. *JHEP*, 03:006, 2001.

[72] Matteo Cacciari, Stefano Frixione, Nicolas Houdeau, Michelangelo L. Mangano, Paolo Nason, and Giovanni Ridolfi. Theoretical predictions for charm and bottom production at the LHC. *JHEP*, 10:137, 2012.

[73] T. Pierog, Iu. Karpenko, J. M. Katzy, E. Yatsenko, and K. Werner. EPOS LHC: Test of collective hadronization with data measured at the CERN Large Hadron Collider. *Phys. Rev. C*, 92(3):034906, 2015.

[74] Jan Uphoff, Oliver Fochler, Zhe Xu, and Carsten Greiner. Elastic and radiative heavy quark interactions in ultra-relativistic heavy-ion collisions. *Journal of Physics G: Nuclear and Particle Physics*, 42(11):115106, oct 2015.

[75] Stefano Frixione and Bryan R. Webber. Matching NLO QCD computations and parton shower simulations. *JHEP*, 06:029, 2002.

[76] Min He, Rainer J. Fries, and Ralf Rapp. Heavy-quark diffusion and hadronization in quark-gluon plasma. *Phys. Rev. C*, 86:014903, Jul 2012.

[77] T. Matsui and H. Satz. J/ψ Suppression by Quark-Gluon Plasma Formation. *Phys. Lett.*, B178:416–422, 1986.

[78] Jaroslav Adam et al. J/ψ suppression at forward rapidity in Pb-Pb collisions at $\sqrt{\mathbf{s}_{\mathrm{NN}}} = \mathbf{5.02}$ TeV. *Phys. Lett.*, B766:212–224, 2017.

[79] Shreyasi Acharya et al. J/ψ elliptic flow in Pb-Pb collisions at $\sqrt{s_{\mathrm{NN}}} = 5.02$ TeV. *Phys. Rev. Lett.*, 119(24):242301, 2017.

[80] Betty Abelev et al. J/ψ suppression at forward rapidity in Pb-Pb collisions at $\sqrt{s_{NN}} = 2.76$ TeV. *Phys. Rev. Lett.*, 109:072301, 2012.

[81] A. Adare et al. J/ψ Production vs Centrality, Transverse Momentum, and Rapidity in Au+Au Collisions at $\sqrt{s_{NN}} = 200$ GeV. *Phys. Rev. Lett.*, 98:232301, 2007.

[82] Ehab Abbas et al. J/ψ Elliptic Flow in Pb-Pb Collisions at $\sqrt{s_{\mathrm{NN}}} = 2.76$ TeV. *Phys. Rev. Lett.*, 111:162301, 2013.

[83] Xiaojian Du, Ralf Rapp, and Min He. Color Screening and Regeneration of Bottomonia in High-Energy Heavy-Ion Collisions. *Phys. Rev.*, C96(5):054901, 2017.

[84] Loïc Grandchamp, Ralf Rapp, and Gerald E. Brown. In-medium effects on charmonium production in heavy-ion collisions. *Phys. Rev. Lett.*, 92:212301, May 2004.

[85] Albert M Sirunyan et al. Measurement of prompt and nonprompt charmonium suppression in PbPb collisions at 5.02 TeV. *Eur. Phys. J. C*, 78(6):509, 2018.

[86] A.M. Sirunyan et al. Measurement of nuclear modification factors of υ(1s), υ(2s), and υ(3s) mesons in pb–pb collisions at $\sqrt{\mathbf{s}_{\mathrm{nn}}} = \mathbf{5.02}$ tev. *Physics Letters B*, 790:270–293, 2019.

[87] Brandon Krouppa, Radoslaw Ryblewski, and Michael Strickland. Bottomonium suppression in heavy-ion collisions. *Nuclear Physics A*, 967:604–607, 2017. The 26th International Conference on Ultra-relativistic Nucleus-Nucleus Collisions: Quark Matter 2017.

[88] Shreyasi Acharya et al. Υ suppression at forward rapidity in Pb-Pb collisions at $\sqrt{s_{\mathrm{NN}}} = 5.02$ TeV. *Phys. Lett.*, B790:89–101, 2019.

[89] Jean-Philippe Lansberg. New Observables in Inclusive Production of Quarkonia. *Phys. Rept.*, 889:1–106, 2020.

[90] Partha Pratim Bhaduri, Nicolas Borghini, Amaresh Jaiswal, and Michael Strickland. Anisotropic escape mechanism and elliptic flow of bottomonia. *Phys. Rev. C*, 100(5):051901, 2019.

[91] L. Grandchamp, S. Lumpkins, D. Sun, H. van Hees, and R. Rapp. Bottomonium production at $\sqrt{s_{NN}} = 200$ gev and $\sqrt{s_{NN}} = 5.5$ tev. *Phys. Rev. C*, 73:064906, Jun 2006.

[92] Shreyasi Acharya et al. Study of J/ψ azimuthal anisotropy at forward rapidity in Pb-Pb collisions at $\sqrt{s_{\mathrm{NN}}} = 5.02$ TeV. *JHEP*, 02:012, 2019.

[93] C. Fabjan and J. Schukraft. The Story of ALICE: Building the dedicated heavy ion detector at LHC. 1 2011.

[94] Betty Abelev et al. Performance of the ALICE Experiment at the CERN LHC. *Int. J. Mod. Phys.*, A29:1430044, 2014.

[95] G. Dellacasa et al. ALICE technical design report of the inner tracking system (ITS). Technical report, CERN, 1999.

[96] A Saba. A few members of the Silicon Pixel Detector working on the completed first half barrel . ALICE Collection., Jan 2007.

[97] K Aamodt et al. Alignment of the ALICE Inner Tracking System with cosmic-ray tracks. *JINST*, 5:P03003, 2010.

[98] J. Alme et al. The ALICE TPC, a large 3-dimensional tracking device with fast readout for ultra-high multiplicity events. *Nucl. Instrum. Meth.*, A622:316–367, 2010.

[99] Antonio Saba. The ALICE Time Projection Chamber: journey from building 2252 to the ALICE cavern . https://cds.cern.ch/record/1011033, Jan 2007.

[100] E. Abbas et al. Performance of the ALICE VZERO system. *JINST*, 8:P10016, 2013.

[101] Shreyasi Acharya et al. The ALICE Transition Radiation Detector: construction, operation, and performance. *Nucl. Instrum. Meth. A*, 881:88–127, 2018.

[102] Jean-Yves Grossiord. The V0 detector is two disks of counters in both sides of the interaction point . ALICE Collection., Oct 2006.

[103] G. Dellacasa et al. ALICE technical design report of the zero degree calorimeter (ZDC). Technical report, CERN, 1999.

[104] Gines Martinez. The Muon spectrometer of the ALICE experiment. *Nucl. Phys. A*, 749:313–319, 2005.

[105] Addendum of the Letter of Intent for the upgrade of the ALICE experiment : The Muon Forward Tracker. Technical Report CERN-LHCC-2013-014. LHCC-I-022-ADD-1, CERN, Geneva, Aug 2013. Final submission of the presetn LoI addendum is scheduled for September 7th.

[106] First collisions of Pb ions in 2018 at the LHC recorded by ALICE . Nov 2018. https://cds.cern.ch/record/2646381.

[107] Gábor Bíró, Gergely Gábor Barnaföldi, Gábor Papp, Miklos Gyulassy, Péter Lévai, Xin-Nian Wang, and Ben-Wei Zhang. Introducing HIJING++: the Heavy Ion Monte Carlo Generator for the High-Luminosity LHC Era. *PoS*, HardProbes2018:045, 2019.

[108] Stefan Roesler, Ralph Engel, and Johannes Ranft. The Monte Carlo event generator DPMJET-III. In *International Conference on Advanced Monte Carlo for Radiation Physics, Particle Transport Simulation and Applications (MC 2000)*, 12 2000.

[109] Torbjörn Sjöstrand. The PYTHIA Event Generator: Past, Present and Future. *Comput. Phys. Commun.*, 246:106910, 2020.

[110] M. Bahr et al. Herwig++ Physics and Manual. *Eur. Phys. J. C*, 58:639–707, 2008.

[111] Centrality determination in heavy ion collisions. 8 2018.

[112] P Buncic, M Krzewicki, and P Vande Vyvre. Technical Design Report for the Upgrade of the Online-Offline Computing System. Technical report, Apr 2015.

[113] Upgrade of the ALICE Time Projection Chamber. Technical report, Oct 2013.

[114] P Antonioli, A Kluge, and W Riegler. Upgrade of the ALICE Readout & Trigger System. Technical report, Sep 2013. Presently we require a LHCC-TDR reference number at a later stage we will fill the required information.

[115] B Abelev and Adam. Technical Design Report for the Upgrade of the ALICE Inner Tracking System. Technical report, Nov 2013.

[116] Technical Design Report for the Muon Forward Tracker. Technical report, Jan 2015.

[117] L. Valencia Palomo. The ALICE experiment upgrades for LHC Run 3 and beyond: contributions from mexican groups. *J. Phys. Conf. Ser.*, 912(1):012023, 2017.

[118] Gianluca Aglieri Rinella. The alpide pixel sensor chip for the upgrade of the alice inner tracking system. *Nuclear Instruments and Methods in Physics Research Section A: Accelerators, Spectrometers, Detectors and Associated Equipment*, 845:583–587, 2017. Proceedings of the Vienna Conference on Instrumentation 2016.

[119] Jochen Klein and Felix Reidt. ALICE ITS Inner Barrel installation. General Photo, May 2021.

[120] MFT Collaboration ALICE. ALICE Muon Forward Tracker (MFT). Dec 2020. General Photo.

[121] Arthur M. Poskanzer and S. A. Voloshin. Methods for analyzing anisotropic flow in relativistic nuclear collisions. *Phys. Rev. C*, 58:1671–1678, 1998.

[122] Fernando G. Gardim, Frederique Grassi, Matthew Luzum, and Jean-Yves Ollitrault. Mapping the hydrodynamic response to the initial geometry in heavy-ion collisions. *Phys. Rev.*, C85:024908, 2012.

[123] Betty Abelev et al. Directed Flow of Charged Particles at Midrapidity Relative to the Spectator Plane in Pb-Pb Collisions at $\sqrt{s_{NN}}$=2.76 TeV. *Phys. Rev. Lett.*, 111(23):232302, 2013.

[124] Ilya Selyuzhenkov and Sergei Voloshin. Effects of non-uniform acceptance in anisotropic flow measurement. *Phys. Rev.*, C77:034904, 2008.

[125] J Adam et al. Quarkonium signal extraction in ALICE. Technical report, CERN, 2015.

[126] Shreyasi Acharya et al. Energy dependence of forward-rapidity J/ψ and ψ(2S) production in pp collisions at the LHC. *Eur. Phys. J.*, C77(6):392, 2017.

[127] Jaroslav Adam et al. Measurement of an excess in the yield of J/ψ at very low p_{T} in Pb-Pb collisions at $\sqrt{s_{\mathrm{NN}}} = 2.76$ TeV. *Phys. Rev. Lett.*, 116(22):222301, 2016.

[128] Muriel Pivk and Francois R. Le Diberder. SPlot: A Statistical tool to unfold data distributions. *Nucl. Instrum. Meth. A*, 555:356–369, 2005.

[129] Albert M Sirunyan et al. Measurement of prompt D^0 meson azimuthal anisotropy in Pb-Pb collisions at $\sqrt{s_{NN}} = 5.02$ TeV. *Phys. Rev. Lett.*, 120(20):202301, 2018.

[130] Albert M Sirunyan et al. Pseudorapidity and transverse momentum dependence of flow harmonics in pPb and PbPb collisions. *Phys. Rev.*, C98(4):044902, 2018.

[131] Betty Abelev et al. Anisotropic flow of charged hadrons, pions and (anti-)protons measured at high transverse momentum in Pb-Pb collisions at $\sqrt{s_{NN}}$=2.76 TeV. *Phys. Lett.*, B719:18–28, 2013.

[132] Georges Aad et al. Measurement of event-plane correlations in $\sqrt{s_{NN}} = 2.76$ TeV lead-lead collisions with the ATLAS detector. *Phys. Rev.*, C90(2):024905, 2014.

[133] J. Adams et al. Azimuthal anisotropy at RHIC: The First and fourth harmonics. *Phys. Rev. Lett.*, 92:062301, 2004.

[134] A. Adare et al. Elliptic and hexadecapole flow of charged hadrons in Au+Au collisions at $\sqrt{s_{NN}} = 200$ GeV. *Phys. Rev. Lett.*, 105:062301, 2010.

[135] Georges Aad et al. Measurement of the azimuthal anisotropy for charged particle production in $\sqrt{s_{NN}} = 2.76$ TeV lead-lead collisions with the ATLAS detector. *Phys. Rev.*, C86:014907, 2012.

[136] S. Acharya et al. Energy dependence and fluctuations of anisotropic flow in Pb-Pb collisions at $\sqrt{s_{\mathrm{NN}}} = 5.02$ and 2.76 TeV. *JHEP*, 07:103, 2018.

[137] S. Acharya et al. Anisotropic flow in Xe-Xe collisions at $\sqrt{\mathbf{s_{\mathrm{NN}}}} = \mathbf{5.44}$ TeV. *Phys. Lett.*, B784:82–95, 2018.

[138] Francesco Scardina, Santosh K. Das, Vincenzo Minissale, Salvatore Plumari, and Vincenzo Greco. Estimating the charm quark diffusion coefficient and thermalization time from D meson spectra at energies available at the BNL Relativistic Heavy Ion Collider and the CERN Large Hadron Collider. *Phys. Rev.*, C96(4):044905, 2017.

[139] Taesoo Song, Hamza Berrehrah, Daniel Cabrera, Juan M. Torres-Rincon, Laura Tolos, Wolfgang Cassing, and Elena Bratkovskaya. Tomography of the Quark-Gluon-Plasma by Charm Quarks. *Phys. Rev. C*, 92(1):014910, 2015.

[140] Shanshan Cao and Steffen A. Bass. Thermalization of charm quarks in infinite and finite QGP matter. *Phys. Rev. C*, 84:064902, 2011.

[141] Shreyasi Acharya et al. Studies of J/ψ production at forward rapidity in Pb-Pb collisions at $\sqrt{s_{\mathrm{NN}}} = 5.02$ TeV. *JHEP*, 02:041, 2020.

[142] Rodrigo Franco and Matthew Luzum. Rapidity-dependent eccentricity scaling in relativistic heavy-ion collisions. *Phys. Lett. B*, 806:135518, 2020.

[143] Vardan Khachatryan et al. Evidence for transverse momentum and pseudorapidity dependent event plane fluctuations in PbPb and pPb collisions. *Phys. Rev.*, C92(3):034911, 2015.

[144] Morad Aaboud et al. Measurement of longitudinal flow decorrelations in Pb+Pb collisions at $\sqrt{s_{\mathrm{NN}}} = 2.76$ and 5.02 TeV with the ATLAS detector. *Eur. Phys. J.*, C78(2):142, 2018.

[145] Kai Zhou, Nu Xu, Zhe Xu, and Pengfei Zhuang. Medium effects on charmonium production at ultrarelativistic energies available at the CERN Large Hadron Collider. *Phys. Rev.*, C89(5):054911, 2014.

[146] P. Huovinen, P. F. Kolb, Ulrich W. Heinz, P. V. Ruuskanen, and S. A. Voloshin. Radial and elliptic flow at RHIC: Further predictions. *Phys. Lett. B*, 503:58–64, 2001.

[147] Shreyasi Acharya et al. Coherent J/ψ photoproduction at forward rapidity in ultra-peripheral Pb-Pb collisions at $\sqrt{s_{\mathrm{NN}}}$ = 5.02 TeV. *Phys. Lett. B*, 798:134926, 2019.

[148] W. Zha, S. R. Klein, R. Ma, L. Ruan, T. Todoroki, Z. Tang, Z. Xu, C. Yang, Q. Yang, and S. Yang. Coherent J/ψ photoproduction in hadronic heavy-ion collisions. *Phys. Rev. C*, 97(4):044910, 2018.

[149] Albert M Sirunyan et al. Measurement of the azimuthal anisotropy of Υ(1S) and Υ(2S) mesons in PbPb collisions at $\sqrt{s_{\mathrm{NN}}}$ = 5.02 TeV. *Phys. Lett. B*, 819:136385, 2021.

[150] Ajaharul Islam and Michael Strickland. Bottomonium suppression and elliptic flow using Heavy Quarkonium Quantum Dynamics. *JHEP*, 03:235, 2021.

[151] Xiaojun Yao, Weiyao Ke, Yingru Xu, Steffen A. Bass, and Berndt Müller. Coupled Boltzmann Transport Equations of Heavy Quarks and Quarkonia in Quark-Gluon Plasma. *JHEP*, 21:046, 2020.

[152] Juhee Hong and Su Houng Lee. $\Upsilon(1S)$ transverse momentum spectra through dissociation and regeneration in heavy-ion collisions. *Phys. Lett. B*, 801:135147, 2020.

[153] Klaus Reygers, Alexander Schmah, Anastasia Berdnikova, and Xu Sun. Blast-wave description of Υ elliptic flow at energies available at the CERN Large Hadron Collider. *Phys. Rev. C*, 101(6):064905, 2020.

[154] Jaroslav Adam et al. Centrality dependence of the pseudorapidity density distribution for charged particles in Pb-Pb collisions at $\sqrt{s_{\mathrm{NN}}}$ = 5.02 TeV. *Phys. Lett.*, B772:567–577, 2017.

[155] L. Adamczyk et al. Measurement of J/ψ Azimuthal Anisotropy in Au+Au Collisions at $\sqrt{s_{NN}}$ = 200 GeV. *Phys. Rev. Lett.*, 111(5):052301, 2013.

[156] Shreyasi Acharya et al. J/ψ elliptic and triangular flow in Pb-Pb collisions at $\sqrt{s_{\mathrm{NN}}}$ = 5.02 TeV. *JHEP*, 10:141, 2020.

[157] Denes Molnar and Sergei A. Voloshin. Elliptic flow at large transverse momenta from quark coalescence. *Phys. Rev. Lett.*, 91:092301, 2003.

[158] Xin-Nian Wang. Jet quenching and azimuthal anisotropy of large p_T spectra in noncentral high-energy heavy-ion collisions. *Phys. Rev. C*, 63:054902, Apr 2001.

[159] Miklos Gyulassy, Ivan Vitev, and Xin-Nian Wang. High p_t azimuthal asymmetry in noncentral $A + A$ at rhic. *Phys. Rev. Lett.*, 86:2537–2540, Mar 2001.

[160] Liang Zheng, Hui Li, Hong Qin, Qi-Ye Shou, and Zhong-Bao Yin. Investigating the NCQ scaling of elliptic flow at LHC with a multiphase transport model. *Eur. Phys. J.*, A53(6):124, 2017.

[161] Subhash Singha and Md. Nasim. Scaling of elliptic flow in heavy-ion collisions with the number of constituent quarks in a transport model. *Phys. Rev.*, C93(3):034908, 2016.

[162] J. Adams et al. Azimuthal anisotropy in Au+Au collisions at s(NN)**(1/2) = 200-GeV. *Phys. Rev.*, C72:014904, 2005.

[163] Barbara Betz, Miklos Gyulassy, Matthew Luzum, Jorge Noronha, Jacquelyn Noronha-Hostler, Israel Portillo, and Claudia Ratti. Cumulants and nonlinear response of high p_T harmonic flow at $\sqrt{s_{NN}} = 5.02$ TeV. *Phys. Rev. C*, 95(4):044901, 2017.

[164] Zi-wei Lin and Denes Molnar. Quark coalescence and elliptic flow of charm hadrons. *Phys. Rev.*, C68:044901, 2003.

[165] Jiangyong Jia and Chun Zhang. Quark number scaling of v_2 in transverse kinetic energy and it's implications for coalescence models. *Phys. Rev.*, C75:031901, 2007.

[166] Shreyasi Acharya et al. Elliptic Flow of Electrons from Beauty-Hadron Decays in Pb-Pb Collisions at $\sqrt{s_{NN}} = 5.02$ TeV. *Phys. Rev. Lett.*, 126(16):162001, 2021.

[167] Shreyasi Acharya et al. Transverse-momentum and event-shape dependence of D-meson flow harmonics in Pb–Pb collisions at $\sqrt{s_{NN}} = 5.02$ TeV. *Phys. Lett. B*, 813:136054, 2021.

[168] A. Emerick, X. Zhao, and R. Rapp. Bottomonia in the Quark-Gluon Plasma and their Production at RHIC and LHC. *Eur. Phys. J. A*, 48:72, 2012.

[169] Peter F. Kolb and Ulrich W. Heinz. Hydrodynamic description of ultrarelativistic heavy ion collisions. 5 2003.

[170] Probing charm quark dynamics via multiparticle azimuthal correlations in 5.02 TeV PbPb collisions. Technical report, CERN, Geneva, 2021.

[171] Li Yan and Jean-Yves Ollitrault. Universal fluctuation-driven eccentricities in proton-proton, proton-nucleus and nucleus-nucleus collisions. *Phys. Rev. Lett.*, 112:082301, 2014.

[172] R. Aaij et al. Measurement of J/ψ production in pp collisions at $\sqrt{s} = 7$ TeV. *Eur. Phys. J. C*, 71:1645, 2011.

[173] Morad Aaboud et al. Prompt and non-prompt J/ψ elliptic flow in Pb+Pb collisions at $\sqrt{s_{\mathrm{NN}}}$ = 5.02 Tev with the ATLAS detector. *Eur. Phys. J.*, C78(9):784, 2018.

[174] Vardan Khachatryan et al. Suppression and azimuthal anisotropy of prompt and nonprompt J/ψ production in PbPb collisions at $\sqrt{s_{\mathrm{NN}}} = 2.76$ TeV. *Eur. Phys. J. C*, 77(4):252, 2017.

[175] Morad Aaboud et al. Prompt and non-prompt J/ψ elliptic flow in Pb+Pb collisions at $\sqrt{s_{\mathrm{NN}}}$ = 5.02 Tev with the ATLAS detector. *Eur. Phys. J. C*, 78(9):784, 2018.

université
PARIS-SACLAY

ÉCOLE DOCTORALE
Particules, hadrons, énergie et noyau :
instrumentation, imagerie, cosmos
et simulation (PHENIICS)

Titre: Anisotropie azimuthale de quarkonium dans des collisions d'ions lourds ultrarelativistes avec ALICE au LHC

Mots clés: Quarkonium, QGP, suppression, régénération, anisotropie azimuthale, ALICE

Résumé: Quelques micro-secondes après le Big Bang l'Univers se trouvait dans un état de plasma de quarks et de gluons (QGP). Un tel état peut être recréé dans les collisions d'ions lourds ultrarelativistes au LHC. L'étude de la production des quarkonia, états liés de quarks lourds, est particulièrement pertinente pour comprendre les propriétés du QGP. Les quarkonia sont des particules rares et lourdes produites aux premiers instants de la collision, avant la formation du QGP, ce qui en fait des sondes idéales du QGP. La production de quarkonia peut être soumise à la suppression (écrantage de la paire quark/anti-quark par les nombreux quarks et gluons), et la régénération (création de quarkonia par recombinaison de quarks). Au LHC, $\Upsilon(1S)$ ($b\bar{b}$) et J/ψ ($c\bar{c}$) sont complémentaires, les premiers sont plus aptes à étudier la suppression séquentielle, alors que les seconds permettent d'étudier la régénération. Cette thèse présente les mesures d'anisotropies dans les distributions azimuthales du J/ψ et de l'$\Upsilon(1S)$ révèlant ainsi des mécanismes bien disctincts dans leurs interactions avec le QGP.

Title: Quarkonium azimuthal anisotropy in ultrarelativistic heavy-ions collisions with ALICE at the LHC

Keywords: Quarkonium, QGP, suppression, regeneration, azimuthal anisotropy, ALICE

Abstract: A few micro-seconds after the Big Bang, the Universe was in a quark gluon plasma (QGP) state. Such state could be reproduced in ultrarelativistic heavy ion collisions at the LHC. Among the various QGP observables, the study of quarkonia is particularly important to understand the properties of the QGP. Quarkonia are rare and heavy particles that are produced in the initial stages of the collision, even before the QGP is formed and are therefore ideal probes of the QGP. The production of quarkonia may be subject to the suppression (quark/anti-quark pair ($Q\bar{Q}$) will get screened by the many free quarks and gluons) or the regeneration (new quarkonia could be produced in the QGP by recombination of heavy quarks). At the LHC, $\Upsilon(1S)$ ($b\bar{b}$) and J/ψ ($c\bar{c}$) are complementary, the former are thought to be more suited than to address the sequential suppression, while the latter should allow the study of regeneration. This thesis presents anisotropy measurements in the azimuthal distributions of J/ψ and $\Upsilon(1S)$ which suggests distinct mechanisms in their interactions with the QGP.

Université Paris-Saclay
Espace Technologique / Immeuble Discovery
Route de l'Orme aux Merisiers RD 128 / 91190 Saint-Aubin, France